The Character Dependence of Interfacial Energies in Magnesia

David M. Saylor
Ph.D. Thesis
Materials Science and Engineering Department
Carnegie Mellon University
Pittsburgh, PA 15213

August 23, 2001

Thesis Committee:
Dr. Gregory S. Rohrer (Advisor, Carnegie Mellon University)
Dr. Brent L. Adams (Brigham Young University)
Dr. Anthony D. Rollett (Carnegie Mellon University)
Dr. Paul Wynblatt (Carnegie Mellon University)

Abstract

The thermodynamic driving force for the formation and evolution of microstructures in polycrystalline materials is provided by the excess free energy per unit area associated with interfaces. Data relating the energy of these interfaces to their character, or crystallographic orientation, are required to understand, predict, and control microstructural evolution. We have developed techniques to extract the population and relative energies for all physically distinct surfaces and grain boundaries and applied the techniques to a polycrystalline magnesia sample. The techniques rely on using microscopic observations to characterize the geometry and crystallography of large quantities of interfaces. From these microscopic measurements, the character of the interfaces can be specified, and at triple junctions, where three interfaces intersect, the local equilibrium condition can be used to calculate the energies from the interfacial geometry and crystallography.

We have evaluated the surface energy anisotropy by making observations of circumferential thermal grooves on the surface of the magnesia sample. By examining 269 circumferential thermal grooves, we find that, for magnesia at $1400°C$, the surface energy has a minimum at (100) and a maximum at (111). The relative energies for the low index planes are $\gamma_{110}/\gamma_{100} = 1.07 \pm 0.04$ and $\gamma_{111}/\gamma_{100} = 1.17 \pm 0.04$. These results are consistent with observations of orientation stability at $1400°C$ and with previous theoretical predictions and experimental results for magnesia surfaces.

From the magnesia sample, we have also extracted the geometric and crystallographic configuration of $5.4mm^2$ of grain boundary area and 19094 grain boundary triple junctions in a volume of $0.15mm^3$. These data have enabled us to specify the population and relative energy of grain boundaries over all five macroscopic parameters. The population exhibits a strong preference for grain boundaries with $\langle 100\rangle$ plane normals. By comparing the character distribution to several boundary energy models, we find that the predicted energies vary inversely with the observed population. Furthermore, we find a substantial inverse correlation between the distribution and the energies calculated from the triple junction measurements ($r_s = -0.77$). In general, we find that boundaries with $\langle 100\rangle$ plane normals have reduced energies, which is probably related to the relatively high coordination number of atoms on this plane and its low surface energy.

Acknowledgments

There are many who need to be acknowledged for their critical roles in the development of this thesis. I would first like to thank my thesis advisor, Gregory Rohrer for directing the development of this thesis and guiding my professional growth over the past five years. I would also like to thank my committee members, Brent Adams, Anthony Rollet, and Paul Wynblatt, for many constructive discussions and for their critical review of the material presented in this thesis. Furthermore, I need to acknowledge those who have contributed to this research. I would like to acknowledge Adam Morawiec, who played a vital role in the development of the numerical methods used in the analysis of the grain boundary data, and Darren Mason, for his help in analyzing the thermal groove data. I would also like to acknowledge David Casasent, Kevin Cherry, Jay Kapur, Sowmya Mahadevan, Heiskell Rogan, Ashit Talukder, and Chun-Te (Richard) Wu for their involvement in the development of the automated grain boundary characterization system. Finally, I would like to acknowledge the National Science Foundation for funding this research.

There are many others without whom this thesis would not have been possible. First, I would like to thank my parents, Ronald and Margaret Saylor, and the rest of my family for their love and support over the last 27 years. A special thanks to Ellen Cerreta for being a devoted friend and for always being there when I needed her. I would also like to thank Bassem El-Dasher, Jennifer Giocondi, and Richard Smith who have not only been great friends, but have also been very helpful with the technical aspects of this thesis. In addition, I need to thank my other friends in the department Chun-Chieh (Jimmy) Chang, Andrea Mcdivett, Frank Johnson, Chang Soo Kim, Herb Miller, Paul Salvador, Tomoko Sano, Suzanne Smith, Sammy Tin, and Jason Wolf for all of the great memories during graduate school. Finally, I would like to thank my long-standing friends outside of the department, Alan Horn, Jeff Jesensky, Chris Knarr, Rob Malkin, Gary Miller, Alex Rutkowski, and Trevor Smith, for their camaraderie and for the great times we have had over the years.

Table of Contents

List of Figures

List of Tables

Chapter 1

Introduction

1.1 Motivation

The vast majority of technologically useful materials are polycrystalline. The properties of these materials depend not only on their composition, but also on their microstructure, which is described by the distribution of grain orientations, sizes, and shapes. During material processing, the fundamental thermodynamic driving force for the formation and evolution of the microstructure is provided by the excess free energy associated with interfaces. In a homophase, polycrystalline material, surfaces and grain boundaries are the most important interfaces. Reducing the area of these interfaces, per unit volume of the polycrystal, lowers the overall free energy of the system. For example, the coalescence of particles in a ceramic compact is driven by the associated reduction in surface area and energy. Similarly, grain growth decreases the total grain boundary area, thereby reducing the overall energy associated with the boundaries. The goal of the research described here is to measure the anisotropy of interfacial energies. These data are needed to specify the driving forces for sintering and grain growth and will thus serve as the basis for models that will ultimately allow us to understand, predict, and control microstructural evolution.

1.2 Approach

The main challenge in quantifying interface energies is that the number of physically distinct interfaces that occur in nature is very large. For example, one must specify five macroscopic degrees of freedom and three microscopic degrees of freedom to uniquely describe a grain boundary. The macroscopic degrees of freedom can be parameterized by three Eulerian angles $(\varphi_1, \Phi, \varphi_2)$ that characterize the misorientation range from zero to 2π, π, and 2π, respectively [1], and two spherical angles (θ, ϕ) that characterize the boundary plane normal range from zero to 2π and π, respectively. The microscopic degrees of freedom are usually represented by a translation vector $(\hat{t}_i)$ which defines the relative translation between the adjacent crystals. A reasonable discretization[1] of this eight parameter space would yield approximately 5×10^{11} distinct grain boundary characters. Although crystal symmetries can reduce this number by up to three orders of magnitude, the number of physically distinct boundaries remains large. Furthermore, the experimental techniques that can be used to probe the microscopic degrees of freedom (high resolution transmission electron microscopy and computer simulation) can be applied to only a limited number of boundaries.

It can be argued that if the translation degrees of freedom minimize the energy of the interface at a fixed temperature, pressure, and chemical potential then, at equilibrium, there should be only one translation vector for any given set of macroscopic degrees of freedom. Therefore, to establish structure-property correlations one need only consider the macroscopic degrees of freedom. This ”mesoscale” approximation reduces the number of grain boundary characters for a material with cubic symmetry to around 2×10^5 if a resolution limit of 5° is considered. Furthermore, the space of surface characters is reduced to only two spherical angles (θ, ϕ) representing the vector normal to the surface that range from zero to 2π and π, respectively. With 3° of resolution, there are only about 10^3 surface characters for a material with cubic symmetry. The recent development of automated EBSP-based mapping systems [2–4] now makes it possible to completely probe these do-

---

[1] Assuming 5° angular resolution over the macroscopic parameters and that the microscopic parameters can be characterized by 10^3 discrete translation vectors.

mains of macroscopic character space. For grain boundaries in particular, the energy and character distributions over the entire domain of the parameter space remain relatively unexplored. The fundamental experimental approach used in thesis is to use EBSP-based mapping systems in concert with traditional microscopy techniques to characterize the geometry and crystallography of large quantities of interfaces. These data can be then be used to specify the distribution of interfacial characters. Furthermore, observations of interfacial geometry and crystallography along the lines where three interfaces intersect can be used to extract the interface character-energy relationship. The thermodynamic condition for local equilibrium at these triple junctions can be used to link the interfacial geometry and crystallography to the energies. Thus, if a sufficient number of triple junctions can be characterized, one can determine the energy over the complete range of physically distinct interfacial characters.

1.3 Objective

The objective of this thesis is to determine the population and excess free energy of all physically distinct surfaces and grain boundaries in a polycrystalline magnesia sample. The first goal is to develop and exploit experimental techniques which will allow us to probe the geometry and crystallography of large quantities of interfaces in reasonable time periods. The next goal will be to use the data generated from these techniques not only to specify the interfacial character distribution over the macroscopic parameter space, but also to extract the relative interfacial energy as a function of interfacial character by fitting the observations at triple junctions to the local equilibrium condition. Finally, we want to apply the information to identify the underlying mechanisms that determine interfacial energy anisotropy and control microstructural evolution.

1.4 References

[1] H.-J. Bunge, Texture Analysis in Materials Science, translated by P.R. Morris; Butterworths, London, (1982).

[2] B.L. Adams, S.I. Wright, and K. Kunze, “Orientation Imaging: The Emergence of a New Microscopy,” *Met. Trans.*, **24A** [4], 819-831 (1993).

[3] W. Yang, B.L. Adams, and M. DeGraef, “Adaptive Orientation Imaging Microscopy,” Proc. of the Twelfth International Conference on Textures of Materials, Montreal, Canada, (1999).

[4] C.T. Wu, B.L. Adams, C.L. Bauer, D. Casasent, A. Morawiec, S. Ozdemir and A. Talukder, “Mapping the Mesoscale Interface Structure in Polycrystalline Materials,” *Ultramicroscopy*, submitted.

Chapter 2

Background

This chapter contains an overview of background information relevant to this thesis. First, a description of the origin of interfacial energies and their variation with interfacial character is presented. Next, a brief overview of representations of surfaces and grain boundaries will be given, along with a description of the domains of “physically distinct” interfaces. The local equilibrium condition which links interfacial geometry to energy is then described. Finally, theoretical predictions and previous experimentally determined grain boundary and surface energies are reviewed.

2.1 Interfacial energy

2.1.1 Origin of interfacial energy

Interfaces may be thought of as two-dimensional defects or departures from the ideal crystal lattice structure. The presence of an interface, such as a surface or a grain boundary, requires that atomic bonds be broken or distorted across the interface. The deviation from a perfect crystal increases the energy of the system. Thermodynamically, the excess free energy, γ, of an interface is defined as the reversible work required to create a unit area of interface at constant temperature, volume (or pressure), and chemical potential.

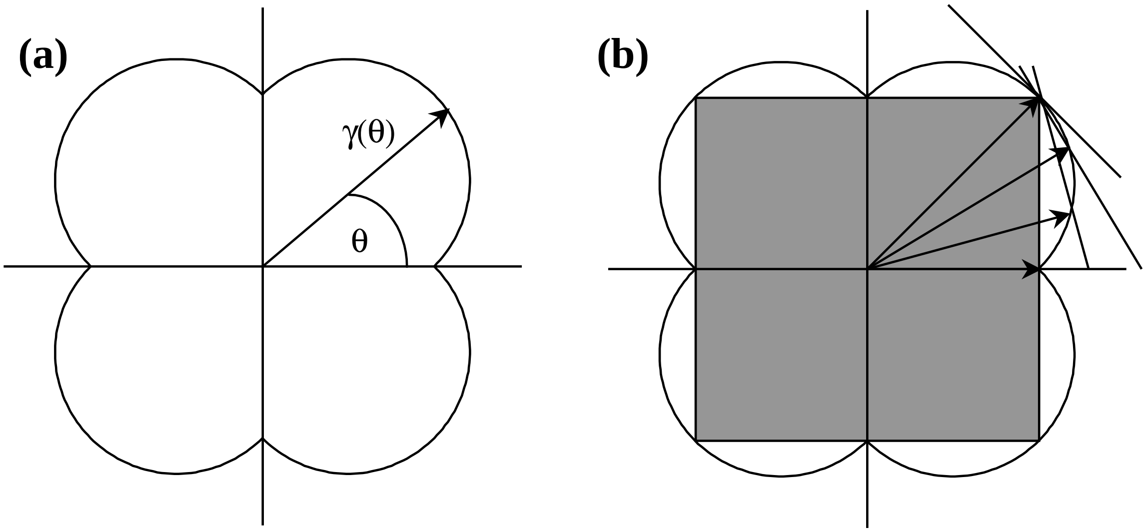

Figure 2.1: Schematic representation of a γ-plot (a) and the corresponding Wulff construction (b). The Wulff construction is generated by first drawing radius vectors from the origin to point where the vector intersects the γ-plot. Lines are then drawn normal to these vectors. The shape formed by the inner envelope of these normals is the equilibrium form which is depicted by the shaded area in (b).

2.1.2 Anisotropy of interfacial energy

In a solid, the crystallinity gives rise to the anisotropy of the energy of a surface or grain boundary. Depending on the crystallography of the interface, the quantity and type of bonds broken or distorted will vary, and therefore the energy of interface will vary. Because the energy is dependent on the crystallography of the interface, the energy should also possess the same symmetries as the crystal structure. A γ-plot can be used to display the energy variation over the space of surface characters and, at a fixed misorientation, the space of grain boundary plane characters. In a γ-plot (see Fig. 2.1a), the direction of the vector represents the orientation of the interface, and the magnitude of the vector is the magnitude of the interfacial energy at that particular orientation. Fig. 2.1a is a simple example where the interface considered is only dependent on only one parameter, θ.

As a system approaches equilibrium, interfaces will attempt to lower their free energy by preferentially increasing the area of crystallographic orientations with relatively low energy at the expense of higher energy orientations. The equilibrium form of the interface can be determined by the Wulff construction. The Wulff construction involves first drawing radius vectors from the origin to the point where the vector intersects the γ-plot. Next, lines are drawn normal to the radius vectors at these intersections. The shape formed by the inner envelope of the normals is the equilibrium form. This process is depicted schematically in Fig. 2.1b. Although this example is given for the simple one parameter case, the same principles apply to the two parameter cases of a surface or a grain boundary plane.

From the Wulff construction, we see that the equilibrium shape will be faceted only if there are singularities (i.e. cusps) in the energy function; however, the presence of facets does not necessarily mean that there are missing orientations on the equilibrium form. If there are missing orientations, the facet will be bounded by a sharp edge; otherwise, the facet will be connected to a smooth curve. Finally, orientations can be missing from the equilibrium form without the presence of facets. If this is the case, the equilibrium form will have smooth curves that meet abruptly at sharp edges.

2.2 Interfacial character

2.2.1 Transformation of coordinate system

Since the character of an interface must be given in terms of crystallographic coordinates, we need a method of transforming laboratory coordinates into crystal coordinates. Although the choice of laboratory reference frame is arbitrary, our laboratory coordinate system, $\hat{e}_i$, is right-handed with $\hat{e}_1$ direction in the plane of the sample pointing away from the observer. The coordinate system is shown schematically in Fig. 2.2a. The transformation from laboratory to crystal coordinates can be denoted by three Eulerian angles $(\varphi_1, \Phi, \varphi_2)$ which are rotations that bring the laboratory reference frame into coincidence with the crystal reference frame ($\hat{e}_i \parallel \hat{e}_i^x$). These angles represent the following rotations: φ_1 is a rotation about $\hat{e}_3$ and the new coordinate system is denoted by $\hat{e}_i'$, Φ is a rotation about $\hat{e}_1'$ which yields the new coordinate system $\hat{e}_i''$, and finally φ_2 is a rotation about $\hat{e}_3''$ which transforms the coordinate system into the crystal coordinate system, $\hat{e}_i^x$. These rotations are shown schematically in Fig. 2.2b-d. Now, we can define a transformation matrix, g, which

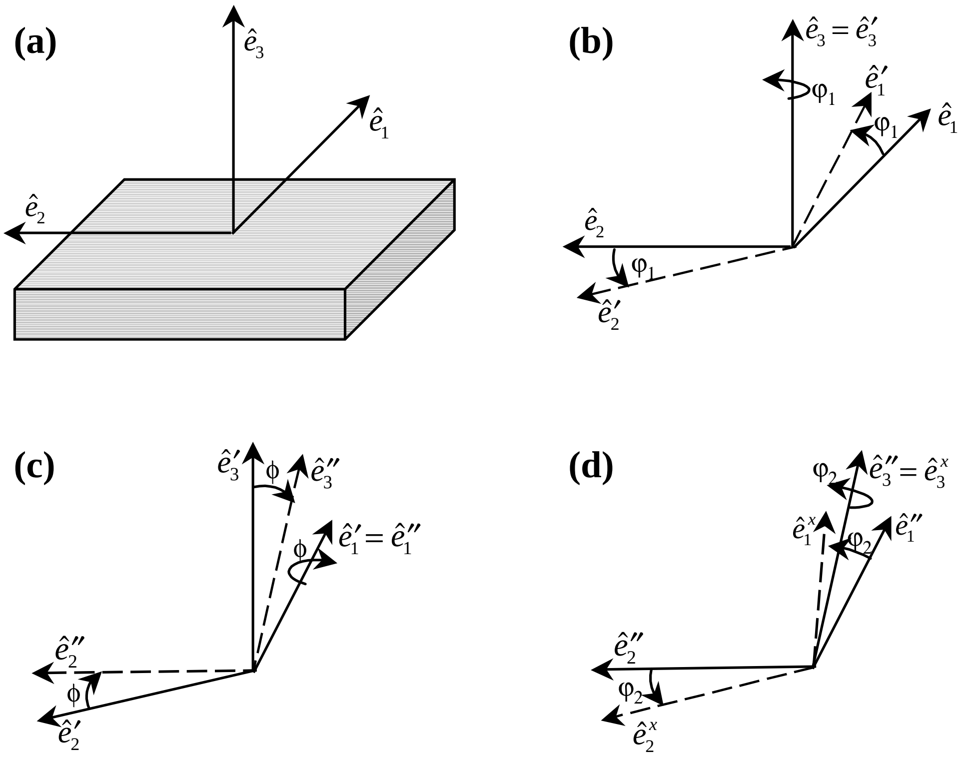

Figure 2.2: Schematic representation of the transformation from the laboratory reference frame $(\hat{e}_i)$ to the crystal reference frame $(\hat{e}_i^x)$ using three Eulerian rotations $(\varphi_1, \Phi, \varphi_2)$. The laboratory reference frame (a) is first rotated by φ_1 about $\hat{e}_3$ and the new coordinate system is denoted by $\hat{e}_i'$ (b). Next, $\hat{e}_i'$ is rotated by Φ about $\hat{e}_1'$ which yields the new coordinate system $\hat{e}_i''$ (c), and finally $\hat{e}_i''$ is rotated by φ_2 about $\hat{e}_3''$ which transforms $\hat{e}_i''$ into the crystal coordinate system,$(\hat{e}_i^x)$ (d).

based on these three rotations transforms laboratory coordinates into crystallographic coordinates, where

$$g(\varphi_1, \Phi, \varphi_2) = \begin{bmatrix} c\varphi_1 c\varphi_2 - s\varphi_1 s\varphi_2 c\Phi & s\varphi_1 c\varphi_2 + c\varphi_1 s\varphi_2 c\Phi & s\varphi_2 s\Phi \\ -c\varphi_1 s\varphi_2 - s\varphi_1 c\varphi_2 c\Phi & -s\varphi_1 s\varphi_2 + c\varphi_1 c\varphi_2 c\Phi & c\varphi_2 s\Phi \\ s\varphi_1 s\Phi & -c\varphi_1 s\Phi & c\Phi \end{bmatrix}, \tag{2.1}$$

and the symbols c and s represent sine and cosine, respectively.

2.2.2 Fundamental zones

Due to crystal symmetries, there exist crystallographically equivalent interfaces within the entire domain of the space of interfacial characters. Thus, it becomes important to clarify a method for selecting a unique representation out of the set of symmetrically equivalent characters. For the common representations of interfaces, which will be discussed in the subsequent sections, crystal symmetries yield contiguous volumes (or areas) of the character space which contain a complete and unique set of interfacial characters. These volumes (or areas) are sometimes referred to as asymmetric domains or fundamental zones. The term “fundamental zone” was first used by Frank [1] to describe the unique volume closest to the origin for the Rodrigues parameterization of orientation space. However, in this document, fundamental zone is used to describe any compact volume of character space that contains a complete and unique set of interfacial characters. Although there are conventions for the choice of a fundamental zone, it is important to note that the choice is arbitrary.

2.2.3 Surface representation

Since the orientation of a surface in independent of in-plane rotations, only two macroscopic parameters which give the vector normal to the surface need to be defined to describe a surface. The normal vector can either be represented by a unit vector in Cartesian coordinates (n_i) or as a point on a unit sphere (θ, ϕ), where the range of θ and ϕ are zero to 2π and π, respectively. If the direction normal to the surface in the laboratory coordinate system, n_i, is determined, the crystallographic direction of the surface, n_i^x, is given by $n_i^x = g_{ij} n_j$. For example, for a surface in the plane of the sample $n_i = \langle 001 \rangle$, thus n_i^x is given by $\langle g_{13}, g_{23}, g_{33} \rangle$.

Ignoring multiplicity, there are 48 symmetrically equivalent orientations for surfaces of a cubic crystal (multiplicity reduces this number for orientations at special positions where there are symmetry elements). The unique zones in the space of surface orientation are shown in the stereographic projection in Fig. 2.3. In this work, we will use the standard stereographic triangle as the fundamental zone for surface orientations. The triangle,

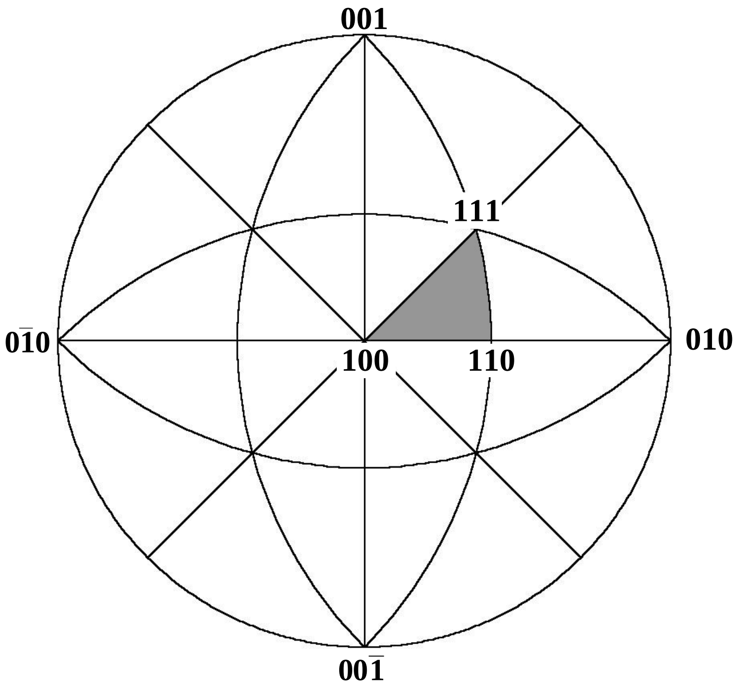

Figure 2.3: A standard stereographic projection. The standard stereographic triangle, a fundamental zone for cubic surface orientations, is denoted by the shaded region. The standard stereographic triangle consists of orientations with $n_i^x \geq 0$ and $n_1^x \geq n_2^x \geq n_3^x$.

shaded in Fig. 2.3, consists of orientations with $n_i^x \geq 0$ and $n_1^x \geq n_2^x \geq n_3^x$.

2.2.4 Grain boundary representation

The grain boundary character can be specified by five macroscopic parameters that define the crystallographic lattice misorientation and boundary plane. The lattice misorientation can be denoted by three Eulerian angles $(\varphi_1, \Phi, \varphi_2)$ with ranges of zero to 2π, π, and 2π, respectively. These angles describe rotations about the laboratory reference frame which will bring the two adjacent crystals into coincidence ($\hat{e}_i^{x_1} \parallel \hat{e}_i^{x_2}$). The boundary plane, similar to a surface, can then be characterized by a unit vector (n_i) or two spherical angles (θ, ϕ) with ranges of 2π and π, respectively.

Misorientation

The lattice misorientation, Δg, is calculated from the measured orientations (g_a, g_b) of adjacent pairs of crystallites. Because it is arbitrary which crystal is rotated into the coincidence with the other, there are $2 \times N^2$ equivalent misorientations, where N is the number of proper symmetry operators for a given crystal symmetry. The $2 \times N^2$ equivalent lattice misorientations are then given by

$$\Delta g_{ab} = g_a g_b^T \quad \text{and} \quad \Delta g_{ab} = (\Delta g_{ab})^T = c_a \Delta g_{ab} c_b, \tag{2.2}$$

where c_a and c_b are proper symmetry operators.

Although the fundamental zone for misorientation in the space of Euler angles has been determined for cubic symmetry [2], the shape is complex and bounded by curved surfaces, and the relationship between Euler angles and crystallographic coordinates is not straightforward. We can avoid these problems by using the Rodrigues parameterization of misorientation [1]. There is a direct relationship between the mapping of misorientations in Rodrigues space and crystallographic coordinates, and the parameterization yields fundamental zones that are regular polygons bounded by planes. In the Rodrigues parameterization, the lattice misorientation is represented as a vector with components, $r_i = n_i \tan(\omega/2)$, where n_i are the components of the unit vector representing the misorientation axis and ω is the misorientation angle. From Δg, ω can be determined from $\omega = \cos^{-1}\left[(\Delta g_{ii} - 1)/2\right]$, and n_i can be determined from $n_i = -\varepsilon_{ijk} \Delta g_{jk}/(2 \sin \omega)$, where ε_{ijk} is the permutation tensor.

For the case of cubic symmetry, there are 24 proper symmetry operators; thus, there exist $2 \times 24^2 = 1152$ equivalent misorientations that need to be considered. Heinz and Neumann [3] were the first to determine the fundamental zone for the Rodrigues parameterization of cubic misorientations, along with the misorientations for hexagonal, orthorhombic, and tetragonal crystal structures. The result was later repeated by Morawiec and Field [4], who found the fundamental zone for misorientations in Rodrigues space for all crystal symmetries. The restricted domain for cubic misorientations is shown in Fig. 2.4. The unique representation is selected such that the misorientation angle, ω, is as small as possible and that the rotation axis lies in the standard stereographic triangle, $n_1 \geq n_2 \geq n_3 \geq 0$.

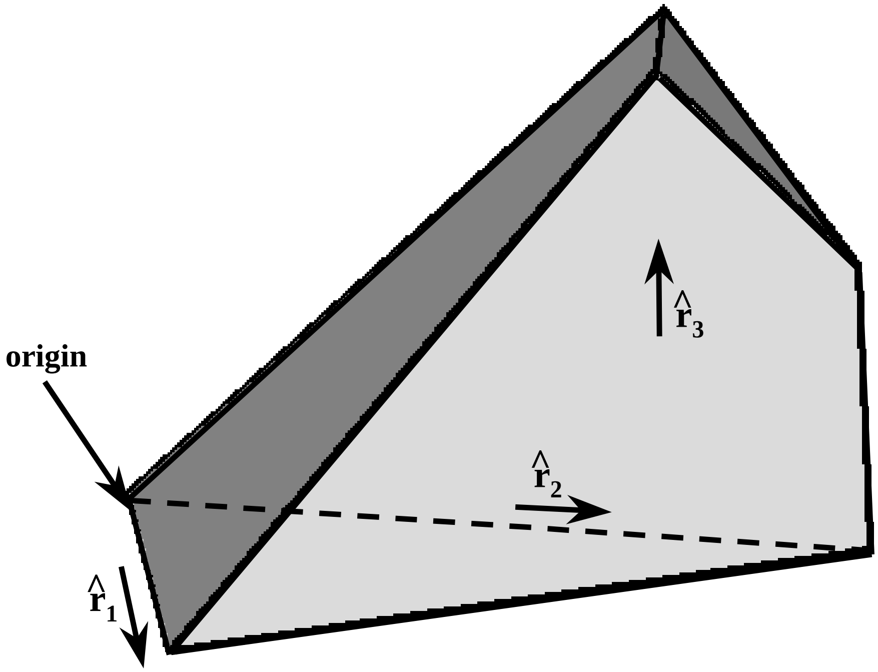

Figure 2.4: The fundamental zone for the Rodrigues parameterization of cubic misorientations. The unique representation is selected such that the misorientation angle, ω, is as small as possible and that the misorientation axis lies in the standard stereographic triangle, $n_1 \geq n_2 \geq n_3 \geq 0$.

Although it is not a unique representation, lattice misorientation is often given in terms of the disorientation angle, θ. The disorientation between two crystallites is defined as the minimum misorientation angle that will bring the crystallites into coincidence. For the case of cubic symmetry, θ ranges from zero to 62.80° [3]. Because the disorientation representation ignores the misorientation axis, many physically distinct misorientations will have identical disorientations. These misorientations will have Rodrigues vectors with the same magnitude; therefore, in Rodrigues space the misorientations corresponding to a given disorientation angle are given by the surface of a sphere with radius $\tan\theta/2$ that is centered on the origin.

Boundary plane

Because there are two indistinguishable choices for the boundary plane normal, the space of boundary planes for a given misorientation has inversion symmetry. It follows that, except for the special case when the misorientation axis is parallel to an axis with rotational symmetry, the fundamental zone for the space of boundary planes will be a hemisphere with θ and ϕ in the range of zero to π. Here, we have chosen the fundamental zone such that the third component of the unit vector parallel to the crystallographic normal of the boundary plane is positive. It is also arbitrary which of the two adjacent crystallites is selected as the reference frame. This ambiguity is avoided by always expressing the plane normal in terms of the first (non-transposed) crystallite reference frame. Furthermore, if the misorientation axis is parallel to an n-fold symmetry axis, the range of the fundamental zone for the space of boundary planes is reduced to θ ranging from zero to $\pi/2$ and ϕ ranging zero to $2\pi/n$. Thus, to represent a boundary in the fundamental zone of the macroscopic grain boundary character space, one must determine both the unique representation of the Rodrigues vector and boundary plane normal.

Twist and tilt

We have already reviewed the five macroscopic parameters that define a grain boundary; however, another common way of describing the boundary plane is in terms of its twist and tilt components. The tilt and twist components of the boundary plane are defined as a rotation about the misorientation axis and a rotation about an axis which lies perpendicular to the misorientation axis, respectively. Thus, if the boundary plane normal is parallel to the misorientation axis, the boundary is considered to be pure twist, and if the boundary plane normal lies perpendicular to the misorientation axis the boundary is pure tilt. Finally, if the boundary plane normal is somewhere in between pure tilt and pure twist, it can be described by a combination of the two.

2.3 Triple junction equilibrium

The condition for local equilibrium at a triple junction with anisotropic interfacial energies that relates the interfacial geometry and crystallography to the energies of the three

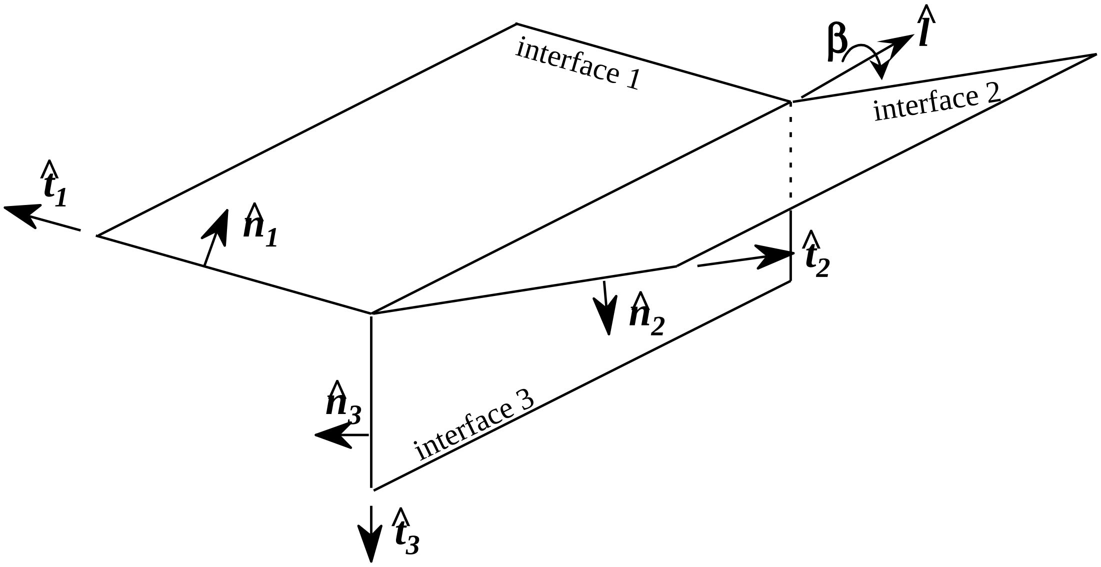

Figure 2.5: Schematic representation of a triple junction where three interfaces intersect. The geometric and crystallographic quantities in the Herring relation (Eqn. 2.3) are also depicted.

interfaces was originally described by Herring [5]:

$$\sum_i \gamma_i \hat{t}_i + \hat{n}_i \frac{\partial \gamma_i}{\partial \beta_i} = 0. \tag{2.3}$$

In Eqn. 2.3, which represents a balance of forces, γ_i is the excess free energy per unit area of the i^{th} interface, $\hat{t}_i$ is the unit vector that lies in the i^{th} interface and is normal to the line of intersection of the three interfaces $(\hat{\ell})$, $\hat{n}_i$ is the unit vector normal to the line of intersection such that $\hat{n}_i = \hat{\ell} \times \hat{t}_i$, and β_i is the right handed angle of rotation about $\hat{\ell}$ for the i^{th} boundary measured from a reference direction. These quantities are depicted schematically in Fig. 2.5.

The interfacial energies in Eqn. 2.3 can be determined if the geometric and crystallographic quantities in Fig. 2.5 can be determined experimentally. However, a problem arises in that there are three unknowns in the Herring relation and only two independent equations. This problem can be circumvented if a sufficient number of triple junctions are characterized, such that interfaces of the same character are found in multiple junctions. If enough interfacial characters overlap, the system of equations can be overdetermined.

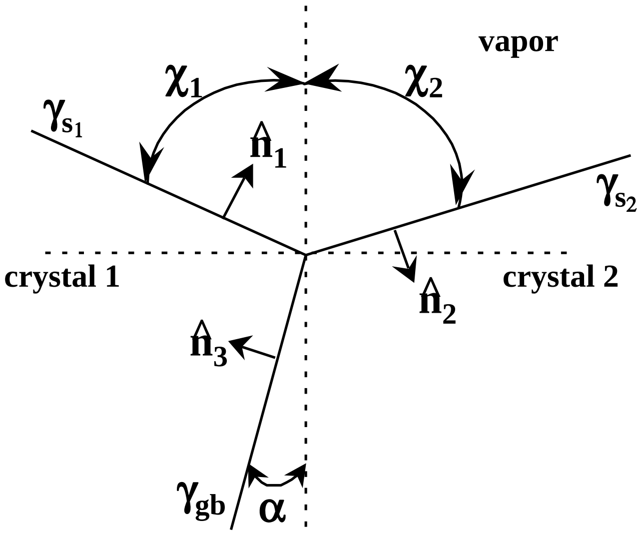

Figure 2.6: Schematic representation of a thermal groove.

2.3.1 Thermal grooves

If sufficient atomic migration is possible, a thermal groove will form at the intersection of a grain boundary and free surface in order to balance the interfacial tensions. Fig. 2.6 shows a schematic of a thermal groove. Again, the geometry and crystallography of the triple junction formed by the thermal groove is linked to the relative energies of the interfaces by the Herring relation. The force balance represented by the Herring relation can be broken down into two perpendicular components. With reference to Fig. 2.6, the force balance normal to the macroscopic sample surface is:

$$\gamma_3 \cos\alpha - \frac{\partial\gamma_3}{\partial\alpha}\sin\alpha = \gamma_1\cos\chi_1 - \frac{\partial\gamma_1}{\partial\chi_1}\sin\chi_1 + \gamma_2\cos\chi_2 - \frac{\partial\gamma_2}{\partial\chi_2}\sin\chi_2, \tag{2.4}$$

and the force balance parallel to the macroscopic sample surface is:

$$-\gamma_3 \sin\alpha - \frac{\partial\gamma_3}{\partial\alpha}\cos\alpha = \gamma_1\sin\chi_1 - \frac{\partial\gamma_1}{\partial\chi_1}\cos\chi_1 + \gamma_2\sin\chi_2 - \frac{\partial\gamma_2}{\partial\chi_2}\cos\chi_2. \tag{2.5}$$

The symbols in Eqns. 2.4 and 2.5 are defined in Fig. 2.6.

Thermal grooves represent a unique type of triple junction where the energies of two different types of interfaces (surfaces and grain boundaries) are linked by the Herring relation. This allows the local equilibrium condition to be simplified if one of the interfacial energies can be held constant. A common method for probing the grain boundary energy is to measure only the surface dihedral angle, ψ_s, ($\chi_1 + \chi_2$ in Fig. 2.6) of a thermal groove. By assuming that the surface energy of the material is isotropic, the grain boundary energy is independent of boundary plane, and the boundary is normal to macroscopic sample surface, the Herring relation simplifies to:

$$\frac{\gamma_{gb}}{\gamma_s} = 2\cos\left[\frac{\psi_s}{2}\right]. \tag{2.6}$$

Using Eqn. 2.6, the relative energy of a grain boundary can be determined from experimental observations of ψ_s. Although it is a common practice to apply these simplifying assumptions, they are not always valid. One of the goals of this thesis is to avoid these assumptions when applying the Herring relation to thermal groove measurements.

2.3.2 Grain boundary triple junctions

The Herring relation can also be applied to grain boundary triple junctions, i.e. the intersection of three grain boundaries (see Fig. 2.7). If we ignore the influence of the grain boundary plane on the energy, the condition for local equilibrium at a grain boundary triple junction reduces to the well known Young equation:

$$\sum_i \gamma_i(\Delta g)\cos\chi_{ij} = 0, \tag{2.7}$$

where γ_i, the energy of the i^{th} boundary, is assumed to be a function only of the misorientation (Δg) and χ_{ij} denotes the angle between $\hat{t}_i$ and $\hat{t}_j$, as shown in Fig. 2.7. Equation 2.7 can also be rewritten in the following form:

$$\frac{\gamma_1}{\sin(\chi_{23})} = \frac{\gamma_2}{\sin(\chi_{31})} = \frac{\gamma_3}{\sin(\chi_{12})}. \tag{2.8}$$

Equation 2.8 is also known as the law of sines and gives the relationship between any two of the three boundaries meeting at a triple junction. However, ignoring the grain boundary plane influence on grain boundary energy is not always a valid assumption. Therefore, in this thesis, we shall apply the Herring relation to grain boundary triple junction measurements without making any simplifying assumptions.

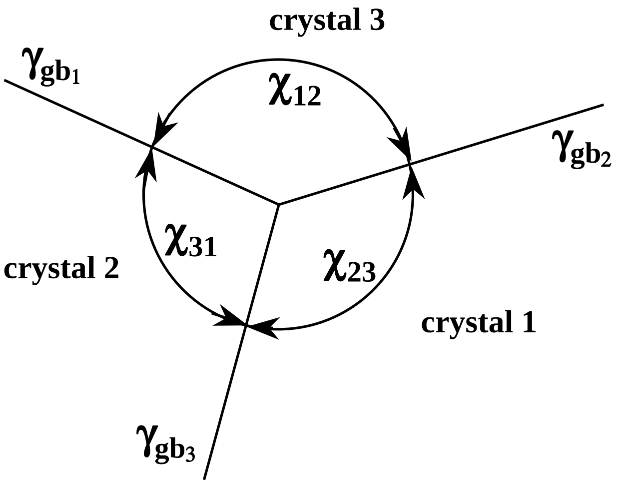

Figure 2.7: Schematic representation of a grain boundary triple junction.

2.4 Surface energy

2.4.1 Theoretical predictions

Broken bond model

The broken bond model is the simplest model for approximating the energy of solid surfaces. The model ignores entropy $(T = 0K)$ and relaxation effects and considers only nearest neighbor interactions. The energy of a surface is given by the total energy of the bonds per unit area that are required to be broken to form that surface. Therefore, using the simplest approximation, the energy of a surface should scale with the density of broken bonds.

In the broken bond model, the energy to form a surface is given as $2\gamma_s$ (two surfaces are formed) is equal to the product of the number of surface atoms per unit area, number of broken bonds per surface atom, and energy per broken bond. For example, in the rock salt structure, each cation forms a bond to 6 anions with a bond energy, ϕ. The (100) surface has 4 atoms per a^2 area with 1 broken bond per atom, and the (110) surface has 4 atoms per $\sqrt{2}a^2$ area with 2 broken bonds per atom, thus $\gamma_{100} = 2\phi/a^2$ and $\gamma_{110} = 2\sqrt{2}\phi/a^2$. To form a (111) surface 3 bonds per atom must be broken, and there are $4/\sqrt{3}a^2$ atoms per area which yields $\gamma_{111} = 2\sqrt{3}\phi/a^2$. Therefore, by using the broken bond model we get the following relationships between the low index planes in rock salt: $\gamma_{110}/\gamma_{100} = \sqrt{2}$ and $\gamma_{111}/\gamma_{100} = \sqrt{3}$. Although this model only gives us a simple approximation of the surface energy, the general trends derived from the model, such as $\gamma_{100} < \gamma_{110} < \gamma_{111}$, are likely to be valid.

The simple bond breaking model also predicts that as the orientation deviates away from a low index orientation the surface energy will increase. Surfaces near low index orientations (vicinal surfaces) will break up into a terrace-step structure where the surface consists of large terraces of the low index orientation separated by monoatomic ledges. Because additional bonds must be broken to form the ledges, the surface energy should be higher than that of the low index orientation. Furthermore, as the deviation from the low index orientation increases, more ledges are required to compensate, thus the energy of the surface should also increase.

Polar surfaces

Although the simple bond breaking model predicts that orientations vicinal to a low index plane have relatively higher energies because additional bonds must be broken to create a terrace-step structure, this rationale does not necessarily apply to a polar surface. It has been argued that because a polar surface has a dipole moment, its energies will always be larger than the energies of other surfaces of the same solid that are either charge neutral or charged, but lacking a dipole moment [6]. In this case, while the step creation does break additional bonds, it also introduces ions of the opposite sign and this reduces the surface charge imbalance. For example, adjacent (111) terraces of the rock salt structure separated by monoatomic steps are terminated by ions of opposite charge. Thus, a decrease in the surface energy with step density can occur if the gain in electrostatic stability is greater than the cost of breaking bonds to create steps.

2.4.2 Experimental measurements

Thermal groove geometry

Methods for extracting the surface energy anisotropy from thermal groove geometry measurements are described in this section. The measurements rely on limiting the variations in the grain boundary energy so that the left hand side of Eqn. 2.4 is constant over many grooves. Because these methods apply only to crystalline materials that twin extensively or can be drawn into wires and recrystallized, they have been applied only to fcc metals such as Ni [7], Cu [8–10], γ-Fe [11], and Au [12]. The maximum anisotropy reported in each of these studies ranged from $2-8\%$.

Mykura [7] was the first to use groove measurements to extract relative surface energies. The key feature of Mykura's [7] method is that all of the thermal groove measurements are made at twin boundaries. By measuring only thermal grooves at grain boundaries with the same character, the potentially overwhelming grain boundary energy anisotropy can be eliminated in such a way that the energies of the free surfaces and their derivatives are the only remaining unknown variables in Eqn. 2.4. By making some simple approximations, Mykura [7] was able to solve for the surface energy derivatives (torque terms) in Eqn. 2.4, and through graphical integration of these derivatives he was able to obtain the orientation dependence of the surface energy.

Mykura's [7] method was advanced by Winterbottom and Gjostein [12,13], who approximated the surface energy as a truncated double Fourier series and used the method of least squares to determine the unknown coefficients of the series which best fit a set of thermal groove observations. One limitation of Mykura's [7] method is that it can be applied only to the relatively small number of materials that exhibit a high population of twin boundaries. McLean and Gale [9,10] devised a more general method involving the characterization of circumferential thermal grooves on the surface of cylindrical wires with a bamboo microstructure. Grooves at different positions around the circumference of the wire are bounded by a range of crystallographically distinct free surfaces, but always have the same grain boundary at the root.

Table 2.1: Relative surface energies of alumina determined from the geometry of internal cavities.

Plane	$1600°C$ [43]	$1600°C$ [44]	$1800°C$ [44]
(0001)	1.0	1.0	1.0
$(10\bar{1}1)$	1.07 ± 0.02	0.947 ± 0.016	1.042 ± 0.019
$(10\bar{1}2)$	1.05 ± 0.02	0.855 ± 0.017	0.950 ± 0.030
$(11\bar{2}0)$	1.22 ± 0.05	0.947 ± 0.026	1.080 ± 0.017
$(11\bar{2}3)$	1.06 ± 0.02	0.957 ± 0.026	1.029 ± 0.016
$(10\bar{1}0)$	> 1.16	> 1.008	> 1.115

Other crystallographically indexed surface features

The thermal groove measurement techniques described above yield a functional form for the orientation dependence of surface energy; however, other crystallographically indexed surface features can be used evaluate surface energy anisotropy. For example, the equilibrium geometries of thermal facets [14,15], small crystallites [16,17], and internal cavities [18–21] have all been used to deduce relative surface energies. Most relevant to this document are the measurements of the relative surface energies in alumina from the geometry of internal cavities [20,21]. The results of these measurements are summarized in Table 2.1. As one would expect, these measurements demonstrate a higher surface energy anisotropy $(14 - 22\%)$ for alumina than the value obtained for fcc metals in the thermal groove experiments. Furthermore, the work of Kitayama and Glaeser [21] shows not only that the total surface energy anisotropy decreases with increasing temperature, but also that the relative values of the energies are temperature dependent. Finally, we must mention that the discrepancies in the two studies between the relative energy values at $1600°C$ are most likely due to a difference in the impurity levels in the two samples.

Table 2.2: Model calculations of surface energy for magnesia, J/m^2.

(100)	(110)	(211)	(111)	Method
1.16	2.92			Electrostatic model [22]
1.43				*Ab initio* Hartree Fock LCAO [23]
1.07	2.78			Electrostatic model [24]
2.64			12.80	Harris-Foulkes function (LDA) [25]
0.98	2.29	4.35		Self-consistent tight binding [26]

Calculations

There have been a number model calculations of the surface energy of ceramic compounds; however, here we shall review only those calculations made for surfaces of magnesia and alumina. The model calculations of the surface energy of magnesia are summarized in Table 2.2 [22–26]. With one exception, these studies place the energy of the (100) surface in the vicinity of $1.0 J/m^2$ at $0K$. Further, in the cases where the energies of more than one surface were computed, the energies of the low index planes are ordered in the same manner predicted by the simple broken bond model $(\gamma_{100} < \gamma_{110} < \gamma_{111})$. A number of studies have also predicted the surface energy of low index planes in alumina [27–30]. A summary of these data is provided in Table 2.3. Although the ordering of the energies vary in these studies, we see that the surface energy of the basal (0001) plane is approximately $2J/m^2$ in all but one case. Furthermore, three of the four studies also predict total anisotropies $(15-27\%)$ that are nearly equivalent to the total anisotropy witnessed in the internal cavity experiments. Finally, we must mention that all surface energy calculations reviewed here ignored entropic effects $(T = 0K)$; therefore, we would expect to see lower anisotropies in any equilibrium experiment conducted at an elevated temperature.

Table 2.3: Model calculations of surface energy for alumina, J/m^2.

(0001)	$(10\bar{1}1)$	$(10\bar{1}2)$	$(11\bar{2}0)$	$(10\bar{1}0)$	Method
2.97	3.27	2.57	2.65	2.89	Interaction model [27]
2.03	2.52	2.29	2.50	2.23	Interaction model [28]
1.76	2.55	1.97	1.86	1.40	First principles [29]
2.04			2.27	2.35	Molecular dynamics [30]

2.5 Grain boundary energy

2.5.1 Theoretical predictions

Read-Shockley

The Read-Shockley [31] model for grain boundary energy is based on the idea that for small angle misorientations, arrays of dislocations compensate for the structural deviations between the two crystals. In this case, the boundary energy is equivalent to the energies of the dislocations. As the misorientation increases from zero, more dislocations are required to compensate for the deviations, and the energy increases. However, as the density of dislocations at the boundary increases with misorientation, the strain fields surrounding them begin to cancel out, and the energy increases at a decreasing rate until it reaches a constant value at some limiting angle. The relationship between the energy of the grain boundary and the misorientation angle is given by $\gamma_{gb} = E_o\alpha(A - \ln\alpha)$, where E_o is a function of the elastic properties of the material, A depends on the core energy of the dislocation, and α is the misorientation angle in radians. The function is only valid to a limiting misorientation angle, typically 15°. When the misorientation angle exceeds the limiting angle, the individual dislocation cores begin to overlap and can not be distinguished. For misorientations greater than the limiting angle, the grain boundary energy is expected to be nearly independent of misorientation based on this model.

Coincidence site lattice (CSL)

For certain discrete misorientations, a number of lattice sites might coincide if the two crystallites were superimposed. These misorientations are known as coincidence site lattices (CSLs). CSLs are characterized by Σ which denotes the reciprocal density of coincident sites, thus as the number of coincident sites decreases, Σ increases. Because atomic bonding is left undistorted at these lattice sites, the energy of a grain boundary with a misorientation at or near a CSL misorientation is expected to have a lower energy than for a general high angle misorientation, especially for low values of Σ. Furthermore, because the number of coinciding sites scales inversely with Σ, the energy of the boundary is also expected to scale inversely with Σ. We must also note that while the fractional lattice coincidence is determined by the misorientation alone, it is only for certain special boundary planes and microscopic translations that the atoms in the intergranular region occupy coincident positions. For other planes separating crystallites of the same misorientation, there is no reason to anticipate that the energy should scale with the lattice coincidence.

For slight deviations from the exact CSL misorientation, the deviation can be accommodated by dislocations in the CSL lattice which conserve the periodicity [32]. The behavior is similar to the Read-Shockley model described above for low angle misorientations. Therefore, we expect the same cusp-like behavior to occur at CSL misorientations; as the deviation from the CSL misorientation increases, more dislocations are required to compensate, and the energy of the boundary increases. Brandon's criterion [32], which corresponds to a relationship based on periodicity alone, is usually used to define the width of the cusp and is given by $\theta_{mis} = \theta_{lim}\Sigma^{-\frac{1}{2}}$. Here, θ_{mis} is the maximum angular deviation from the CSL misorientations and θ_{lim} is the angular limit for a low angle boundary, typically 15°.

Broken bond model

An alternative method for theoretically predicting the energy of a grain boundary is to extend the broken bond model used for the surface energy. The energy of a grain boundary, γ_{gb} can be thought of as the sum of the energies of the two surface planes, γ_{s_i}, minus a binding energy, E_b, which is the energy that is recovered from creating bonds when the two surfaces are joined to form the boundary, $\gamma_{gb} = \gamma_{s_1} + \gamma_{s_2} - E_b$. For general grain boundaries, those not near “special” crystallographic positions, the binding energy can be approximated as a constant value, and the boundary energy should scale linearly with the sum of the energies of the two surfaces. This should be a reasonable approximation because, for a general grain boundary, the combined repeat units of the two surfaces making up the boundary will not form a commensurate structure. Therefore, essentially every atom on the boundary plane will be subject to a different set of interatomic forces. Since the contributions from different atoms can vary only between certain limits and the interatomic forces will be averaged over a very large number of atoms, the energy recovered by forming the boundary (E_b) will average to a constant. Note that the approximation does not hold for grain boundaries near “special” crystallographic positions where there are substantially fewer broken or distorted bonds than a general boundary; however, these boundaries are rare in random polycrystals [33] and, therefore, are of questionable significance. Although there are no experimental data that substantiate the relationship between the surface and grain boundary energies, it has been demonstrated in the results of computer simulations for fcc metals reported by Wolf [34]. By comparing calculated values of the surface and grain boundary energies, Wolf showed that, for general boundaries, the grain boundary energy varies linearly with the sum of the two surface energies of the terminating planes, and that it intercepts the sum of the two surface energies ($\gamma_{gb} = 0$) at a positive finite value (E_b). Based on these results, it appears that the sum of the two surface energies of the boundary planes should be a reasonable approximation of the energy of a general grain boundary.

2.5.2 Experimental measurements

Thermal grooves

The surface dihedral angle of a thermal groove can be used as a direct measure of the relative grain boundary energy using Eqn. 2.6. In the past, a variety of techniques have been used to measure the surface dihedral angles of thermal grooves in ceramic systems, including profilometry [35], optical microscopy [36], optical interferometry [37–40], carbon reference line (CRL) [41,42], and metal reference line (MRL) [43,44]. These data were reviewed by Handwerker *et al.* [43,44] who showed that the systematic errors in the measurement decrease as the resolution limit increases. In the same study, Handwerker *et al.* [43,44] made MRL measurements on grooves in magnesia, alumina, and magnesia-doped alumina and corrected their measurements to account for the resolution limit of the technique. Thus, these measurements based on MRL observations are the most reliable pre-existing measurements of the surface dihedral angle. The corrected MRL observations yielded median values of the surface dihedral angle to be $105°(\gamma_{gb}/\gamma_s = 1.22)$, $106°(\gamma_{gb}/\gamma_s = 1.20)$, and $113°(\gamma_{gb}/\gamma_s = 1.10)$ for magnesia, alumina, and magnesia-doped alumina, respectively.

There have also been a number of bicrystal studies [35,39,40,45] on ceramic systems where the misorientation dependence of γ_{gb}/γ_s has been probed using groove measurements for a series of tilt and twist boundaries misoriented along low index axes. Both Ready and Jech [35] and Dhalenne *et al.* [39] examined the variation of γ_{gb}/γ_s with misorientation angle for symmetric $\langle 100\rangle$ tilt boundaries in NiO. The studies yielded similar results; they found that the grain boundary energy variation with misorientation angle for these special boundaries was consistent with the Read-Shockley model. The energy increased from zero at zero misorientation to an approximately constant value after $20°$. However, in both cases the results were not consistent with the CSL model. The relative energy measured near the $\Sigma 5$ misorientation $36.86°$ was not significantly different than the other high angle boundaries that were examined.

A number of other bicrystal studies on ceramic materials are not only consistent with the Read-Shockley model at low misorientations, but also demonstrate the validity of the CSL model. Kimura *et al.* [45] and Dhalenne *et al.* [40] examined the variation of γ_{gb}/γ_s with misorientation angle for $\langle 110\rangle$ symmetric tilt boundaries, in magnesia and nickel oxide, respectively. For boundaries with misorientations greater than approximately $20°$, they discovered that those with a high degree of coincidence had a relatively lower energy than those that did not. These studies also demonstrate the effect of the boundary plane on energy for CSL misorientations. For example, rotations of $70.53°$ and $109.47°$ about $[110]$

are both $\Sigma3$ misorientations; however, a high degree of coincidence in the intergranular region occurs only for symmetric $\{111\}$ boundary planes. This configuration is realized by a symmetric 70.53° rotation, but not for the symmetric 109.47° rotation. In the case of magnesia, the energy of 109.47° $\Sigma3$ rotation was approximately 40% higher than the 70.53° $\Sigma3$ rotation [45]. The effect was even larger in the nickel oxide case where the energy of the 109.47° $\Sigma3$ rotation was 300% higher than the 70.53° $\Sigma3$ rotation [40].

Grain boundary triple junctions

Numerous studies [46-50] have been conducted to quantify the geometry of grain boundary triple junctions. Although the observations in these studies are mostly limited to distributions of grain boundary dihedral angles, in a few cases the dihedral angle measurements were used to extract relative energies and their dependence on grain boundary character. For example, Dunn and Lionetti [47] made dihedral angle measurements from grain boundaries in a series of silicon ferrite tricrystals. The crystals were fabricated such that all boundaries had a $\langle 110\rangle$ tilt character and that each tricrystal had one boundary misoriented by approximately 15°. Because each tricrystal had one boundary with equivalent character, Eqn. 2.8 could be used to extract the relative energies of all boundaries with respect to the common one. The results showed Read-Shockley behavior at low misorientations with the function approaching a maximum at approximately 25°. Furthermore, the energy function showed a distinct cusp in the vicinity of the 70.53° $\Sigma3$ rotation.

Calculations

Much like the bicrystal studies discussed above, the use of computer simulation to calculate grain boundary energy dependence on character for ceramic materials is limited to symmetric tilt and twist rotations about low index axes. The present discussion is limited to ceramic materials which have the rock salt structure. Wolf [51,52] has determined the energy variation with misorientation angle for $\langle 100\rangle$ twist boundaries in magnesia [51] and a series of alkali-halide compounds [52]. For each of these materials, a grain boundary energy variation consistent with the Read-Shockley model was found. In each case, as the misorientation angle increased, the energy increased at a decreasing rate until a limiting angle of approximately $20 - 25^\circ$. For larger misorientations, the energy was nearly independent of rotation angle. A similar trend was demonstrated by Duffy and Tasker [53] for $\langle 100 \rangle$ symmetric tilt boundaries in nickel oxide; however, they did find evidence of a cusp in the energy function at the $\Sigma 5$ misorientation. Duffy and Tasker [54] have also computed the grain boundary energy for symmetric $\langle 110 \rangle$ tilt boundaries in nickel oxide. The calculations demonstrated the existence of a strong cusp at the 70.53° rotation $(\Sigma 3)$.

2.6 Summary

In the preceding sections, we have reviewed previous experimental measurements of grain boundary and surface energies, and we find that the scope of these studies is quite limited. We have described a number of different methods that have been used to experimentally deduce relative surface energies. However, these techniques have a limited range of applicability because they demand either special microstructural features or specimen geometries. Furthermore, previous experimental measurements of relative grain boundary energies have focused on one-dimensional slices through the five-dimensional grain boundary character space, and the vast majority of the space of grain boundary types remains completely unexplored. Therefore, more generally applicable techniques capable of probing the entire ranges of interfacial character space are required so that we can adequately characterize these interfacial energies for any material. The development and implementation of these techniques are the subject of the rest of this document.

2.7 References

[1] F.C. Frank, “Orientation Mapping,” *Met. Trans.*, **19A** [3], 403-408 (1988).

[2] J. Zhao and B.L. Adams, “Definition of an Asymmetric Domain for Intercrystalline Misorientation in Cubic Materials in the Space of Euler Angles,” *Acta. Cryst.*, **A44**, 326-336 (1988).

[3] A. Heinz and P. Neumann, “Representation of Orientation and Disorientation Data for Cubic, Hexagonal, Tetragonal, and Orthorhombic Crystals,” *Acta Cryst.*, **A47** [6], 780-789 (1991).

[4] A. Morawiec and D.P. Field, “Rodrigues Parameterization for Orientation and Misorientation Distributions,” *Phil. Mag. A*, **73** [4], 1113-1130 (1996).

[5] C. Herring, pp. 143-79 in The Physics of Powder Metallurgy. Edited by W.E. Kingston. McGraw Hill, New York, 1951.

[6] P.W. Tasker, “The Stability of Ionic Crystal Surfaces,” *J. Phys. C: Solid State Phys.*, **12** [22], 4977-4984 (1979).

[7] H. Mykura, “The Variation of the Surface Tension of Nickel with Crystallographic Orientation,” *Acta Met.*, **9** [6], 570-576 (1961).

[8] W.M. Robertson and P.G. Shewmon, “Variation of the Surface Tension with Orientation in Copper,” *Trans. Metall. Soc. AIME*, **224** [4], 804-811 (1962).

[9] M. McLean and B. Gale, “Surface Energy Anisotropy by an Improved Thermal Grooving Technique,” *Philos. Mag.*, **20** [167], 1033-1045 (1969).

[10] B. Gale, R.A. Hunt, and M McLean, “An Analysis of Surface Energy Anisotropy Data using Lattice Harmonics,” *Philos. Mag.*, **25** [4], 947-960 (1972).

[11] M. McLean and H. Mykura, “The Orientation Dependence of Surface Tension for Face-Centered-Cubic Iron,” *Acta Met.*, **12** [3], 326-328 (1964).

[12] W.A.Winterbottom and N.A. Gjostein, “Determination of the Anisotropy of Surface Energy of Metals - II: Experimental γ-plot of Au,” *Acta Met.*, **14** [9], 1041-1052 (1966).

[13] W.A.Winterbottom and N.A. Gjostein, “Determination of the Anisotropy of Surface Energy of Metals - I: Theoretical Analysis,” *Acta Met.*, **14** [9], 1033-1040 (1966).

[14] A.J.W. Moore, “The Influence of Surface Energy on Thermal Etching,” *Acta Met.*, **6** [4], 293-304 (1958).

[15] A.J.W. Moore; pp. 155-198 in Metal Surfaces: Structure, Energetics, and Kinetics. Edited by N.A. Gjostein and W.D. Robertson. American Society for Metals, Metals Park (1963).

[16] J.C. Heyraud and J.J. Métois, “Equilibrium Shape and Temperature; Lead on Graphite,” *Surface Science*, **128** [2/3], 334-342 (1983).

[17] J.C. Heyraud and J.J. Métois, “Equilibrium Shape of Gold Crystallites on a graphite Cleavage Surface: Surface Energies and Interfacial Energy,” *Acta Met.*, **28** [12], 1789-1797 (1980).

[18] R.S. Nelson, D.J. Mazey, and R.S. Barnes, “The Thermal Equilibrium Shape and Sizes of Holes in Solids,” *Philos. Mag.*, **11** [109], 91-111 (1965).

[19] Z.Y. Wang, M.P. Harmer, Y.T. Chou, “Pore-Grain Boundary Configurations in Lithium Fluoride,” *J. Am. Ceram. Soc.*, **69** [10], 735-740 (1986).

[20] J.-H. Choi, D.-Y. Kim, B.J. Hockey, S.M. Wiederhorn, C.A. Handwerker, J.E. Blendell, W.C. Carter, A.R. Roosen, "Equilibrium Shape of Internal Cavities in Sapphire," *J. Am. Ceram. Soc.*, **80** [1], 62-68 (1997).

[21] M. Kitayama and A.M. Glaeser, "The Energetics and Kinetics of Pore Shape Changes in Alumina," *Key Engineering Materials*, **159-160** 193-204 (1999).

[22] P.W. Tasker and D.M. Duffy, "The Structure and Properties of the Stepped Surfaces of MgO and NiO," *Surface Science*, **137** [1], 91-102 (1984).

[23] M. Causa, R. Dovesi, C. Pisani, C. Roetti, "*Ab Initio* Hartree-Fock Study of the MgO (001) Surface," *Surface Science*, **175** [3], 551-560 (1986).

[24] W.C. Mackrodt, "Atomistic Simulation of Oxide Surfaces," *Phys. Chem. Minerals*, **15** [3], 228-237 (1988).

[25] A. Gibson, R. Haydock, J.P. LaFemina, "Electronic Structure and Relative Stability of the MgO (001) and (111) Surfaces," *J. Vac. Sci. Techol. A*, **10** [4], 2361-2366 (1992).

[26] J. Goniakowski and C. Noguera, "Electronic Structure of Clean Insulating Oxide Surfaces I. A Numerical Approach," *Surface Science*, **319** [1/2], 68-80 (1994).

[27] P.W. Tasker, pp. 176-189 in Advances in Ceramics, Vol. 10, Edited by W.D. Kingery, The American Ceramic Society, Columbus, OH (1984).

[28] W.C. Mackrodt, R.J. Davey, S.N. Black, and R. Docherty, "The Morphology of α-Al2O3 and α-Fe2O3: The Importance of Surface Relaxation," *J. Crystal Growth*, **80** 441-446 (1987).

[29] I. Manassidis and M.J. Gillan, "Structure and Energetics of Alumina Surfaces Calculated from First Principles," *J. Am. Ceram. Soc.*, **77** [2], 335-338 (1994).

[30] S. Blonski and S.H. Garofalini, "Molecular Dynamics Simulations of α-Alumina and γ-Alumina Surfaces," *Surface Science*, **295** [2], 263-274 (1993).

[31] W.T. Read and W. Shockley, "Dislocation Models of Crystal Grain Boundaries," *Phys. Rev.*, **78** [3], 275-289 (1950).

[32] D.G. Brandon, "The Structure of High Angle Grain Boundaries," *Acta Met.*, **14**, 1479-1484 (1966).

[33] D.H. Warrington and M. Boon, "Ordered Structures in Random Grain Boundaries; Some Geometrical Probabilities," *Acta Met.*, **23**, 599-607 (1975).

[34] D. Wolf, "Correlation Between Structure, Energy, and Ideal Cleavage Fracture for Symmetrical Grain Boundaries in FCC Metals," *J. Mater. Res.*, **5** [8], 1708-1730 (1990).

[35] D.W. Readey and R.E. Jech, "Energies and Grooving Kinetics of [001] Tilt Boundaries in NiO," *J. Amer. Ceram. Soc.*, **51** [4], 201-208 (1968).

[36] W.D. Kingery, "Metal-Ceramic Interactions: IV, Absolute Measurement of Metal Ceramic Interfacial Energy and Interfacial Adsorption of Silicon From Iron-Silicon Alloys," *J. Am. Ceram. Soc.*, **37** [2], 42-45 (1954).

[37] J.F. Shackelford and W.D. Scott, "Relative Energies of $[\bar{1}100]$ Tilt Boundaries in Aluminum Oxide," *J. Am. Ceram. Soc.*, **51** [12], 688-691 (1969).

[38] R.L. Coble, personal communication in W.D. Kingery and B. Francois, "The Sintering of Crystalline Oxides, I. Interactions between Grain Boundaries and Pores," p. 471-499 in Sintering and Related Phenomena, Edited by G.C. Kuczynski, N. Hooten, and C. Gibbon, Gordon and Breach, New York (1967).

[39] G. Dhalenne, A. Recolevschi, and A. Gervais, "Grain Boundaries in NiO I. Relative Energies of $\langle 001 \rangle$ Tilt Boundaries," *Phys. Status Solidi A*, **56**, 267-276 (1979).

[40] G. Dhalenne, M. Dechamps, and A. Gervais, "Relative Energies of $\langle 110 \rangle$ Tilt Boundaries in NiO," *J. Am. Ceram. Soc.*, **65** [1], C-11,C-12 (1982).

[41] G. Achutaramayya, "Twins and Low-Angle Tilt Boundaries in Alumina. Surface Diffusion and Interfacial Energies from Groove Profiles," Ph.D. Thesis, University of Washington, Seattle, WA (1972).

[42] T. Ikegami, K. Kotani, and K. Eguchi, "Some Roles of MgO and TiO2 in Densification of a Sinterable Alumina," *J. Am. Ceram. Soc.*, **70** [12], 885-890 (1987).

[43] C.A. Handwerker, J.M. Dynys, R.M. Cannon, and R.L. Coble, "Metal Reference Line Technique for Obtaining Dihedral Angles from Surface Thermal grooves," *J. Amer. Ceram. Soc.*, **73** [5], 1365-1370 (1990).

[44] C.A. Handwerker, J.M. Dynys, R.M. Cannon, and R.L. Coble, "Dihedral Angles in Magnesia and Alumina: Distributions from Surface Thermal Grooves," *J. Amer. Ceram. Soc.*, **73** [5], 1371-1377 (1990).

[45] S. Kimura, E. Yasuda, and M. Sakaki, "Grain Boundaries in MgO Bicrystals," *Yogyo-Kyokai-Shi*, **94** [8], 795-800 (1986).

[46] C.S. Smith, "Grains, Phases, and Interfaces: An Interpretation of Microstructure," *Trans. AIME*, **175**, 15-51 (1948).

[47] C.G. Dunn and F.J. Lionetti, "The Effect of Orientation Difference on Grain Boundary Energies," *Trans. AIME*, **185**, 125-132 (1949).

[48] C.G. Dunn and F.J. Lionetti, "The Effect of Orientation Difference on Grain Boundary Energies," *Trans. AIME*, **185**, 860-862 (1949).

[49] B. Chalmers, "Some Crystal-Boundary Phenomena in Metals," *Proc. Roy. Soc.* (London), **A196**, 64-73 (1949).

[50] T.I. Zhukova and L.K. Fionova, "Investigation of the Orientational Dependence of the Energy of Special Grain Boundaries," *Sov. Phys. Solid State*, **23** [3], 472-476 (1983).

[51] D. Wolf, "Energy and Structure of (001) Coincident-site Twist Boundaries and the Free (001) Surface in MgO - a Theoretical Study," *J. Am. Ceram Soc.*, **67** [1], 1-13 (1984).

[52] D. Wolf, "Properties of High-Angle (001) Twist Grain Boundaries in Alkali-Halide Bicrystals," *Phil. Mag. A*, **49** [6], 823-844 (1984).

[53] D.M. Duffy and P.W. Tasker, "Computer Simulation of $\langle 001 \rangle$ Tilt Grain Boundaries in Nickel Oxide," *Phil. Mag. A*, **47** [6], 817-825 (1983).

[54] D.M. Duffy and P.W. Tasker, "Computer Simulation of $\langle 110 \rangle$ Tilt Grain Boundaries in Nickel Oxide," *Phil. Mag. A*, **48** [1], 155-162 (1983).

Chapter 3

Experimental

In this chapter, we will describe the synthesis and preparation of the polycrystalline magnesia sample, as well as the characterization techniques, used throughout this thesis. Furthermore, the experimental and analytical techniques developed to extract the data required to specify the interfacial characters and reconstruct the energies are also discussed. These techniques rely on characterizing the geometry and crystallography of large quantities of thermal grooves and grain boundary triple junctions for the analysis of the surface and grain boundary energies, respectively. This chapter also includes a detailed description of algorithms that were used to reconstruct the geometric and crystallographic configuration of a three-dimensional volume of microstructure from two-dimensional slices; a procedure that is required to reliably extract the necessary data from grain boundary triple junctions and to specify the areal distribution of grain boundary characters over the five mesoscopically observable parameters.

3.1 Sample

The polycrystalline magnesia samples used for the surface and grain boundary energy analyses were prepared by first forming magnesia powder by decomposing 99.7% pure magnesium carbonate (Fisher Scientific) at $997°C$ in air. Uniaxial compaction in a hot press at $1700°C$ for one hour at $61MPa$ produced a disc with a diameter of $50mm$ and an average thickness of $1.5mm$. Specimens cut from this disc were then packed in a magnesia crucible with the parent powder and annealed for $48h$ at $1600°C$ in air. This procedure yielded translucent specimens with a $\langle 111 \rangle$ axial texture that was 11 times random at the maximum. The geometric measurements used to characterize the thermal groove and grain boundary triple junction geometry require samples that are flat and have two parallel faces. Appropriate surfaces were prepared using an automatic polisher (Logitech PM5). The surfaces were initially lapped with a $9\mu m$ alumina slurry and the final polish was achieved using an alkaline ($pH \sim 10$) colloidal silica ($0.05\mu m$) slurry. The flatness of the final surface was measured using an inductive axial movement gauge head with a resolution of $0.1\mu m$. (Brown and Sharpe, TESR, Model TT22); surfaces were determined to be flat within $\pm 0.3\mu m$ over lateral dimensions of $1cm$. The surface was thermally grooved by annealing it in air for $5h$ at $1400°C$. The average grain size of the sample was $109\mu m$. At this stage, one sample was analyzed for impurities. The sample contained 0.2% Ca, 0.02% Al, 0.03% Fe, 0.02% Si, and 0.03% Y.

3.2 Characterization techniques

3.2.1 Atomic force microscopy (AFM)

Atomic force microscopy (AFM) is a scanning probe technique in which topographic images of the surface are generated by rastering a small probe attached to a cantilever across the surface of a sample. The technique can be thought of as an ultra-sensitive profilometer. As the probe rasters over the surface, changes in topography cause the deflection of the cantilever to change. The extent of the deflection is monitored by using a position-sensitive photodetector to sense changes in the position of a laser beam which is reflected off of the cantilever. All of the images obtained in this thesis were made in constant force mode where the vertical position of the tip or sample is continuously adjusted by a piezoelectric device to maintain a constant cantilever deflection. The adjustments made to the vertical position to maintain the constant deflection are a direct measure of the topography of the surface.

Two different AFM's were used in this study to measure the surface geometry of thermal grooves under ambient conditions. The first instrument consisted of a Digital Instruments StandAlone AFM (SAA-125) positioned above the sample mounted on an X-Y translation stage (Burleigh Instruments TSE-150), with a range of $6.25cm$ in both directions, capable of reproducibly positioning the sample with $50nm$ resolution. The advantage of this system is that once a coordinate system and reference frame are established (with respect to an intentionally introduced fiducial mark), it is possible to return to identical positions on the sample surface after repeated thermal treatments or to position the sample based on lower resolution data from the AFM or other microscopes. $\mathrm{Si_3N_4}$ cantilevers (DI Model LNP) were used as probes. The second microscope was a Park Scientific Instruments Autoprobe CP. For this instrument, the probes consisted of gold coated $\mathrm{Si_3N_4}$ cantilevers with pyramidal $\mathrm{Si_3N_4}$ (Park Scientific Instruments, MSCT-AUMT-A).

In this thesis, we have used AFM to characterize the surface geometry of thermal grooves. The AFM images in this document are topographic. The highest positions on the surface are indicated by the lightest shading and the lowest positions by the darkest shading. AFM was used in place of the accepted techniques described in 2.5.2 because of its height resolution advantage. Using AFM, height differences less than $1nm$ are easily resolved. It is also advantageous to use AFM because it is much less labor intensive than the techniques described in 2.5.2; therefore, it is possible to measure a larger quantity of thermal grooves. Several hundred boundaries can easily be characterized in a time scale of days.

3.2.2 Orientation imaging microscopy (OIM)

Orientation imaging microscopy (OIM) [1] is a technique that determines the orientations of individual crystallites by automatically indexing electron backscattered diffraction patterns (EBSP). The sample is placed in a scanning electron microscope (SEM) at a steep angle to the electron beam. The electron beam is focused on a single point and the electrons that penetrate the sample and meet the Bragg condition are backscattered to form a cone of diffracted electrons. The cone is intercepted by a phosphor screen connected to a high gain intensified silicon, intensified target (SIT) video camera. As the electrons strike the phosphor screen, a diffraction pattern similar to a Kikuchi pattern is formed where the bands represent planes and the intersections of two or more bands represent zone axes. After the image has been digitized, a Hough transform is applied to the image which yields the locations of the most intense bands in the image. Using the geometry of the bands, along with the user specified unit cell, diffraction intensity, and pattern center data, the orientation of the crystallite is calculated. This process can be done either by manually pointing the electron beam or by computer control where the computer automatically rasters the beam over the sample surface.

Unless otherwise specified, all orientation data presented in this document were generated with a Philips XL40FEG SEM which was controlled by a PC. The patterns were indexed with OIM 2.5 and 2.6 software (TSL) on a SGI workstation. We have estimated that the error in absolute orientation (g) and misorientation (Δg) derived from this system to be $\pm 5^\circ$ and $\pm 0.5^\circ$, respectively.

3.3 Surface energy measurements

3.3.1 Experimental approach

When examining a well-annealed, polycrystalline microstructure, one occasionally finds a small grain enclosed within a larger grain. We refer to the smaller, surrounded crystal as an island grain and the larger crystal as the matrix grain. A planar section illustrating this situation is shown schematically in Fig. 3.1a; an island grain observed in magnesia is illustrated in Fig. 3.2. In Fig. 3.2, the boundary separating the island grain from the matrix grain is easily distinguished by the thermal groove. Assuming that the triple junction at the groove root is in local thermodynamic equilibrium, Eqns. 2.4 and 2.5 should then be satisfied at all points, P_i. The quantities in these equations are depicted schematically in Fig. 3.1b. If the orientations of both grains ($\hat{n}_i$) are determined by backscattered elec-

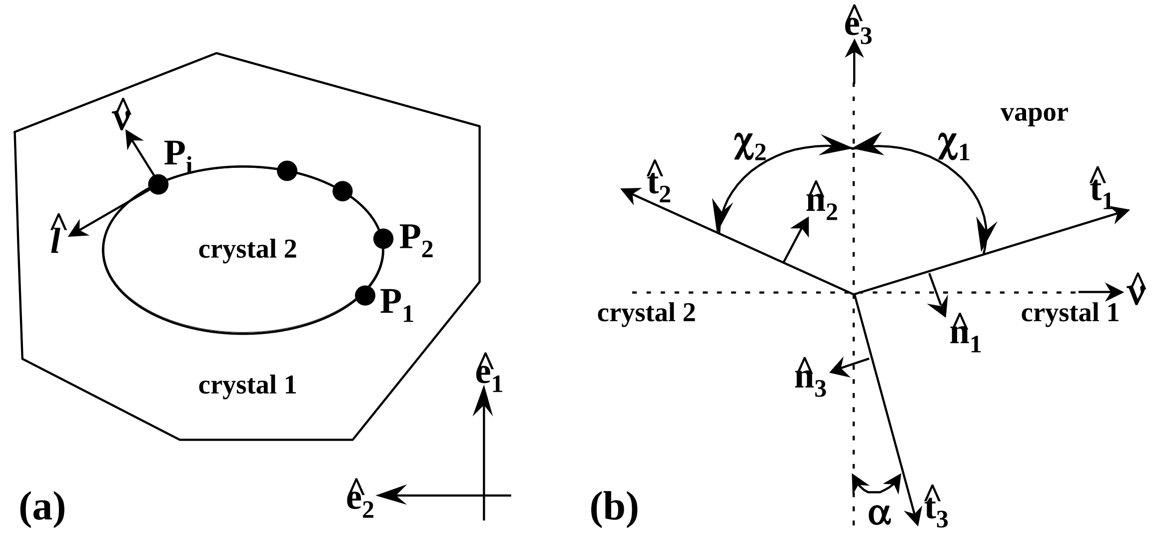

Figure 3.1: The coordinate system used for the surface energy measurements. (a) A schematic plane view of an island grain (crystal 2) within a matrix grain (crystal 1). Multiple groove measurements are made around the circumference of the island grain, at points labeled P_i. (b) A schematic cross-sectional view of a triple junction. Note that $\hat{\ell}$ points into the plane of the paper.

tron diffraction and the inclinations of the three interfaces (defined by χ_1, χ_2, and α) are determined by microscopic analysis at N points along the boundary, then it is possible to specify all of the quantities in Eqns. 2.4 and 2.5, except the interface energies and their derivatives. The advantage of making these measurements on island grains is that we can assume that the grain boundary energy is a function only of the misorientation and not the boundary plane. Although we address the grain boundary energy dependence on boundary plane later in chapter 6, for these measurements we assume $\partial\gamma_{gb}/\partial\alpha = 0$; this is identical to the approximation applied in the earlier work involving the characterization of circumferential thermal grooves on the surface of cylindrical wires with a bamboo microstructure [2,3] discussed in 2.4.2. Since the misorientation is fixed at all points across the boundary, the grain boundary energy (γ_3) is the same in each of the N equations. While the subject of this thesis is polycrystalline magnesia, it should be possible to conduct similar measurements on any polycrystalline specimen that has a grain size larger than $30\mu m$ and contains some enclosed or partially enclosed grains.

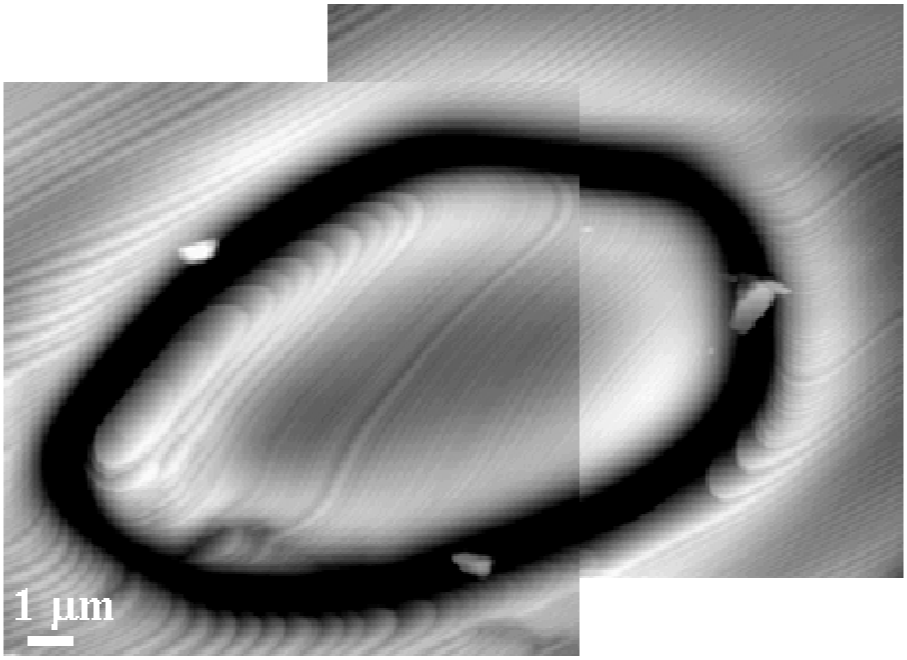

Figure 3.2: A montage of AFM images showing an island grain. The black-to-white vertical contrast is $200nm$. Contrast discontinuities occur at the points where images have been pieced together.

3.3.2 Data collection

We have applied the approach described above to the polycrystalline magnesia sample. After the grooving treatment ($5h$ at $1400°C$), a significant number of island grains (~ 10 in a $1cm^2$ area) could be identified on the sample surface. The island grains were all found to have a low misorientation angle ($< 7°$) and presumably formed when a higher mobility grain boundary swept past during the coarsening of the microstructure. Five of these island grains were selected for characterization, and a total 269 groove measurements were made.

One of the assumptions which underpins our measurements is that the groove morphology is determined at $1400°C$ and that it does not change in a significant way during cooling. Considering the fact that the lateral and vertical dimensions of the grooves and surface facets scale with the annealing time and that groove traces left by migrating boundaries are not observed, this seems to be a good approximation.

Sample positioning

To characterize the quantities in Fig. 3.1b, we must combine data collected from several microscopy techniques; therefore, it is important that the sample reference frame be coincident with the reference frame of the microscopes. To assist with alignment, two of the lateral edges of the sample were cut so that they formed a right angle with each other and the analysis surface. On each microscope stage, these external features were used to align the specimen. We estimate that the uncertainty in the orientation of the characterized interfaces that results from sample positioning errors is not greater than 2°.

Surface characterization

The inclinations of the free surfaces bounding the groove between the island grain and the matrix grain were determined by AFM. The procedure used to accurately measure groove inclinations with AFM are described in detail in Appendix A. After imaging the island grain with AFM, measurements are made at each point (P_i) around the circumference of the island grain. From these measurements, the inclinations (χ_i) of the free surfaces are determined. The AFM data were also used to determine the angle, τ, between $\hat{e}_1$ and $\hat{\nu}$ (see Fig. 3.1).

The orientations of the free surfaces at the groove root were determined by combining χ_i and τ from each AFM measurement with orientation data derived from EBSPs. Based on the AFM data, the normal of the surface at the groove root ($\hat{n}_i$) has the following components in the laboratory reference frame:

$$\begin{aligned} n_{i,1} &= \cos\chi_i \cos\tau, \\ n_{i,2} &= \cos\chi_i \sin\tau, \\ n_{i,3} &= (-1)^i \sin\chi_i \end{aligned} \tag{3.1}$$

In Eqn. 3.1, the subscript i refers to the surfaces labeled in Fig. 3.1b. Note that the normal vector $\hat{n}_1$ is defined as pointing into the crystal. In the crystal reference frame, the components of the surface normal (z_i) are specified according to the following transformation:

$$z_i = g_{ij} n_j, \tag{3.2}$$

where g_{ij} is given by Eqn. 2.1 and φ_1, Φ, φ_2 in Eqn. 2.1 are the Euler angles denoting the orientation of the grain.

Grain boundary inclinations

The boundary inclinations (α) were determined for each point (P_i) in the following manner. Optical micrographs of each island grain were recorded before and after a thin layer of the sample was removed by polishing. The field of view for these micrographs included approximately 20 additional grains in the adjacent microstructure so that the relative lateral positions of the two images could be determined by visually maximizing the overlap of all the grain boundaries in the image. Based on measurements of the amount of material removed and the apparent lateral shift of the boundary between the two images, the inclination (α) at each point (P_i) was determined. Considering the magnitude of the vertical distance ($6 \pm 0.3 \mu m$) and our estimated uncertainty in the lateral registry between the two layers ($1.5 \mu m$), we anticipate that the maximum uncertainty on α is approximately 14°.

3.4 Grain boundary character and energy measurements

3.4.1 Experimental approach

To reliably specify the distribution of grain boundary characters and energies, over all five mesoscopically observable grain boundary parameters, it is necessary to characterize the geometry and crystallography of large quantities of contiguous crystallites. This was accomplished using an automated scanning electron microscope (SEM) mapping system that controls both the stage and beam position as well as the acquisition of images and electron backscattered diffraction patterns (EBSPs). When the mapping is conducted, the sample surface is initially divided into sectors. At each sector, a secondary electron image is recorded, and EBSP measurements of crystallite orientation are made at regular intervals within the sector. When the sector characterization is complete, the microscope stage is automatically moved to the next sector. The entire procedure is carried out under computer control. Because we use SEM images to determine grain boundary positions, the orien-

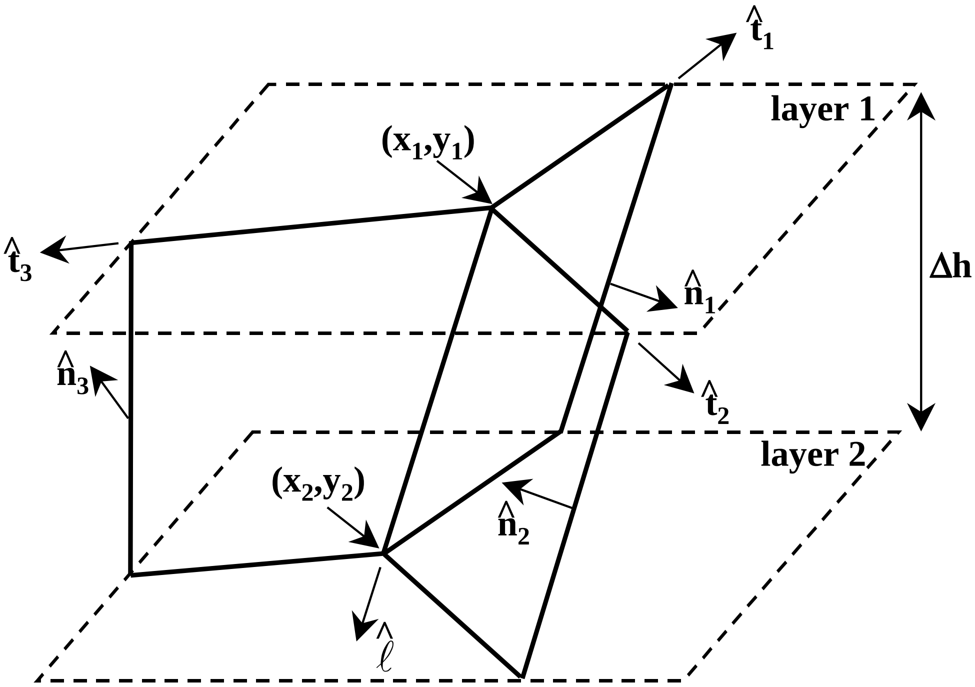

Figure 3.3: Schematic representation of the geometric parameters required to characterize a grain boundary triple junction.

tation measurements can be conducted at relatively coarse intervals. Thus, compared to the conventional OIM methods, we are able to resolve the boundary positions accurately without accumulating redundant orientation data [1]. After an area is mapped, high precision serial sectioning is used to remove a thin layer and the process is repeated so that the three-dimensional characteristics of the grain boundary network can be determined.

From these data, we can reconstruct the geometric and crystallographic configuration of the microstructure in three dimensions. These data allow us to extract the three-dimensional grain boundary network, thus we can specify the areal distribution of grain boundaries over the entire five parameter space. Furthermore, from the reconstructed volume, we can specify the geometry and crystallography for each triple junction (see Fig. 3.3) within the characterized volume of material. First, the EBSP measurements are used to specify the orientations of the crystallites bounding the triple junction (g_i). From the microscopic images we can measure the grain boundary tangents in the section plane ($\hat{t}_i$) and the triple junction locations on each layer (x_i, y_i). The triple junction locations, along with the removal depth, Δh, can be used to determine the triple line direction, $\hat{\ell}$, assuming that the curvature of the triple line is negligible. This approximation should be valid as long as Δh is small compared to the grain size. The grain boundary normals ($\hat{n}_i$) are given by $\hat{\ell} \times \hat{t}_i$, and the grain boundary crystallography can be derived from the crystallite orientations (g_i). Thus, we can specify all of the quantities in the local equilibrium condition (Eqn. 2.3), except for the grain boundary energies and their derivatives.

3.4.2 Grain boundary crystallography

From experimental measurements of the crystallite orientations adjacent to the boundary (Δg_i) and the vector normal to the boundary plane ($\hat{n}$), the crystallographic character of the grain boundary may be specified. The misorientation (Δg) is given by $\Delta g = g_1 g_2^T$ and the boundary plane normal (n') can be expressed in terms of either crystal coordinate system ($n' = g_1 n$ or $n' = g_2 n$). Note that in this document the ambiguity in the reference frame for n' is avoided by always expressing n' in terms of the first (non-transposed) crystallite reference frame. However, due to the presence of crystal symmetries, numerous different sets of Δg and n' represent physically indistinguishable grain boundaries. These symmetrically equivalent boundaries are enumerated in the following manner. In the case of cubic symmetry, for each g there are 24 equivalent g given by Cg, where C are the proper symmetry operators for cubic symmetry, thus $\Delta g = C_i g_1 (C_j g_2)^T$. Further, Δg can be expressed as the misorientation between the first grain and the second grain or vice-versa. Therefore, we also have $\Delta g = C_j g_2 (C_i g_1)^T$. Although the boundary plane normal is always expressed in terms of the *first* crystallite reference frame, it is arbitrary whether it is directed towards the first or second grain, so $n' = -n'$. Thus, for each grain boundary there exist $2 \times 2 \times 24^2 = 2304$ symmetrically equivalent grain boundaries that need to be considered.

3.4.3 Data collection

The automated mapping system described above was integrated with a Phillips XL40 FEG SEM. The magnesia sample was carbon coated and tilted at 60° for imaging and acquisition of the EBSPs. On each layer, three scan areas consisting of a 14×14 grid of sectors were characterized. In each of the 196 sectors, a tilt-corrected image was taken at $750\times$ magnification, and 300 uniformly distributed EBSPs were recorded. The patterns were indexed using an algorithm previously described by Morawiec [4], which returns a set of Euler rotation angles (φ_1, Φ,φ_2) relating the crystal reference frame to the sample reference frame. The error in absolute orientation (g) obtained in this manner is estimated to be 5°. After scanning was completed on each layer, approximately $7\mu m$ of material was removed (Δh) and the entire process was repeated. For each layer removed in this manner, the error in Δh is approximately $\pm 0.3\mu m$. On each layer, each of the three scan areas were visually aligned to cover the same area as the corresponding scan on the previous layer. This was repeated until data from five layers was accumulated and approximately $0.15mm^3$ volume of material had been characterized.

3.4.4 3-D reconstruction

Because the amount of material removed between section planes ($\Delta h \sim 7\mu m$) was small compared to the grain size ($109\mu m$), it is possible to reconstruct the geometric configuration of the characterized volume of microstructure with reasonable accuracy. By first reconstructing the microstructure in three-dimensions, the quantity and quality of triple junction data extracted from the data collected is optimized. The procedures used to reconstruct the three-dimensional microstructure and extract the necessary data are described in the following sections. These algorithms allow us to not only recover the geometry and crystallography of all of the possible triple junctions in the characterized volume of microstructure, but also reconstruct the grain boundary network, which is necessary to accurately specify the distribution of grain boundaries found in the sample.

Crystallite geometry

The initial step in the volume reconstruction procedure is to extract the geometry of the crystallites on each characterized layer. This involves transforming the grayscale secondary electron images to spatially correct, binary images of the grain boundary skeleton. Although the recorded images were initially tilt-corrected, substantial geometric distortions may still arise. Thus, these distortions were characterized using a lithographically produced standard grating with known dimensions and corrected using the algorithm described by Kapur and Casasent [5]. This procedure produced spatially correct images with a pixel-to-pixel separation of approximately $0.25\mu m$ in both lateral dimensions. To accurately specify the crystallite geometry in each image the grain boundaries were manually digitized. This was accomplished by “drawing” small, connecting line segments over the grain boundaries in each image; a process which yielded not only accurate grain boundary skeletons, but also allowed us to accurately specify the location (x, y) and slope of the three boundaries in the section plane $(\hat{t}_i)$ of the triple junctions in each image. A typical distortion corrected SEM image and the corresponding skeletonized image are shown in Fig. 3.4.

Section plane reconstruction

Further analysis of the geometric and crystallographic data requires that we combine the skeletonized images and crystallite orientation measurements from the sectors to produce high-resolution orientation maps for each 14×14 scan area. This requires that we first establish the relative positions of the sectors within each scan with more accuracy than the positions provided by the microscope stage coordinates. To determine the relative positions of the images in each planar section, we used the following two step procedure. Adjacent images in each planar section are deliberately recorded so that all adjacent sectors overlap; this makes it possible to determine an offset between each neighbor pair by maximizing the contrast correlation in the overlapped region [6]. However, when 196 images in a 14×14 array are positioned using only nearest neighbor offsets, significant cumulative errors arise. In other words, if the distance between two points in distant images is computed by summing the nearest neighbor offsets along two different paths through the array of images, the distances usually differ. So, the second step of the image positioning algorithm is to randomly select paths through the image array and reposition the images to minimize the differences between distances computed in the global reference frame and those determined by summing the nearest neighbor offsets along equivalent random paths. The errors associated with positioning the images in this manner were usually less than one pixel.

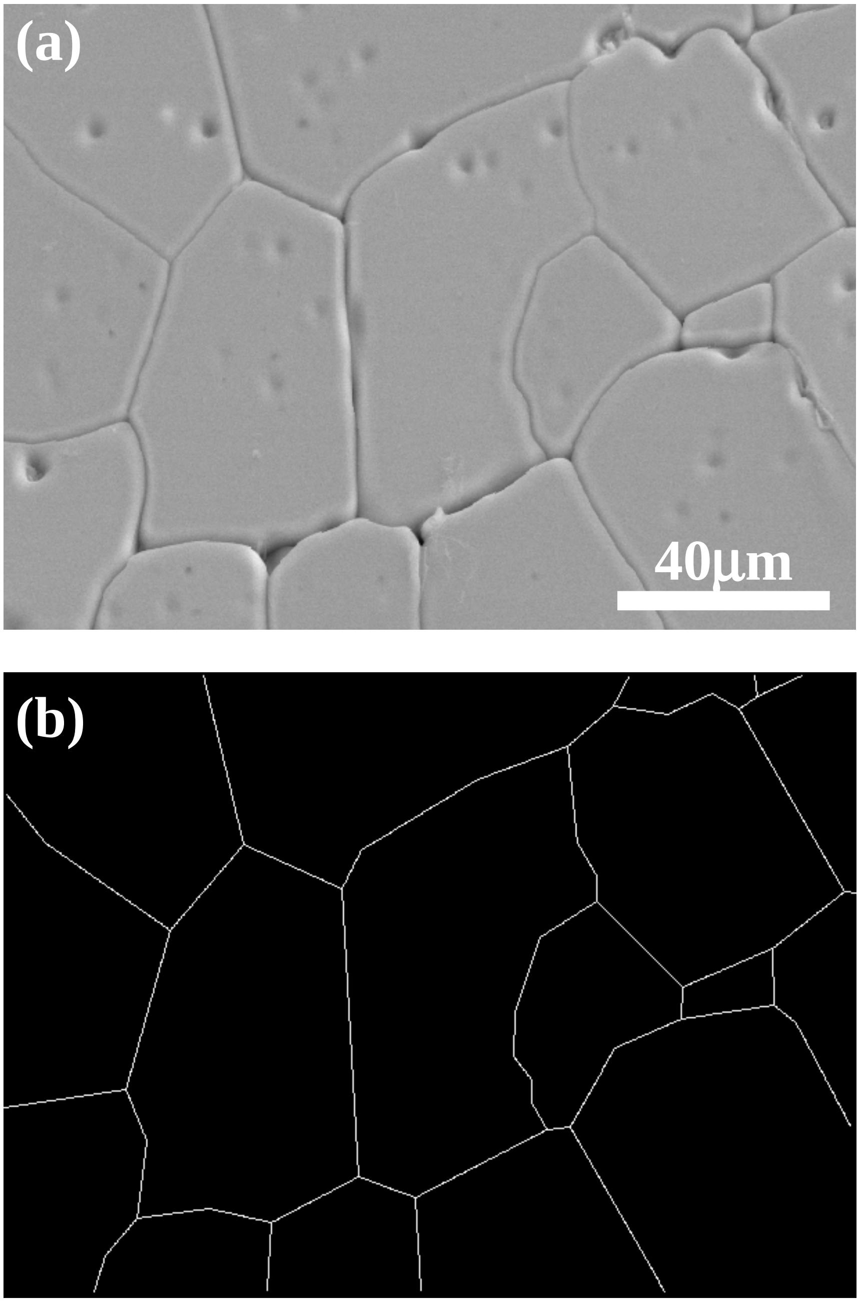

Figure 3.4: A typical grayscale SEM image that has been distortion corrected (a), and the corresponding skeletonized image (b).

Once the relative sector positions are known, the individual sector data were combined to form high-resolution orientation maps. First, the relative positions of images were used to construct large mosaic maps of the grain boundaries and orientation measurements for each scan area. An example of a mosaic grain boundary skeleton map for a typical scan area is shown in Fig. 3.5. To produce orientation maps from these data, every grain in the scan area, defined by contiguous pixels not associated with a grain boundary, was identified and assigned an orientation. Because multiple orientation measurements were made in each grain, minority orientations resulting from errors in the indexing had to be excluded. The remaining majority orientations, which contained some scatter, were averaged using the algorithm described by Morawiec [7,8] to make the final orientation assignment for each grain.

Section plane alignment

Once the high-resolution orientation maps from each layer were obtained, it was necessary to align the maps to establish the same global reference frame for all layers in a given column. Here, we chose the first layer as the global reference frame. The transformation from all subsequent layers to the first layer is given by $Ax + t$ where x is a two dimensional vector which represents the position within a given layer, A is a 2×2 affine transformation matrix, and t is a two dimensional translation vector. To find (A, t) for each layer, we initially find (A, t) that maximizes the area of overlap between positions with the same orientations on adjacent layers by using a downhill simplex minimization routine (AMOEBA [9]) to find the components of A and t that minimize $(N_t - N_o)/N_t$, where N_t is the total number of pixel positions used in the minimization and N_o is the number of overlapping pixel positions. A pixel position is considered to overlap if the orientations at the position are within $5°$. After A and t are determined, the results were checked visually. Fig. 3.6 shows grain boundary maps from adjacent layers after the alignment process. We then use the (A, t) describing the transformation that aligns adjacent layers to calculate the (A, t) that aligns each layer with the initial layer.

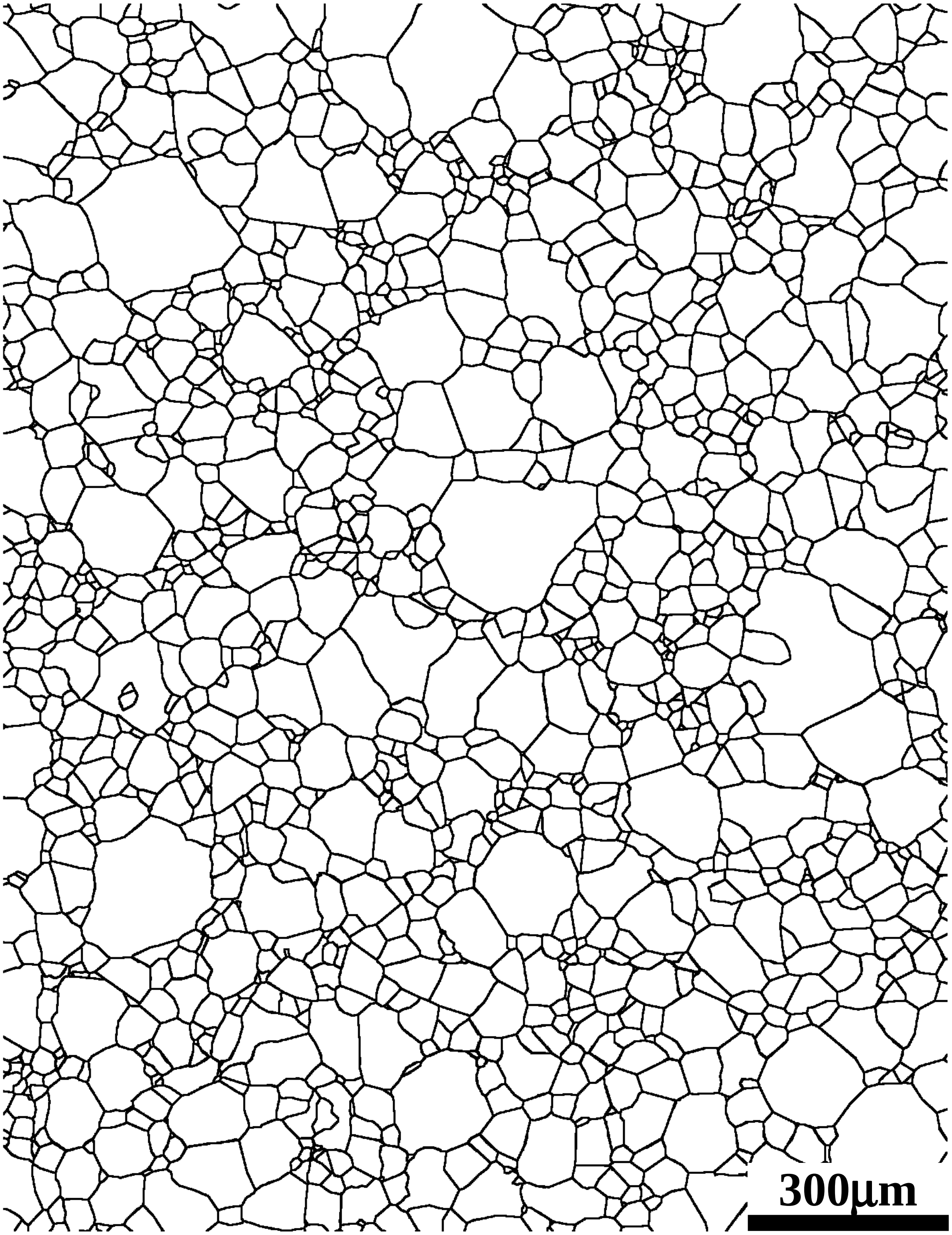

Figure 3.5: A typical mosaic grain boundary skeleton map.

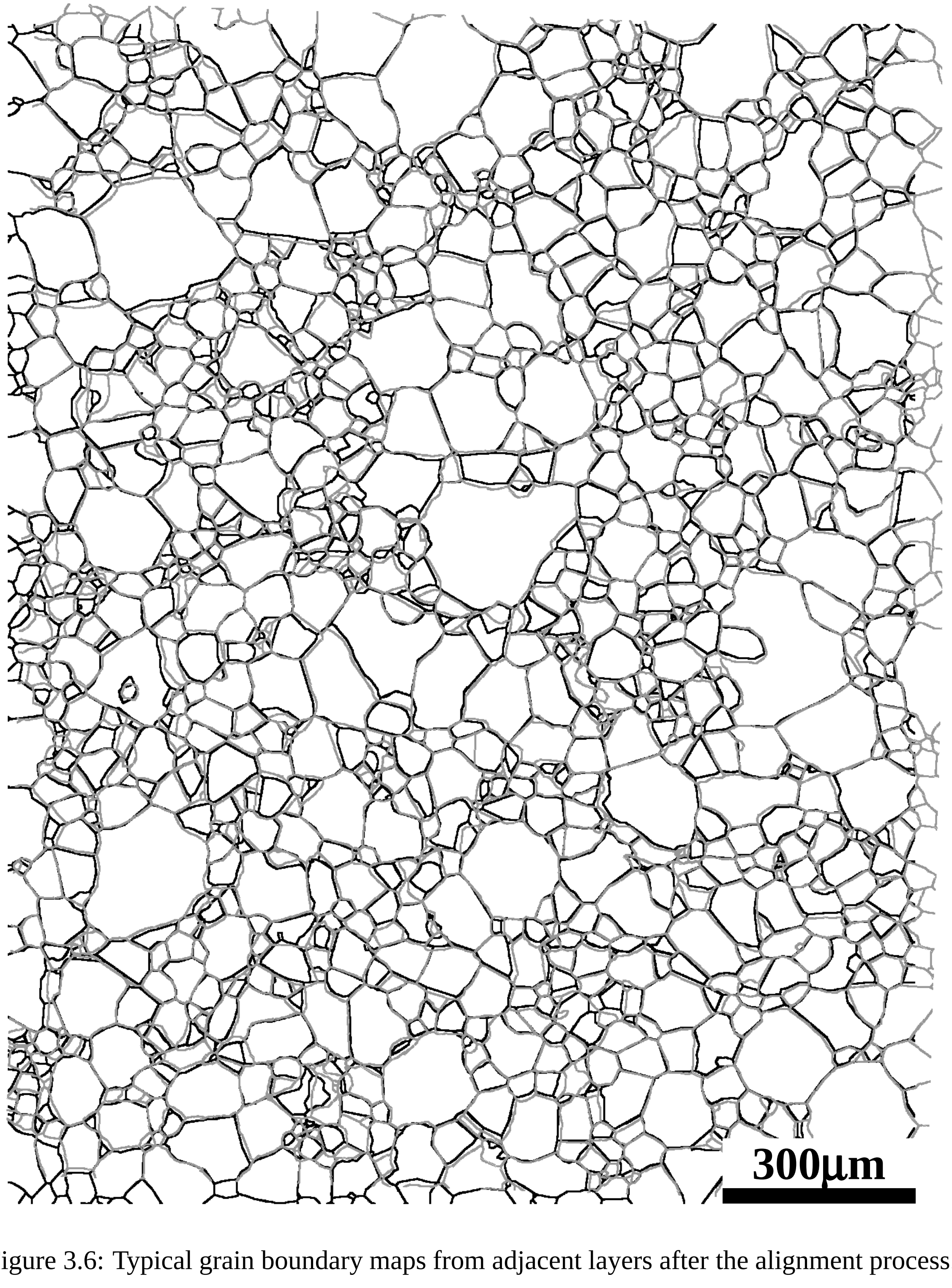

Figure 3.6: Typical grain boundary maps from adjacent layers after the alignment process.

Grain connectivity

After all layers were transformed into the global reference frame, the final step in the "reconstruction" of the microstructure is to specify the connectivity of the grains through the layers. Once the connectivity is established, the geometric configuration of all crystallites, along with their orientation, throughout the volume will be known. The following algorithm is used to identify the common grains through all the layers. First, the area of overlap between all grain pairs on adjacent layers was determined. The pair of grains that has the largest area of overlap is identified as being two sections of the same grain. The pair with the second largest area of overlap is then assigned in the same way. The process continues until all grains have been assigned or do not overlap any grains that have not been assigned. Through visual inspection, we have determined that the algorithm successfully matches the correct grains on adjacent layers 99.5% of the time. The success of this algorithm derives from the fact that the distance between adjacent layers is much smaller than the average grain size. After the grain connectivity was established, the orientations of the crystallites were reassigned by repeating the process that was used in each layer, but now considering all of the orientation data from different section planes of the same grain.

Triple junction extraction

After "reconstructing" the microstructure, we are now in a position to extract the relevant data from the triple junctions for the energy determination. The first step is to establish the location of each triple junction in the global reference frame. This is accomplished by first using the relative sector positions to determine the triple junction locations within the section plane. Next, the same transformations that were applied to the orientation maps in each layer are applied to the triple junction locations to place them in the same global reference frame. The in-plane slopes of the grain boundaries were not adjusted because the corrections from the transformations ($\pm 2^\circ$) were small compared to the error in the measurement process, which we approximate to be $\pm 10^\circ$. By superimposing the transformed triple junction locations with the transformed orientation maps, the three grains bounding each triple junction (with known orientations) could be identified. Using the bounding grains as identifiers, duplicate triple junctions in each section plane, resulting from the overlap of sector images, were identified and removed. Next, the bounding grains were again used to identify common triple junctions on adjacent sections. Using the lateral offsets (x_i, y_i) between the triple junction locations on adjacent sections and the amount of material removed between sections (Δh), the triple line direction ($\hat{\ell}$) was determined. The grain boundary plane normals ($\hat{n}_i$) were then determined by $\hat{\ell} \times \hat{t}_i$. Due to boundary curvature and experimental errors, the apparent grain boundary tangents ($\hat{t}_i$) are not necessarily identical on adjacent layers. To average out the effect of these differences, the geometry of each triple junction was determined twice; once considering $\hat{t}_i$ for the top layer and once for the bottom layer. Thus, each valid triple junction was considered two times in our data set. Now, since the crystallography of the bounding crystallites is already known, all of the quantities in the Herring relation (Eqn. 2.3) are known except for the grain boundary energies and their derivatives. A total of 19094 junctions were identified in this manner.

Grain boundary meshing

Although we have already obtained the data required to reconstruct the grain boundary energy over all five mesoscopic parameters, the distribution of these boundaries can also be extracted from the data that we have collected. This requires that we determine the total area of each grain boundary character in the volume of microstructure that we have characterized. This was accomplished by identifying the planes that connect the grain boundary skeletons on each layer. The grain boundary surfaces were meshed with triangular elements using the following algorithm. First, the pixels from common grain boundaries on adjacent layers were extracted from the orientation maps. These pixels were identified by comparing the two crystallites adjacent to the boundary on each layer. Using the triple junction locations as end-points, the grain boundary pixels from both layers were ordered in the same manner. To mesh the grain boundary, the pixel positions on the second layer were projected onto the plane of the first and every fourth pixel position on both layers was considered as a vertex of a triangular element. Triangular elements were constructed from the vertices by first connecting one of the sets of triple junction locations. Next, the distance to the next vertex position for each layer (d_i) was calculated. The vertex corresponding to the shortest

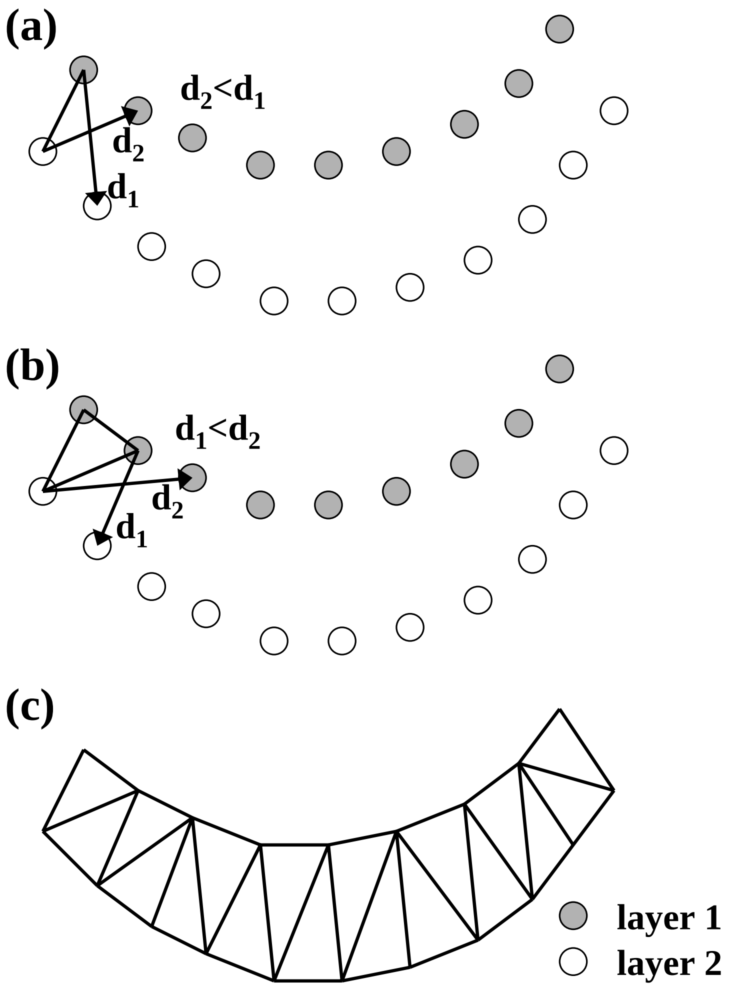

Figure 3.7: Illustration of the grain boundary meshing algorithm. First, the pixel positions on the second layer are projected onto the plane of the first layer. Next, the first set of triple junction locations are connected, and the distance to the next vertex position for each layer (d_i) is calculated (a). The vertex corresponding to the shortest distance is used to create the first element, and the process is repeated (b). This continues until all pixels on both layers are connected (c).

distance was used to create the first element. For the next element, the last connected vertex on each layer was used and the shortest distance criterion was again applied to determine the third vertex. This process continued in this manner until the last pixel from both layers was connected.

From the triangular mesh representing the grain boundary network in the characterized volume of material, it was possible to determine the distribution of grain boundaries over all five mesoscopically observable parameters. Using the vertices of the triangles in the mesh, the area and normal vector for each triangle were determined. Next, the normal vector and the orientations of the crystallites bounding each triangle were used to specify all five grain boundary parameters (misorientation and boundary plane normal), and the total boundary area associated with each grain boundary type can be calculated. Thus, we are now in a position to calculate the areal distribution of boundary types over the mesoscopic grain boundary parameters.

3.5 References

[1] B.L. Adams, S.I. Wright, and K. Kunze, "Orientation Imaging: The Emergence of a New Microscopy," *Met. Trans.*, **24A** [4], 819-831 (1993).

[2] M. McLean and B. Gale, "Surface Energy Anisotropy by an Improved Thermal Grooving Technique," *Philos. Mag.*, **20** [167], 1033-1045 (1969).

[3] B. Gale, R.A. Hunt, and M McLean, "An Analysis of Surface Energy Anisotropy Data using Lattice Harmonics," *Philos. Mag.*, **25** [4], 947-960 (1972).

[4] A. Morawiec, "Automatic Orientation Determination from Kikuchi Patterns," *J. Appl. Cryst.*, **32** [4], 788-798 (1999).

[5] J. Kapur and D. Casasent, "Geometric Correction of SEM Images," *Proceedings SPIE*, **4044**, 165-176 (2000).

[6] S. Mahadevan and D. Casasent, *Proceedings SPIE*, submitted.

[7] M. Humbert, N. Gey, J. Muller, and C. Esling, "Determination of a Mean Orientation from a Cloud of Orientations. Application to Electron Back-scattering Pattern Measurements," *J. Appl. Cryst.*, **29**, 662-666 (1996).

[8] A. Morawiec, "A Note on Mean Orientation," *J. Appl. Cryst.*, **31**, 818-819 (1998).

[9] W.H. Press, B.P. Flannery, S.A. Teukolsky, and W.T. Vetterling, Numerical Recipes in Pascal; Cambridge University Press, Cambridge, 1989.

Chapter 4

Energy Reconstruction

In this chapter, we shall describe various methods for reconstructing both the surface and grain boundary energies from the experimental data and discuss the relative advantages and disadvantages of each. To illustrate the applicability of these methods, we have created simulated data sets based on model energy functions. After adding random perturbations to the simulated data that mimic the random errors in the real data, we reconstructed the energy functions using selected methods. This procedure not only shows the reliability and accuracy of the reconstruction methods, but also allows us to compare the performance between methods.

4.1 Methods

The experiments described in this thesis rely on measuring the geometry and crystallography of large quantities of triple junctions and then using the Herring relation to link the observations to the interfacial energies. However, for every observed triple junction there are three unknown interface energies and only two equilibrium conditions, thus the reconstruction methods require some level of approximation. The approximation is based on reducing the number of unknowns required to describe the energy variation over all possible interfaces. One approach is to represent the energy variation over the domain of interfacial characters as a finite series [1–4], such that the number of unknowns is limited to coefficients of the series. The other approach is to discretize the space into a set of predefined interfaces [5], thus limiting the total number of unknown energies.

4.1.1 Series expansion methods

The series expansion methods are based on representing the energy variation as a finite series of selected basis functions. The unknown coefficients of the series are then determined by fitting the observations to the local equilibrium condition at a triple junction. One limitation of the series expansion methods is that the assumption of particular basis functions for the finite series constrains the form of the resulting surface energy function. The comparative advantages and disadvantages of different basis functions were described by Gale *et al.* [4], who evaluated the orientation dependence of the surface energy of an Fe-3% Si alloy. This work showed that while a conventional trigonometric series can produce cusps in the surface energy function, it does not have the correct symmetry. Spherical harmonic basis functions can be used to produce a surface energy with the correct symmetry, but the finite extent of the series makes it impossible to produce sharp cusps at low energy orientations. The following sections describe these two techniques and their application to the surface energy (Fourier series) and grain boundary energy (spherical harmonics) measurements.

Fourier series

To extract the surface energy anisotropy from the circumferential thermal groove measurements using Fourier series expansion, we must first transform the surface normals into the fundamental zone (standard stereographic triangle) where the normal vector (z_i') is given by $z_i' = M_{ik} z_k$. The components of z_i' are permutations of the absolute values of z_k such that $z_1' \leq z_2' \leq z_3'$ and the values of M_{ik} are $0, 1$, or -1 and are assigned in the following way: If $z_i' \neq |z_k|$ then $M_{ik} = 0$. If $z_i' = |z_k|$, then $M_{ik} = 1$ for positive z_k and $M_{ik} = -1$ for negative z_k. This step is required since the Fourier series does not have the correct symmetry for the space of cubic surface normals. Furthermore, we must note that for the same reason the series will not be valid outside of the fundamental zone.

Next, the surface energy is parameterized in terms of the spherical coordinates θ and ϕ; the relationship between these variables and the components of the surface normal are $\theta = \cos^{-1}(z'_1)$ and $\phi = \tan^{-1}(z'_3/z'_2)$. We now use Winterbottom and Gjostein's [1] method of approximating the surface energy as a truncated double Fourier series. We selected the following form for the function:

$$\begin{aligned}\gamma_s(\theta,\phi) = 1 + \textstyle\sum_{i=1}^{R}\sum_{j=0}^{R}[a_{ij}\{\cos(2i\theta)-1\}\cos(j\phi) + b_{ij}\sin(2i\theta)\cos(j\phi) \\ +c_{ij}\{\cos(2i\theta)-1\}\sin(j\phi) + d_{ij}\sin(2i\theta)\sin(j\phi)].\end{aligned} \tag{4.1}$$

In Eqn. 4.1, the energy of the (100) orientation ($\theta = 0$) is normalized to equal 1.0. Using this approximation, the surface energy and its derivatives at each point are determined by the inclination and orientation of the surfaces bounding the groove and a finite set of unknown coefficients. For a series of order R, the number of coefficients is $2R(2R+1)$ so that for a set of N observations along the circumferences of G island grains, the total number of unknowns is $U = 2R(2R+1) + G$. Because approximately 50 observations can be made at each island grain, an increment in G increases N much more than U. Thus, for even a small number of island grains, N is much greater than U, and a set of best fit coefficients and grain boundary energies can be determined using a conventional linear least squares procedure.

The torque terms in Eqns. 2.4 and 2.5 can be evaluated using the following expression:

$$\frac{\partial\gamma_i}{\partial\chi_i} = \frac{\partial\theta}{\partial\chi_i}\frac{\partial\gamma_i}{\partial\theta} + \frac{\partial\phi}{\partial\chi_i}\frac{\partial\gamma_i}{\partial\phi}. \tag{4.2}$$

Analytical expressions for $\partial\gamma_i/\partial\theta$ and $\partial\gamma_i/\partial\phi$ are easily obtained from Eqn. 4.1. Although the terms $\partial\theta/\partial\chi_i$ and $\partial\phi/\partial\chi_i$ can be derived exactly, for computational ease they where approximated as difference quotients, $\Delta\theta/\Delta\chi_i$ and $\Delta\phi/\Delta\chi_i$, calculated by dividing the change that occurs in θ or ϕ ($\Delta\theta$ or $\Delta\phi$) as the surface normal vector is rotated through a small, fixed angle about $\hat{\ell}$, by the rotation angle ($\Delta\chi_i$). The values of $\Delta\theta$ and $\Delta\phi$ were determined using a rotation matrix with elements R_{ij}:

$$R_{ij} = \delta_{ij}\cos(\Delta\chi) - \varepsilon_{ijk}\ell_k\sin(\Delta\chi) + (1-\cos(\Delta\chi))\ell_i\ell_j. \tag{4.3}$$

In Eqn. 4.3, ℓ_i are the components of the vector $\hat{\ell}$, δ_{ij} is the Kronecker delta, and ε_{ijk} is the permutation tensor. The magnitude of the torque terms were insensitive to choices of $\Delta\chi$ less than 1°.

After the approximate expression for the surface energy (Eqn. 4.1), along with the torque terms, is substituted into Eqns. 2.4 and 2.5, the only unknowns in the equations are the coefficients of the series. Now, a standard linear least squares procedure can be used to determine the functional form of the surface energy.

Spherical harmonics

To illustrate the application of symmetrized spherical harmonic functions to extract grain boundary energies from the grain boundary triple junction data, we shall ignore the influence of the grain boundary plane on the energy. Under this assumption, the grain boundary energy is a function of only misorientation ($\gamma_{gb} = \gamma_{gb}(\Delta g)$) and the local equilibrium condition is reduced to Eqn. 2.7. Next, the grain boundary energy is approximated as a finite series of harmonic basis functions which have the symmetry of cubic misorientation space:

$$\gamma(\Delta g) = \sum_{\ell=1}^{\infty} \sum_{\mu=1}^{M(\ell)} \sum_{\nu=1}^{M(\ell)} C_{\ell\mu\nu} \ddot{\dot{T}}_{\ell}^{\mu\nu}(\Delta g), \tag{4.4}$$

where $\ddot{\dot{T}}_{\ell}^{\mu\nu}(\Delta g)$ are cubic-cubic symmetric generalized spherical harmonic functions, $C_{\ell\mu\nu}$ are the coefficients of the series, and $M(\ell)$ are the number of linearly independent solutions which are enumerated by the index μ or ν [6]. These cubic-cubic functions can be used to represent any property which is a function of misorientation in a homophase cubic system. However, we know that the grain boundary energy function should exhibit certain properties and this allows us to introduce boundary conditions. In the limit that the misorientation between adjacent grains goes to zero, the energy function must also be zero:

$$\gamma(I) = 0, \tag{4.5}$$

where I is the identity misorientation. Also, since the energies can only be determined in a relative sense, we have normalized the function such that the average energy is equal to one. Introducing these two boundary conditions leads to the following expression for the grain boundary energy as a function of misorientation:

$$\gamma(\Delta g) = \left[1 - \ddddot{T}_4^{11}(\Delta g)\right] + \sum_{\ell=6}^{\infty} \sum_{\mu=1}^{M(\ell)} \sum_{\nu=1}^{M(\ell)} C_{\ell\mu\nu} \left[\ddddot{T}_\ell^{\mu\nu}(\Delta g) - \ddddot{T}_\ell^{\mu\nu}(I)\ddddot{T}_4^{11}(\Delta g)\right]. \qquad (4.6)$$

After substituting the grain boundary energy (Eqn. 4.6) into the local equilibrium condition (Eqn. 2.7) the only unknowns are the coefficients of the series ($C_{\ell\mu\nu}$). Again, the coefficients can be determined using a standard linear least squares technique.

4.1.2 Discrete method

In this section, we shall describe an alternative method for reconstructing the interfacial energy anisotropy that does not parameterize the energy in terms of a finite series of basis functions. Here, we employ a procedure developed by Morawiec [5] that provides a discrete value of the energy for a predefined set of interfacial characters. This discrete analysis is facilitated by use of the Cahn-Hoffman [7,8] formalism for the capillarity vector which makes it possible to include the torque terms in the equilibrium equation without having to compute differentials. This method will be referred to as the capillarity vector reconstruction method.

The local equilibrium condition (Eqn. 2.3) can be rewritten in terms of the Cahn-Hoffman [7,8] capillarity vector, $\vec{\xi}$. The capillarity vector is formed by combining the two scalar quantities γ_i and $\partial\gamma_i/\partial\beta_i$ with unit vectors normal and parallel to the plane of the interface, respectively. The component of the capillarity vector normal to the interface is equal in magnitude to γ, thus $\vec{\xi}_n = \gamma\hat{n}$. Note that $\vec{\xi}_n \times \hat{\ell}$ is a tension in the plane of the interface that is perpendicular to $\hat{\ell}$ and has a magnitude of γ:

$$\vec{\xi}_n \times \hat{\ell} = \gamma\hat{t}. \qquad (4.7)$$

Furthermore, the capillarity vector has a component in the plane tangent to the interface that is related to the change in γ with orientation given by $\vec{\xi}_t = (\partial\gamma/\partial\beta)_{max}\hat{t}_o$ where $\hat{t}_o$ points in the direction of maximum increase of γ. Therefore, $\vec{\xi}_t \times \hat{\ell}$ is a vector perpendicular to the interface whose magnitude is given by the component of $\vec{\xi}_t$ perpendicular to $\hat{\ell}$. This is a measure of the so-called torque force that is normal to the interface and urges it to rotate about the line of intersection. In other words,

$$\vec{\xi}_t \times \hat{\ell} = \frac{\partial \gamma}{\partial \beta} \hat{n}. \tag{4.8}$$

Substituting the left hand sides of Eqns. 4.7 and 4.8 into Eqn. 2.3, we see that the local equilibrium condition for a triple junction can be expressed in the following way:

$$(\vec{\xi}_1 + \vec{\xi}_2 + \vec{\xi}_3) \times \hat{\ell} = 0. \tag{4.9}$$

By discretizing the space of interfacial characters and fitting experimental observations to Eqn. 4.9, the capillarity vectors for the interfaces bounding a triple junction can be determined without evaluating any differential terms. The capillarity vector field for a discrete set of interfaces is solved using an iteration process which is described in detail for both the surface and grain boundary measurements in Appendix B. After solving the capillarity vector field, the interfacial energy is then given by the magnitude of the capillarity vector normal to the interface plane, $\gamma = \vec{\xi} \cdot \hat{n}$.

4.2 Simulated data results

The accuracy and performance of the energy reconstruction methods were tested by creating simulated data sets based on model energy functions with the correct symmetries for a material with cubic crystal symmetry. These data sets were generated such that they mimic the data sets extracted from thermal grooves (surface energy) and grain boundary triple junctions (grain boundary energy).

4.2.1 Surface energy

Model function

The model function was isotropic ($\gamma = 1$) everywhere except for a cusp around (111). The cusp had a width of $15°$ and a depth of $0.6\gamma_{isotropic}$ and was shaped by an analogy to the Read-Shockley expression for the energy of low angle boundaries. The functional form is given by:

$$\begin{aligned} &\gamma(0) = 0.6 && \\ &\gamma(\theta_{111}) = 0.4\left(\tfrac{\theta_{111}}{15}\right)\left(1 - \ln\left(\tfrac{\theta_{111}}{15}\right)\right) + 0.6 && 0 < \theta_{111} \leq 15^{\circ} \\ &\gamma(\theta_{111}) = 1 && \theta_{111} > 15^{\circ} \end{aligned} \tag{4.10}$$

where θ_{111} is the angular separation, in degrees, between the surface orientation and $[111]$.

Triple junction generation

The model thermal grooves were generated by first assigning Euler angles (φ_1, Φ,φ_2) to both the enclosed and matrix grains. Values for χ_1 and $\hat{\nu}$ were then randomly generated. Next, the values of χ_2 and α that balance the interfacial energies according to Eqn. 2.3 were determined using a downhill simplex method (AMOEBA [9]). Parameter sets for simulated grooves were considered valid if the absolute values of the perpendicular and parallel components in Eqn. 2.3 summed to less than 0.01. The procedure was repeated until 50 valid grooves were found for each of five enclosed grain/matrix grain pairs. In other words, the number of observations in the model data set was selected to mimic as nearly as possible the real data set. Since the real data contains experimental errors, the groove parameters (χ_1, χ_2, $\hat{\nu}$, and α) were perturbed by a random angle generated according to a Gaussian distribution with standard deviations of 1°, 1°, 1°, and 5°, respectively.

Energy reconstruction

The model energy function is shown in fig. 4.1 together with a comparison of the results from the Fourier series fitting method and the capillarity vector reconstruction. The fitting for the series reconstruction method was conducted by substituting an $R = 1$ series into Eqn. 2.4 and a standard linear least squares program (LSFIT [9]) was used to solve for the unknown coefficients. The Fourier series fit results in a smoothly varying function that approximates the shape of the actual surface energy function. However, the true depth of the cusp is severely underestimated.

For the capillarity vector reconstruction method, the sub-domain of surface characters (θ and ϕ in the range of 0 to 90°) was divided into 15 equal sections in $\cos\theta$ and ϕ (this provides a resolution of about 6°). The relaxation factor for the iterative solution was chosen as the inverse of the maximum number of equations that any one interfacial character was involved in, and the iteration process was stopped when the change in the sum of the magnitude of all of the deviations vectors is less than 1% of the change during the first iteration. The iteration process converged after 573 steps. For each surface normal, the energy was taken as the average of the 6 symmetrically equivalent cells that correspond to the surface normal.

Although there are some outlying points, the calculated surface energies are close to the model function. While the true depth of the cusp at (111) is not reproduced, the capillarity vector reconstruction method performs better than the series fitting method. Note that the only point where the discrete reconstructed data deviates significantly from the model function is at the (111) orientation. On later inspection, it was found that the randomly generated data set contained no grooves with these surfaces. While denser and more uniform trial data sets can be used to generate better reconstructions, the results shown in Fig. 4.1 are characteristic of the experimental data at hand and illustrate the challenges associated with discerning sharp features in the surface energy. 95% of the surface energies determined using the capillarity vector reconstruction method deviated from the model function by less than 3.6%. In our reconstruction of the experimental data, we shall use this figure as a measure of the uncertainty in the result.

4.2.2 Grain boundary energy - misorientation only

Model function

The Read-Shockley model was used as the model function for the grain boundary energy as a function of misorientation alone. In this model, the grain boundary energy is a function a single misorientation parameter, θ_{mis}, which is the minimum angle of misorientation (disorientation) about the rotation axis common to the two grains. The functional form is

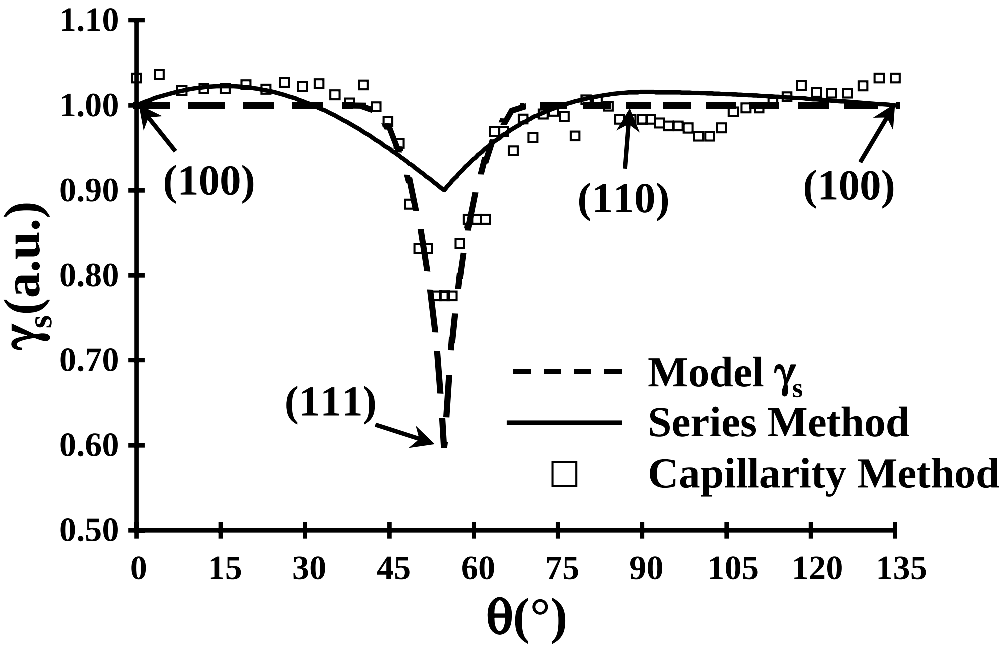

Figure 4.1: Plot of relative surface energies reconstructed from model data using both the series and capillarity methods. The plot shows orientations around the perimeter of the unit triangle, from (100) to (111), then to (110), and back to (100).

given by:

$$\begin{aligned} &\gamma(0) = 0 \\ &\gamma(x) = x(1 - \ln x) \quad && 0 < x \leq 1 \\ &\gamma(x) = 1 && x > 1, \end{aligned} \tag{4.11}$$

where $x = \theta_{mis}/15°$.

Triple junction generation

The triple junctions were generated by first assigning three random grain orientations (g_i) and calculating the disorientation between each grain orientation (θ_{ij}). Using the model energy function, the dihedral angles at the triple junctions were calculated by solving Eqn. 2.7 with respect to $\cos \chi_{ij}$ and using these values to calculate χ_{ij}. A total of 1555 triple junctions were generated in this manner. To account for the experimental errors, the ideal dihedral angles were altered by randomly generated angles ($\Delta\chi$) with a population governed by the von-Mises distribution, $\exp(k \cos \Delta\chi)$, with $k = 300$. This distribution is peaked at $\Delta\chi = 0$ and values outside the limits of $\pm 10^\circ$ are very unlikely.

Energy reconstruction

To reconstruct the grain boundary energy function based on misorientation alone, we represented the data as a series of symmetrized spherical harmonics. For this analysis, the functional form of the grain boundary energy (Eqn. 4.6) was truncated at $\ell = 12$. By truncating the series at this point, the minimum period of oscillations that can be reproduced in 7.5°. The functional form for the grain boundary energy was then substituted into the local equilibrium condition (Eqn. 2.7), and a standard linear least squares program (LSFIT [9]) was used to solve for the unknown coefficients. A comparison between the Read-Shockley model and the fit function for the $\langle 110 \rangle$ misorientation axis is shown in Fig. 4.2. The fit function shows the same general trends as the model; it increases as the misorientation angle increases from zero to an angle of $\sim 20^\circ$. For misorientation angles larger than 20°, the function flattens and oscillates around one. However, the exact shape of the Read-Shockley model is not reproduced by the approximate function, especially near the origin. Instead of a sharp cusp at zero misorientation and a constant energy value of one for misorientations greater than the limiting angle, the slope of the function vanishes at zero misorientation and there are oscillations (± 0.12) about one for the higher angle misorientations. This is an unavoidable consequence of approximating the energy as a finite series of harmonic functions. While adding additional terms to the series can improve the approximation, these characteristic features will, to some extent, persist as long as this particular set of basis functions is used.

4.2.3 Grain boundary energy - five parameter

Model function

The model function for the grain boundary energy over all five parameters is based on a uniform energy distribution with cusps shaped in analogy to the Read-Shockley expression

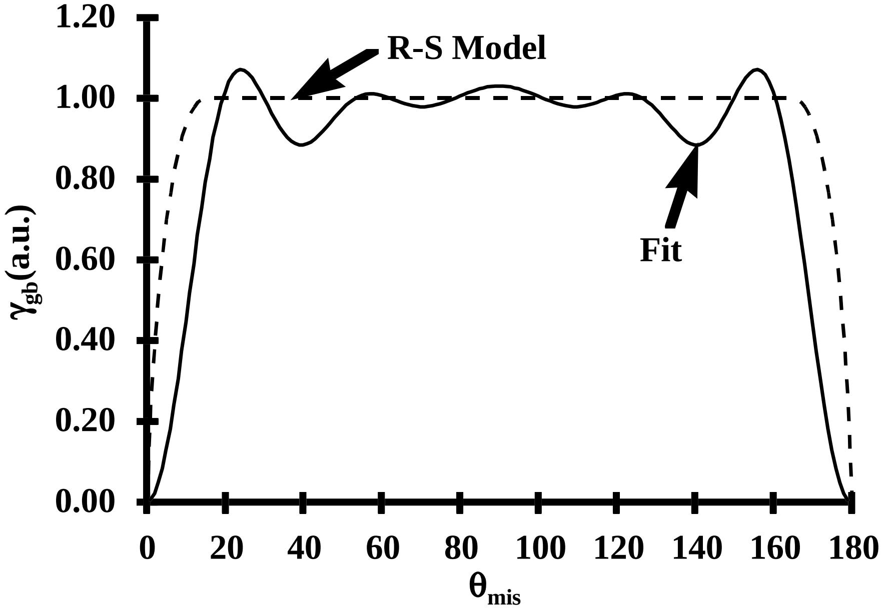

Figure 4.2: Comparison of the model grain boundary energy function based on misorientation alone and an approximate function fit to a data set generated from the model.

for the energy of low angle boundaries. The functional form is given by:

$$\begin{aligned}
&\gamma(0,a) = 1 - a && \\
&\gamma(x,a) = ax(1 - \ln x) + (1 - a) && 0 < x \le 1 \\
&\gamma(x,a) = 1 && x > 1
\end{aligned} \tag{4.12}$$

where x is the ratio of the angular distance from the center of the cusp (ω) to the maximum width of the cusp (W), and a corresponds to the depth of the cusp. The distance ω between two boundaries is given by $\omega = 5 - tr(\Delta g_1^T \Delta g_2) - n_1 \cdot n_2 - (\Delta g_1^T n_1) \cdot (\Delta g_2^T n_2)$ [5]. For the simulated data set, the model energy function had two cusps of this type: one corresponding to a misorientation of $60°$ about $[111]$ with a boundary plane normal to $[111]$ and one corresponding to a misorientation of $45°$ about $[110]$ with a boundary plane normal to $[110]$. For both cusps, $a = 1/\sqrt{5}$ and $W = 15°$. The model function also had a special cusp at zero misorientation that was independent of boundary plane. In this case, the same functional form was used with $a = 1$ and $W = 15°$, except ω is given simply by the minimum misorientation angle between the adjacent crystallites.

Triple junction generation

The details of the procedure to generate grain boundary triple junctions from the model function are given in [5]. The procedure involves first generating three random grain orientations (g_i) and a random unit vector corresponding to the direction of the triple line ($\hat{\ell}$). Next, the vector normal to the first boundary plane ($\hat{n}_1$) is selected randomly with the condition that it is perpendicular to the triple line ($\hat{n}_1 \cdot \hat{\ell} = 0$). The remaining boundary plane normals, $\hat{n}_2$ and $\hat{n}_3$, are determined such that they minimize the deviation of the magnitude of the vector calculated from the left hand side of Eqn. 4.9 from zero. If the deviation does not reach a sufficiently small value, the junction is rejected and the procedure is repeated. A total of 2×10^4 junctions were generated in this manner, such that the number of junctions in the simulated data set was nearly identical to the number in the real data set. Again, errors were added to the junctions to mimic the presence of experimental errors in the real data set. The geometric parameters of the triple junctions, the unit vectors $\hat{\ell}$ and $\hat{n}_i$, were expressed in terms of spherical angles θ and ϕ. For each vector, θ and ϕ were perturbed by a random angle generated according to a Gaussian distribution with a standard deviation of 5°.

Energy reconstruction

For the grain boundary energy reconstruction, the space of grain boundaries was discretized in the following manner. The space was parameterized by φ_1, $\cos\Phi$, φ_2, $\cos\theta$ and ϕ, where φ_1, Φ, and φ_2 are three Eulerian angles specifying the boundary misorientation and θ and ϕ are spherical angles specifying the boundary plane normals. We chose the convenient subdomain of this space such that φ_1 and φ_2 were in the range of 0 to $\pi/2$, $\cos\Phi$ and $\cos\theta$ were in the range of 0 to 1, and ϕ was in the range of 0 to 2π. The sub-domain was tessellated into equal partitions such that $\Delta\varphi_1 = \Delta\varphi_2 = \Delta\phi = 10^\circ$, and $\Delta\cos\Phi = \Delta\cos\theta = 1/9$, yielding a resolution over the space of about 10°. The relaxation factor for the iterative solution was chosen as 10 times the inverse of the maximum number of equations that any one interfacial character was involved in, and the iteration process was stopped when the change in the sum of the magnitude of all of the deviations vectors is less than 1% of the

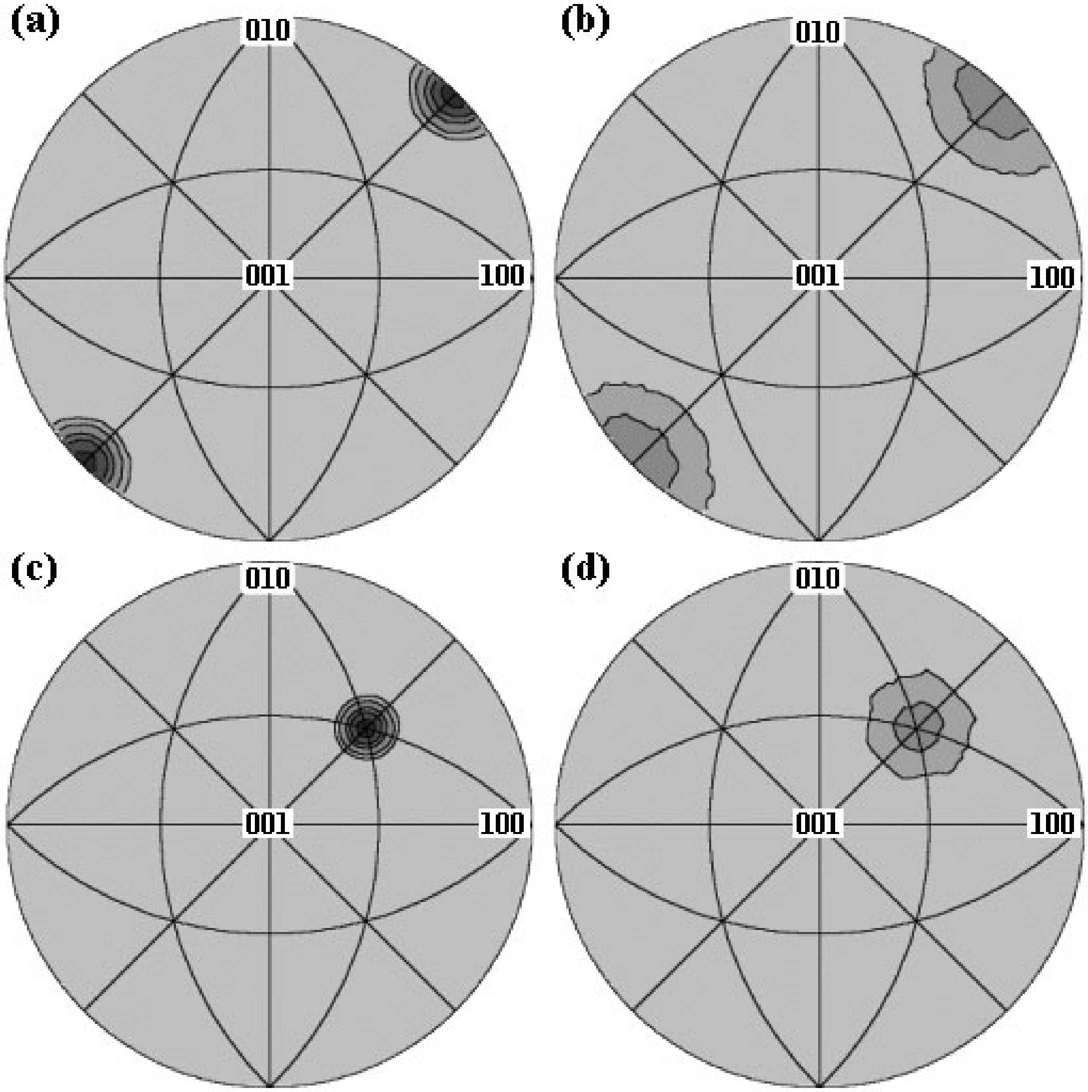

Figure 4.3: Stereographic contour plots of the model and reconstructed grain boundary energies. (a) and (b) are the model and reconstructed energies, respectively, corresponding to $\Delta g = [110], 45°$, and (c) and (d) are the model and reconstructed energies, respectively, corresponding to $\Delta g = [111], 60°$. The energies in the plots increase as the shading varies from dark to light and the contour isolines in all plots correspond to relative energy values of 0.98, 0.96, 0.92, 0.88, and 0.80.

change during the first iteration. The iteration process converged after 48 steps. For each grain boundary type, the energy was taken as the average of all 36 symmetrically equivalent cells that correspond to the boundary type.

The model function, along with the results of the reconstruction, for the misorientations corresponding to $[110], 45^\circ$ and $[111], 60^\circ$ are shown in Fig. 4.3. The plots in Fig. 4.3 show that the general trends in the energy function are reproduced by the reconstruction; however, the depths of the cusps are severely underestimated. This occurs due to the relatively large cell size ($\sim 10^\circ$) required for the limited number of triple junctions used in the reconstruction and the smoothing procedure. It has been shown that denser data sets that allow a finer discretization of the grain boundary space and do not require the smoothing procedure yield more accurate reconstructions [5]. Based on the results of the reconstruction, we conclude that at the current data density we can reconstruct the general trends in the energy function with reasonable accuracy; however, the extent of the energy anisotropy will not be accurately reproduced.

4.3 References

[1] W.A.Winterbottom and N.A. Gjostein, "Determination of the Anisotropy of Surface Energy of Metals - I: Theoretical Analysis," *Acta Met.*, **14** [9], 1033-1040 (1966).

[2] W.A.Winterbottom and N.A. Gjostein, "Determination of the Anisotropy of Surface Energy of Metals - II: Experimental γ-plot of Au," *Acta Met.*, **14** [9], 1041-1052 (1966).

[3] M. McLean and B. Gale, "Surface Energy Anisotropy by an Improved Thermal Grooving Technique," *Philos. Mag.*, **20** [167], 1033-1045 (1969).

[4] B. Gale, R.A. Hunt, and M McLean, "An Analysis of Surface Energy Anisotropy Data using Lattice Harmonics," *Philos. Mag.*, **25** [4], 947-960 (1972).

[5] A. Morawiec, "Method to Calculate the Grain Boundary Energy Distribution over the Space of Macroscopic Boundary Parameters from the Geometry of Triple Junctions," *Acta Mater.*, **48**, 3525-3532 (2000).

[6] H.-J. Bunge, Texture Analysis in Materials Science, translated by P.R. Morris; Butterworths, London, (1982).

[7] D.W. Hoffman and J.W. Cahn, “A Vector Thermodynamics for Anisotropic Surfaces - I. Fundamentals and Application to Plane Surface Junctions,” *Surface Science*, **31**, 368-388 (1972).

[8] J.W. Cahn and D.W. Hoffman, “A Vector Thermodynamics for Anisotropic Surfaces - II. Curved and Faceted Surfaces,” *Acta Met.*, **22**, 1205-1214 (1974).

[9] W.H. Press, B.P. Flannery, S.A. Teukolsky, and W.T. Vetterling, Numerical Recipes in Pascal; Cambridge University Press, Cambridge, 1989.

Chapter 5

Surface Energy

In this chapter, we will discuss the reconstruction of the surface energy from the groove measurements taken from around the circumference of island grains in the polycrystalline magnesia specimen. We have used both the Fourier series and capillarity vector reconstruction methods to extract the surface energy. The results from both methods are compared to orientation stability data to assess which result more nearly represents the actual surface energy anisotropy. Finally, the reconstructed surface energies are compared with previous theoretical predictions and experimental results for magnesia surfaces.

5.1 Fourier series reconstruction

5.1.1 Linear least squares analysis

The approximate Fourier series expression for the surface energy (Eqn. 4.1) was substituted into Eqns. 2.4 and 2.5, and a standard linear least squares procedure (LSFIT [1]) was used to determine the best fit values of the coefficients. The quality of the fit was assessed by the ratio (ρ) of the sum of the squares of the residuals to the difference between the number of equations and the number of free parameters. We found ρ to be sensitive to the choice of equilibrium equation (Eqn. 2.4 and/or Eqn. 2.5) and series order, R.

Equilibrium equations

The Herring relation can be broken down into two independent equations, Eqns. 2.4 and 2.5, which represent the balance of the vertical and horizontal components, respectively. Although fits which included both equations yielded qualitatively similar results, ρ was five times smaller when only the balance of the vertical components (Eqn. 2.4) was considered. The reason for this is evident when one compares the form of the equations. In both Eqns. 2.4 and 2.5, the magnitude of the left hand side is determined by α, a measured parameter that is typically near zero (78% of the observations fall in the range $-20^\circ \leq \alpha \leq 20^\circ$) and contains the highest degree of experimental uncertainty. The left hand side of Eqn. 2.4 scales with $\cos\alpha$ and the left hand side of Eqn. 2.5 scales with $\sin\alpha$ so that when α is small, measurement errors are magnified by Eqn. 2.5 and diminished in Eqn. 2.4. For example, a 15° error in the measurement of α near zero leads to an uncertainty on the left hand side of Eqn. 2.4 of 3.5%; for Eqn. 2.5, the same error leads to an uncertainty of 26%. Thus, we shall only consider Eqn. 2.4 in our analysis.

Series order

Using a series of $R = 1$, fitting the data to Eqn. 2.4 yields a ρ value of 6.76×10^{-3}. When the data set is randomly partitioned into two smaller segments, fitting to each segment leads to nearly identical results (within the standard deviation of the fit). When more terms are included in the series, there are additional oscillations in the function, and ρ decreases slightly. For example, when $R = 2$, $\rho = 5.47 \times 10^{-3}$. In this case, the ordering of the relative energies at the low index surfaces is the same as for the $R = 1$ fit. However, when the $R = 2$ function is fit to the randomly partitioned data sets, the results differ from one another and from the results obtained using the complete data set. For this reason, we take the result from the $R = 1$ series to be the more reliable result.

5.1.2 Surface energy function

We have determined that fitting only to Eqn. 2.4 and using a series of order $R = 1$ yields the best representation of the data. The best fit coefficients derived from this fitting procedure for the series in Eqn. 5.4 are listed in Table 5.1. Based on these values, we calculate the energies of the low index planes to have the following relations:

$$\begin{aligned}\frac{\gamma_{110}}{\gamma_{100}} &= 1.040 \pm 0.008 \\ \frac{\gamma_{111}}{\gamma_{100}} &= 1.072 \pm 0.010\end{aligned} \tag{5.1}$$

The uncertainties in the values of the energy were determined from the variances and co-variances of the fit coefficients [2]. The maximum energy occurs at the (111) orientation and the minimum at (100). The functional dependence is illustrated in Fig. 5.1, where the energy contours are plotted in the unit triangle of distinguishable orientations, and the value of the surface energy function along the perimeter of the unit triangle is graphed in Fig. 5.2. The best fit grain boundary energies for each of the island grains are listed in Table 5.2. In each case, the energy is less than that of the (100) surface.

Table 5.1: Best fit coefficients.

a_{10}	0.118 ± 0.060
b_{10}	0.084 ± 0.036
a_{11}	-0.130 ± 0.060
b_{11}	-0.056 ± 0.034
c_{11}	-0.100 ± 0.022
d_{11}	-0.044 ± 0.012

Table 5.2: Best fit grain boundary energies.

γ_{gb}/γ_{100}	$\theta_{mis}(^\circ)$
0.52 ± 0.01	2.02
0.90 ± 0.01	2.33
0.55 ± 0.01	3.14
0.80 ± 0.01	6.25
0.87 ± 0.01	6.31

5.2 Capillarity vector reconstruction

5.2.1 Energy reconstruction

To apply the capillarity reconstruction procedure to the island grain thermal groove measurements, we used the same sub-domain of surface characters (θ and ϕ between 0 and 90°) that was used with the simulated data. The sub-domain of was divided into 15 equal sections in $\cos\theta$ and ϕ. Again, the relaxation parameter was selected such that it was equal to the inverse of the maximum number of equations that any one interfacial character was

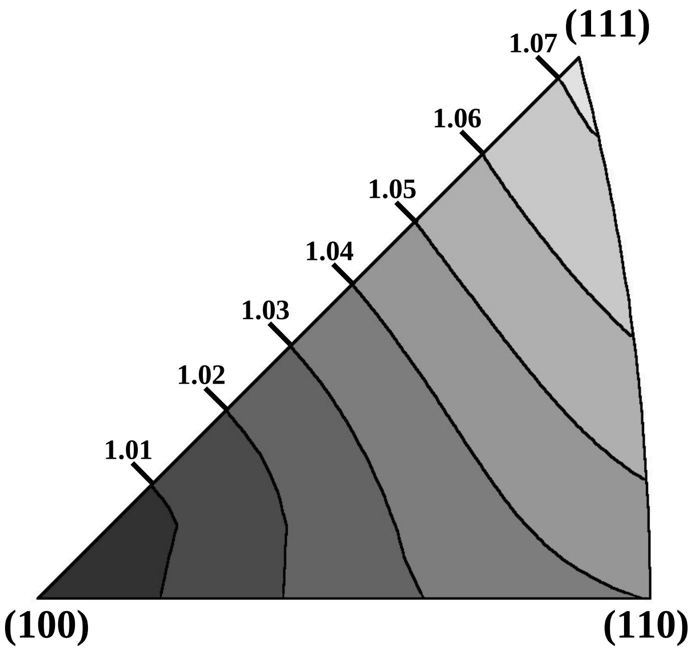

Figure 5.1: A surface energy contour plot for magnesia at $1400°C$ constructed from the best fit Fourier series.

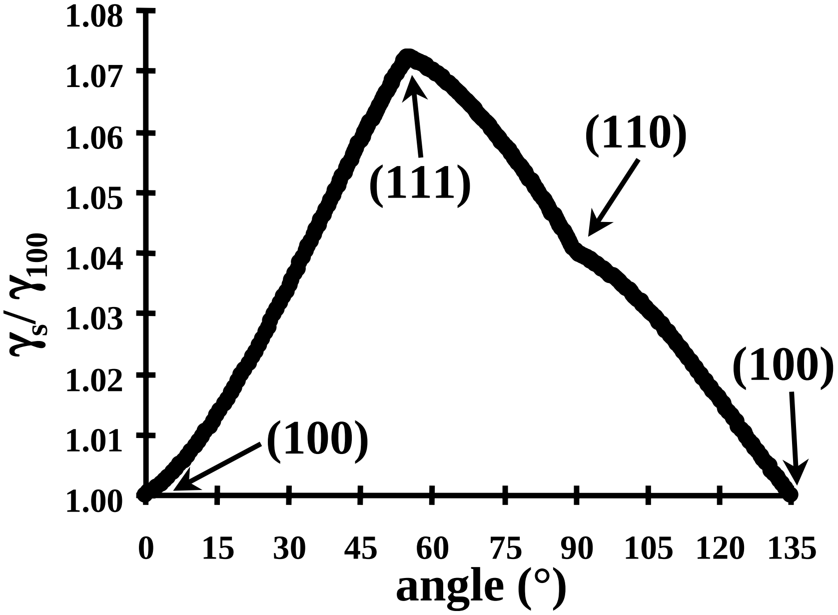

Figure 5.2: Plot of the relative surface energy derived from the Fourier series method around the perimeter of the standard stereographic triangle, from (100) to (111), then to (110), and back to (100).

involved in, and the iteration process was stopped when the change in the sum of the magnitude of all of the deviations vectors is less than 1% of the change during the first iteration. The iteration process converged after 27 steps. For each surface normal, the energy was taken as the average of the 6 symmetrically equivalent cells that correspond to the surface normal.

5.2.2 Surface energy function

A contour plot illustrating the orientation dependence of the surface energy is shown in Fig. 5.3, and the values of the reconstructed surface energy at intervals around the perimeter of the unit triangle are shown in Fig. 5.4. Based on the capillarity vector reconstruction method, the energies of the low index planes have the following relationships:

$$\begin{aligned} \frac{\gamma_{110}}{\gamma_{100}} &= 1.07 \pm 0.04 \\ \frac{\gamma_{111}}{\gamma_{100}} &= 1.17 \pm 0.04 \end{aligned} \tag{5.2}$$

While the trends in the results from the series fitting method and the capillarity vector reconstruction method are the same, the latter shows significantly more anisotropy. This is consistent with the results from model data sets in 4.2.1. The reconstructed grain boundary energies are listed in Table 5.3.

Table 5.3: Reconstructed grain boundary energies.

γ_{gb}/γ_{100}	$\theta_{mis}(^\circ)$
0.56	2.02
0.46	2.33
0.64	3.14
0.75	6.25
0.74	6.31

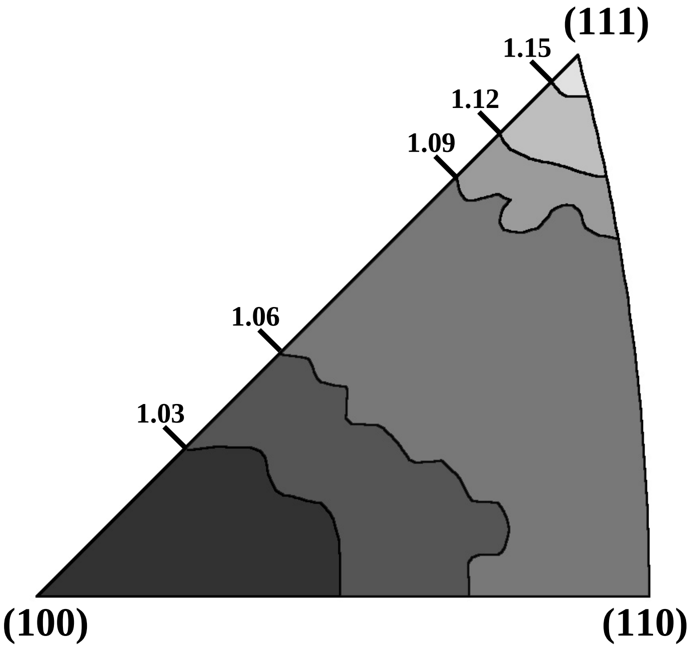

Figure 5.3: A surface energy contour plot for magnesia at $1400°C$ based on the results of the capillarity vector reconstruction method.

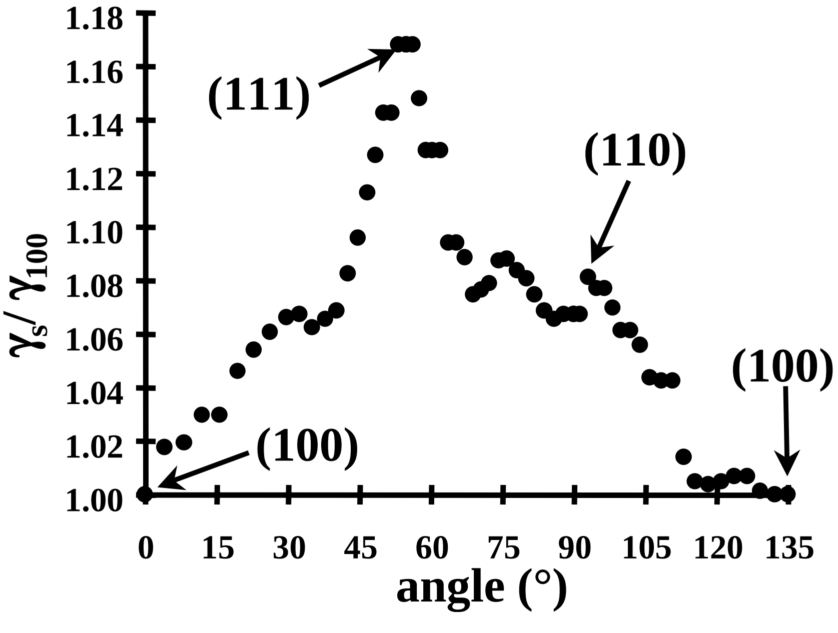

Figure 5.4: Plot of the relative surface energy derived from the capillarity vector reconstruction method around the perimeter of the standard stereographic triangle, from (100) to (111), then to (110), and back to (100).

5.3 Comparison of the methods

The results from the capillarity vector reconstruction method suggest that the total anisotropy in the surface energy of magnesia is 17% while the results from the series fit method on the same data suggest an anisotropy of 7%. Based on the results from the reconstruction of the model data (4.2.1), we are led to believe that the capillarity vector reconstruction method produces the more accurate results. Because the series fit results are constrained by the form of the basis functions, the full anisotropy can not be reproduced. The question is, which results more nearly represent the actual anisotropy? To discriminate between the two results, we can make a quantitative comparison between the faceting behavior of the magnesia polycrystal and the reconstructed surface energies.

5.3.1 Orientation stability map

AFM images of the specimen revealed that the surfaces of some grains were faceted while others were smooth (see Fig. 5.5). The bounded and extended grain surfaces that have orientations that are part of the equilibrium crystal shape will remain flat during annealing. The surfaces of grains with missing orientations will form facets. The faceted surfaces always contained ridges formed by the intersection of two planes, but no corners. When the surface inclination changes, as it does near a thermal groove, the ridges exhibit smoothly curved edges. Thus, all missing surface orientations can be made up of two stable planes. To map the orientations that are stable or unstable with respect to faceting, the surfaces of more than 100 grains whose orientations were previously determined based EBSP data were imaged by AFM. If steps with heights greater than $2.1nm$ were observed (this corresponds to five times the lattice spacing), the grain was labeled as faceted. If no steps or steps less than this height were observed, it was labeled as smooth. These data were used to construct the orientation stability map shown in Fig. 5.5c. With the exception of two outliers and a small amount of overlap in the distributions, the faceted and smooth orientations are well separated. Based on these data, it seems clear that orientations near the (100) and (111) poles are unstable with respect to faceting.

A careful examination of the faceted orientations has led us to the conclusion that within

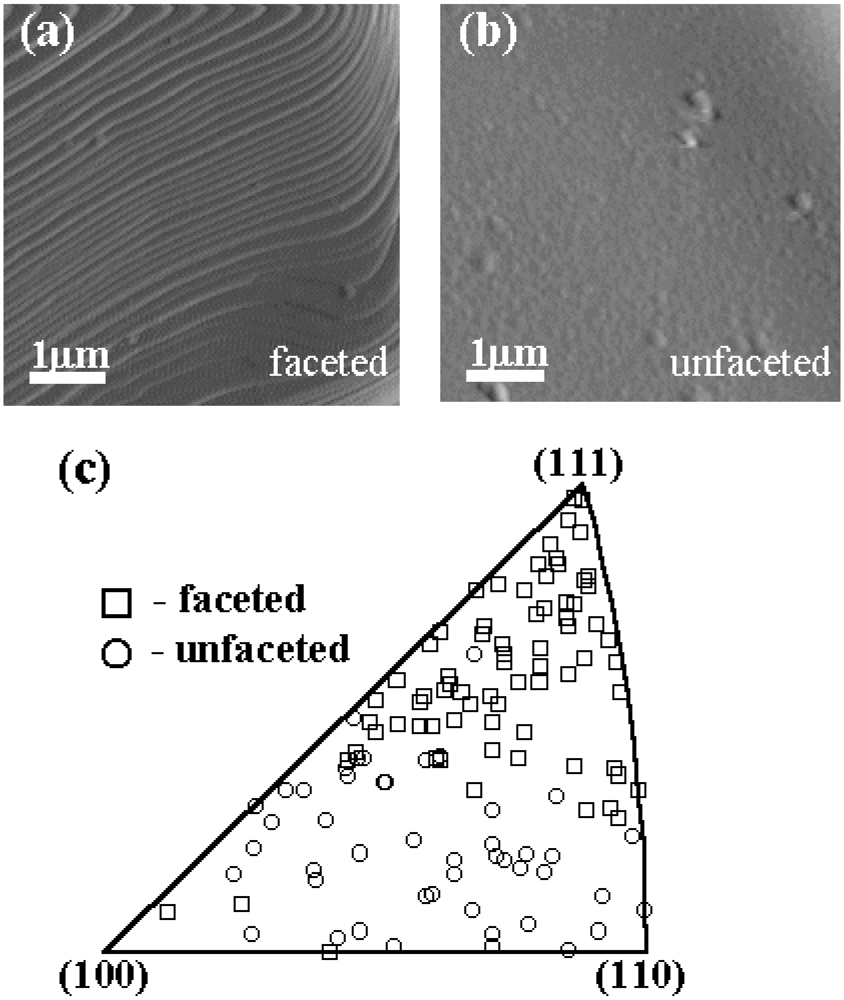

Figure 5.5: Examples of AFM images of (a) faceted and (b) unfaceted magnesia surfaces at $1400°C$. AFM images of more than 100 surfaces were used, along with EBSP data, to construct the orientation stability map shown in (c).

about $15°$ of $\{100\}$, we find that surfaces facet to $\{100\}$ plane and a complex facet. Further, all orientations within about $25°$ of $\{111\}$ form two facets that are always complex. In other words, the $\{111\}$ surface, and those vicinal to it, are missing from the equilibrium shape. For any given orientation in this range, the facets and the macroscopic orientation must share a common axis. This means that the missing orientation and the complex facets are in the same zone and lie on a great circle. Further, if the complex facets at the boundary of the unstable region have the same energy, then the circle should be the one that intersects the macroscopic orientation and has the minimum length through the unstable region. The

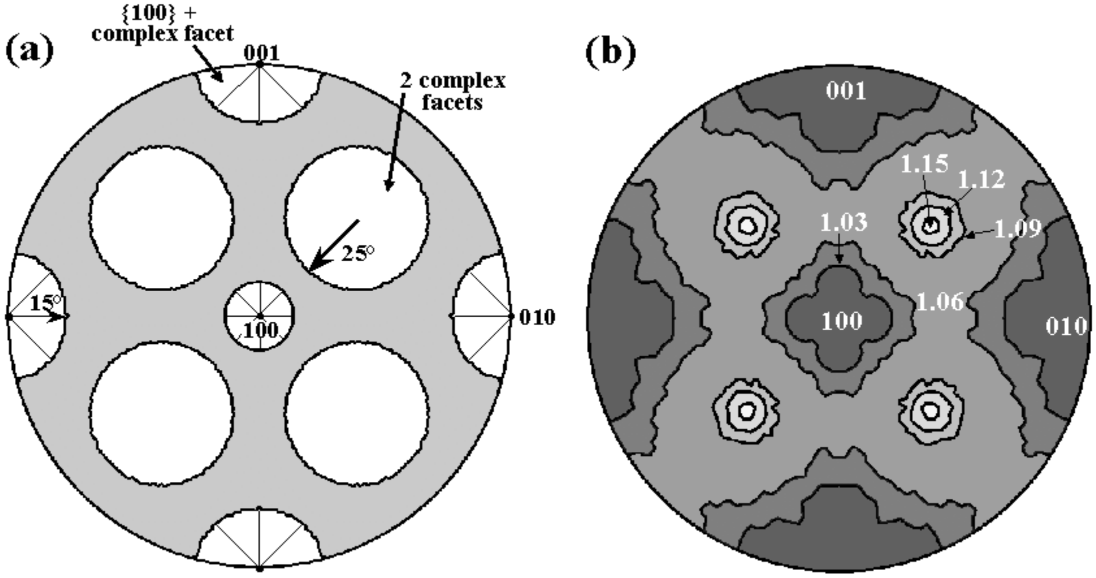

Figure 5.6: (a) Schematic n-diagram determined from measurements of orientation stability for magnesia at $1400°C$. Orientations near $\{100\}$ are unstable with respect to faceting into the $\{100\}$ orientation and a complex facet. The white regions around $\{111\}$ correspond to unstable orientations which form two complex facets, while orientations in the shaded region are stable with respect to faceting. (b) Contour map on a stereographic projection of the relative surface energies derived from the capillarity method for magnesia at $1400°C$.

orientation of the complex facets will be found at the intersection of this great circle and the boundary between the faceted and flat orientations. Using this information, we have constructed a schematic n-diagram [3], which is a stereographic projection of the surfaces present at equilibrium, for magnesia at $1400°C$ shown in Fig. 5.6a. For comparison, a contour map of the relative surface energies derived from the capillarity method are also shown in Fig. 5.6b.

5.3.2 Facet local equilibrium

The results from both the Fourier series fit method and the capillarity vector reconstruction method agree qualitatively with the observed faceting. To make a more quantitative comparison, we can assume that a local equilibrium is established at the intersections of the surface facets. From the observations of orientation stability, we find that orientations within about $15°$ of $\{100\}$ facet to a $\{100\}$ plane and a complex facet. Applying Herring's equation to this situation, we find that [4,5]:

$$\frac{\gamma_{100}}{\gamma_c} = \cos\omega - \frac{1}{\gamma_c}\frac{\partial\gamma_c}{\partial\omega}\sin\omega, \tag{5.3}$$

where ω is the angle between the facets, and γ_{100} and γ_c are the energies of the singular (100) and complex surface, respectively. Assuming that the torque is small enough for the final term to be ignored, then the relative energy of two intersecting facets is given by $\cos\omega$. If the (100) surface and the neighboring complex facets are separated by 15°, then $\gamma_c/\gamma_{100} = 1.035$. Although both methods predict less anisotropy, this value is more consistent with the capillarity vector results. However, it is most likely an underestimate since the results from both methods predict $\partial\gamma_c/\partial\omega$ to be positive (the energy increases as ω increases away from the complex orientation). In fact, using the reconstructed energies from the capillarity vector method, we estimate $\partial\gamma_c/\partial\omega$ to be about 0.115; therefore, γ_c/γ_{100} is equal to 1.068. Therefore, it appears as though extent of the energy cusp at $\langle 100\rangle$ has been underestimated by both reconstruction methods The underestimation of the anisotropy of the energy at a cusp is an artifact of the reconstruction procedures, which we observed from the reconstruction of model data in Chapter 4. We can also consider the equilibrium between complex facets formed by orientations within 25° of $\{111\}$. Since the (111) facet is replaced by complex facets inclined by 25°, we conclude that γ_{111}/γ_c is 1.103. If we assume isotropy in this region of stable orientations, then the anisotropy we should expect between γ_{100} and γ_{111} must be the product of γ_c/γ_{100} and γ_{111}/γ_c, or about 18%. This is nearly equivalent to the anisotropy predicted by the capillarity vector method and is approximately two and a half times the amount of anisotropy predicted by the Fourier series fit method, which, in fact, predicted missing orientations only 4° from (100) and 5.5° from (111). Although both techniques underestimate the extent of the energy cusp at (100), the observed range of faceting is more consistent with the results from the capillarity vector reconstruction method. Thus, we conclude that the capillarity vector results more nearly represent the actual surface energy anisotropy in the magnesia polycrystal.

5.4 Previous results comparison

5.4.1 Broken bond model

Ignoring relaxation effects, the relative surface energy of different crystallographic planes should scale with the broken bond density. Magnesia has the rock salt structure and only one bond per atom must be broken to create the (100) surface. Two and three bonds per atom must be broken to form the (110) and (111) surfaces, respectively. When the broken bond densities per unit area (σ) are compared, one finds that the (100) surface has the smallest value and that $\sigma_{110}/\sigma_{100} = \sqrt{2}$ and $\sigma_{111}/\sigma_{100} = \sqrt{3}$. Therefore, the measured surface energies occur in the same order as the density of nearest neighbor broken bonds on the surface. As one would expect, however, the measured variation in the energies in the real system (17%) is much smaller than that predicted by the simple bond breaking model.

5.4.2 Model calculations

There have been a number of model calculations of the surface energy of magnesia which were summarized in Table 2.2 [6–10]. With one exception, these studies place the energy of the (100) surface in the vicinity of $1.0 J/m^2$ at $0K$. Further, in the cases where the energies of more than one surface were computed, the energies have the same order as those observed in the present study ($\gamma_{100} < \gamma_{110} < \gamma_{111}$). The magnitude of the anisotropy predicted by these $0K$ calculations is larger than experimentally observed and, in fact, is larger than it would be possible to observe in any equilibrium experiment. For example, if the energy of the (110) surface of a cubic crystal were more than $\sqrt{2}$ times the energy of the (100) surface, then the surface would lower its energy by faceting into (100) and (010) surfaces that would meet along lines in the $[001]$ direction and form ridges. Therefore, the energy of the (110) orientation has an upper limit of $\sqrt{2}\gamma_{100}$. Similarly, if the energy of the (111) surface were more than $\sqrt{3}$ times the energy of the (100) surface, it would lower its energy by faceting into trigonal pyramids bound by (100), (010), and (001) facets. Thus, the results of our experiments fall within the upper bounds set by the equilibrium condition.

5.4.3 Experimental observations

Earlier experimental studies of magnesia surfaces have been conducted in temperature ranges above and below the current study (but at different partial pressures of oxygen). For example, Henrich [11] annealed an ion bombarded magnesia (111) surface in ultra-high vacuum to temperatures as high as $1127°C$ and found that the surface faceted into trigonal pyramids bounded by (100) planes. This would imply a higher degree of anisotropy than what we have observed, which would be consistent with the lower temperatures used for the annealing. When the magnesia (111) surface was examined by reflection electron microscopy after being annealed at $1550°C$ to $1700°C$ in oxygen, it was found to be smooth (but reconstructed on the atomic-scale) and stable against faceting [12]. While the widely different partial pressures of oxygen used in the aforementioned studies might make a rigorous comparison inappropriate, it is worth noting that the transition from a faceted surface at $1127°C$ [11] to a partially faceted surface at $1400°C$ (the current study) and to a smooth surface at $1500°C$ [12] is consistent with the reduction in anisotropy that is expected at elevated temperatures. In fact, this transition might be analogous to that observed in the isostructural compound, halite, for which smooth (111) surfaces are only observed above $650°C$ [13]. In the present and previous studies, Ca was the major impurity and this is known to segregate to the surface [14]. Reflection electron microscopy experiments have shown that the step structure on the (100) surface can be altered by Ca segregation [15]; therefore, we must conclude that the exact form of the surface energy function is sensitive not only to the temperature and partial pressure of oxygen, but also to the concentration of dissolved (and segregated) impurities.

Although the differences of the relative energies of magnesia surfaces have not been experimentally quantified, the current observations (17%) are consistent with the anisotropy reported for other ceramic compounds, such as LiF (18%) [16] and sapphire ($14 - 22\%$) [17,18]. Furthermore, our observations are higher than the anisotropy reported for fcc metals ($2 - 8\%$) [19–25], which is expected since it is believed that more energy is required to break ionic bonds than metallic bonds.

5.4.4 Polar surfaces

The conventional view is that orientations vicinal to a low index plane have relatively higher energies because additional bonds must be broken to create a terrace-step structure. However, our observations show the energy decreases as the orientation deviates from the (111) surface. The observation can be rationalized if we consider that the (111) surface of magnesia is polar (terminated by ions with the same charge). We have previously mentioned that because a polar surface has a dipole moment, its energies will always be larger than the energies of other surfaces of the same solid that are either charge neutral or charged, but lacking a dipole moment [26]. In this case, while the step creation does break additional bonds, it also introduces ions of the opposite sign and this reduces the surface charge imbalance. For example, adjacent (111) terraces of the rock salt structure separated by monoatomic steps are terminated by ions of opposite charge. Thus, a decrease in the surface energy with step density can occur if the gain in electrostatic stability is greater than the cost of breaking bonds to create steps.

5.5 References

[1] W.H. Press, B.P. Flannery, S.A. Teukolsky, and W.T. Vetterling, Numerical Recipes in Pascal; Cambridge University Press, Cambridge, 1989.

[2] Snedecor and Cochran, Statistical Methods; Seventh Edition, The Iowa State University Press, Ames, Iowa, 1980.

[3] J.W. Cahn and C.A. Handwerker, “Equilibrium Geometries of Anisotropic Surfaces and Interfaces,” *Mater. Sci. Engng. A*, **A162** [1-2], 83-95 (1993).

[4] A.J.W. Moore; pp. 155-198 in Metal Surfaces: Structure, Energetics, and Kinetics. Edited by N.A. Gjostein and W.D. Robertson. American Society for Metals, Metals Park (1963).

[5] C. Herring, pp. 143-179 in The Physics of Powder Metallurgy. Edited by W.E. Kingston. McGraw Hill, New York, 1951.

[6] P.W. Tasker and D.M. Duffy, “The Structure and Properties of the Stepped Surfaces of MgO and NiO,” *Surface Science*, **137** [1], 91-102 (1984).

[7] M. Causa, R. Dovesi, C. Pisani, C. Roetti, “*Ab Initio* Hartree-Fock Study of the MgO (001) Surface,” *Surface Science*, **175** [3], 551-560 (1986).

[8] W.C. Mackrodt, “Atomistic Simulation of Oxide Surfaces,” *Phys. Chem. Minerals*, **15** [3], 228-237 (1988).

[9] A. Gibson, R. Haydock, J.P. LaFemina, “Electronic Structure and Relative Stability of the MgO (001) and (111) Surfaces,” *J. Vac. Sci. Techol. A*, **10** [4], 2361-2366 (1992).

[10] J. Goniakowski and C. Noguera, “Electronic Structure of Clean Insulating Oxide Surfaces I. A Numerical Approach,” *Surface Science*, **319** [1/2], 68-80 (1994).

[11] V.E. Henrich, “Thermal Faceting of the (110) and (111) Surfaces of MgO,” *Surface Science*, **57** [1], 385-392 (1976).

[12] M. Gajdardziska-Josifovska, P.A. Crozier, and J.M. Cowley, “A $(\sqrt{3} \times \sqrt{3})R30^\circ$ Reconstruction on Annealed (111) Surfaces of MgO,” *Surface Science Letters*, **248** [1/2], L259-L264 (1991).

[13] J.C. Heyraud and J.J. Métois, “Equilibrium Shape of an Ionic Crystal in Equilibrium with its Vapour (NaCl),” *J. Cryst. Growth*, **84** [3], 503-508 (1987).

[14] R.C. McCune and P. Wynblatt, “Calcium Segregation to a Magnesium Oxide (100) Surface,” *J. Amer. Ceram. Soc.*, **66** [2], 111-117 (1983).

[15] M. Gajdardziska-Josifovska, P.A. Crozier, M.R. McCartney, and J.M. Cowley, “Ca Segregation and Step Modifications on Cleaved and Annealed MgO(100) Surfaces,” *Surface Science*, **284** [1/2], 186-199 (1993).

[16] Z.Y. Wang, M.P. Harmer, Y.T. Chou, “Pore-Grain Boundary Configurations in Lithium Fluoride,” *J. Am. Ceram. Soc.*, **69** [10], 735-740 (1986).

[17] J.-H. Choi, D.-Y. Kim, B.J. Hockey, S.M. Wiederhorn, C.A. Handwerker, J.E. Blendell, W.C. Carter, and A.R. Roosen, “Equilibrium Shape of Internal Cavities in Sapphire,” *J. Am. Ceram. Soc.*, **80** [1], 62-68 (1997).

[18] M. Kitayama and A.M. Glaeser, “The Energetics and Kinetics of Pore Shape Changes in Alumina,” *Key Engineering Materials*, **159-160** 193-204 (1999).

[19] H. Mykura, “The Variation of the Surface Tension of Nickel with Crystallographic Orientation,” *Acta Met.*, **9** [6], 570-576 (1961).

[20] W.M. Robertson and P.G. Shewmon, “Variation of the Surface Tension with Orientation in Copper,” *Trans. Metall. Soc. AIME*, **224** [4], 804-811 (1962).

[21] M. McLean and H. Mykura, “The Orientation Dependence of Surface Tension for Face-Centered-Cubic Iron,” *Acta Met.*, **12** [3], 326-328 (1964).

[22] W.A.Winterbottom and N.A. Gjostein, “Determination of the Anisotropy of Surface Energy of Metals - I: Theoretical Analysis,” *Acta Met.*, **14** [9], 1033-1040 (1966).

[23] W.A.Winterbottom and N.A. Gjostein, “Determination of the Anisotropy of Surface Energy of Metals - II: Experimental γ-plot of Au,” *Acta Met.*, **14** [9], 1041-1052 (1966).

[24] M. McLean and B. Gale, “Surface Energy Anisotropy by an Improved Thermal Grooving Technique,” *Philos. Mag.*, **20** [167], 1033-1045 (1969).

[25] B. Gale, R.A. Hunt, and M McLean, “An Analysis of Surface Energy Anisotropy Data using Lattice Harmonics,” *Philos. Mag.*, **25** [4], 947-960 (1972).

[26] P.W. Tasker, “The Stability of Ionic Crystal Surfaces,” *J. Phys. C: Solid State Phys.*, **12** [22], 4977-4984 (1979).

Chapter 6

Grain Boundary Character and Energy

In this chapter, we discuss the distribution of grain boundary character types extracted from the triangular mesh of the grain boundary network described in Chapter 3. We compare the character distribution to previous experimental results and established models for the grain boundary energy. Established models relating grain boundary character to energy that we consider are the dislocation model for the energy of low angle grain boundaries, the hypothesis that the grain boundary is comprised of two surfaces and that its energy should scale with the sum of the two free surface energies, and the coincidence site lattice (CSL) model. Finally, we describe the results of the grain boundary energy distribution reconstructed from the grain boundary triple junction measurements, compare the energies to the character distribution, and discuss some of the problems associated with the energy reconstruction.

6.1 Grain boundary character distribution

While the distribution of lattice misorientations is frequently derived from the analysis of planar sections, grain boundary inclinations are rarely reported for more than a handful of boundaries [1,2]. Using the experimental techniques described in Chapter 3, we have determined the geometry and crystallography of a $5.4mm^2$ area of the grain boundary network in the magnesia polycrystal. Thus, we are now in a position to comment on the areal distribution of grain boundaries over all five mesoscopically observable parameters.

6.1.1 Distribution calculation

To specify the areal distribution of boundary characters over all five parameters, we have discretized the domain of distinct grain boundaries in the same manner as in the energy reconstruction described in Chapter 4. The misorientations, each described by three Eulerian angles (φ_1, Φ,φ_2), were parameterized by φ_1, $\cos\Phi$, and φ_2 in the range of zero to $\pi/2$, 1, and $\pi/2$, respectively. The boundary plane normals (inclinations), described by two spherical angles, θ and ϕ, were parameterized by $\cos\theta$ and ϕ in the range of zero to 1 and 2π, respectively. This particular parameterization was used because it yields cells of equal volume when the parameters are equally partitioned. Within this domain, 36 symmetrically equivalent grain boundaries exist for each combination of five parameters. Thus, the area of each triangle in the mesh is associated with 36 cells within the domain.

After specifying the domain of grain boundary characters, the next step in calculating the distribution is to tessellate the space into cells, such that each cell represents a discrete grain boundary type. To choose an appropriate cell size, the cells must be large enough such that the average cell contains a sufficient number of observations to be statistically significant and small enough such that they maintain an adequate resolution over the domain. Assuming that for each boundary between adjacent sections the grain boundary elements can typically be specified by two discrete boundary characters, then we have $\sim 3 \times 10^5$ observations. Thus, by taking $\Delta\varphi_1 = \Delta\varphi_2 = \Delta\phi = 10°$, and $\Delta\cos\Phi = \Delta\cos\theta = 1/9$, on average there are about 4.5 observations per cell with a resolution of approximately $10°$.

To determine the distribution, the area from each triangle in the mesh is summed in each of the 36 symmetrically equivalent cells that correspond to the character specified by the misorientation and boundary normal of the element. After the areas of all mesh elements have been summed in the appropriate cells, the cells are normalized such that the average value is one. Thus, because the cells are of equal volume, the cell values now represent multiples of a random distribution (MRD). We can now determine the MRD value for any grain boundary type. By specifying the character of a grain boundary, the MRD value is given as the average of the MRD values of the corresponding 36 symmetrically equivalent cells within the domain.

6.1.2 Distribution of boundary types

Because the distribution of boundary types is a function of five parameters, it is difficult to examine the entire space. If we consider the distribution of misorientations alone, averaged over the space of inclinations, a strong peak is exhibited at low angle misorientations ($\sim 14\times$ random at maximum). Furthermore, large angle misorientations ($> 15^\circ$) primarily consisted of those described by rotations about $\langle 111\rangle$ due to the sample's axial texture. To probe the distribution over all five mesoscopically observable parameters, we use the following scheme. A fixed misorientation is chosen based on an axis-angle pair, and the distribution of inclinations are plotted on an inverse pole figure. Figs. 6.1–6.3 show the distribution of inclinations for rotations about the low index axes, $[100]$, $[110]$, and $[111]$, respectively, and Fig 6.4 shows the distribution for rotations about $[952]$, which lies in the center of the three low index axes. The distribution of inclinations for more fixed misorientations can be found in Appendix C.

In Fig. 6.2a, which shows the distribution of inclinations for a 5° misorientation about $[110]$, we observe that the distribution is high along the great circle 90° from the misorientation axis ($[110]$), which are inclinations from $[\bar{1}10]$ (A), through $[001]$, to $[1\bar{1}0]$ (B). Because these inclinations are perpendicular to the misorientation axis, they correspond to pure tilt boundaries. Furthermore, the plot shows that there is a particular preference for $\langle 110\rangle$ type tilt boundaries (A and B). However, there is an inherent problem with probing the distribution along a particular axis for a low angle misorientations using the current parameterization and discretization scheme. In the space of Euler angles, the angular distance between misorientation axes goes to zero as the misorientation angle approaches zero. In other words, the discrete cells in the sub-domain of boundary space that correspond to misorientations of less than approximately 10° contain all possible misorientation

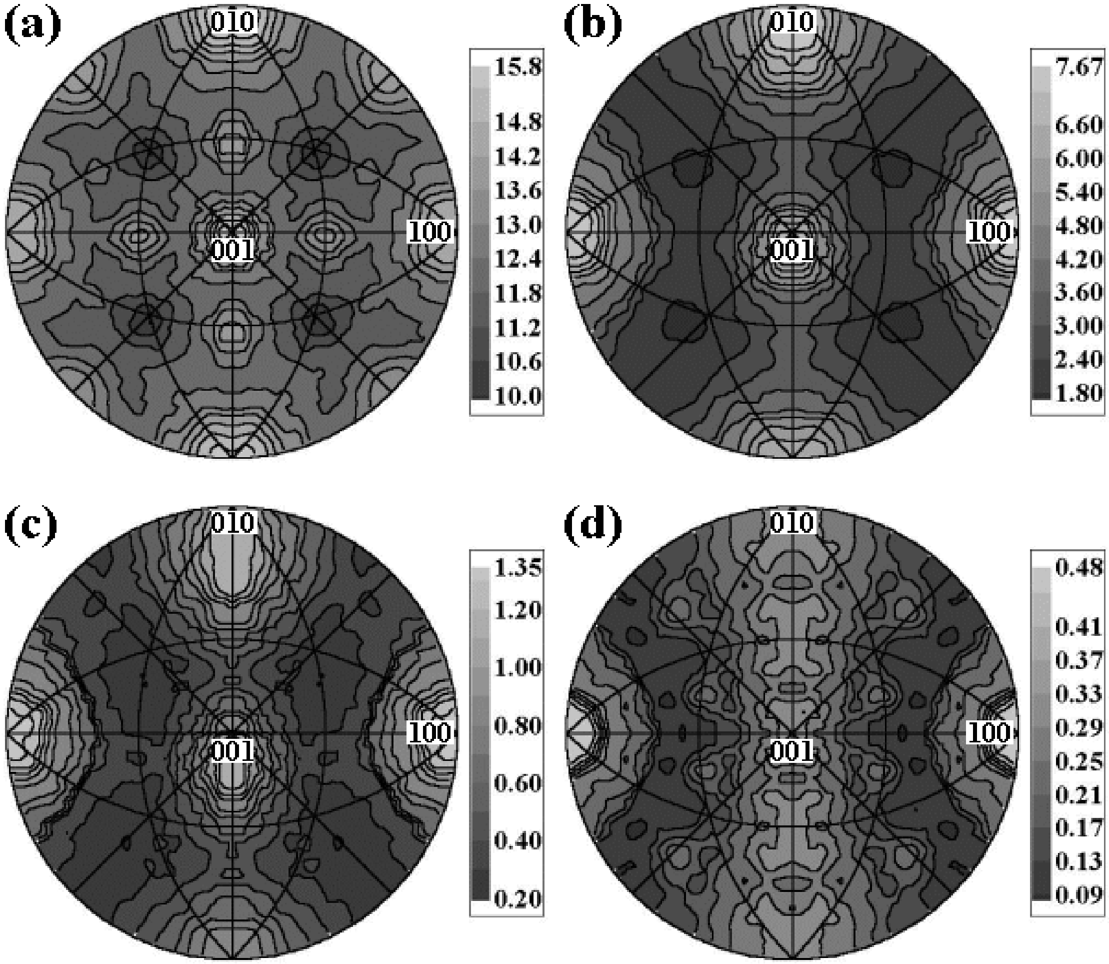

Figure 6.1: Contour plots in stereographic projection of the grain boundary character distribution for misorientations with rotations of (a) 5, (b) 15, (c) 30, and (d), 45° about $[100]$. The value of the distribution increases as the shading in the plots varies from dark to light, and the scale bar shows the contour values.

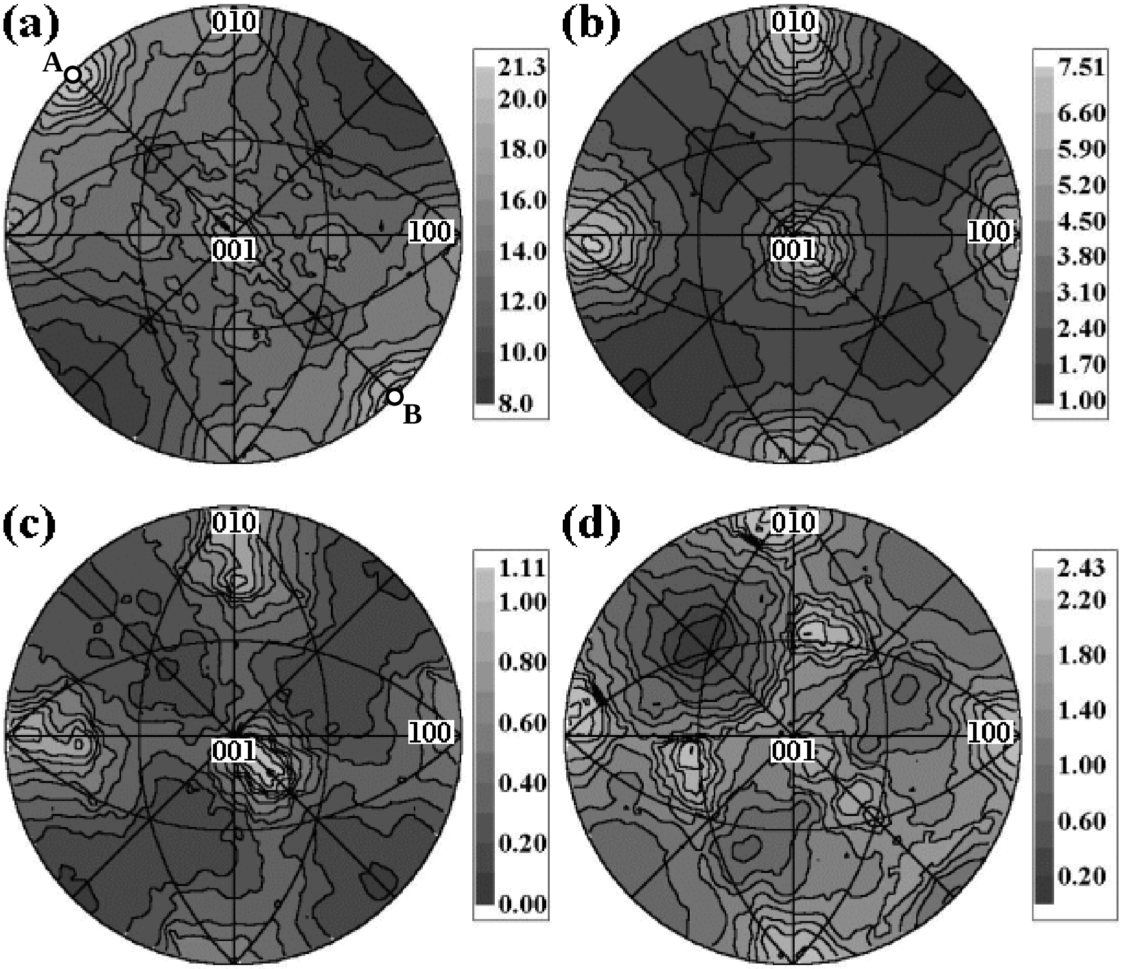

Figure 6.2: Contour plots in stereographic projection of the grain boundary character distribution for misorientations with rotations of (a) 5, (b) 20, (c) 40, and (d), 60° about $[110]$. The value of the distribution increases as the shading in the plots varies from dark to light, and the scale bar shows the contour values. The labels are described in the text.

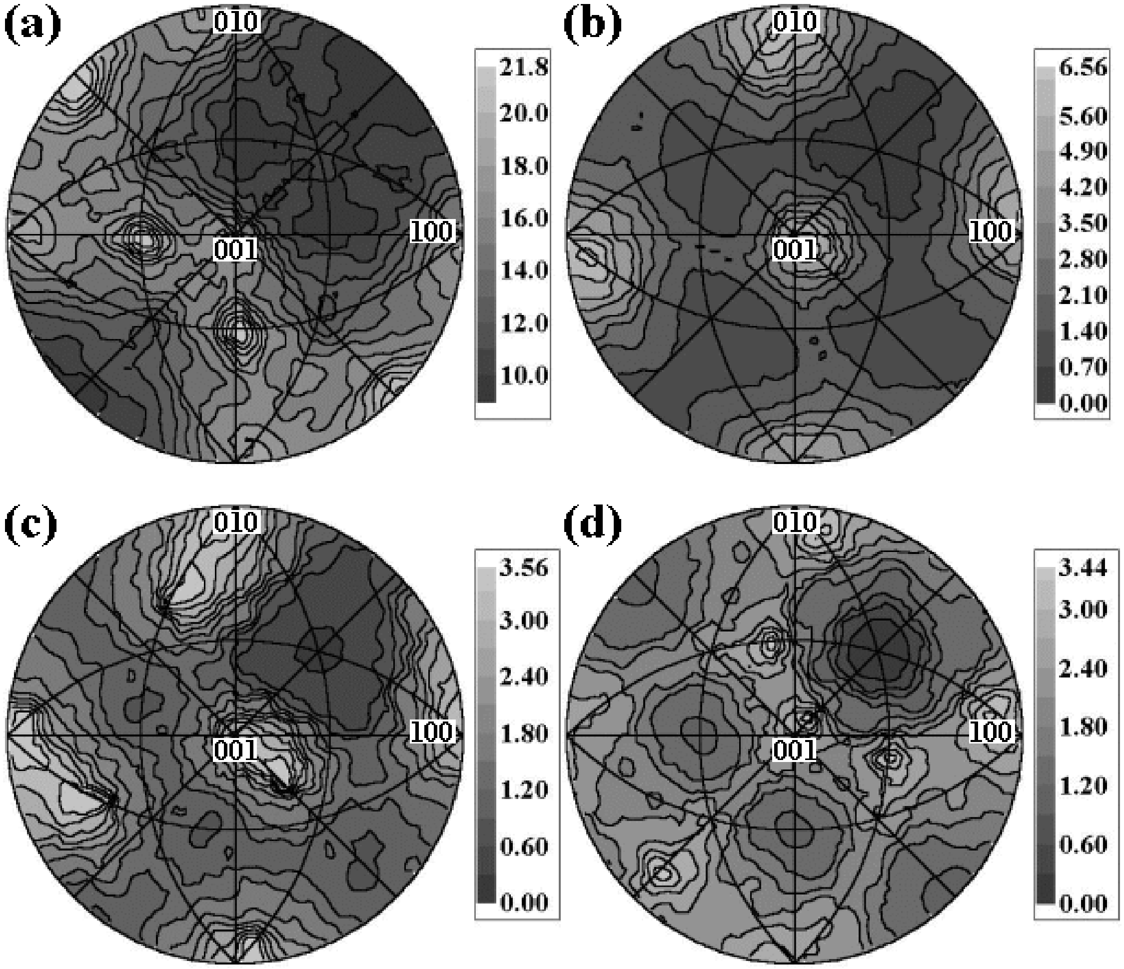

Figure 6.3: Contour plots in stereographic projection of the grain boundary character distribution for misorientations with rotations of (a) 5, (b) 20, (c) 40, and (d), 60° about $[111]$. The value of the distribution increases as the shading in the plots varies from dark to light, and the scale bar shows the contour values.

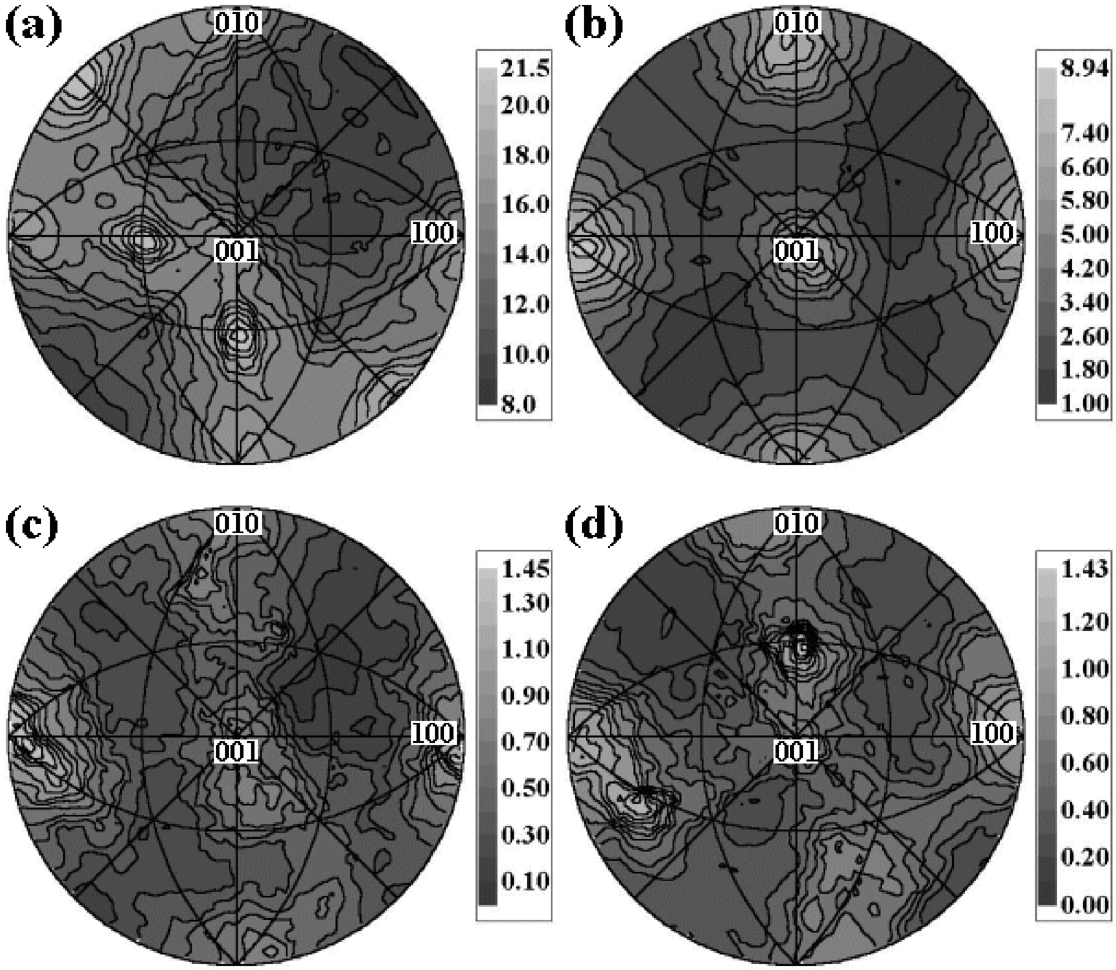

Figure 6.4: Contour plots in stereographic projection of the grain boundary character distribution for misorientations with rotations of (a) 5, (b) 20, (c) 40, and (d), $60°$ about $[952]$. The value of the distribution increases as the shading in the plots varies from dark to light, and the scale bar shows the contour values.

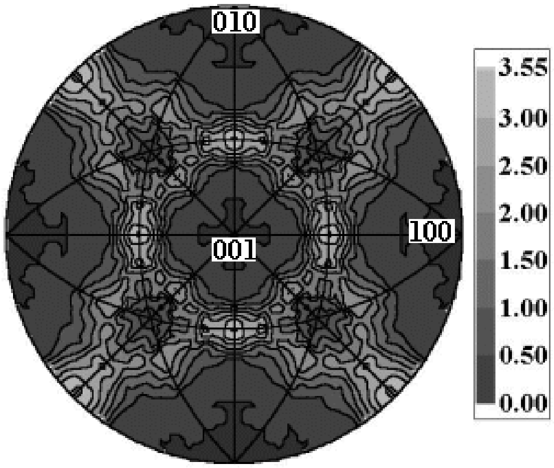

Figure 6.5: Contour plot in stereographic projection of the distribution of misorientation axes for low angle ($< 10°$) misorientations. The value of the distribution increases as the shading in the plots varies from dark to light, and the contour values are given on the scale bar.

axes. Therefore, the plots for $5°$ of misorientation in Figs. 6.1a–6.4a are generated from approximately the same cells in the sub-domain. Varying the axis of misorientation in this region does not have a substantial effect on the distribution calculation, except to change the symmetry conditions and the tilt and twist components of the inclinations. Therefore, to resolve the effect of different misorientation axes on the distribution of inclinations for low angle misorientations, a different parameterization or finer discretization would be required. We have, however, determined the distribution of misorientation axes for grain boundaries with a misorientation angle less than $10°$, which is shown in Fig. 6.5. From the plot in Fig. 6.5, we observe that the misorientation axes for low angle grain boundaries are restricted to those greater than approximately $35°$ from $\langle 100\rangle$ and $10°$ from $\langle 111\rangle$, with a strong maximum at $\langle 110\rangle$. Because the $\langle 110\rangle$ misorientation axes have the strongest representation in the low angle regime, we conclude that Fig. 6.2a is and adequate representation of the inclination distribution for low angle misorientations about $[110]$. Furthermore, for the $[100]$, $[111]$, and $[952]$ axes, the calculated distribution may not be representative of the actual distribution at low angle misorientations.

Fig. 6.2a also shows local maxima in the distribution for boundaries with $\langle 100\rangle$ inclinations. From the other plots in Figs. 6.1–6.4, we see that this trend appears for every

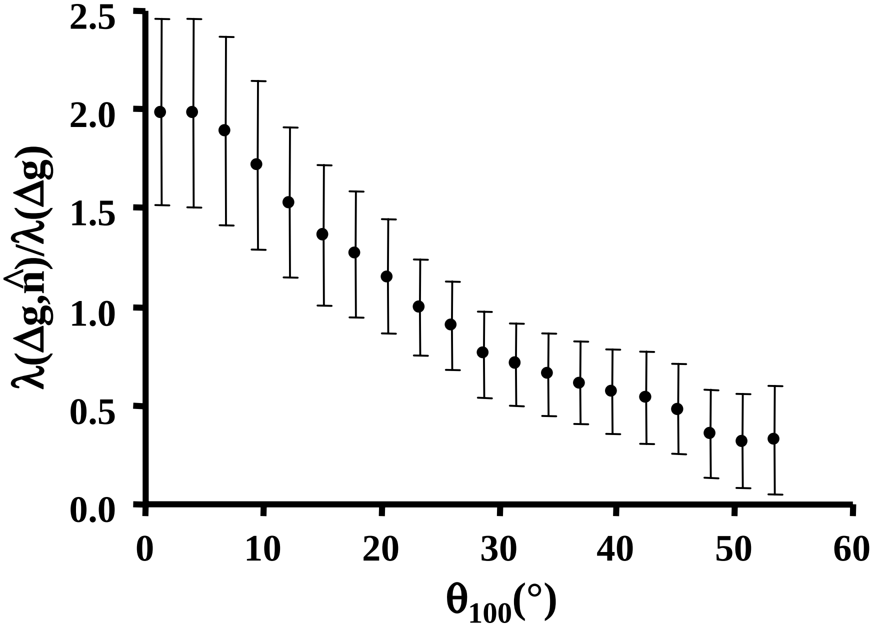

Figure 6.6: Normalized values of the grain boundary character distribution as a function of the minimum angular deviation of the two boundary plane normals from $\langle 100\rangle$, θ_{100}.

fixed misorientation shown. In fact, with the exception of the $\langle 110\rangle$ peaks in the plots corresponding to $5°$ misorientations, the maxima in each plot correspond to grain boundaries that have one or both boundary planes near $\langle 100\rangle$. However, the plots in Figs. 6.1–6.4 represent a small fraction of the entire grain boundary space. To demonstrate that this trend persists over the entire space, we have examined the dependence of the distribution ($\lambda(\Delta g, \hat{n})$) on the minimum angular deviation of the two boundary plane normals from $\langle 100\rangle$ (θ_{100}) for the boundary characters that correspond to the center of all cells in the sub-domain of the boundary space. However, since we are interested in the effect of only the inclination parameters on the distribution, we first need to remove the bias from the misorientation texture. For each fixed misorientation, ($\lambda(\Delta g, \hat{n})$) was normalized by dividing by the value of the distribution when only misorientations are considered ($\lambda(\Delta g)$). The dependence of the normalized distribution on θ_{100} is illustrated in Fig. 6.6. For equal increments of θ_{100}, the average of all the normalized values of the distribution are shown on the plot and the error bars correspond to one standard deviation above and below the mean. From the plot, we see that boundaries with a plane normal near $\langle 100\rangle$ are typically twice as populated as

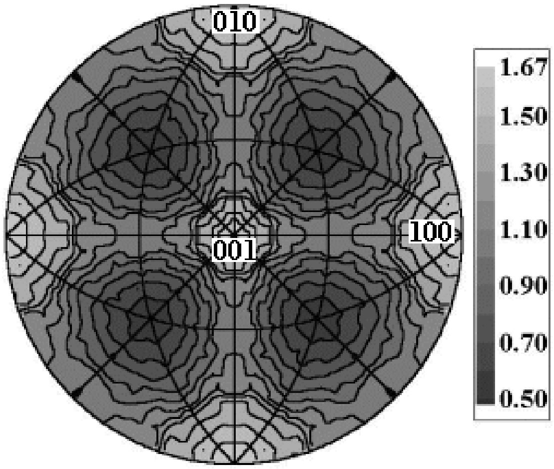

Figure 6.7: Contour plot in stereographic projection of the crystallographic distribution of triple line directions. The value of the distribution increases as the shading in the plots varies from dark to light, and the contour values are given on the scale bar.

the average boundary for each particular misorientation, and this value decreases as θ_{100} increases.

In addition to the distribution of grain boundary types, we can calculate the crystallographic distribution of triple line directions from the experimental measurements of grain boundary triple junctions described in Chapter 3. The distribution, which is shown in Fig. 6.7, exhibits a maximum at $\langle 100 \rangle$ of approximately 1.5 times random. This result should be expected considering the preference for grain boundaries with $\langle 100 \rangle$ inclinations. If two grain boundaries with $\langle 100 \rangle$ inclinations meet at a triple junction, the triple line direction must also be $\langle 100 \rangle$. Therefore, the peak in the crystallographic distribution of triple junctions at $\langle 100 \rangle$ further illustrates the general preference for grain boundaries with $\langle 100 \rangle$ inclinations.

The apparent trend of preferred inclinations appears to be consistent for all fixed misorientations. While it is well known that grain boundary misorientations are not necessarily distributed randomly over the domain of possibilities, the current results illustrate that the inclinations of the grain boundaries can also exhibit texture. In the following sections, we shall address the question of whether or not certain points in the grain boundary space are preferentially occupied because they represent low energy configurations. We shall attempt to reconcile the distribution results with what we know about the grain boundary energy of magnesia.

6.2 Comparison with previous results of boundary energy

In Chapter 2, a number of theoretical predictions and experimental results concerning the energy of grain boundaries were reviewed. To explore the idea that the volumes of grain boundary space with high populations represent low energy configurations, we shall compare the observed distribution of boundary types with hypothetical grain boundary energies.

6.2.1 Dislocation model

The Read-Shockley model [3] predicts that the energies of grain boundaries with low misorientation angles ($\Sigma 1$) will vary with the density and energy of the dislocations that compensate for the misfit. The number and type of dislocations required for a given grain boundary ultimately depends on both the misorientation and the boundary plane. Thus, by determining the dislocation densities for low angle boundaries we can estimate the relative energy variation and compare it to the observed distribution.

Dislocation density calculation

To calculate dislocation densities we have utilized Frank's formula for a general grain boundary [4]. Given the boundary character ($\Delta g, \hat{n}$) and a set of three noncoplanar Burgers vectors (b_i), the formula allows the density and orientation of the i^{th} set of dislocations (corresponding to b_i) that make up the boundary to be determined. The dislocation model, N_i, is calculated from

$$N_i = b_i^* \times u - n(n \cdot b_i^* \times u), \tag{6.1}$$

where u is the misorientation axis, n is the boundary plane normal, and b_i^* are the reciprocal vectors given by

$$b_1^* = \frac{b_2 \times b_3}{b_1 \cdot b_2 \times b_3}, \tag{6.2}$$

with similar relations for b_2^* and b_3^* obtained by rotating subscripts. The magnitude and direction of the vector N_i specify the density and orientation, respectively, of the i^{th} set of dislocations. The density is given by $\theta|N_i|$, where θ is the misorientation angle, and the direction of N_i is normal to the dislocation lines.

For magnesia, we have considered dislocations with $b = a/2\langle 110\rangle$ and $b = a/2\langle 100\rangle$; therefore, there exist many possible combinations of three noncoplanar Burgers vectors each corresponding to a different dislocation model. To find the "best" model we evaluated all possible combinations, and the one which yielded the lowest density was considered to be correct. The plots in Figs. 6.8–6.11 show the calculated dislocation densities for boundary planes with misorientations corresponding to a 5° rotation about $[100]$, $[110]$, $[111]$, and $[952]$, respectively. In Fig. 6.9a, which shows the dislocation densities for a 5° misorientation about $[110]$, we observe that the densities are lowest for pure tilt boundaries, from $[\bar{1}10]$ (A), through $[001]$, to $[1\bar{1}0]$ (B), and highest for pure twist, $[110]$ (C) and $[\bar{1}\bar{1}0]$ (D). These trends are also apparent in the other misorientation axes shown. Furthermore, misorientations about the low index axes exhibit particularly low densities for $\langle 110\rangle$ type tilts.

Distribution comparison

Although we have not differentiated between edge and screw type dislocations, which may have different energies, the plots in Figs. 6.8–6.11 show the total dislocation density, which should be at the very least a rough indication of the relative grain boundary energy. The plots show that the dislocation density is lowest for tilt boundaries. Therefore, we can assume that these boundaries have low energies compared to other boundary planes at the same misorientation. Conversely, the dislocation densities are highest for twist boundaries, and these boundaries should have relatively high energies. However, to make the comparison with the character distribution, we have to again consider the ambiguity in the misorientation axes for low angle misorientations in the distribution. As we discussed above, the distribution grain boundaries at low angle misorientations is strongly biased by $\langle 110\rangle$ misorientation axes. Thus, for the $[100]$, $[111]$, and $[952]$ axes at low misorientation angles, the calculated distribution may not be representative of the actual distribution; only

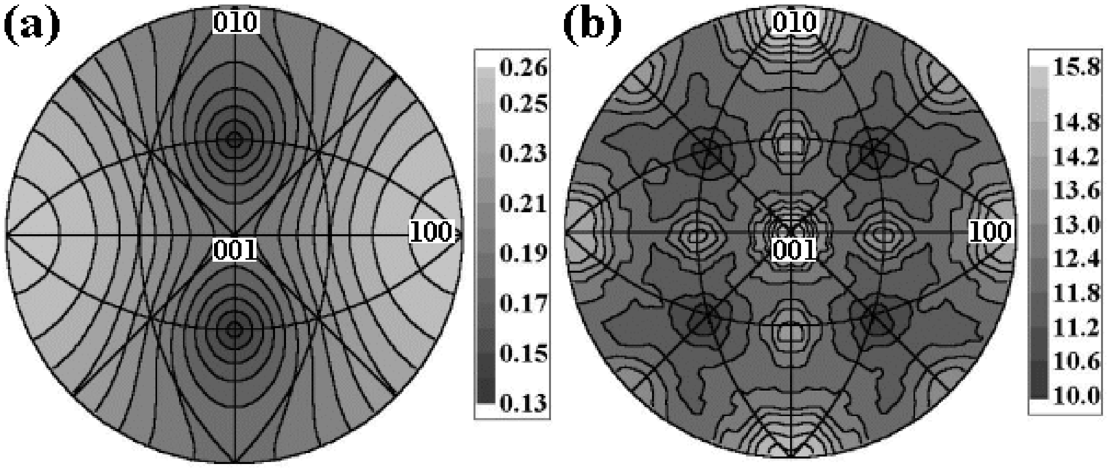

Figure 6.8: Calculated dislocation densities plotted in stereographic projection for the misorientation corresponding to a 5° rotation about $[100]$ are shown in (a). The density increases as the shading in the plots varies from dark to light. The contour values are shown in the scale bar and have units of $dislocations/nm^2$. For reference the grain boundary character distribution is shown in (b).

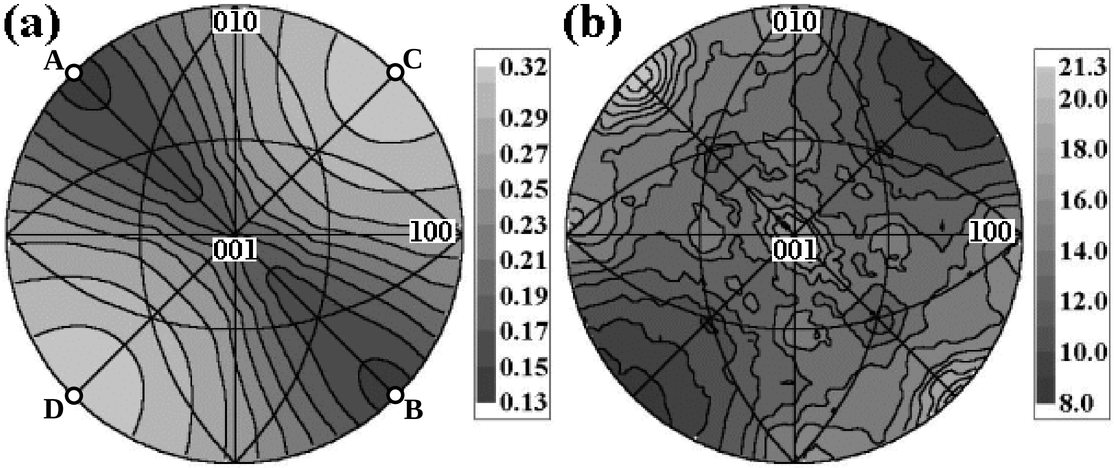

Figure 6.9: Calculated dislocation densities plotted in stereographic projection for the misorientation corresponding to a 5° rotation about $[110]$ are shown in (a). The density increases as the shading in the plots varies from dark to light. The contour values are shown in the scale bar and have units of $dislocations/nm^2$. The labels are described in the text. For reference the grain boundary character distribution is shown in (b).

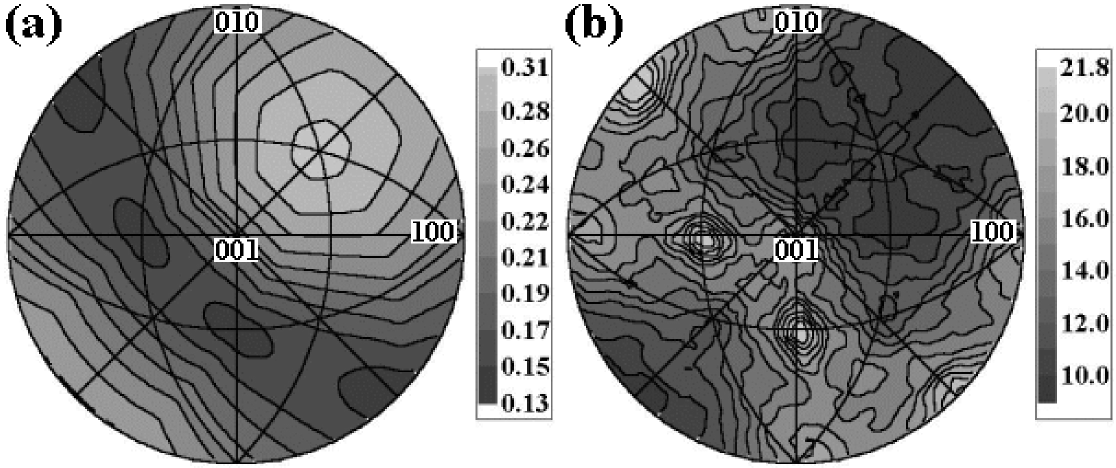

Figure 6.10: Calculated dislocation densities plotted in stereographic projection for the misorientation corresponding to a 5° rotation about $[111]$ are shown in (a). The density increases as the shading in the plots varies from dark to light. The contour values are shown in the scale bar and have units of $dislocations/nm^2$. For reference the grain boundary character distribution is shown in (b).

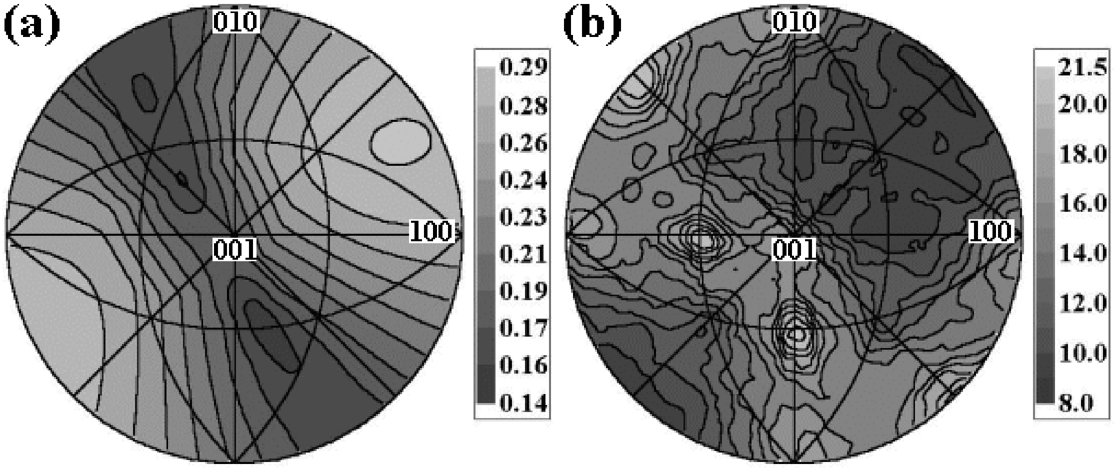

Figure 6.11: Calculated dislocation densities plotted in stereographic projection for the misorientation corresponding to a 5° rotation about $[952]$ are shown in (a). The density increases as the shading in the plots varies from dark to light. The contour values are shown in the scale bar and have units of $dislocations/nm^2$. For reference the grain boundary character distribution is shown in (b).

the distribution in Fig. 6.9b (5° about $[110]$) is an adequate representation the inclination distribution for small angle misorientations. By comparing the calculated dislocation densities in Fig. 6.9a with the distribution in Fig. 6.9.b, we find that highly populated regions of the distribution, which correspond to tilt boundaries (especially $\langle 110 \rangle$ type tilts), are also the regions of low energy indicated by low dislocation densities. Furthermore, for the underpopulated regions in the vicinity of the pure twist boundaries, the dislocation densities, and therefore the energies, are high. This result supports the idea that the population of boundaries is controlled by the boundary energies and that highly populated boundary types correspond to low energy configurations. There are, however, also maxima in the distribution at $\langle 100 \rangle$ inclinations, which are not predicted by the dislocation densities. The preference for these boundary types is addressed the next section. In general, we find that at low angle misorientations, the distribution we observe should correspond to a configuration of reduced boundary energy (relative to a random configuration) as predicted by the dislocation densities.

6.2.2 Boundary energy derived from the surface energy

The energy of a grain boundary, γ_{gb}, can be thought of as the sum of the energies of the two surface planes, γ_{s_i}, minus a binding energy, E_b, which is the energy that is recovered from creating bonds when the two surfaces are joined to form the boundary, $\gamma_{gb} = \gamma_{s_1} + \gamma_{s_2} - E_b$. For general grain boundaries, those not near “special” crystallographic positions, the binding energy can be approximated as a constant value, and the boundary energy should scale linearly with the sum of the energies of the two surfaces. This should be a reasonable approximation because, for a general grain boundary, the combined repeat units of the two surfaces making up the boundary will not form a commensurate structure. Therefore, essentially every atom on the boundary plane will be subject to a different set of interatomic forces. Since the contributions from different atoms can vary only between certain limits and the interatomic forces will be averaged over a very large number of atoms, the energy recovered by forming the boundary (E_b) will average to a constant. Note that the approximation does not hold for grain boundaries near “special” crystallographic positions where there are substantially fewer broken or distorted bonds than a general boundary. However, these boundaries are rare in random polycrystals [5] and, therefore, are of questionable significance. Although there are no experimental data that substantiate this relationship, it has been demonstrated in the results of calculated energies for fcc metals reported by Wolf [6]. We have already demonstrated that the boundary distribution decreases as the minimum angular deviation of one of the boundary planes from $\langle 100 \rangle$ increases. Furthermore, in Chapter 5 we have shown that the surface energy is minimum at (100) and increases as orientation deviates from this orientation and maximizes at (111). Thus, from these trends it appears that the distribution may vary inversely with the boundary energy derived from the sum of the two surface energies. Therefore, to facilitate a more detailed analysis, we have calculated hypothetical grain boundary energies based on the surface energies determined from the capillarity vector reconstruction method in Chapter 5.

Energy calculation

To calculate a grain boundary energy from the surface energies, we first specify the boundary in terms of $\Delta g, \hat{n}$. Given ($\Delta g, \hat{n}$), we determine the boundary plane normal with respect to the second crystallite ($\hat{n}' = \Delta g^T \hat{n}$). We then calculate the surface energy for both $\hat{n}$ and $\hat{n}'$, and since we have no knowledge of the magnitude or variability of the binding energy, the grain boundary energy is simply taken to be the sum of these two energies. Figs. 6.12–6.15 show the variation of these energies with inclination for misorientations corresponding to rotations of 20° about $[110]$, 60° about $[110]$, 20° about $[111]$, and 60° about $[111]$, respectively. For reference, the variation of the character distribution for these misorientations is also shown on the plots. The distribution of the hypothetical boundary energy derived from the surface energies for more fixed misorientations can be found in Appendix C.

Distribution comparison

From the plots in Fig. 6.12 (20° about $[110]$), we observe that the hypothetical grain boundary energy varies inversely with the character distribution. For $\langle 100 \rangle$ inclinations, the sum of the surface energies of the two boundary planes is low, while the character distribution has maxima at these positions. Further, the opposite occurs at $\langle 111 \rangle$ inclinations (indicated

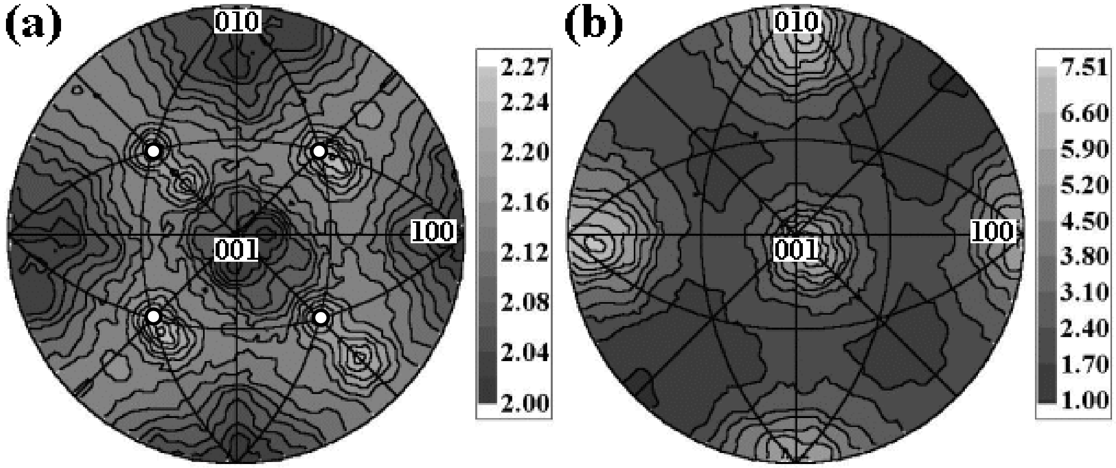

Figure 6.12: Hypothetical grain boundary energies derived from the surface energies plotted in stereographic projection for the misorientation corresponding to a 20° rotation about $[110]$ are shown in (a). The density increases as the shading in the plots varies from dark to light, and the contour values are shown in the scale bar. The markers are described in the text. For reference the grain boundary character distribution is shown in (b).

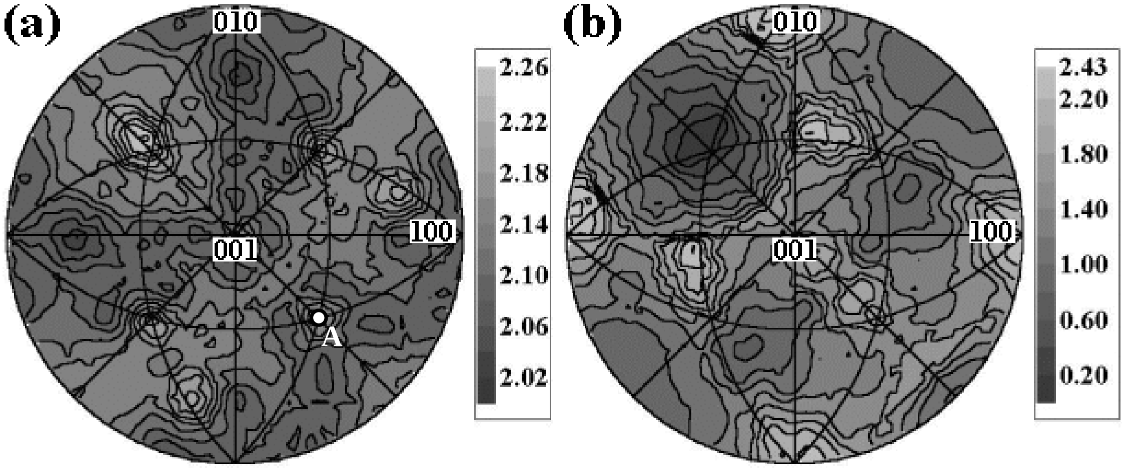

Figure 6.13: Hypothetical grain boundary energies derived from the surface energies plotted in stereographic projection for the misorientation corresponding to a 60° rotation about $[110]$ are shown in (a). The density increases as the shading in the plots varies from dark to light, and the contour values are shown in the scale bar. The label is described in the text. For reference the grain boundary character distribution is shown in (b).

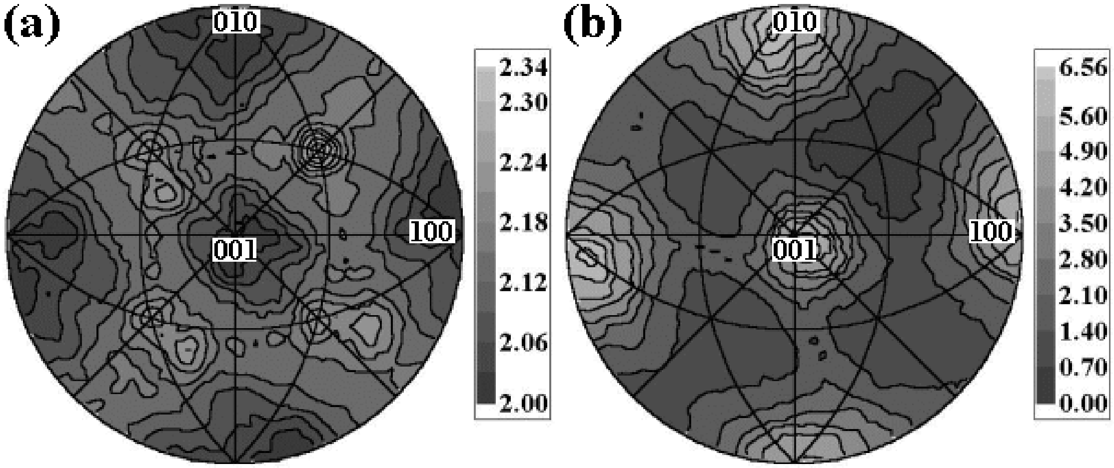

Figure 6.14: Hypothetical grain boundary energies derived from the surface energies plotted in stereographic projection for the misorientation corresponding to a 20° rotation about $[111]$ are shown in (a). The density increases as the shading in the plots varies from dark to light, and the contour values are shown in the scale bar. For reference the grain boundary character distribution is shown in (b).

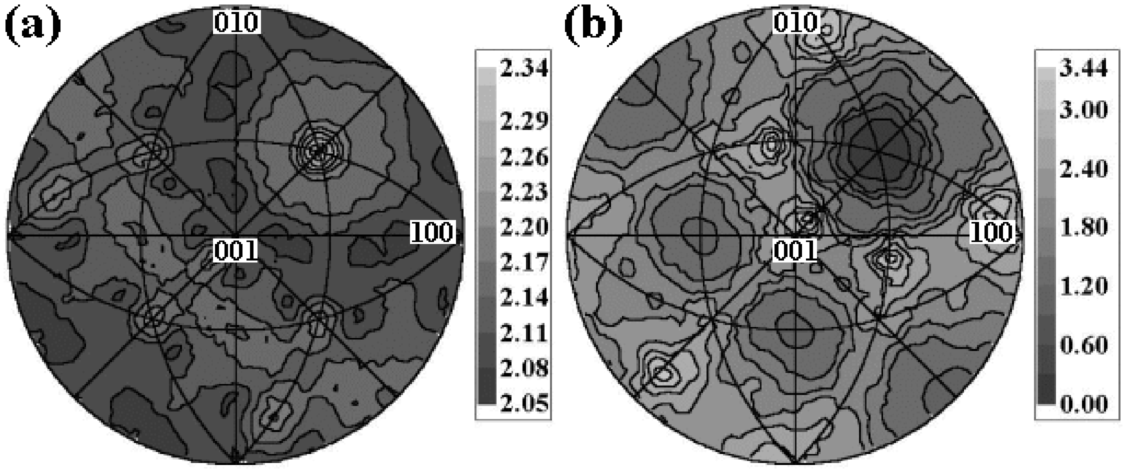

Figure 6.15: Hypothetical grain boundary energies derived from the surface energies plotted in stereographic projection for the misorientation corresponding to a 60° rotation about $[111]$ are shown in (a). The density increases as the shading in the plots varies from dark to light, and the contour values are shown in the scale bar. For reference the grain boundary character distribution is shown in (b).

in Fig. 6.12 by open circles). In these cases, the sum of the two surface energies is high, and the population of grain boundaries is low. From the other plots in Figs. 6.13–6.15, we see that the hypothetical energy variation is almost exactly the inverse of the character distribution at each fixed misorientation shown.

Although for the fixed misorientations shown in Figs. 6.12–6.15 it appears that there is an inverse relationship between the sum of the surface energies of the two boundary planes and the character distribution, it is important to examine the relationship over the entire parameter space. Therefore, we shall consider the values of the distributions for the boundary characters that correspond to the center of all cells in the sub-domain of the parameter space. Further, we remove the bias from the misorientation texture by normalizing the character distribution $\lambda(\Delta g, \hat{n})$ at each fixed misorientation by dividing by the value of the distribution when only misorientations are considered ($\lambda(\Delta g)$). Next, to quantify the extent of the relationship we have used the Spearman rank-order correlation coefficient, r_s (SPEAR [7]). For N pairs of measurements (x_i, y_i),

$$r_s = \frac{\sum_{i=1}^{N}(R_i - \bar{R})(S_i - \bar{S})}{\sqrt{\sum_{i=1}^{N}(R_i - \bar{R})^2}\sqrt{\sum_{i=1}^{N}(S_i - \bar{S})^2}}, \tag{6.3}$$

where R_i is the rank of x_i among other x's, and S_i is the rank of y_i among other y's. The values of r_s range from -1 to 1, which indicate perfect negative and positive correlation, respectively, and for $r_s = 0$, no correlation exists. Comparing the hypothetical grain boundary energy and the normalized character distribution, we find an r_s equal to -0.76, which is indicative of a high degree of (negative) correlation and a marked relationship between the two distributions [8].

Although there is substantial correlation between the hypothetical grain boundary energy and the character distribution, there are grain boundary types for which the relationship does not hold. For example, in Fig. 6.13 (60° about $[110]$), both distributions are high at $[1\bar{1}1]$ (A). In this case, the other boundary plane normal is very close to $[001]$. In fact, we find that, in general, the distributions deviate from each other when one of the boundary plane normals is near $\langle 100 \rangle$ and one is far from $\langle 100 \rangle$. If we assume that the boundary energy model is correct, these differences can be attributed to inaccuracies in the character distribution or the reconstructed surface energies. Because the character distribution is calculated directly from the experimental measurements, we assume that it is more accurate than the reconstructed surface energies. From our observations of orientation stability in Chapter 5, we found that the extent of the energy cusp at $\langle 100 \rangle$ was probably underestimated in the surface energy experiment. It follows that for all boundaries with one or both plane normal near $\langle 100 \rangle$ the grain boundary energy derived from the sum of the two surfaces energies can be considered an overestimate. Considering this, the maxima in the character distribution corresponding to plane normals near $\langle 100 \rangle$ at all fixed misorientations can be attributed to a low grain boundary energy estimated by the sum of the surface energies of the two boundary planes.

The population of “random” boundaries, which are the majority of possible boundary types, exhibits a negative correlation with the hypothetical grain boundary energy estimated from the surface energies. Assuming that the boundary energy model is correct, this suggests that the grain boundary character distribution that developed during grain growth is controlled by the grain boundary energies. Conversely, if we assume that the distribution we observe corresponds to a configuration of reduced boundary energy, then the sum of the surface energies of the two boundary planes is an excellent indicator of the grain boundary energy anisotropy at a fixed misorientation. Finally, between the hypothetical grain boundary energy derived from the surface energies and the variation in the dislocation densities at low angle boundaries, the majority of the variability in the character distribution can be attributed to variations in the grain boundary energy.

6.2.3 Coincidence site lattice (CSL) model

Although the dislocation densities at low angle boundaries and the boundary energy as the sum of the two surface energies explain most of the variation over the five parameter grain boundary space, it is common to view grain boundaries in terms of the CSL model. Therefore, even though these boundaries comprise a very small fraction of the possible boundary types, we shall compare the observed character distribution to the existing results from CSL boundaries in magnesia. In Chapter 2 a number of studies were reviewed that focused on the energy of grain boundaries in magnesia [9] and isostructural nickel oxide

[10–12] with low Σ CSL misorientations where the boundary plane was known. The studies showed that grain boundaries with misorientations near low Σ CSLs were not necessarily associated with low energy. Only some grain boundaries with special boundary planes corresponding to a high density of coinciding sites across the boundary were determined to have lower energy. Thus, assuming that the distribution of boundaries is controlled by the energy, we expect the population of grain boundary misorientations to be independent of CSL misorientation. Only in case of "special" boundary planes might we see a higher density of boundary characters.

Distribution comparison

Table 6.1 lists the values of the distribution for misorientations alone ($\lambda(\Delta g)$) for the CSL misorientations up to $\Sigma 11$ and shows that the population of these misorientations are not significantly higher than random. The CSL misorientations that are greater than random correspond to rotations about $\langle 111 \rangle$, and are high due to the $\langle 111 \rangle$ texture of the sample. This is consistent with the idea that a boundary with a near-CSL misorientation does not necessarily have low energy. However, we have also listed the values of the five parameter distribution ($\lambda(\Delta g, \hat{n})$) for the boundaries that have either been determined experimentally or calculated in either magnesia or nickel oxide to have low energies. With the exception of $\Sigma 3$, all of these are greater ($1.35 - 2\times$) than the averaged distribution for that particular misorientation. Thus, there appears to be a preference for special boundary planes at CSL misorientations. The ratios $\lambda(\Delta g, \hat{n})/\lambda(\Delta g)$ are similar to the values for grain boundaries with boundary planes near $\langle 100 \rangle$ ($2\times$). It should be noted that our ability to observe the distribution of boundaries corresponding to $\Sigma 3$ with $\hat{n} = \langle 111 \rangle$ is limited by the sample geometry. Because the experiment was conducted by sectioning along the axis of the $\langle 111 \rangle$ sample texture, $\langle 111 \rangle$ twist boundaries have the greatest probability of being parallel to the section plane and are less likely to be observed.

If we again assume that the character distribution we observe corresponds to a configuration of reduced boundary energy, the results of the character distribution for low Σ CSL boundaries suggest that a CSL misorientation alone has no effect on boundary energy. Only for special grain boundary planes with a high density of coinciding sites should a reduction in boundary energy be observed. However, in general, these boundaries are insignificant because they are extremely rare in random polycrystals. Furthermore, these results are consistent with previous experimental evaluations of grain boundary energy in materials with a rock salt crystal structure.

Table 6.1: Distribution of CSL boundaries.

Σ	Δg	$\lambda(\Delta g)$	$\hat{n}$	$\lambda(\Delta g, \hat{n})$
3	$[111], 60.00°$	1.82	$[111]$	0.01
5	$[100], 36.86°$	0.25	$[100]$	0.51
7	$[111], 38.21°$	1.70	N/A	N/A
9	$[110], 38.94°$	0.56	$[\bar{2}21]$	0.76
11	$[110], 129.53°$	0.41	$[\bar{1}13]$	0.82

6.3 Reconstructed grain boundary energies

From the experimental measurements of grain boundary triple junctions described in Chapter 3, we can also obtain relative boundary energies by reconstructing the grain boundary energy distribution. However, due to the limited number of triple junctions and the texture throughout the five parameter space, large volumes of the grain boundary parameter space will be significantly underpopulated. Therefore, the accuracy of the reconstructed energies, especially in the underpopulated regions of the parameter space, will be questionable. We have, however, reconstructed the energies using the capillarity vector reconstruction method and compared the results to the observed population of grain boundary characters.

6.3.1 Energy reconstruction

We have applied the capillarity vector reconstruction method to the grain boundary triple junctions measurements. To apply the reconstruction procedure, we used the same subdomain of grain boundary characters with the same discretization that was used in the energy reconstruction with simulated data in Chapter 4 and in the grain boundary distribution calculation described above. The relaxation factor for the iterative solution was chosen as ten times the inverse of the maximum number of equations that any one interfacial character was involved in, and the iteration process was stopped when the change in the sum of the magnitude of all of the deviations vectors is less than 1% of the change during the first iteration. The iteration process converged after 279 steps. For each grain boundary type, the energy was taken as the average of all 36 symmetrically equivalent cells that correspond to the boundary type.

6.3.2 Energy function

The reconstruction from the simulated data discussed in Chapter 4 shows that with the current data density and discretization of grain boundary space, the energy reconstruction procedure reproduces the general trends in the function; however, the relative anisotropies are severely underestimated. Furthermore, the simulated data was generated such that the grain boundaries were more or less evenly distributed through the space. This is not the case for the real data set. As one would expect, the texture we observed in the character distribution also occurs in the distribution of grain boundary types meeting at triple junctions. Therefore, the relative anisotropy predicted by the reconstructed energies will be underestimated, and the reliability of the energies, especially in the underpopulated regions, will be questionable. Taking these potential problems with the reconstruction into consideration, we proceed with the analysis of the reconstructed energies. Figs. 6.16–6.19 show the reconstructed relative grain boundary energies for rotations of 5, 20, 40, and 60° about $\langle 110 \rangle$. For reference the character distribution results are also shown in the figures. The distribution of the reconstructed grain boundary energy for more fixed misorientations can be found in Appendix C.

6.3.3 Distribution comparison

Fig. 6.16a shows the reconstructed relative boundary energies for a misorientation corresponding to a 5° rotation about $[110]$. From the plot, we see that the reconstructed ener-

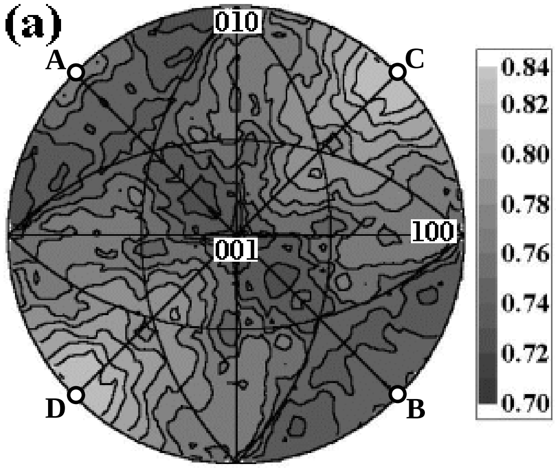

Figure 6.16: Reconstructed grain boundary energies plotted in stereographic projection for the misorientation corresponding to a 5° rotation about $[110]$ are shown in (a). The density increases as the shading in the plots varies from dark to light, and the contour values are shown in the scale bar. The labels are described in the text. For reference the grain boundary character distribution is shown in (b).

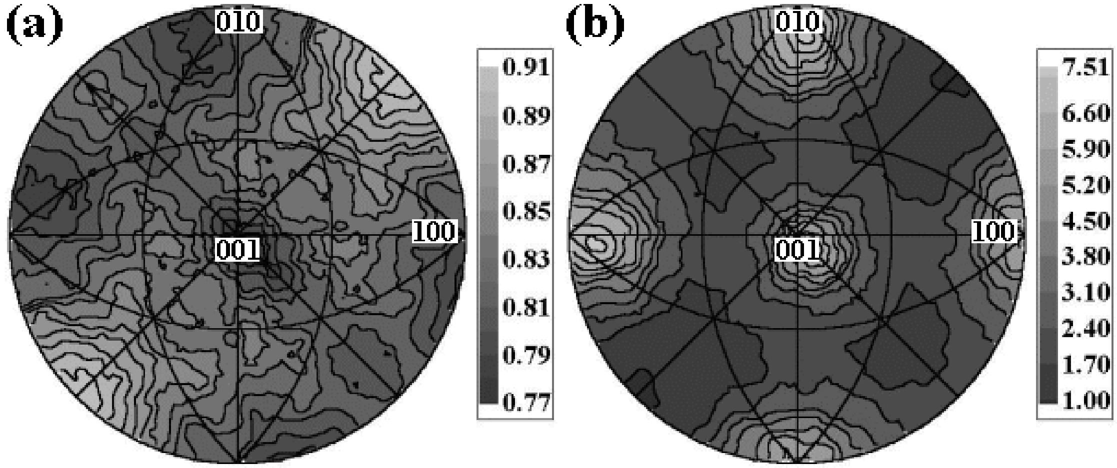

Figure 6.17: Reconstructed grain boundary energies plotted in stereographic projection for the misorientation corresponding to a 20° rotation about $[110]$ are shown in (a). The density increases as the shading in the plots varies from dark to light, and the contour values are shown in the scale bar. For reference the grain boundary character distribution is shown in (b).

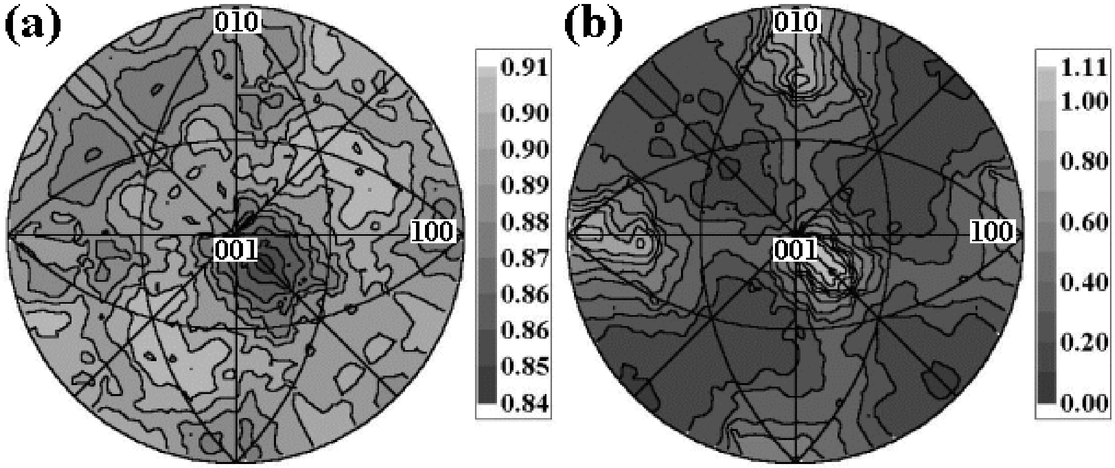

Figure 6.18: Reconstructed grain boundary energies plotted in stereographic projection for the misorientation corresponding to a 40° rotation about $[110]$ are shown in (a). The density increases as the shading in the plots varies from dark to light, and the contour values are shown in the scale bar. For reference the grain boundary character distribution is shown in (b).

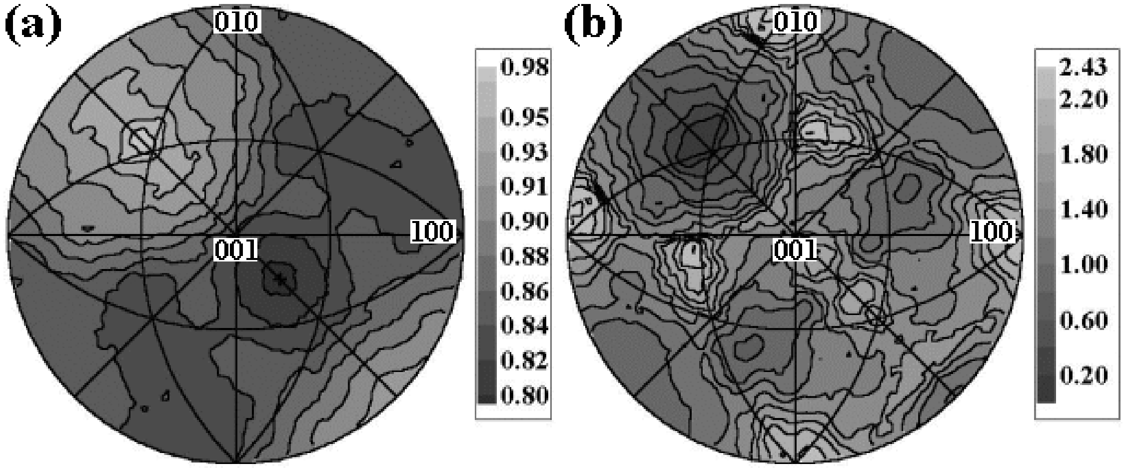

Figure 6.19: Reconstructed grain boundary energies plotted in stereographic projection for the misorientation corresponding to a 60° rotation about $[110]$ are shown in (a). The density increases as the shading in the plots varies from dark to light, and the contour values are shown in the scale bar. For reference the grain boundary character distribution is shown in (b).

gies are lowest for pure tilt boundaries, from $[\bar{1}10]$ (A), through $[001]$, to $[1\bar{1}0]$ (B), and highest for pure twist, $[110]$ (C) and $[\bar{1}\bar{1}0]$ (D). The opposite trends are observed in character distribution, where tilt boundaries are highly populated, while relatively few twist boundaries were observed. Furthermore, low relative energies at boundaries with planes normal to $\langle 100\rangle$ are also exhibited in Fig. 6.16a, as well at the other fixed misorientations (Figs. 6.17a-6.19a). As previously discussed, these boundaries correspond to maxima in the character distribution. Thus, it appears that reconstructed energy does exhibit some inverse correlation with the character distribution. This would indicate the microstructure has evolved to a reduced energy configuration during grain growth. There are, however, definite deviations from this correlation. For example, Fig. 6.16b shows distinct maxima in the character distribution at $\langle 110\rangle$ tilt boundaries, while the reconstructed energy for these boundaries is higher than all other tilt boundaries.

To illustrate the average relationship between the population and reconstructed energies, we again consider the character types corresponding to center of the cells in the subdomain of the five parameter space. After discretizing the range of energies into equal partitions, we determined the mean and standard deviation of $\ln(\lambda + 1)$ for all boundaries in each partition. This procedure allows us to examine the correlation over the entire space, and the results are illustrated in Fig. 6.20. The plot convincingly shows that as γ_{gb} increases, λ decreases. Furthermore, we can quantify the extent of the relationship between the two distributions over the entire parameter space using the Spearman rank-order correlation coefficient, r_s. We have calculated r_s between the two distributions equal to -0.77, which is indicative of a high degree of (negative) correlation. However, if we normalize the distributions at each fixed misorientation, we find r_s to be only -0.40. Therefore, there appears to be only low to moderate correlation over the boundary plane normals alone and most of the correlation arises from the fact that, on average, the distributions vary inversely over the misorientation parameters ($r_s = -0.98$). This is most likely due to the fact with the current data and reconstruction procedure, we are much more likely to estimate the misorientation dependence accurately than the variation over the inclination parameters. The estimated experimental errors in the misorientation calculation ($\pm \sim 0.5^\circ$) are significantly less than those associated with determining the boundary plane normal ($\pm \sim 15^\circ$). Fur-

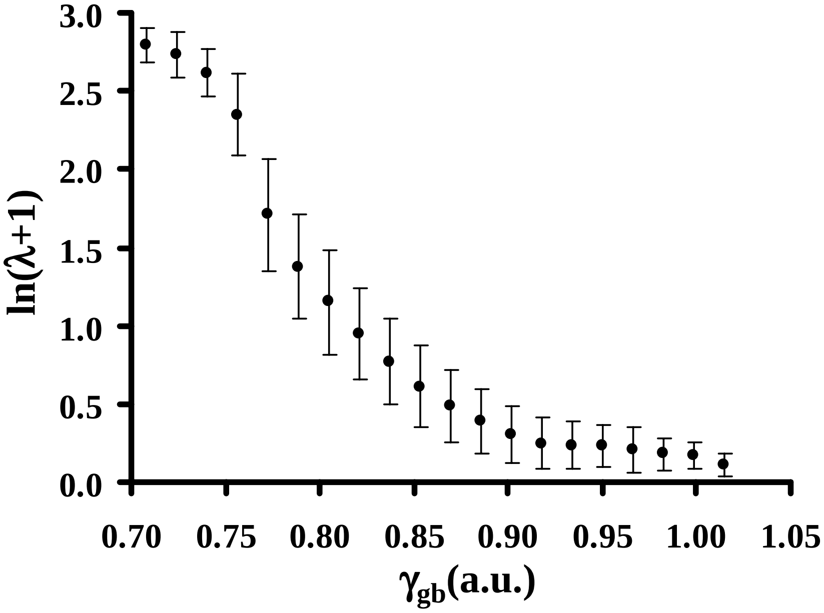

Figure 6.20: Values of the grain boundary character distribution as a function of reconstructed grain boundary energies.

thermore, we expect variations with larger amplitudes over the misorientation parameters, which are more likely to be reconstructed accurately.

In general, the reconstructed relative grain boundary energies and the character distribution exhibit a high degree of (negative) correlation over the five parameter grain boundary space. If we assume that the reconstructed energies are reasonable, then the correlation is further evidence that the microstructure has evolved to a reduced energy state during grain growth. By reinforcing the assumption that the character distribution corresponds to a reduced energy configuration, the correlation also further substantiates the validity of the energy models discussed above, which we have also found to possess strong inverse correlations with the character distribution. Finally, the observation of strong inverse correlations between the grain boundary character distribution and energies lead us to the conclusion that, for the polycrystalline magnesia sample, grain boundary energy was the primary factor influencing grain growth and the distribution of grain boundaries in the final state microstructure.

6.4 References

1] J. Pospiech, K. Sztwiertnia, and F. Haessner, “The Misorientation Distribution Function,” *Textures Microstruct.*, **6**, 201-215 (1986).

1] F. Heidelbach, H.R. Wenk, S.R. Chen, J. Pospiech, and S.I. Wright, “Orientation and Misorientation Characteristics of Annealed, Rolled and Recrystallized Copper,” *Mater. Sci. Engng. A*, **A215**, 39-49 (1996).

[3] W.T. Read and W. Shockley, “Dislocation Models of Crystal Grain Boundaries,” *Phys. Rev.*, **78** [3], 275-289 (1950).

[4] F.C. Frank, Carnegie Institute of Technology Symposium on the Plastic Deformation of Crystalline Solids (Pittsburgh Report), Office of Naval Research, 150-151 (1950).

[5] D.H. Warrington and M. Boon, “Ordered Structures in Random Grain Boundaries; Some Geometrical Probabilities,” *Acta Met.*, **23**, 599-607 (1975).

6] D. Wolf, “Correlation Between Structure, Energy, and Ideal Cleavage Fracture for Symmetrical Grain Boundaries in FCC Metals,” *J. Mater. Res.*, **5** [8], 1708-1730 (1990).

[7] W.H. Press, B.P. Flannery, S.A. Teukolsky, and W.T. Vetterling, Numerical Recipes in Pascal; Cambridge University Press, Cambridge, 1989.

[8] F. Williams, Reasoning with statistics, Harcourt Brace Jovanovich College Publishers, Fort Worth, 1992.

[9] S. Kimura, E. Yasuda, and M. Sakaki, “Grain Boundaries in MgO Bicrystals,” *Yogyo-Kyokai-Shi*, **94** [8], 795-800 (1986).

[10] D.W. Readey and R.E. Jech, “Energies and Grooving Kinetics of [001] Tilt Boundaries in NiO,” *J. Amer. Ceram. Soc.*, **51** [4], 201-208 (1968).

[11] G. Dhalenne, A. Recolevschi, and A. Gervais, “Grain Boundaries in NiO I. Relative Energies of $\langle 001 \rangle$ Tilt Boundaries,” *Phys. Status Solidi A*, **56**, 267-276 (1979).

[12] G. Dhalenne, M. Dechamps, and A. Gervais, “Relative Energies of $\langle 110 \rangle$ Tilt Boundaries in NiO,” *J. Am. Ceram. Soc.*, **65** [1], C-11,C-12 (1982).

Chapter 7

Summary

The fundamental thermodynamic driving force for the formation and evolution of microstructures in polycrystalline materials is provided by the excess free energy per unit area associated with interfaces. Data relating the energy of these interfaces to their character are required to ultimately understand, predict, and control microstructural evolution. The objective of this thesis is to determine the population and relative excess free energy of all physically distinct surfaces and grain boundaries in a polycrystalline magnesia sample. These data have allowed us to identify the underlying mechanisms that determine interfacial energy anisotropy and control microstructural evolution.

The experimental techniques developed to acquire the geometric and crystallographic data necessary to specify the interfacial character and energy distributions rely on using electron backscattered diffraction patterns (EBSP) to determine the interfacial crystallography and traditional microscopy techniques, such as scanning electron microscopy (SEM) or atomic force microscopy (AFM), in concert with serial sectioning to characterize the three dimensional interfacial geometry. Using these techniques, all of the unknowns in the local equilibrium condition for triple junctions except for the interfacial energies and their derivatives can be determined. The techniques, which should be applicable to any polycrystal, were applied to a polycrystalline magnesia sample. The geometric and crystallographic measurements required to determine the relative surface energy anisotropy were made on circumferential thermal grooves where it is assumed that the grooves are in local equilibrium and that the grain boundary energy is independent of its boundary plane. To determine the grain boundary character and energy distribution, we have developed techniques that allow the geometry and crystallography of a large quantity of contiguous crystallites to be determined in three dimensions. From the geometric and crystallographic configuration of these crystallites, it is possible to specify the grain boundary character distribution and the triple junction information required for the extraction of the relative grain boundary energies.

We have applied both continuous and discrete methods to reconstruct the character dependence of the relative interfacial energies from the microscopic observations at triple junctions. The continuous method involved representing the energy variation as a trigonometric series of finite order with linear coefficients. By substituting the series representation into the local equilibrium condition, the unknown coefficients of the series were determined as those that best fit the experimental observations. In the discrete method, the space of interfacial characters was tessellated into cells. Each cell is considered to be a single interfacial character and an unknown in a system of linear equations based on the local equilibrium condition. The energy for each cell is then determined using an iterative procedure to solve the system of equations. To test the reconstruction procedures, we have generated simulated triple junctions based on model energy functions that mimic the surface and grain boundary energy measurements. The results suggest that the interfacial energies can be accurately reconstructed and that the discrete method produces more reliable results. However, the results also suggest that the even the discrete method will underestimate the true anisotropy of the energies.

The experimental technique developed to determine the anisotropy of the surface energy was applied to the polycrystalline magnesia specimen. I have applied both the series fit and discrete reconstruction methods to 269 circumferential thermal grooves equilibrated at $1400°C$. Both results produce a surface energy function that has a minimum at (100) and a maximum at (111). However, the capillarity vector results ($\gamma_{110}/\gamma_{100} = 1.07 \pm 0.04$ and $\gamma_{111}/\gamma_{100} = 1.17 \pm 0.04$) suggests larger anisotropies than the results from the series fit ($\gamma_{110}/\gamma_{100} = 1.040 \pm 0.008$ and $\gamma_{111}/\gamma_{100} = 1.072 \pm 0.010$). By comparing the results from both techniques to the observed faceting behavior, we find that the results from the discrete method more nearly represent the actual surface energy anisotropy in the magnesia polycrystal. Furthermore, the observed anisotropy compares favorably to previous theoretical predictions and experimental results for magnesia surfaces.

Using the techniques developed to determine the geometry and crystallography of large quantities of contiguous crystallites, we have extracted the grain boundary character distribution from the polycrystalline magnesia specimen that had been annealed for $48h$ at $1600°$. Data extracted from $5.4mm^2$ of grain boundary area in a volume of $0.15mm^3$ has enabled us to specify the distribution of grain boundaries over all five mesoscopic parameters. We find that strong texture exists in the space of grain boundary plane normals, a domain that has not previously been explored. For grain boundaries with low angle misorientations, the results suggest a preference for tilt boundaries, especially those with boundary plane normals near $\langle 110 \rangle$. For all fixed misorientations, there also appears to be a preference for boundaries with a boundary plane normal in the vicinity of $\langle 100 \rangle$. These boundaries are typically twice as populated as the average boundary for each fixed misorientation.

To demonstrate that the highly populated boundary types correspond to low energy configurations, and vice versa, we have compared the observed character distribution to several models for the relative grain boundary energy. We find that the observed variations in population are consistent with the dislocation model of boundary energy for low angle misorientation boundaries. Furthermore, the character distribution correlates (inversely) with a hypothetical grain boundary energy derived from the sum the surface energies of the two boundary planes ($r_s = -0.76$). This result also demonstrates that, at a fixed misorientation, the grain boundary energy can be adequately approximated as the sum of the two surface energies. The character distribution also compares favorably to the existing results on the energies of coincidence site lattice (CSL) boundaries. Finally, from the characterized volume of material, we have also extracted the geometry and crystallography of 19094 grain boundary triple junctions. These data were used to determine the grain boundary energies using the discrete energy reconstruction method. Although the reliability of the reconstruction from these data is questionable, there is a substantial (inverse) correlation between the reconstructed energies and the character distribution ($r_s = -0.77$). In general, we find that, at any fixed misorientation, grain boundaries with $\langle 100 \rangle$ boundary planes have reduced energies, which is probably related to the relatively high coordination number of atoms on this plane and its low surface energy.

We have found that the grain boundary character distribution exhibits a negative correlation with the relative grain boundary energies derived from the dislocation densities for low angle misorientations and from the sum of the reconstructed surface energies of the two boundary planes for all fixed misorientations. Assuming that the models are correct, then the majority of the variability in the character distribution can be attributed to variations in the grain boundary energy, and the microstructure evolved to a reduced energy configuration during grain growth. The strong negative correlation we observe between the character distribution and the reconstructed grain boundary energies also provides evidence that the microstructure has evolved to a reduced energy state during grain growth. These (inverse) correlations demonstrate that boundary energy was the primary factor influencing grain growth and the distribution of grain boundary characters in the final state microstructure. Furthermore, if the character distribution we observe does, in fact, correspond to a reduced energy configuration, then the combination of the dislocation model and sum of the two surface energies model for the grain boundary energy would reasonably estimate the energy over all five mesoscopic parameters. If this is true, then the problem of determining grain boundary energies would be greatly simplified. To estimate the grain boundary energy anisotropy (five parameters) for any material, one would only have to determine the surface energies (two parameters) and have some knowledge of the dislocation slip systems.

Appendix A

Thermal Groove Measurements

In this appendix, we shall describe a facile method of measuring the surface geometry of thermal grooves using atomic force microscopy (AFM). First, procedures for minimizing the error in the geometric measurements are described. To test the validity of these procedures, both kinetic and static observations of thermal grooves were made on ceramic polycrystals. These observations are presented and compared to previous results using more labor intensive techniques. Finally, we shall examine the misorientation dependence of relative grain boundary energy given by groove geometries in selected polycrystalline ceramics.

A.1 AFM imaging

The microscope used in this thesis was capable of making topographic, contact AFM images at any point on a sample surface in a $6.25cm^2$ area. This instrument consisted of a Digital Instruments StandAlone AFM (SAA-125) positioned above the sample mounted on an X-Y translation stage (Burleigh Instruments TSE-150) capable of reproducibly positioning the sample with $50nm$ resolution. The advantage of this system is that once a coordinate system and reference frame are established (with respect to an intentionally introduced fiducial mark), it is possible to return to identical positions on the sample surface after repeated thermal treatments or to position the sample based on lower resolution data from the AFM or other microscopes. $\mathrm{Si_3N_4}$ cantilevers (DI Model LNP) were used as probes.

A.1.1 Error analysis

AFM is a facile tool for measuring the surface geometry of thermal grooves; however, when attempting to make quantitative measurements of thermal groove geometry with an AFM, there are factors that potentially contribute to errors in the measurements. These factors include the scanner calibration, the information density of the image, the definition of the surface normal, the background subtraction, the convolution of the tip shape with the sample surface, and the use of a linear fit to determine the slope at the groove root. Each of these experimental factors, and the procedures used to minimize their impact, are described briefly below.

Scanner calibration

The lateral and vertical calibrations for our AFM were established using a lithographically produced standard grating supplied by the manufacturer. The calibration was checked for consistency with the scanners on other microscopes in our lab, which have been calibrated using surface crystallographic features [1].

Information density

The second consideration is the information density of the images from which the measurements are made. The topographic data are collected pixel-by-pixel and the lateral resolution limit is determined by the pixel spacing. Groove measurements were made using images composed of 512 lines, with 512 pixels per line, and linear dimensions of 4 to $10\mu m$. Therefore, the lateral resolution limit is between 8 and $28nm$ and the shape of each groove is defined by a minimum of 80 pixels. Typically, groove traces consisted of several hundred pixels. In the vertical dimension, height differences of less than $1nm$ are typically resolved.

Definition of surface normal

Since the objective is to measure topographic deviations from the average surface plane, it is important that the sample has flat, parallel surfaces and that the surface plane is parallel to the AFM scanning plane. Because the AFM scanning plane is somewhat arbitrary in that it can be altered with the instrumental tilts, we make sure that the sample has two flat, parallel surfaces before the measurement. This is accomplished by polishing the sample using an automatic polisher (Logitech, PM5) and measuring the deviations from planarity using an inductive axial movement gauge head (TESR, Model TT22) with a resolution of $0.1\mu m$. Based on these macroscopic measurements, samples can be prepared which are flat to $\pm 0.3\mu m$ over lateral distances of $1cm$, and the deviation from parallelism is undetectable within the resolution limits of the gauge head. After mounting the sample on the AFM stage, the flat surface then serves as a reference plane and the instrumental tilts are adjusted so that the angle between the sample surface plane and the image plane is less than 1° over a $100\mu m$ scan area.

Background subtraction

It is especially important to base geometric measurements on uncorrected topographic data. Many AFM operating systems automatically subtract background planes; an operation that distorts the actual topography. The only background subtraction used for our measurements was a constant offset that was applied equally to each pixel. This operation is used to center the contrast range and does not distort the topography.

Probe Convolution

The convolution of the AFM probe shape with the sample surface topography is a well-known problem in AFM imaging. This problem is greatest when attempting to measure concave shapes, such as grain boundary grooves. The central issue is illustrated in Fig. A.1. As the AFM probe descends into the groove, its vertical position is actually determined by a point on the side of the tip, not by the point at the end of the tip. For relatively steep and/or narrow grooves, this leads to a systematic underestimation of the depth and slope.

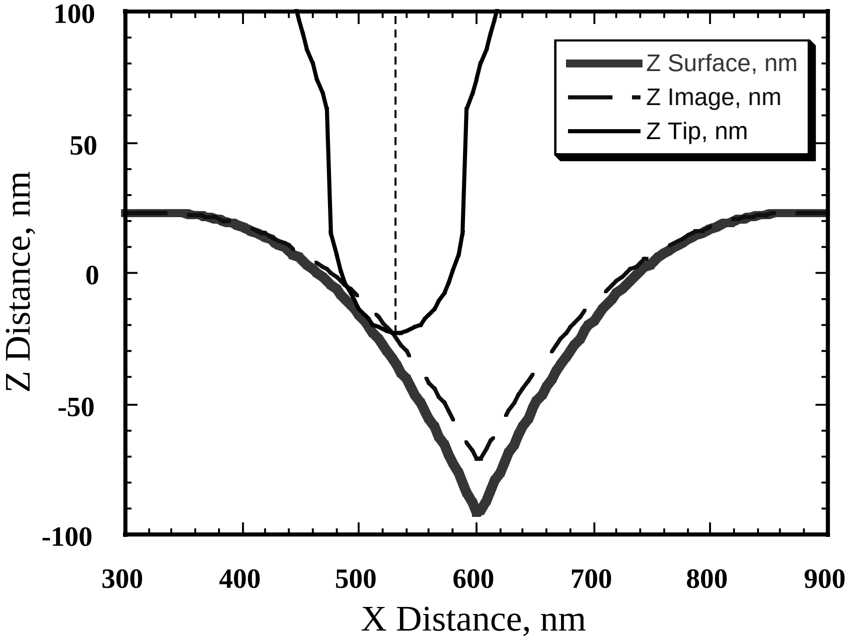

Figure A.1: Illustration of why AFM topographs systematically underestimate the depths of narrow, deep grooves. Because the point at which the tip contacts the groove surface is not on the tip axis, the slope of the concave shape and its depth are systematically underestimated. Note that the vertical axis is amplified with respect to the horizontal axis; this aspect ratio distorts the actual shape of the tip, which has an inner angle of 35°.

The magnitude of this systematic error depends on the aspect ratios (width to depth) of the groove and the tip. Using established simulation methods, it is possible to determine the systematic errors associated with measuring specific shapes with specific probes [2–4]. Thus, we have the choice of either correcting the observed data or finding domains for the experimental parameters where the errors are small enough to be tolerated.

To explore the errors involved in measuring grooves by AFM, we used the envelope reconstruction simulation method [2]. We began by developing model surface groove topographies with a variety of dihedral angles and widths using the solution to the quasi-static groove profile developed by Mullins [5] (see Fig. A.2). We should note that while the ideal Mullins groove shape is convenient to use, it does not accurately describe the shapes of grooves with small surface dihedral angles ($\Psi_s < 140^\circ$). Robertson's [6] numerical determination of the quasi-static groove profile shows that for a given dihedral angle and groove width, the profile predicted by Mullins' [5] equation is too deep. In other words,

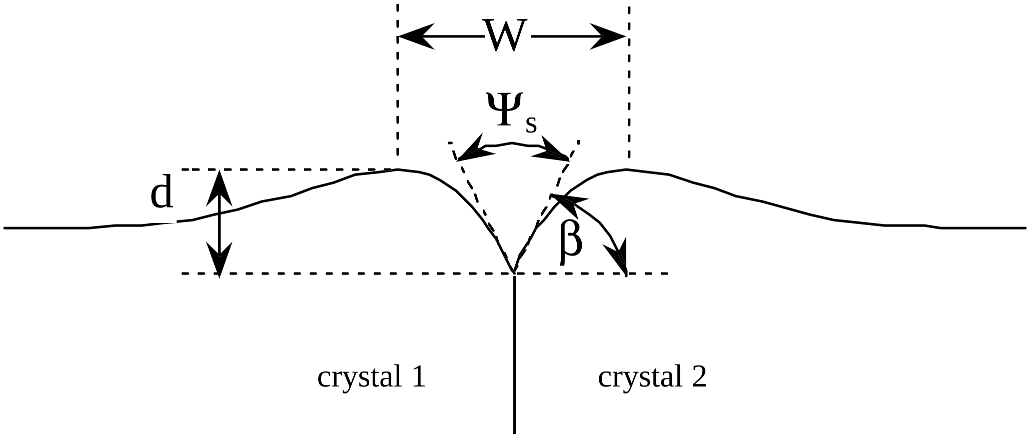

Figure A.2: Schematic representation of the quasi-static groove profile derived by Mullins [5].

the Mullins shape is actually more challenging to measure than the expected groove shape. Thus, by simulating profiles measured from the Mullins [5] groove profile, we can be certain of obtaining an upper limit for the systematic error. Our two-dimensional model probe tip is a triangle with an inner angle of $35°$ that is capped by a circle with a radius of $60nm$ (probes with smaller inner angles are commercially available, but not as robust). This shape conforms to the maximum size specified by the manufacturer and is consistent with high resolution SEM images of probe tips after use. Again, we choose the most pessimistic dimensions because we are interested in determining the maximum error. Based on simulated images of predefined grooves that span the range of expected geometries, we have calculated the error in the measured groove width, W, groove depth, d, and groove angle β. (These parameters are defined in Fig. A.2) The results, summarized in Fig. A.3, show that the error in β, determined from measurements of d and W, diminishes as the groove width increases.

Based on the results of the simulations, we draw the following conclusions. First, the convolution of the tip shape and the surface topography does not create an error in our measurement of the groove width, W. Second, the inner angle of the tip limits the range of dihedral angles that can be reliably measured to $\beta \leq 55° (\Psi_s \geq 70°)$. However, based on previously reported measurements of dihedral angles, we expect the population

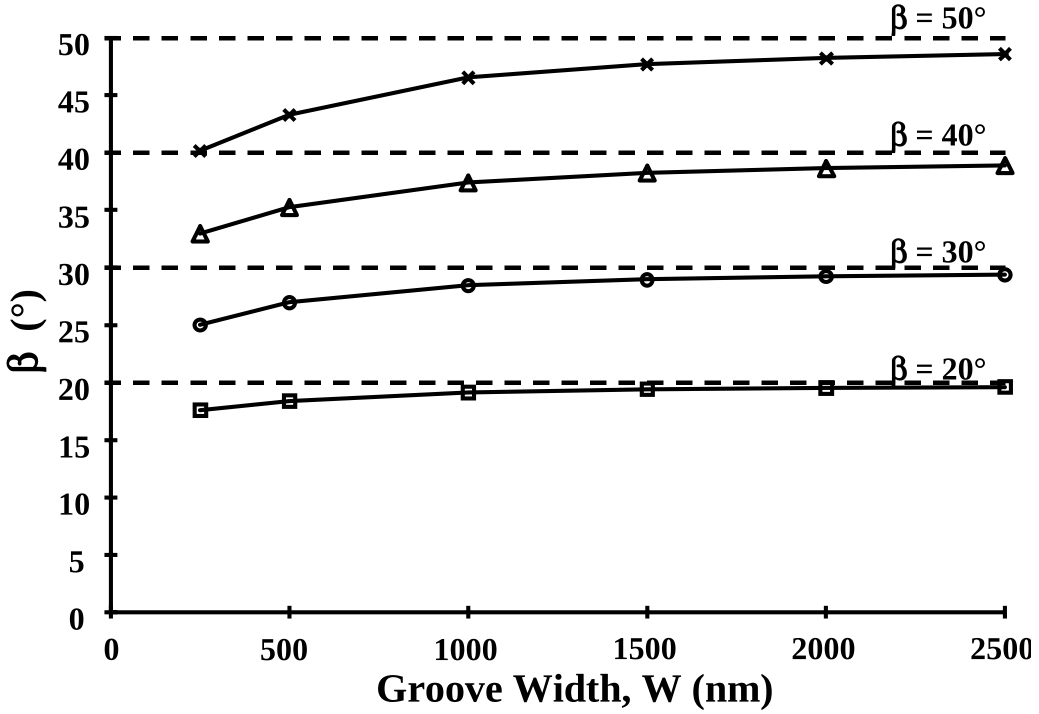

Figure A.3: A comparison of the values of the angle β, determined from measurements of W and d, with the actual values for model thermal grooves of different width (W) and angle (β). As the grooves become wider, the measured and actual values converge.

of inaccessible boundaries to be very small or non-existent [7]. Finally, we note that as the boundary width increases, both the depth (d) and the angle (β) are measured with acceptable accuracy. Based on these results, we confine our observations to grooves with an average width of greater than $2\mu m$.

Direct slope measurement

Finally, we note that determining the dihedral angle from measurements of d and W, rather than from direct measurements of β, eliminates the errors associated with measuring the slope. To compute β, we must determine the slope from at least 10 pixels near the groove root. Because the slope continuously decreases with distance from the groove root, the averaging necessary for the calculation of a slope leads to a systematic underestimation of β. This is essentially the same problem analyzed by Handwerker *et al.* [8] for groove measurements using other techniques. We can eliminate this particular source of error by computing β based on the known relationship between W and d determined by Robertson [6]. While a systematic error in the measurement of d remains, the simulation results show that it is relatively small. Specifically, the simulation results show that in the worst case, we underestimate the depth of a $2\mu m$ wide groove by less than 5%.

A.1.2 Measurement procedure

The consideration of the potential systematic errors leads us to the following procedure for determining surface dihedral angles. First, the specimens are polished so that they have two flat, parallel surfaces. Second, thermal treatments are used to groove the surfaces so that the average width is at least $2\mu m$. Before collecting data, the AFM is adjusted so that the image plane is parallel to the surface plane. Based on low resolution maps of the surface, the X-Y translation stage is used to seek triple junctions such that AFM topographs, 4 to $10\mu m$ on each side, can be recorded with an information density of 512 pixels per row and 512 rows. In each image, the triple junction is centered so that there are three grain boundaries. We then measure the geometry of each boundary by selecting linear traces over each of the three boundaries, and searching the traces for maximum and minimum points at each groove. This procedure is illustrated graphically in Fig. A.4. Using three traces over each boundary provides three measurements of W and d for each groove, which are averaged to yield final values from which the surface dihedral angle is determined. In several cases, we made 10 measurements of W and d at different positions along boundaries with some curvature, where there are potential differences in the indices of the free surfaces bounding the groove and in the grain boundary tangent plane. Based on such measurements, we estimate that the standard deviation resulting from measuring different positions in the same groove is 4° in Ψ_s. When this process was repeated on straight boundaries, where all three of the interfaces bounding the groove remain constant, the standard deviation associated with the random errors in our measurement procedure is 1° in Ψ_s for each boundary.

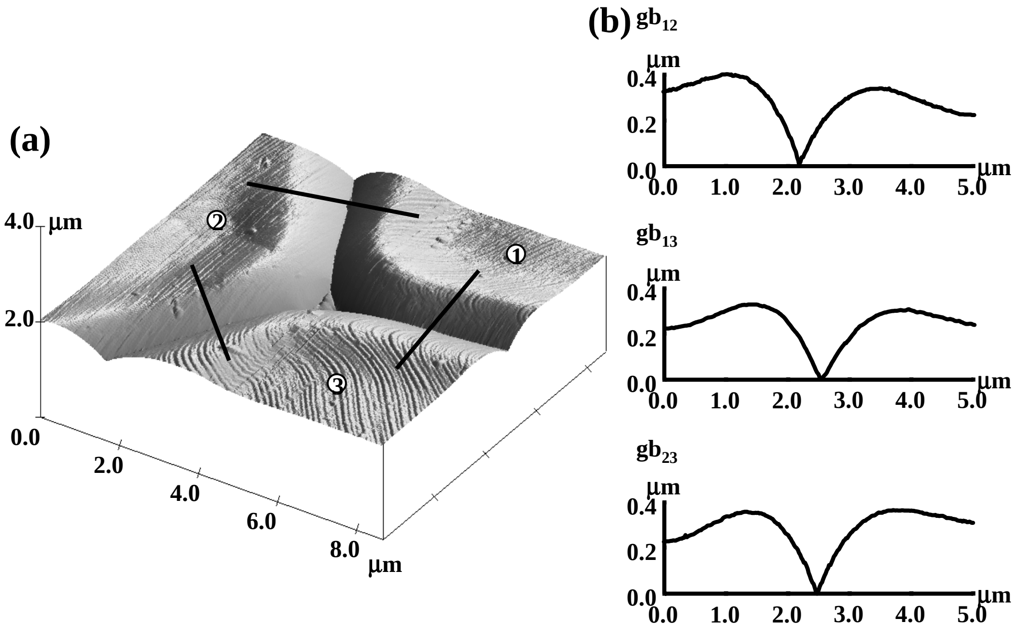

Figure A.4: (a) A typical contact AFM image of the point where a triple junction intersects the surface of a magnesia polycrystal. The black lines show the locations at which the three topographic traces in (b) were obtained. Values of W and d are obtained from each trace. The final values of W and d are determined by averaging three measurements from profiles at different locations on each groove. The standard deviation of the data acquired in this manner is $4°$.

A.2 Technique validation

It is important to verify that the AFM measurements described here lead to results that are consistent with previous studies using accepted techniques. The existing data on polycrystalline ceramics have been generated using optical microscopy [9], optical interferometry [10], and SEM [7,8,11]. These data include both distributions of surface dihedral angles [7–9,11] and measurements of grooving kinetics [10]. To validate the procedure described above, we have repeated some of these experiments and compared the observations with the results of these previous studies.

A.2.1 Grooving kinetics

The quasi-static groove profile determined by Robertson [6] assumes that the dominant atomic removal mechanism in the formation of grooves is surface diffusion. To test the

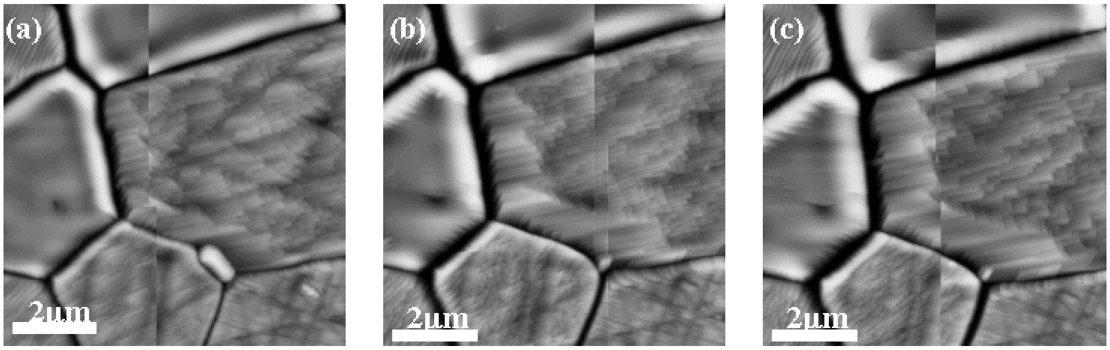

Figure A.5: AFM image montages of the same area of an alumina surface after annealing for $1h$ (a), $6h$ (b), and $10h$ (c) at $1400°C$. In all images, the vertical contrast from black-to-white is $100nm$. Contrast discontinuities occur at the boundaries between separate images with different average contrast levels.

assumption and make a comparison with previous studies we have examined the kinetics of groove formation in a polycrystalline alumina sample. The grain boundaries of the sample were thermally grooved in air at $1400°C$ and selected boundaries were repeatedly examined by AFM using the procedure described above after $1, 2, 3, 4, 6, 8, 10$, and $20h$ of annealing. The AFM images in Fig. A.5 show the same region of the surface at different times ($1, 6$, and $10h$) during the anneal. Note that as the annealing time increases, the boundaries become deeper and wider, and the facets on the grain surfaces coarsen.

At each interval during the anneal, the widths of 3 different boundaries were monitored. While depth measurements of such narrow boundaries would be unreliable, the width measurement is unaffected by the tip/groove convolution. Mullins [5] showed that the quasi-static groove profile depends on the atomic removal mechanism and that the slope (m) of a $\ln(W)$ v. $\ln(time)$ plot can be used to differentiate between surface diffusion ($m = 0.25$), volume diffusion ($m = 0.33$), and evaporation/condensation ($m = 0.50$) mechanisms. The time dependence of the width of three separate grooves is illustrated in Fig. A.6. The slopes of the three curves ($m = 0.21, 0.24$, and 0.24) are closer to the slope predicted by assuming a surface diffusion mechanism ($m = 0.25$) than the alternatives, and it should be acceptable to use Robertson quasi-static profile in our measurement procedure.

Assuming that the grooves are formed by surface diffusion, the groove width data can be used to compute a surface diffusion coefficient. Based on Mullins' [5] analysis, the

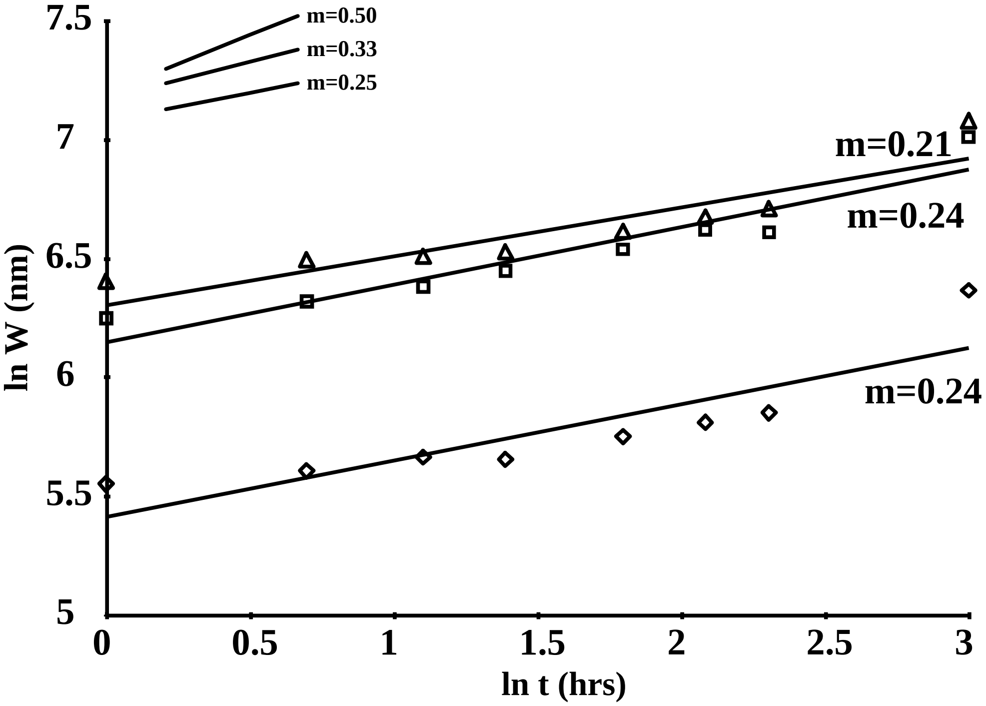

Figure A.6: The time (t) evolution of the groove width (W) for three grooves on an alumina polycrystal heated in air at $1400°C$. The slopes of the lines indicate that the dominant atomic removal mechanism is surface diffusion.

surface diffusion coefficient (D_s) is given by the following equation.

$$D_s = \frac{W^4 kT}{4.6^4 \gamma_{sv} \Omega^2 N t} \tag{A.1}$$

Surface diffusion data for alumina has been previously reviewed by Tsoga and Nikolopoulos [10]. The constants from Eqn. A.1 were taken from this earlier work to facilitate a comparison with the current data. Specifically, the molecular volume (Ω) is $2.11 \times 10^{-23} cm^3/molecule$, the surface energy ($\gamma_{sv}$) is $1.25 J/m^2$, and the number of diffusing species (N) is $\Omega^{-2/3}$; k and T are Boltzmann's constant and the absolute temperature ($1673K$), respectively. Tsoga and Nikolopoulos [10] used optical interferometry measurements to determine the groove width as a function of time and, based on their findings, D_s at $1400°C$ in air should be $4.9 \times 10^{-9} cm^2/s$. It should be noted that this number was computed based on average widths and ignores the anisotropy of the surface energy and diffusivity. Results from other groups were cited in the same paper and when extrapolated to $1400°C$, they vary from 5×10^{-10} to $1 \times 10^{-7} cm^2/s$. The widths from the three boundaries we measured led to surface diffusion coefficients of $9.4 \times 10^{-10} cm^2/s$, $1.4 \times 10^{-9} cm^2/s$, and $5.3 \times 10^{-11} cm^2/s$. The average of these three numbers falls in the lower end of the range observed in past studies [10]. The scatter in our measurements from different boundaries is likely to be an indication of the anisotropy of the surface diffusivity and/or surface energy. The lowest of our three values, which derives from a shallow, narrow boundary, falls outside the range of previous observations. However, because of its size, such boundaries would be overlooked in an optical study. After $20h$ of annealing, the width of this particular boundary was less than $500nm$, half the size of the smallest boundary reported in the earlier work. Thus, it appears that the AFM derived surface diffusivity data are consistent with previous measurements using more laborious techniques.

A.2.2 Dihedral angle distributions

Using the procedures described above, we have generated distributions of surface dihedral angles from grain boundaries from both an alumina and a magnesia polycrystal. The alumina sample was grooved in air at $1600°C$ for $1h$, while the magnesia sample was grooved in air at $1400°C$ for $5h$. These treatments yielded average groove widths of $2.3\mu m$ and $2.4\mu m$ for the alumina and magnesia samples, respectively.

Fig. A.7 shows the distribution of dihedral angles that we observed for alumina (a) and magnesia (b), determined from AFM measurements of W and d. In the past, a variety of techniques have been used to measure thermal grooves on similar samples. These data were reviewed by Handwerker *et al.* [7,8] who showed that the systematic errors in the measurement decrease as the resolution increases. Thus, the most reliable pre-existing measurements are based on metal reference line (MRL) observations. Handwerker *et al.* [7,8] corrected the MRL observations to account for the resolution limit of the technique, and we have plotted the corrected data for comparison in Fig. A.7. The median values of the distributions measured by AFM and the MRL techniques are the same, $106°$ for alumina and $105°$ for magnesia.

While the AFM and MRL results give the same median values for the surface dihedral angle distribution, there are some noteworthy differences in the details of the distribution.

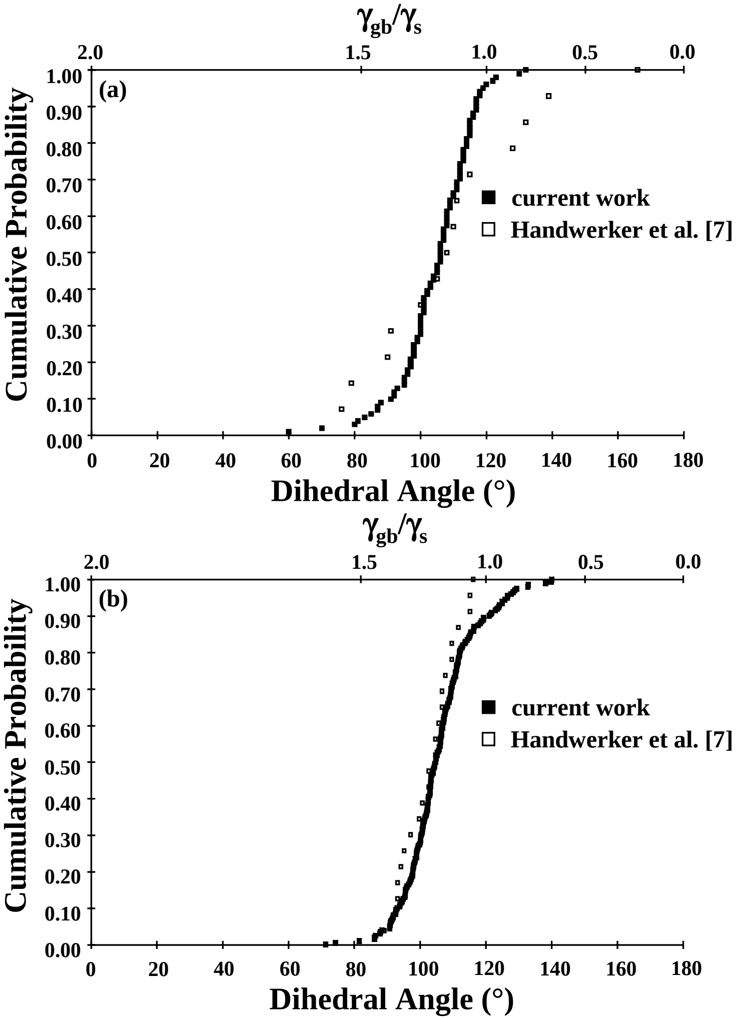

Figure A.7: (a) Distribution of thermal grooves in alumina, etched for $1h$ at $1600°C$ in air. (b) Distribution of thermal grooves in magnesia, etched for $5h$ at $1400°C$ in air. For comparison, equivalent data from [7] is plotted on each graph.

For example, the AFM measured magnesia distribution is wider on both sides of the median. There are several potential sources for the differences. The first might be the number of points in each distribution. For alumina, there are 14 MRL observations and 101 AFM observations. Similarly, for magnesia, there are 23 and 201 observations for MRL and AFM, respectively. The second potential reason for the differences might be related to sample purity and texture. For example, the alumina samples examined by Handwerker *et al.* [7] were sintered in vacuum. The alumina samples described here were sintered in air and might, therefore, have a greater impurity concentration. The relatively large number of low angle boundaries detected in our magnesia specimen might be the result of crystallographic texture introduced during processing. The sample described here has a $\langle 111 \rangle$ texture, measured by OIM to be 6.5 times random, while the texture of the samples examined by MRL was not reported. Although there are differences in the details of the surface dihedral angle distributions derived from the MRL and AFM techniques, the results illustrate an acceptable degree of consistency. Thus, we can conclude that by following the procedures outlined in A.1.2, AFM can be used to accurately measure the surface geometry of thermal grooves.

A.3 References

[1] R. L. Smith, G. S. Rohrer, K. S. Lee, D.-K. Seo and M.-H. Whangbo, “A Scanning Probe Microscopy Study of the (001) Surfaces of V_2O_5 and V_6O_{13},” *Surface Science*, **367** [1], 87-95 (1996).

[2] D.J. Keller and F.S. Franke, “Envelope Reconstruction of Probe Microscope Images,” *Surface Science*, **294** [3], 409-419 (1993).

[3] J.S. Villarrubia, “Morphological Estimation of Tip Geometry for Scanned Probe Microscopy,” *Surface Science*, **321** [3], 287-300 (1994).

[4] J.S. Villarrubia, “Scanned Probe Microscopy Tip Characterization Without Calibrated Tip Characterizers,” *J. Vac. Sci. Technol. B*, **14** [2], 1518-1521 (1996).

[5] W.W. Mullins, “Theory of Thermal Grooving,” *J. Appl. Phys.*, **28** [3], 333-339 (1957).

[6] W.M. Robertson, “Grain-Boundary by Surface Diffusion for Finite Surface Slopes,” *J. Appl. Phys.*, **42** [1], 463-467 (1971).

[7] C.A. Handwerker, J.M. Dynys, R.M. Cannon, and R.L. Coble, “Dihedral Angles in Magnesia and Alumina: Distributions from Surface Thermal Grooves,” *J. Amer. Ceram. Soc.*, **73** [5], 1371-1377 (1990).

[8] C.A. Handwerker, J.M. Dynys, R.M. Cannon, and R.L. Coble, “Metal Reference Line Technique for Obtaining Dihedral Angles from Surface Thermal grooves,” *J. Amer. Ceram. Soc.*, **73** [5], 1365-1370 (1990).

[9] W.D. Kingery, “Metal-Ceramic Interactions: IV, Absolute Measurement of Metal Ceramic Interfacial Energy and Interfacial Adsorption of Silicon From Iron-Silicon Alloys,” *J. Amer. Ceram. Soc.*, **37** [2], 42-45 (1954).

[10] A. Tsoga and P. Nikolopoulos, “Groove Angles and Surface Mass Transport in Polycrystalline Alumina,” *J. Amer. Ceram. Soc.*, **77** [4], 954-960 (1994).

[11] T. Ikegami, K. Kotani, and K. Eguchi, "Some Roles of MgO and TiO_2 in Densification of a Sinterable Alumina," *J. Amer. Ceram. Soc.*, **70** [12], 885-890 (1987).

Appendix B

Capillarity Vector Reconstruction Method

This appendix contains a detailed description of the capillarity vector method for the reconstruction of interfacial energies. The procedure, originally developed by Morawiec [1], involves setting up a system of linear equations based on Eqn. 4.9, discretizing the space of interfacial characters, and solving the system of equations for a set of discrete capillarity vectors, $\vec{\xi}_i$, using an iterative procedure. After the capillarity vector for each discrete interface is determined, the vector field is smoothed to accommodate for the effect of experimental errors and underpopulated cells. Here, we not only review the procedure, but also its application to both the surface and grain boundary energy measurements.

B.1 System of linear equations

The capillarity vector reconstruction method involves finding a consistent set vectors, $\vec{\xi}_i$, that satisfy Eqn. 4.9 as nearly as possible for all of the observed thermal grooves. To accomplish this we must set up a system of linear equations based on the triple junction measurements. While we wish to know the capillarity vectors with respect to the crystal coordinate system, Eqn. 4.9 holds only for vectors in the sample coordinate system. The orthogonal matrix, g_{jl}, that transforms a vector from the sample reference frame to the crystal reference frame is given in Eqn. 2.1. We can therefore rewrite Eqn. 4.9 as:

$$\varepsilon_{ijk}\ell_k g^s_{lj}\vec{\xi}^s_\ell = 0, \tag{B.1}$$

where ε_{ijk} is the permutation tensor and the superscript s enumerates the respective interface. For the grain boundary triple junctions, s simply enumerates the grain boundaries and g is given by the orientation of the appropriate crystallite. The case of the thermal groove measurements is more complex. For thermal grooves, s goes from 1 to 3 to represent surface 1, surface 2, and the grain boundary, respectively. For s equal to 1 or 2, the Eulerian angles yield the transformation matrix g_{lj} are those describing the orientation of the appropriate crystallite with respect to the sample reference frame. Since we do not sample enough of the possible grain boundary characters, we are forced to assume that the grain boundary torque is negligible. In other words, $\partial\gamma_3/\partial\beta = 0$ and $\vec{\xi}_3$ must be perpendicular to the grain boundary plane. To apply this constraint, only the first component of $\vec{\xi}_3$ is considered (if $s = 3$, $l = 1$). Therefore, the Eulerian angles for the grain boundary ($s = 3$), are given by θ, $3/2\pi$, and $\pi - \alpha$, respectively.

For each of the J observed triple junctions, there are three equilibrium equations enumerated by i. To solve these equations, we first tessellate the space of interfacial characters into cells, with each cell enumerated by an index, β. Next, we make the substitution that for an interface in cell β, $A^{\beta}_{il} = W\varepsilon_{ijk}\ell_k g_{lj}$, where W is selected so that $A^{\beta}_{il}A^{\beta}_{il} = 1$, with no summation over i. The set of J linear equations representing the balance of interfacial tensions is now:

$$A^{\beta}_{Jil}\xi^{\beta}_{l} = 0. \tag{B.2}$$

B.2 Discretization of character space

Because we seek a discrete set of capillarity vectors, the space of interface characters must be discretized over a fixed domain. One can chose the entire domain of possible interfacial characters, the fundamental zone of indistinguishable characters, or an appropriate subdomain containing a integer number of fundamental zones. In both cases (surfaces and grain boundaries), we used a convenient sub-domain of the character space.

For the thermal groove measurements, the sub-domain of surface characters was selected such that it contains all directions specified by vectors that have all three perpendicular components greater than or equal to zero, thus, considering cubic symmetry, the sub-domain contains 6 complete fundamental zones. If we specify these directions using the spherical coordinates, these are the values of θ and ϕ between 0 and $90°$. This sub-domain is then discretized in units of $\Delta\cos\theta$ and $\Delta\phi$, which makes the range of surface normals in each cell the same. Because we are assuming $\partial\gamma_3/\partial\beta = 0$, each enclosed grain boundary has only one character. Thus, the space of grain boundaries is discretized simply by the enclosed grain from which the measurement was taken.

In the case of the grain boundary triple junction measurements, the only interfaces are the grain boundaries. Here, we represent the character of a grain boundary by three Eulerian angles (φ_1, Φ,φ_2) describing the crystallite misorientation and two spherical coordinates (θ, ϕ) describing the boundary plane orientation. The sub-domain of grain boundaries was selected such that φ_1,Φ, and φ_2 are in the range of 0 to $90°$, and θ and ϕ are in the range of 0 to $90°$ and 0 to $360°$, respectively. Assuming cubic symmetry, this sub-domain contains 36 fundamental zones. To create cells of equal volume, the sub-domain is discretized in units of $\Delta\varphi_1$, $\Delta\cos\Phi$, $\Delta\varphi_2$, $\Delta\cos\theta$, and $\Delta\phi$.

As previously mentioned, the cells in both cases are enumerated with an index, β. For all interfaces that fall within a given cell, the capillarity vector is approximated by the value of $\vec{\xi}_\beta$ assigned to that cell.

B.3 Iterative solution

The system of equations (Eqn. B.2) is solved using the iterative method. The process begins with the assumption that $\xi_l^\beta = n_l^\beta$ where n_l^β is the normal vector at the center of each cell. At each step, the deviation vector, Δ_{Ji}, in the sample coordinate system is calculated according to:

$$A_{Jil}^{\beta}\xi_l^{\beta} = \Delta_{Ji}. \tag{B.3}$$

Because our sub-domain of interfacial character space contains symmetrically indistinguishable cells for each possible normal vector, there are equivalent equations for each observed triple junction. Therefore, the deviation vector for each triple junction is actually the average of the symmetrically equivalent equations. After Δ_{Ji} is calculated for each thermal groove, the capillarity vector is modified by the product of the deviation vector (in the crystal coordinate system) and a relaxation factor, ω. On the k^{th} iteration, it is modified in the following way:

$$\xi^{\beta}_{l[k]} = \xi^{\beta}_{l[k-1]} - \omega A^{\beta}_{Jil} \Delta_{Ji[k-1]}. \tag{B.4}$$

At the end of each iteration, the $\vec{\xi}$ values are normalized by dividing them by the average magnitude of all $\vec{\xi}$ at the current iteration step.

B.4 Smoothing of vector field

Because of the data collection technique does not generate a uniform distribution of interfacial characters, the cell population is nonuniform and many of the cells are underpopulated. This can create some sharp variations in what we expect to be a continuous and relatively smooth field of capillarity vectors. For this reason, the field of capillarity vectors is smoothed after the last iteration. The value of $\vec{\xi}_{\beta}$ in each cell is replaced by an average of that cell and the adjacent cells in the matrix. Cells at the edges and corners of the matrix are averaged only with their existing neighbors and if a cell contains zero or one observation, the cell is not used in the smoothing process. Tests on model data sets suggest that with a denser distribution of data, the smoothing process is not required.

After smoothing the field of $\vec{\xi}$, the energy (γ) for each orientation, $\hat{n}$, is determined by $\gamma = \vec{\xi} \cdot \hat{n}$. The energy of each interface is taken to be the average of the energies in all symmetrically equivalent cells.

B.5 References

[1] A. Morawiec, “Method to Calculate the Grain Boundary Energy Distribution over the Space of Macroscopic Boundary Parameters from the Geometry of Triple Junctions,” *Acta Mater.*, **48**, 3525-3532 (2000).

Appendix C

Grain boundary character and energy distributions

This appendix contains additional plots of the grain boundary character distribution, along with both the boundary energy distribution estimated from the sum of the surface energies of the two boundary planes and the energy reconstructed from the grain boundary triple junction measurements. The plots in each figure correspond to a fixed misorientation and show the variations over the boundary plane parameters in stereographic projection. The fixed misorientations explored are in 5° increments about $[100]$, $[110]$, $[111]$, and $[952]$.

C.1 $[100]$ misorientations

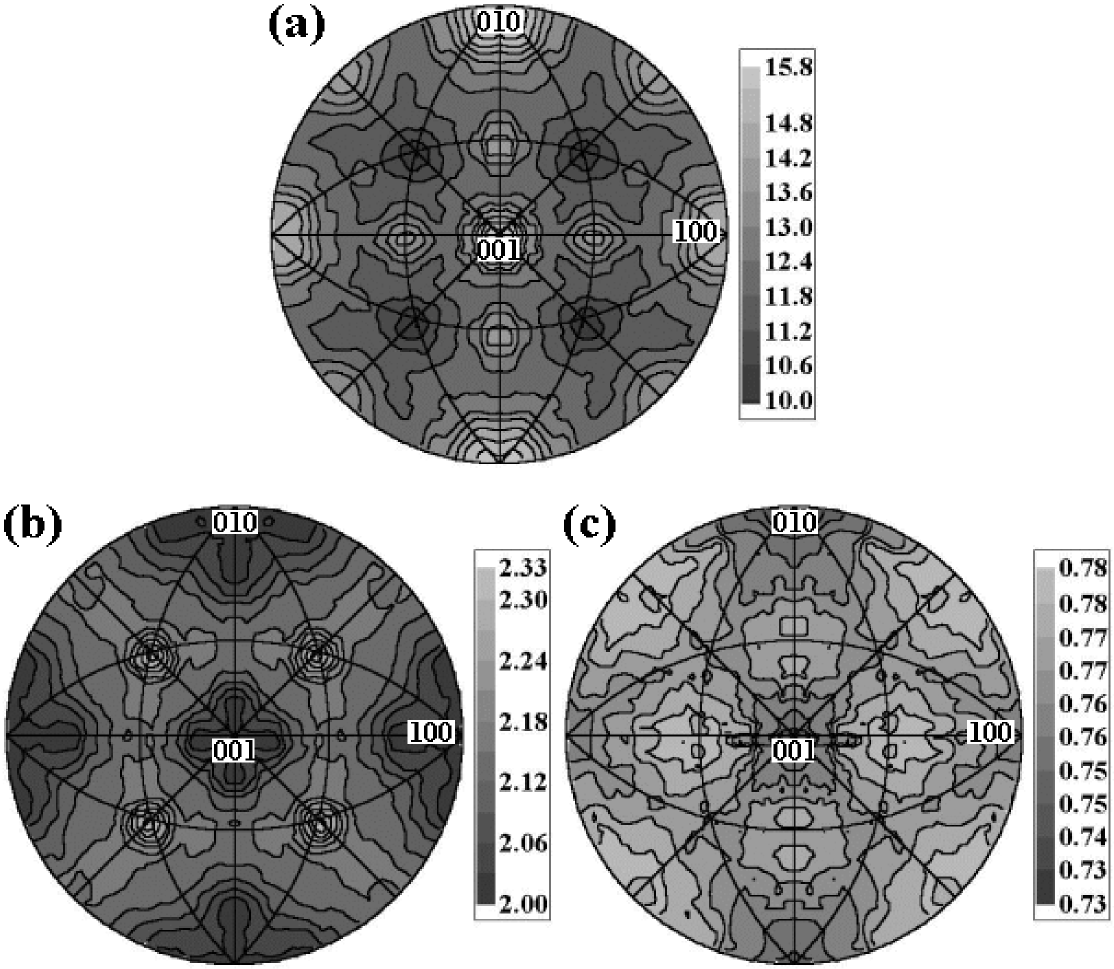

Figure C.1: Grain boundary character and energy distributions for the misorientation corresponding to a 5° rotation about $[100]$. The character distribution is shown in (a), while (b) and (c) show the boundary energy estimated from the surface energies and reconstructed from the triple junction measurements, respectively.

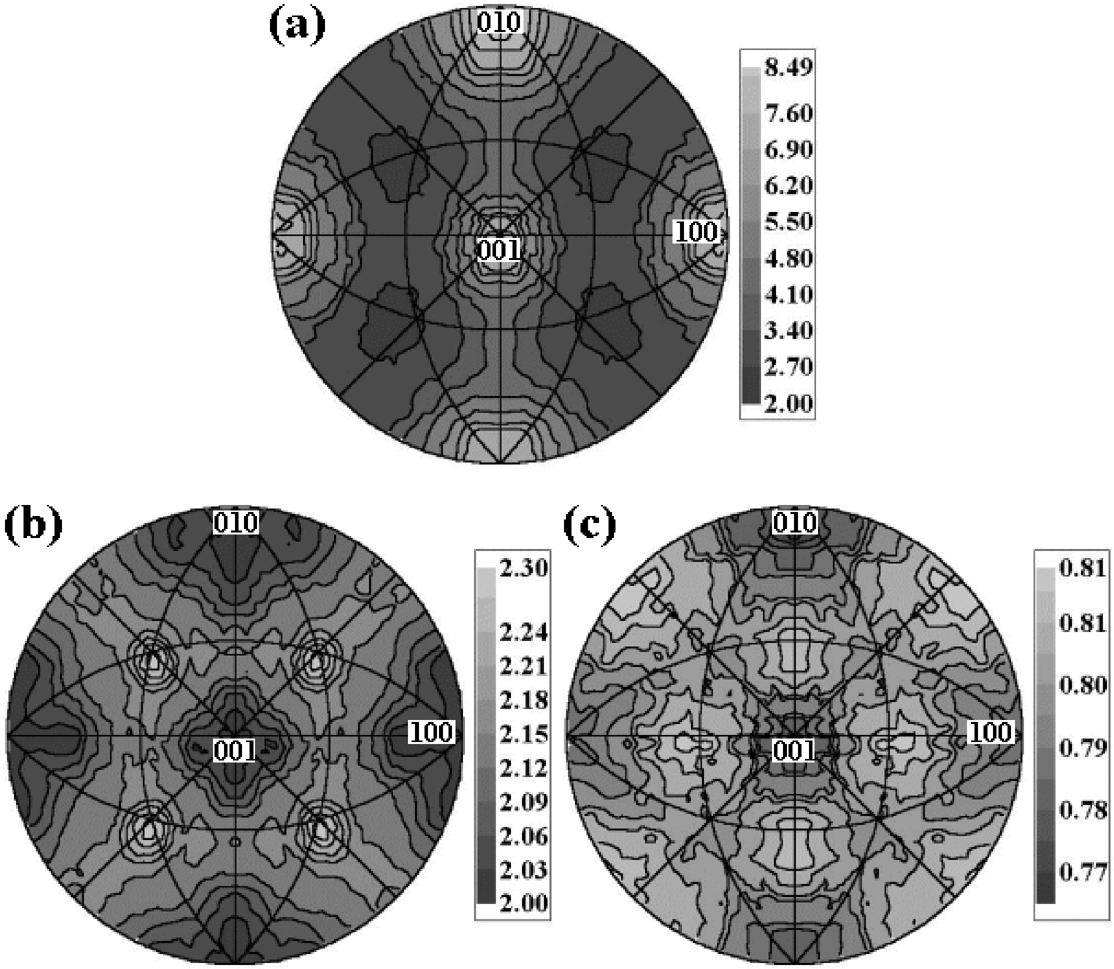

Figure C.2: Grain boundary character and energy distributions for the misorientation corresponding to a $10°$ rotation about $[100]$. The character distribution is shown in (a), while (b) and (c) show the boundary energy estimated from the surface energies and reconstructed from the triple junction measurements, respectively.

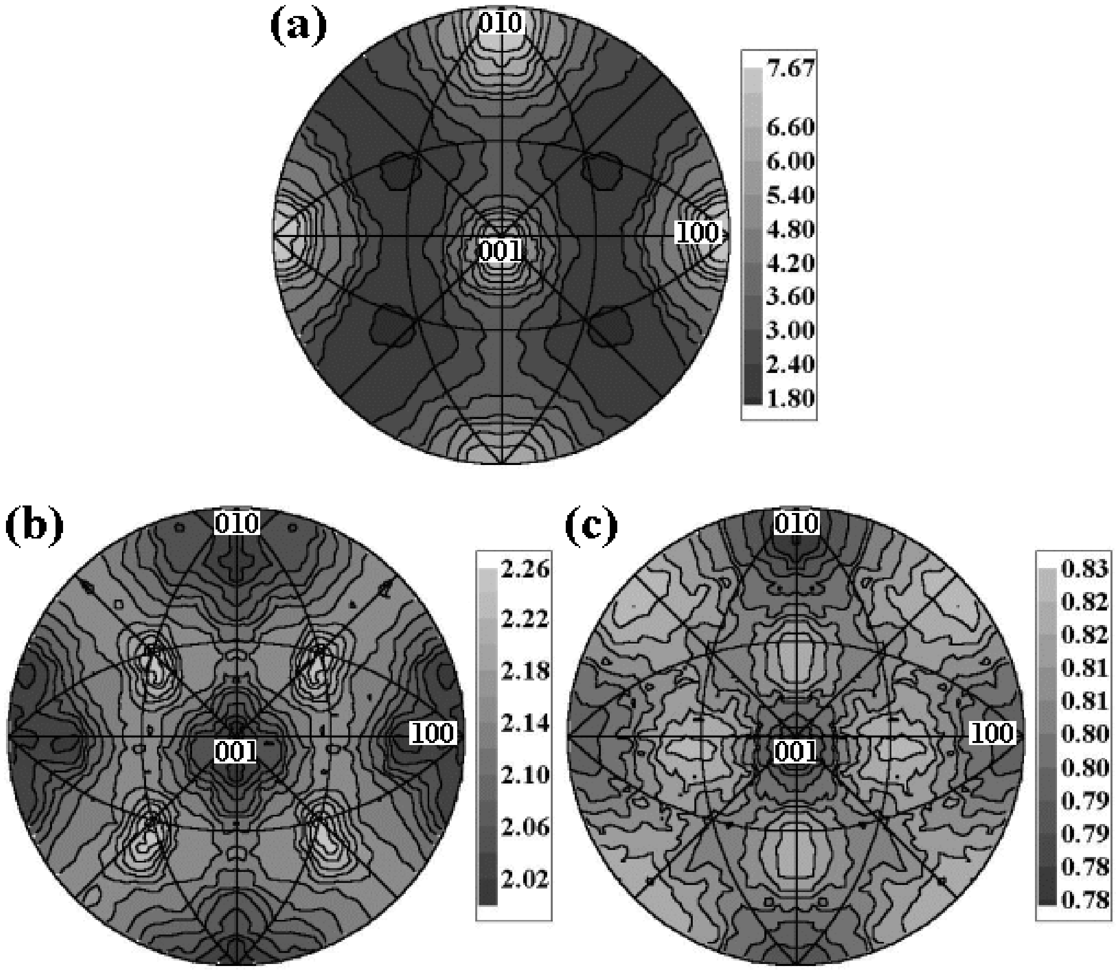

Figure C.3: Grain boundary character and energy distributions for the misorientation corresponding to a 15° rotation about $[100]$. The character distribution is shown in (a), while (b) and (c) show the boundary energy estimated from the surface energies and reconstructed from the triple junction measurements, respectively.

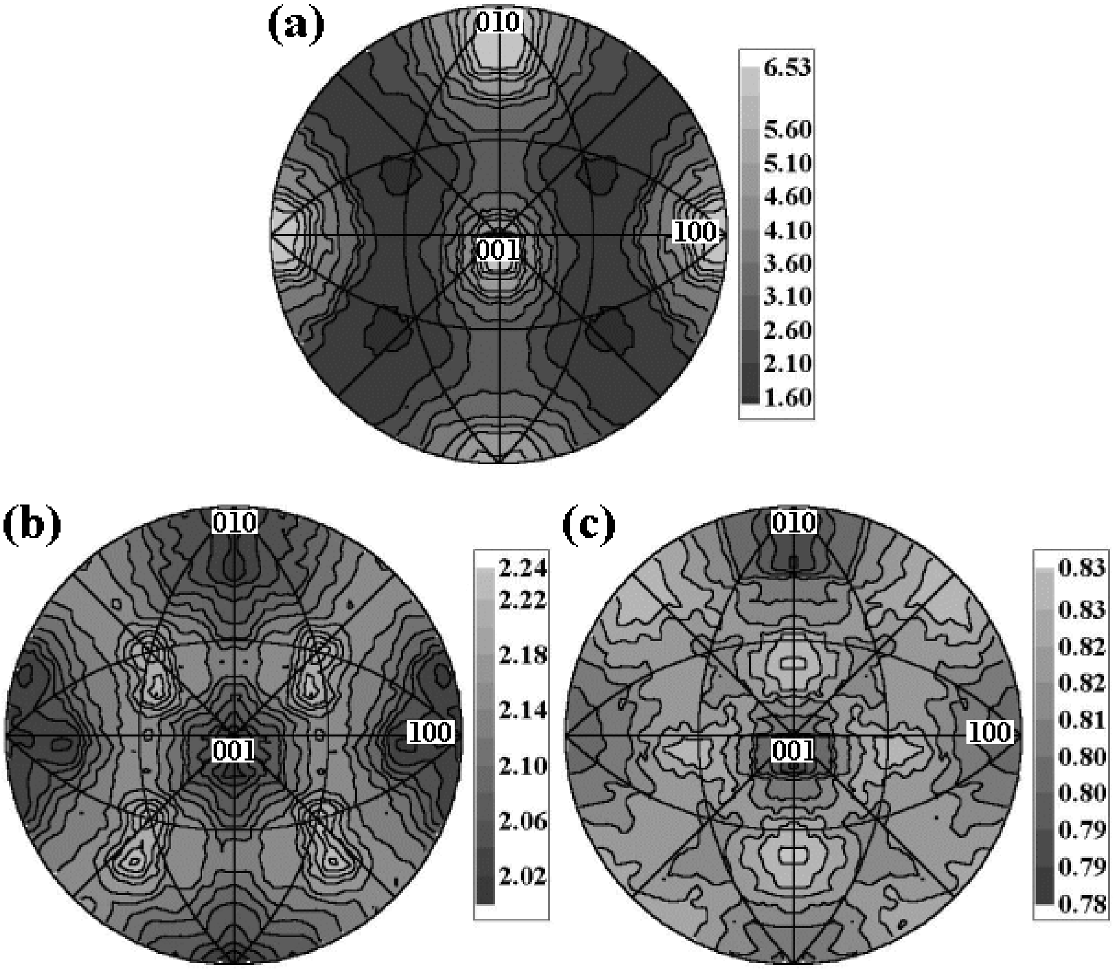

Figure C.4: Grain boundary character and energy distributions for the misorientation corresponding to a 20° rotation about $[100]$. The character distribution is shown in (a), while (b) and (c) show the boundary energy estimated from the surface energies and reconstructed from the triple junction measurements, respectively.

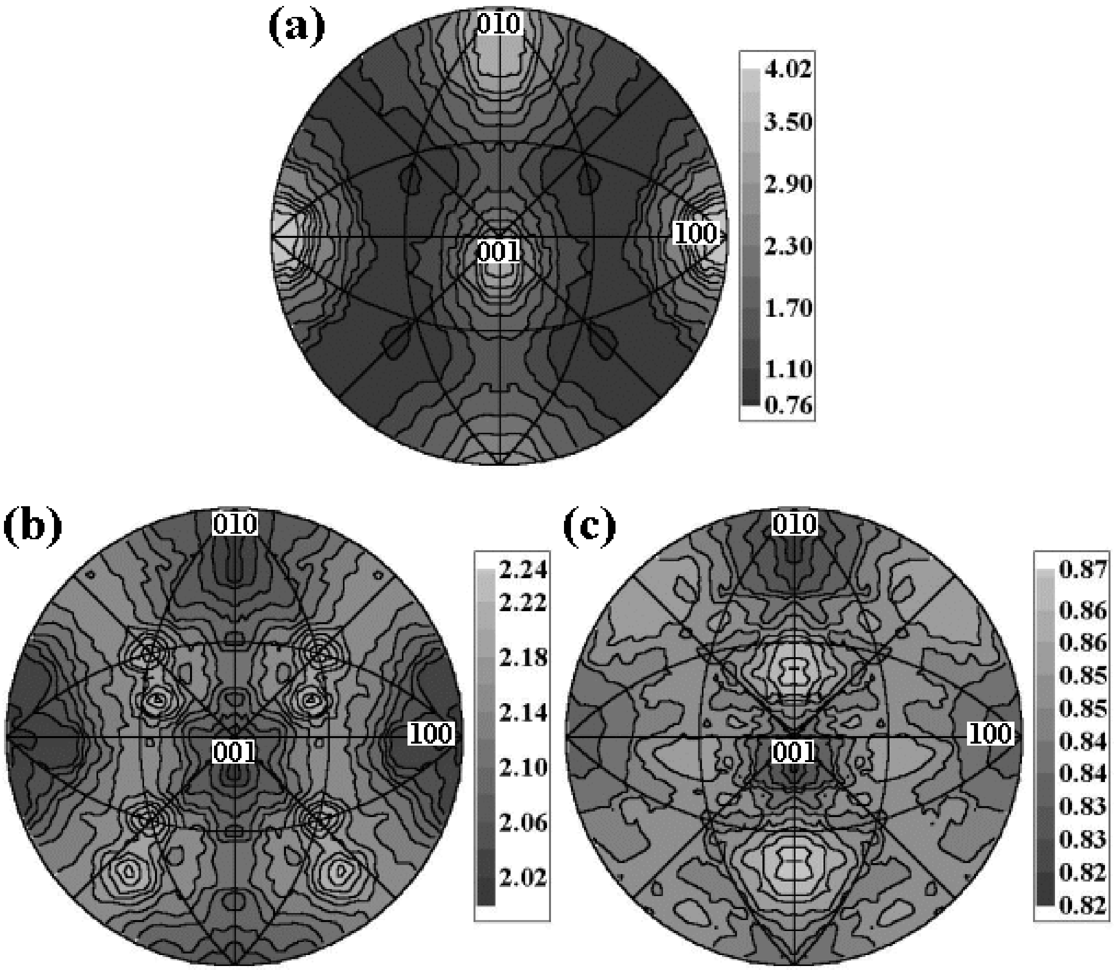

Figure C.5: Grain boundary character and energy distributions for the misorientation corresponding to a 25° rotation about $[100]$. The character distribution is shown in (a), while (b) and (c) show the boundary energy estimated from the surface energies and reconstructed from the triple junction measurements, respectively.

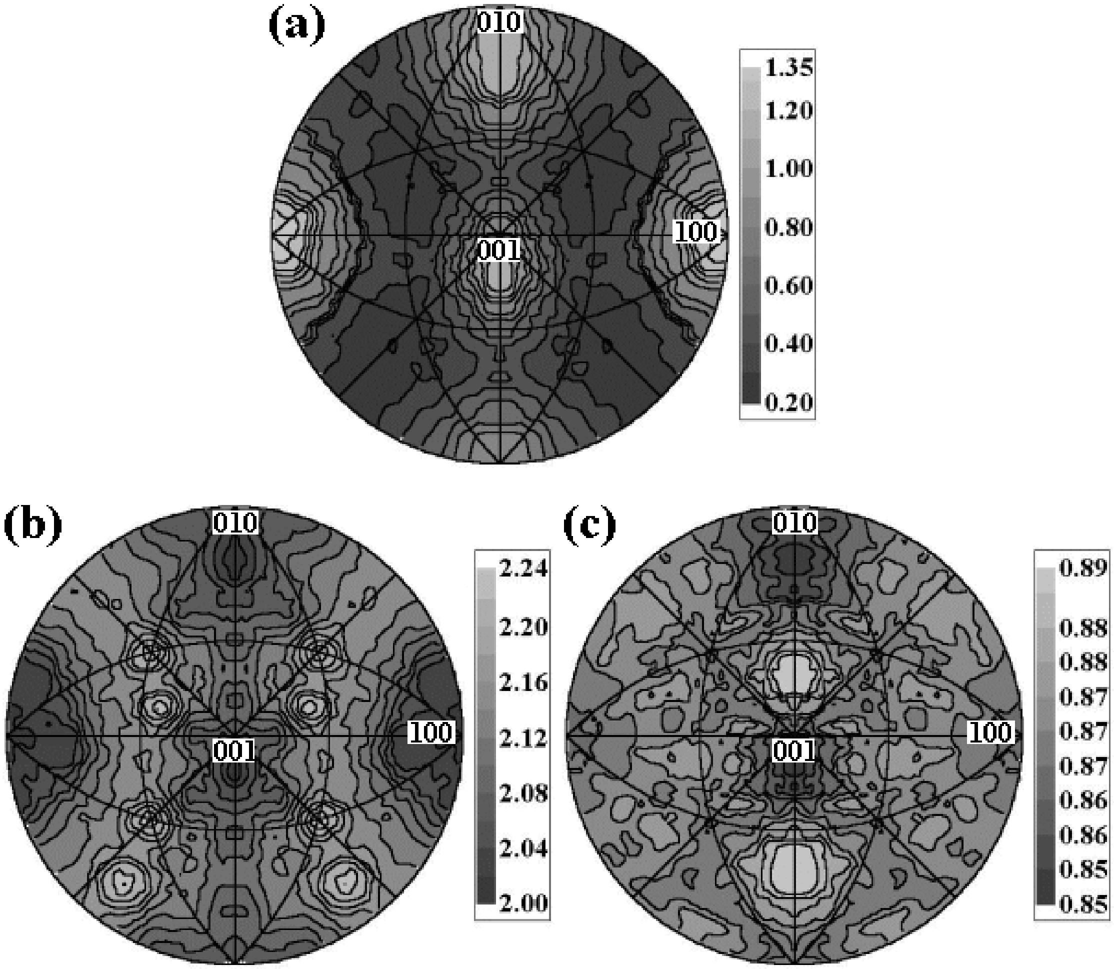

Figure C.6: Grain boundary character and energy distributions for the misorientation corresponding to a 30° rotation about $[100]$. The character distribution is shown in (a), while (b) and (c) show the boundary energy estimated from the surface energies and reconstructed from the triple junction measurements, respectively.

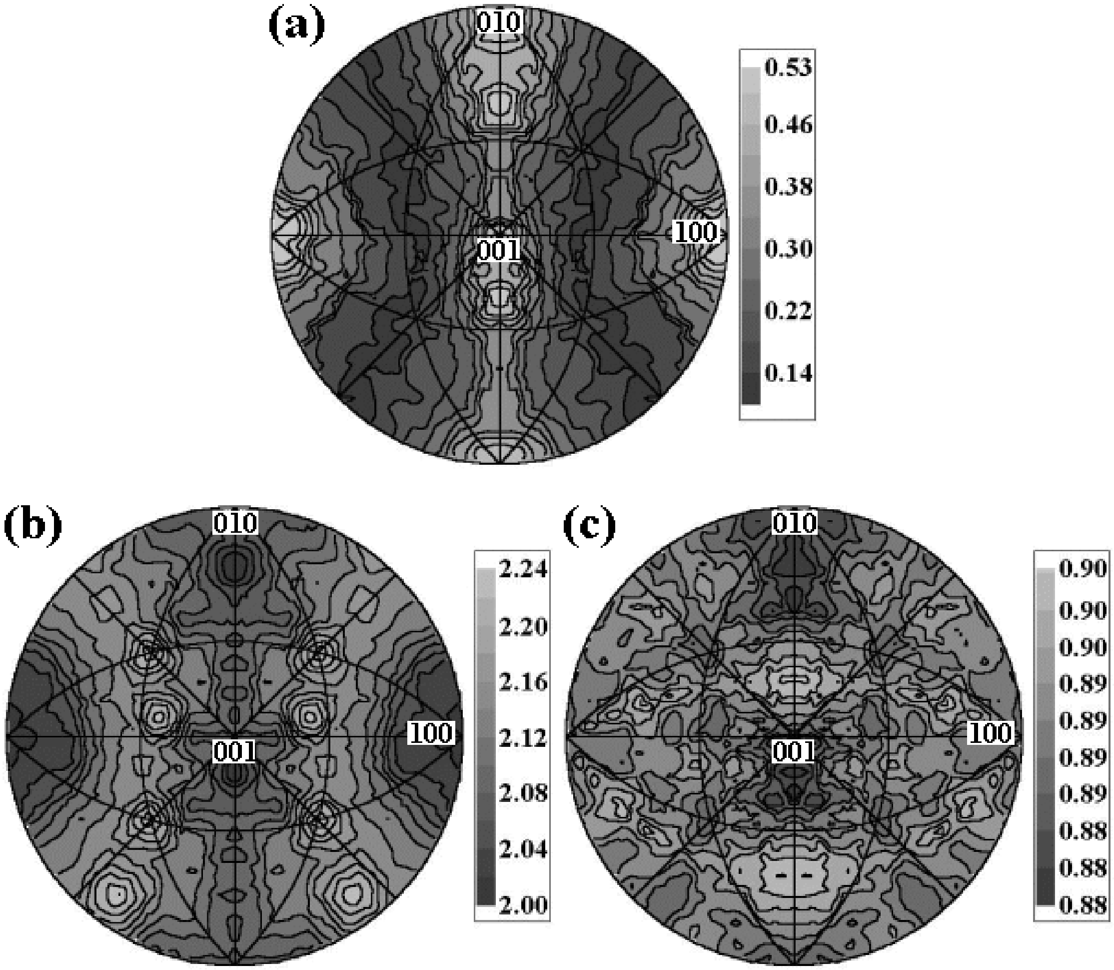

Figure C.7: Grain boundary character and energy distributions for the misorientation corresponding to a 35° rotation about $[100]$. The character distribution is shown in (a), while (b) and (c) show the boundary energy estimated from the surface energies and reconstructed from the triple junction measurements, respectively.

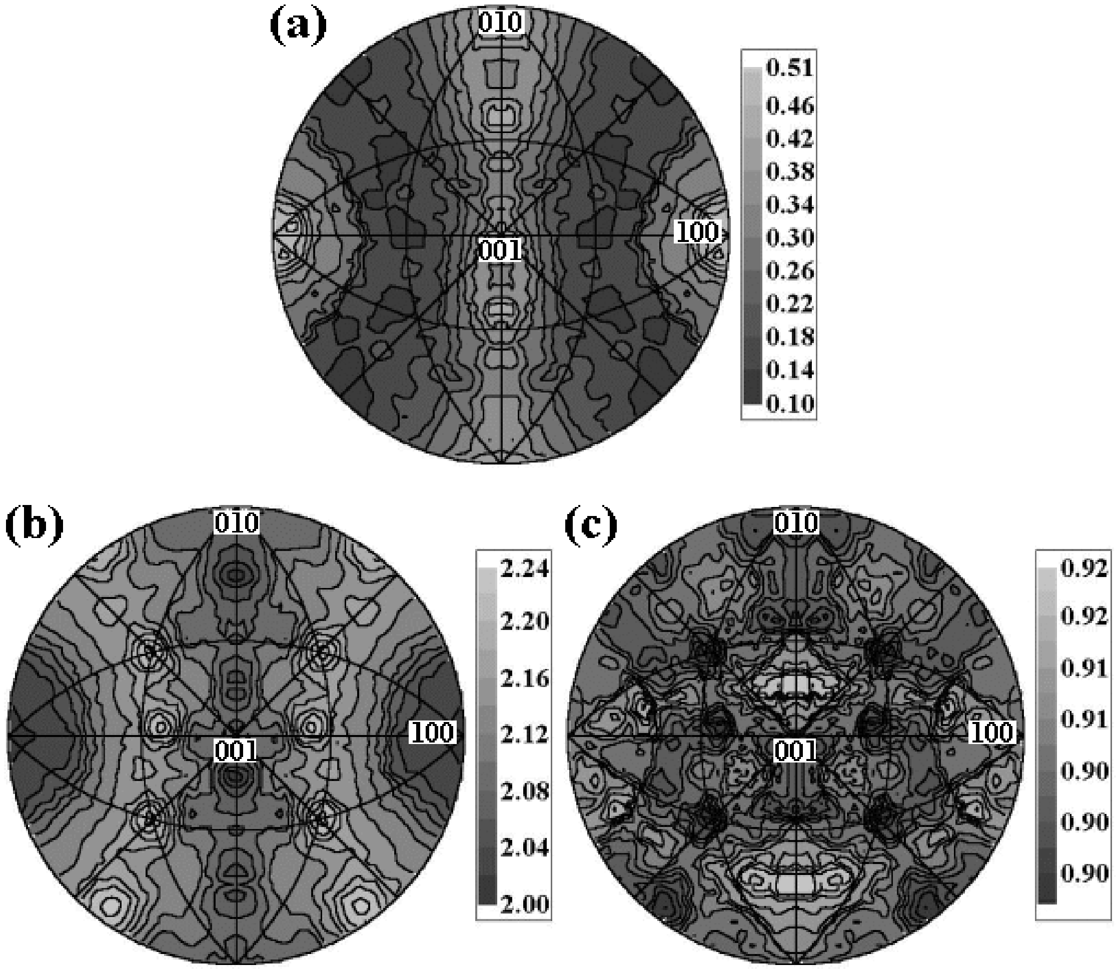

Figure C.8: Grain boundary character and energy distributions for the misorientation corresponding to a 40° rotation about $[100]$. The character distribution is shown in (a), while (b) and (c) show the boundary energy estimated from the surface energies and reconstructed from the triple junction measurements, respectively.

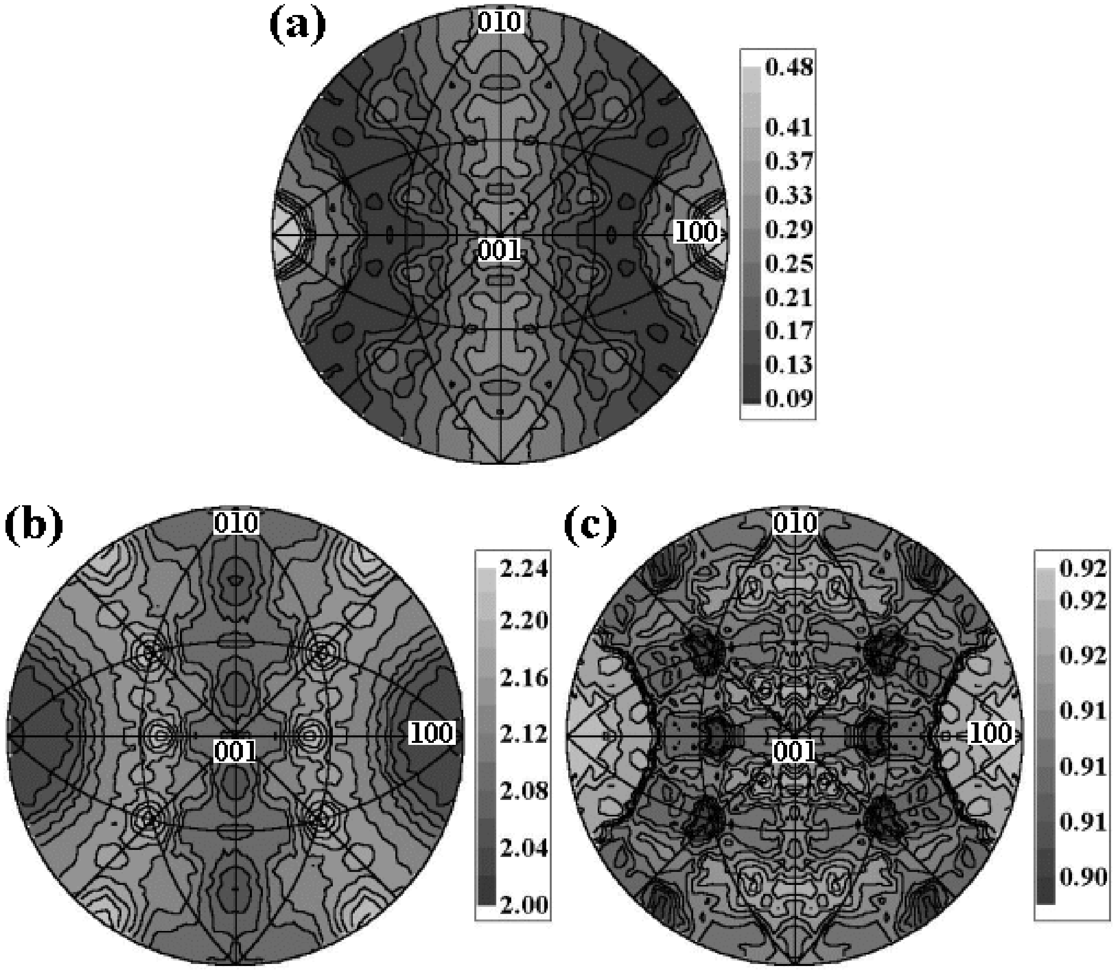

Figure C.9: Grain boundary character and energy distributions for the misorientation corresponding to a $45°$ rotation about $[100]$. The character distribution is shown in (a), while (b) and (c) show the boundary energy estimated from the surface energies and reconstructed from the triple junction measurements, respectively.

C.2 $[110]$ misorientations

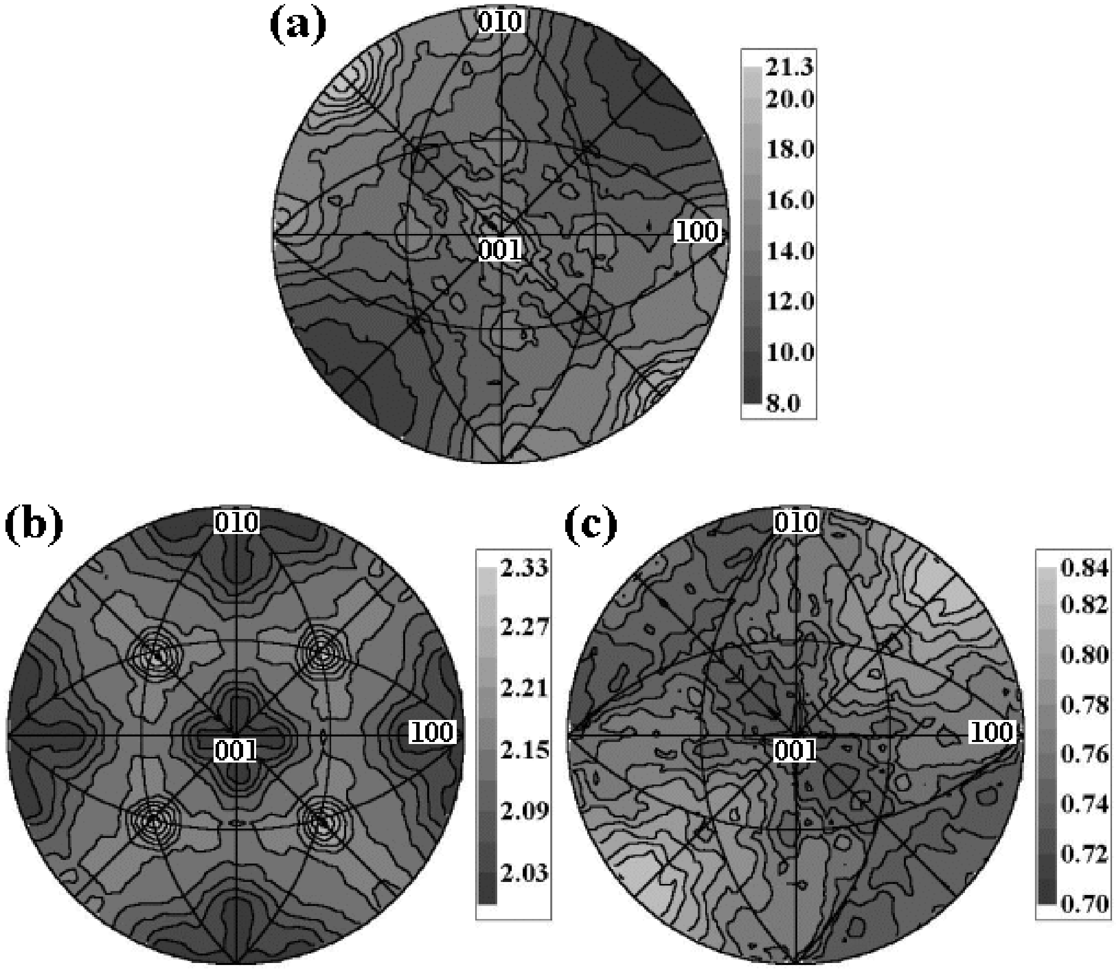

Figure C.10: Grain boundary character and energy distributions for the misorientation corresponding to a $5°$ rotation about $[110]$. The character distribution is shown in (a), while (b) and (c) show the boundary energy estimated from the surface energies and reconstructed from the triple junction measurements, respectively.

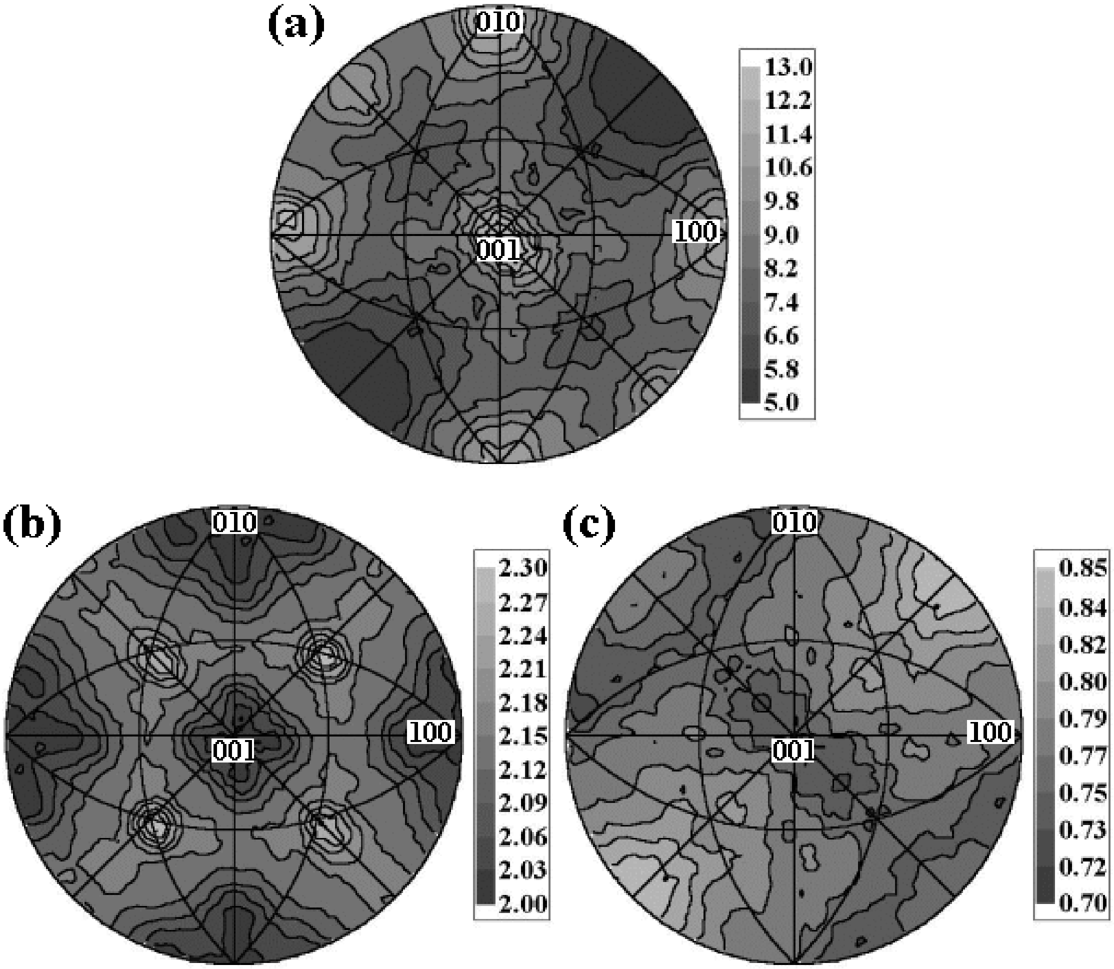

Figure C.11: Grain boundary character and energy distributions for the misorientation corresponding to a 10° rotation about $\langle 110 \rangle$. The character distribution is shown in (a), while (b) and (c) show the boundary energy estimated from the surface energies and reconstructed from the triple junction measurements, respectively.

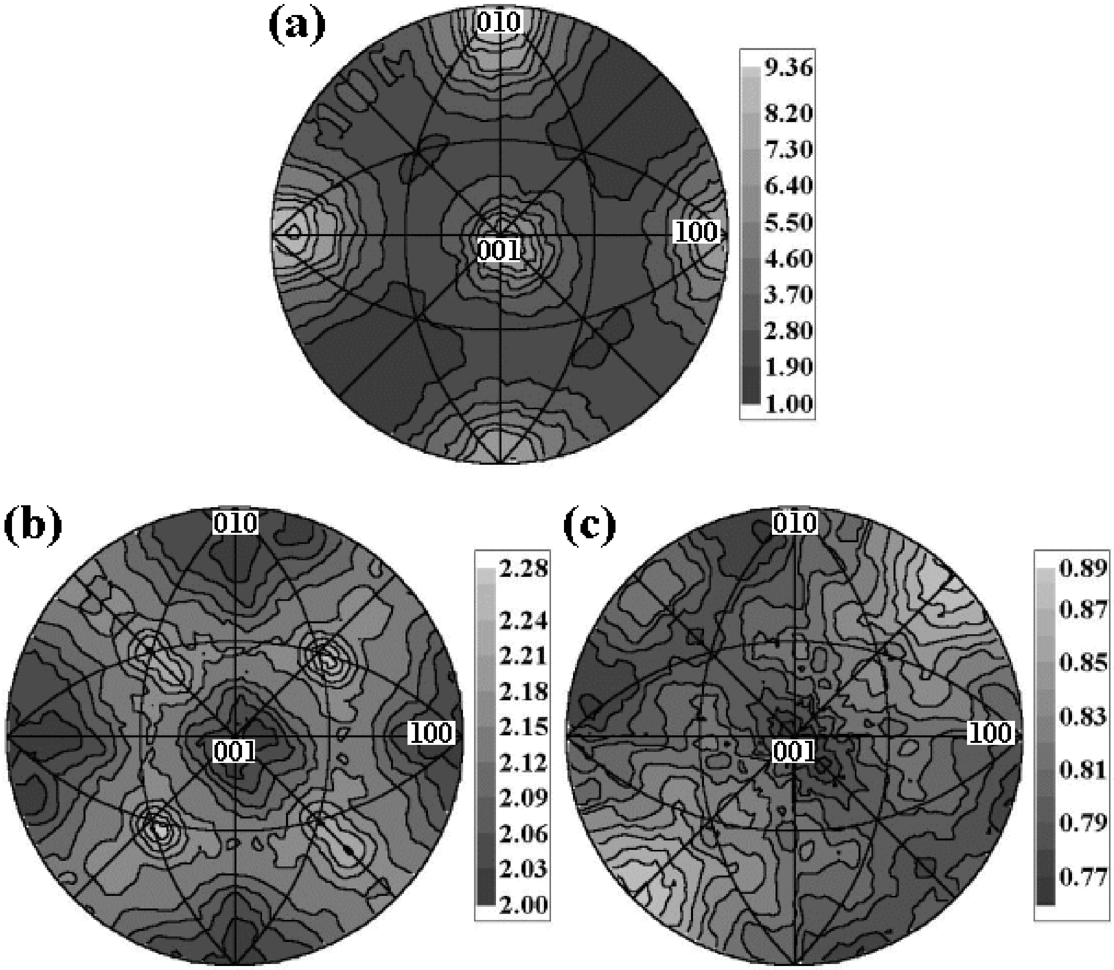

Figure C.12: Grain boundary character and energy distributions for the misorientation corresponding to a $15°$ rotation about $[110]$. The character distribution is shown in (a), while (b) and (c) show the boundary energy estimated from the surface energies and reconstructed from the triple junction measurements, respectively.

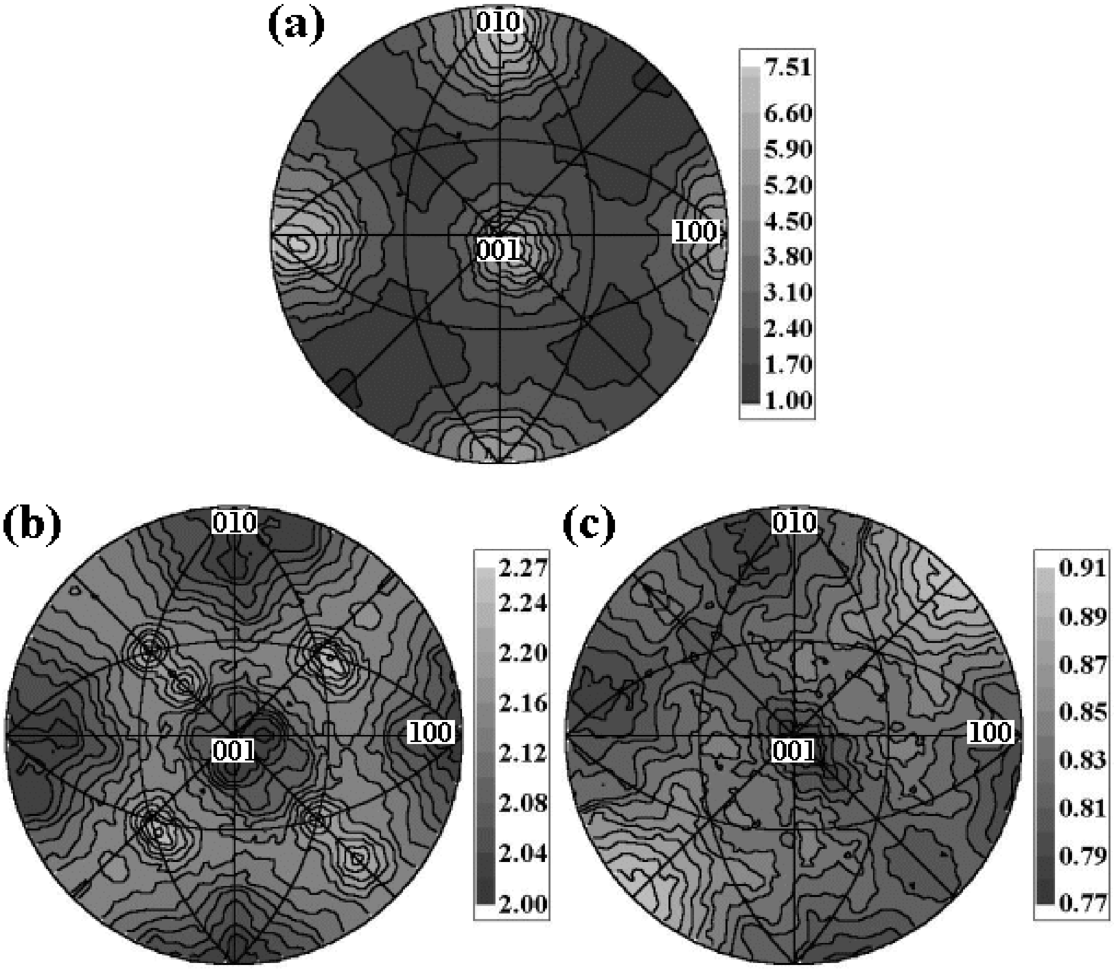

Figure C.13: Grain boundary character and energy distributions for the misorientation corresponding to a 20° rotation about $[110]$. The character distribution is shown in (a), while (b) and (c) show the boundary energy estimated from the surface energies and reconstructed from the triple junction measurements, respectively.

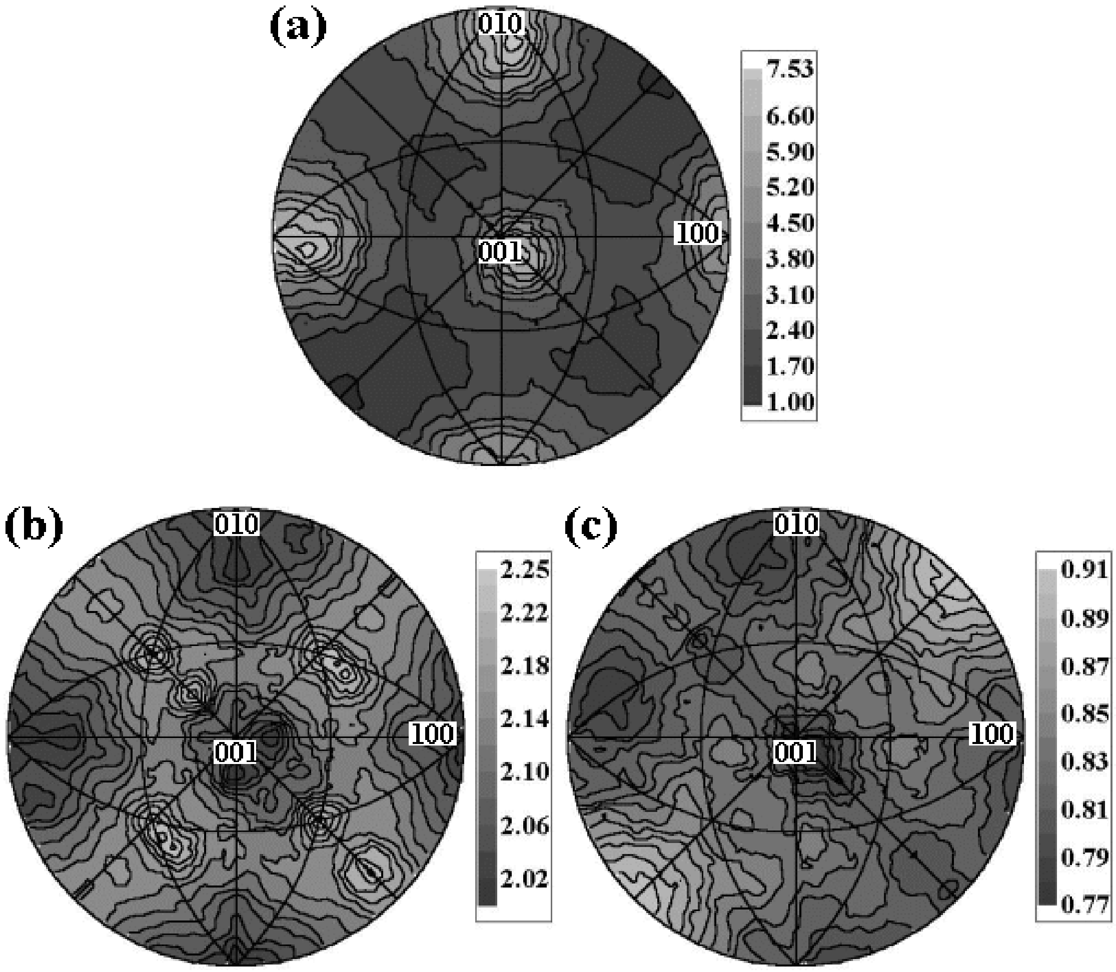

Figure C.14: Grain boundary character and energy distributions for the misorientation corresponding to a $25°$ rotation about $[110]$. The character distribution is shown in (a), while (b) and (c) show the boundary energy estimated from the surface energies and reconstructed from the triple junction measurements, respectively.

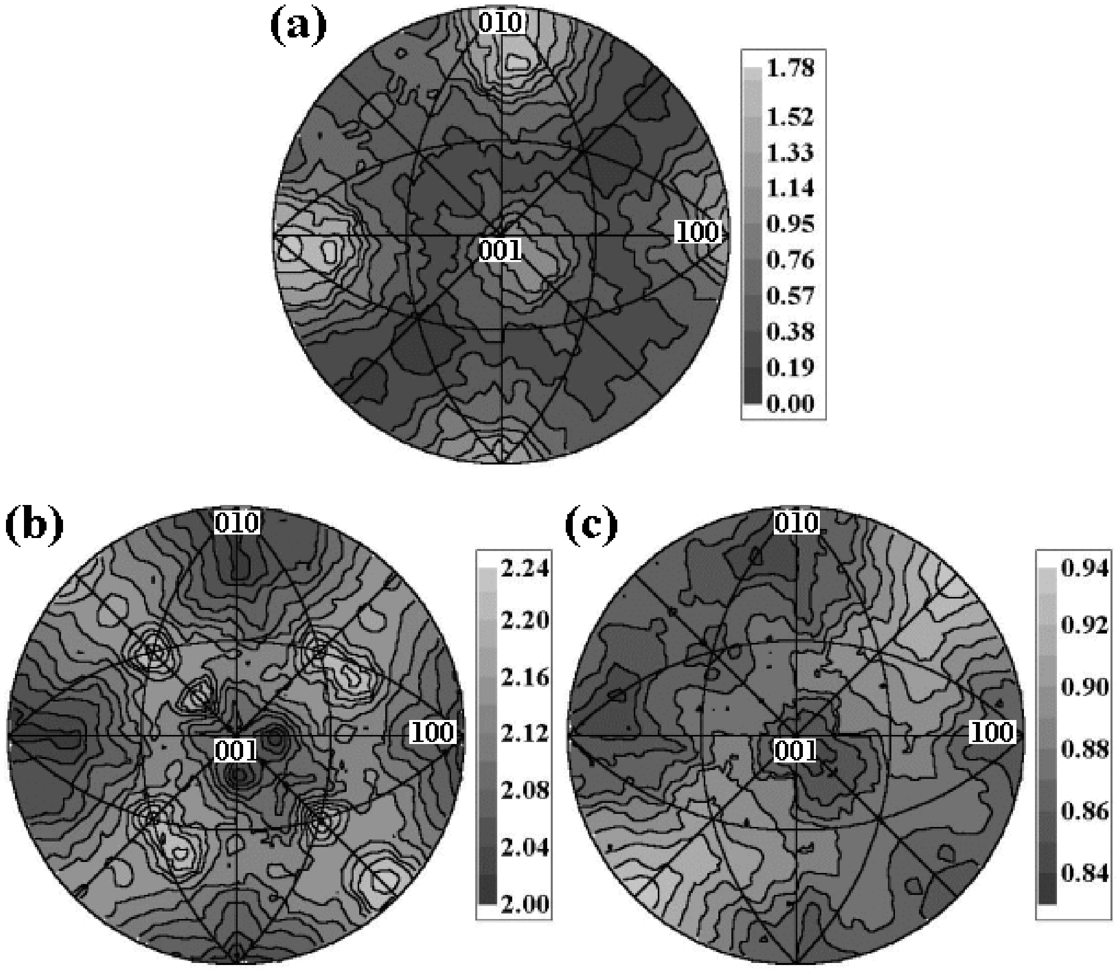

Figure C.15: Grain boundary character and energy distributions for the misorientation corresponding to a 30° rotation about $[110]$. The character distribution is shown in (a), while (b) and (c) show the boundary energy estimated from the surface energies and reconstructed from the triple junction measurements, respectively.

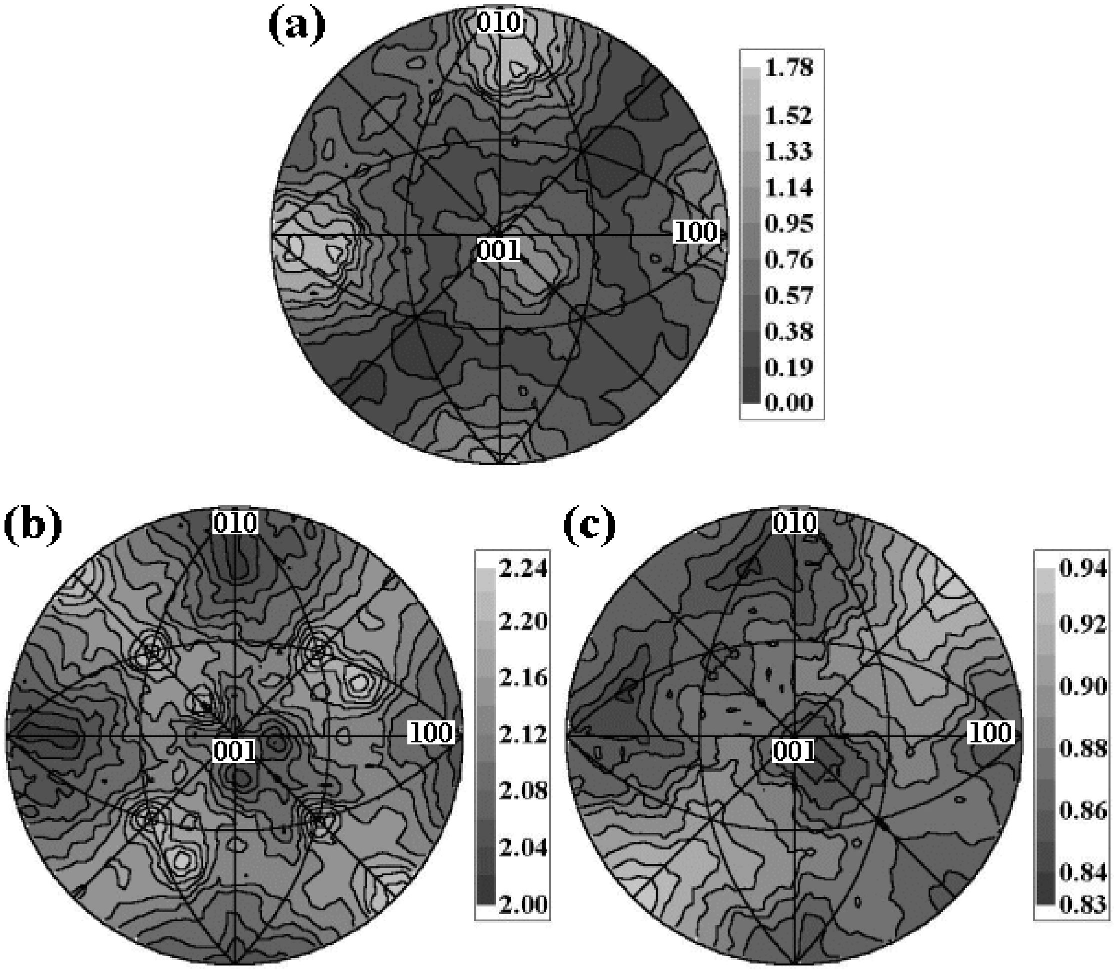

Figure C.16: Grain boundary character and energy distributions for the misorientation corresponding to a 35° rotation about $[110]$. The character distribution is shown in (a), while (b) and (c) show the boundary energy estimated from the surface energies and reconstructed from the triple junction measurements, respectively.

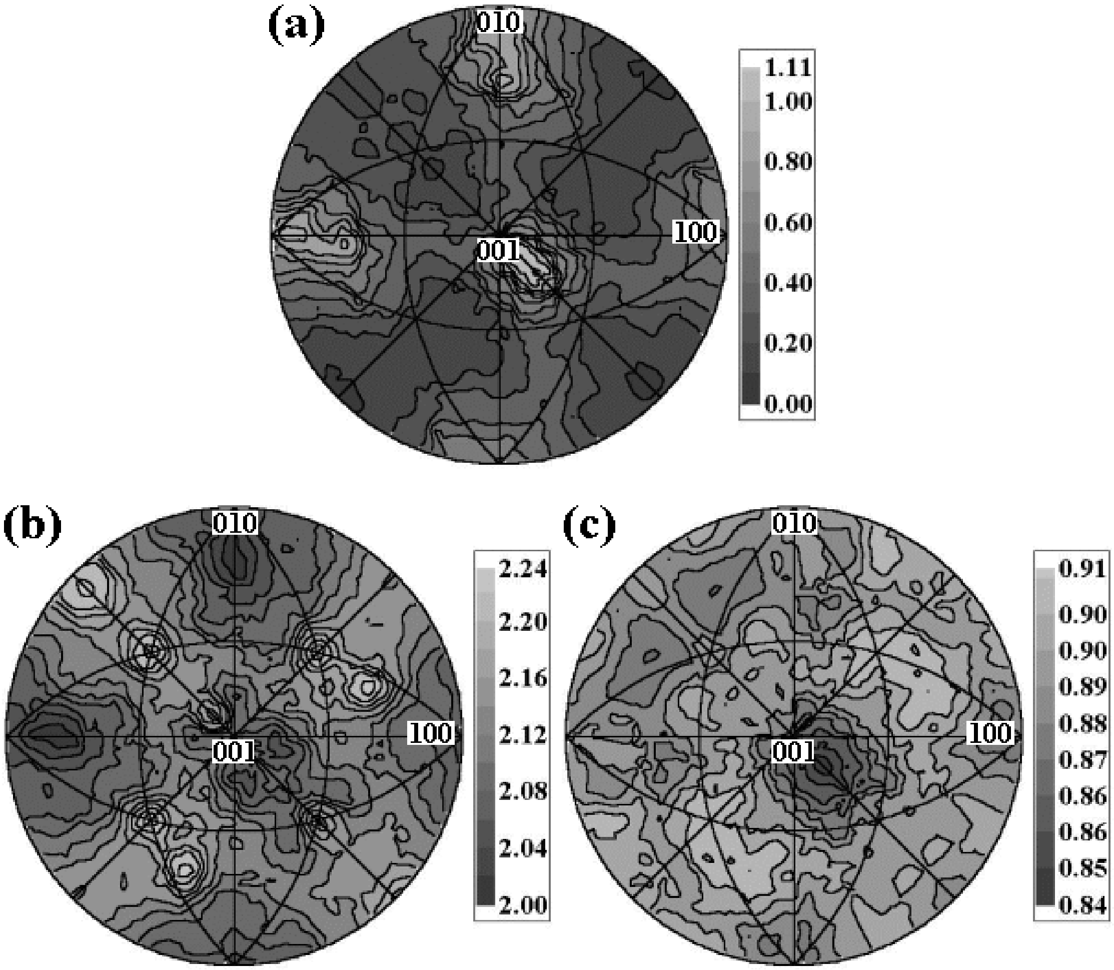

Figure C.17: Grain boundary character and energy distributions for the misorientation corresponding to a 40° rotation about $[110]$. The character distribution is shown in (a), while (b) and (c) show the boundary energy estimated from the surface energies and reconstructed from the triple junction measurements, respectively.

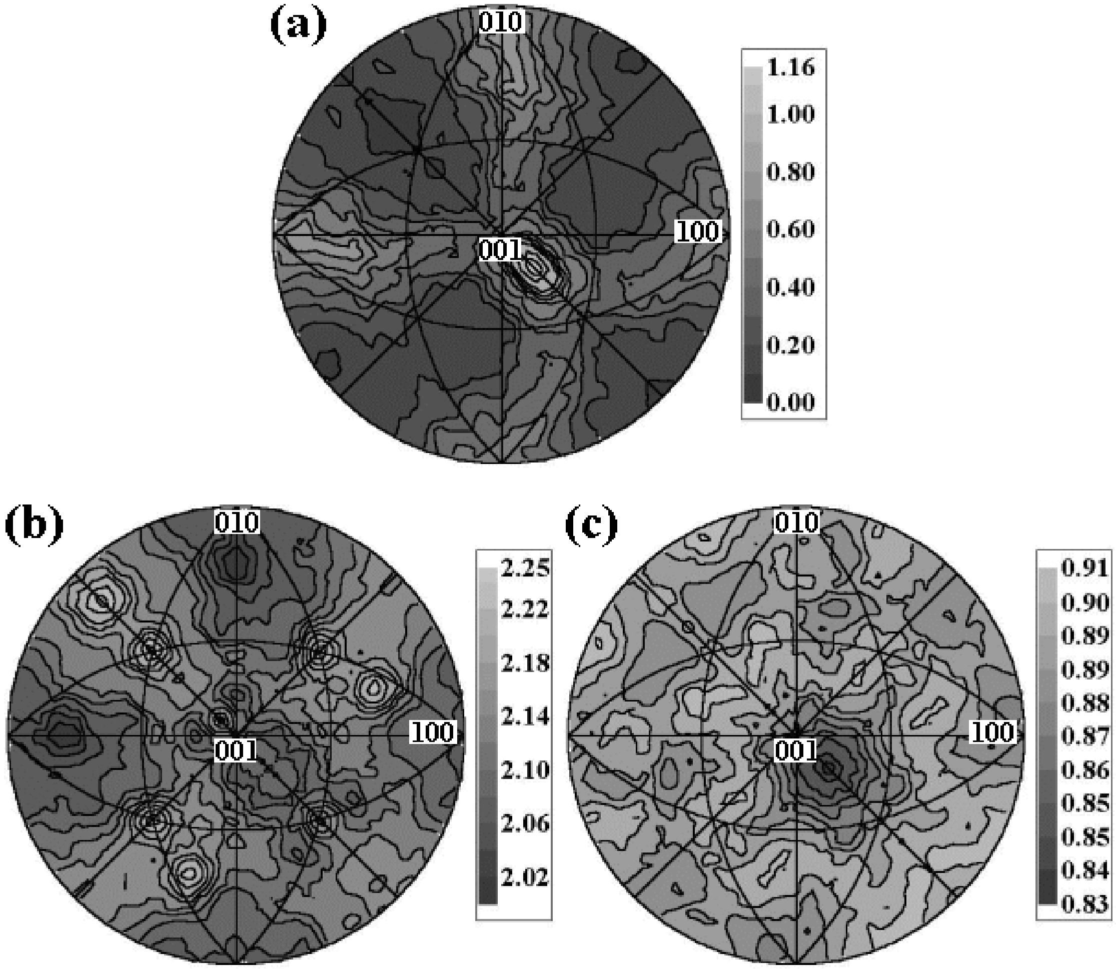

Figure C.18: Grain boundary character and energy distributions for the misorientation corresponding to a $45°$ rotation about $[110]$. The character distribution is shown in (a), while (b) and (c) show the boundary energy estimated from the surface energies and reconstructed from the triple junction measurements, respectively.

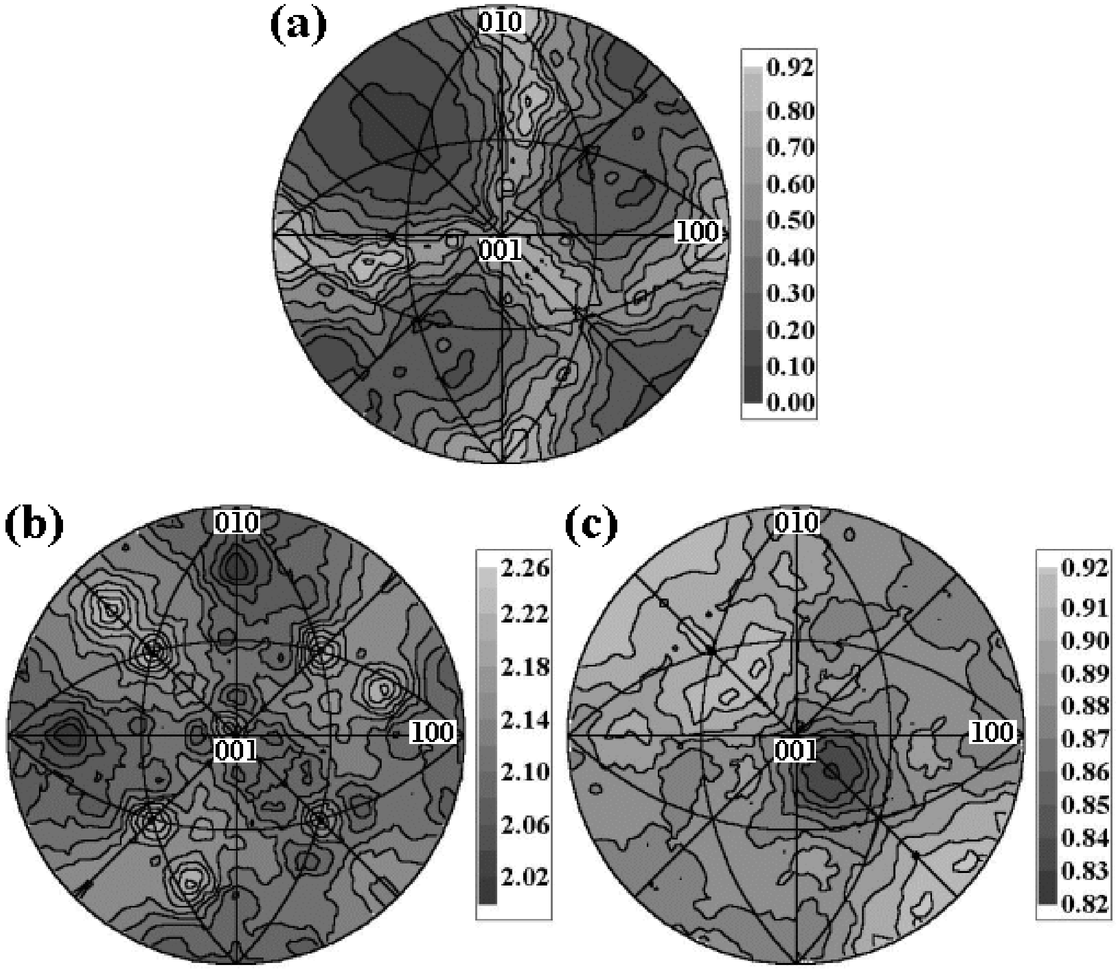

Figure C.19: Grain boundary character and energy distributions for the misorientation corresponding to a 50° rotation about $[110]$. The character distribution is shown in (a), while (b) and (c) show the boundary energy estimated from the surface energies and reconstructed from the triple junction measurements, respectively.

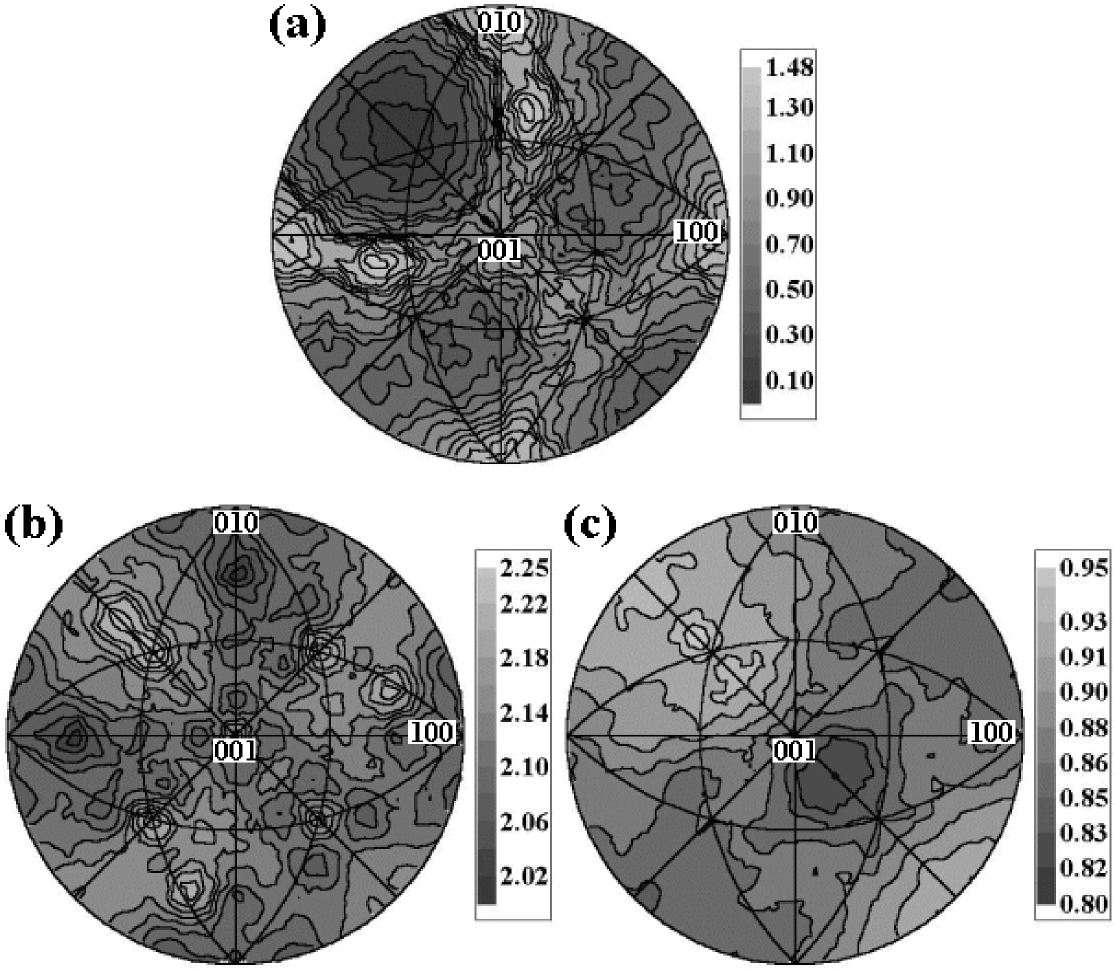

Figure C.20: Grain boundary character and energy distributions for the misorientation corresponding to a 55° rotation about $[110]$. The character distribution is shown in (a), while (b) and (c) show the boundary energy estimated from the surface energies and reconstructed from the triple junction measurements, respectively.

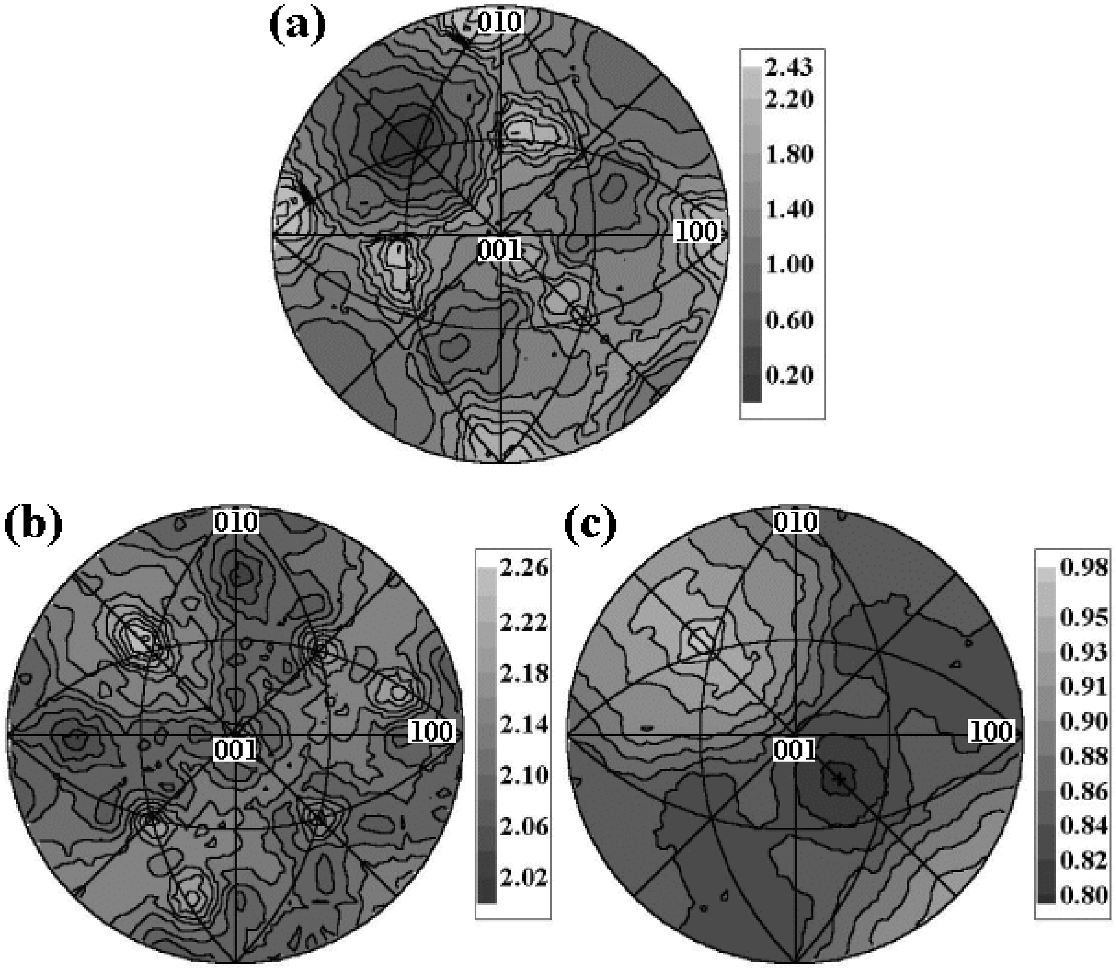

Figure C.21: Grain boundary character and energy distributions for the misorientation corresponding to a 60° rotation about $[110]$. The character distribution is shown in (a), while (b) and (c) show the boundary energy estimated from the surface energies and reconstructed from the triple junction measurements, respectively.

C.3 $[111]$ misorientations

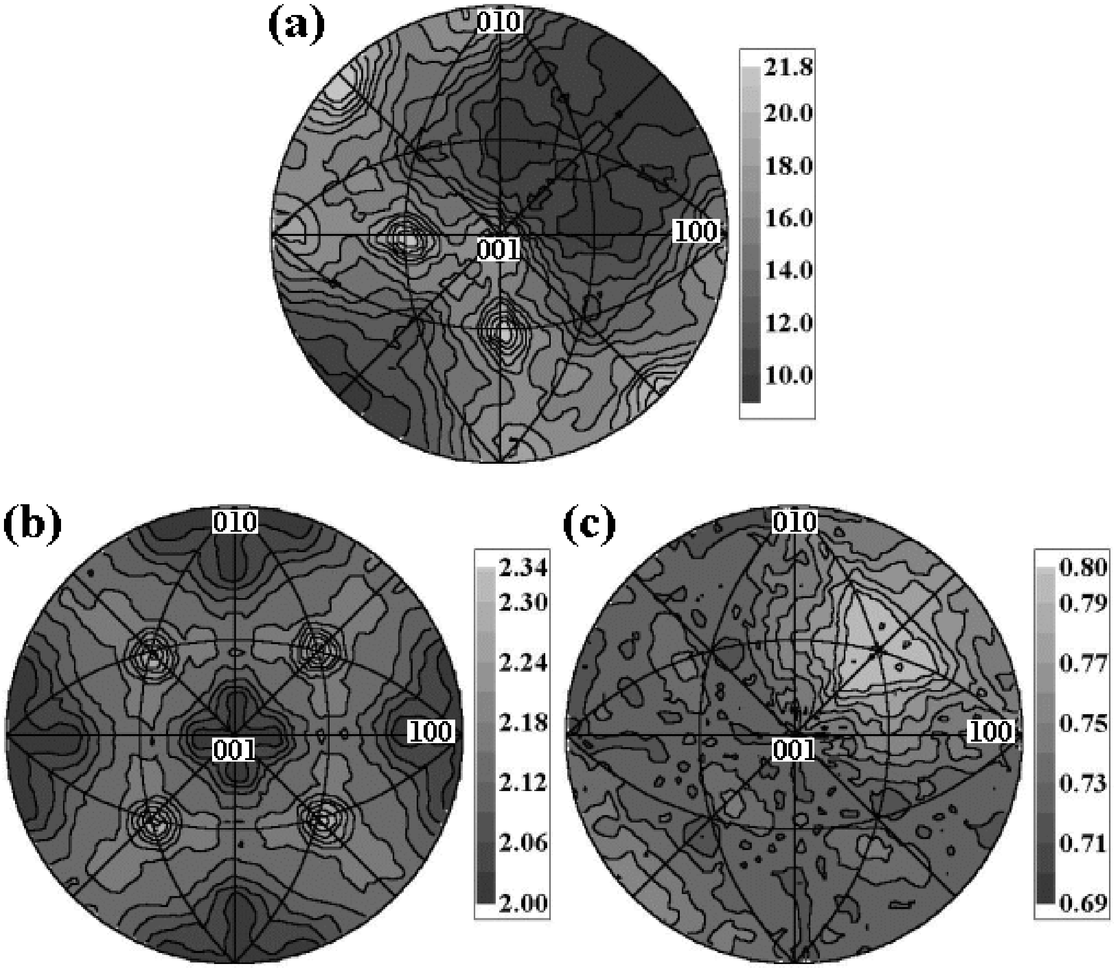

Figure C.22: Grain boundary character and energy distributions for the misorientation corresponding to a 5° rotation about $[111]$. The character distribution is shown in (a), while (b) and (c) show the boundary energy estimated from the surface energies and reconstructed from the triple junction measurements, respectively.

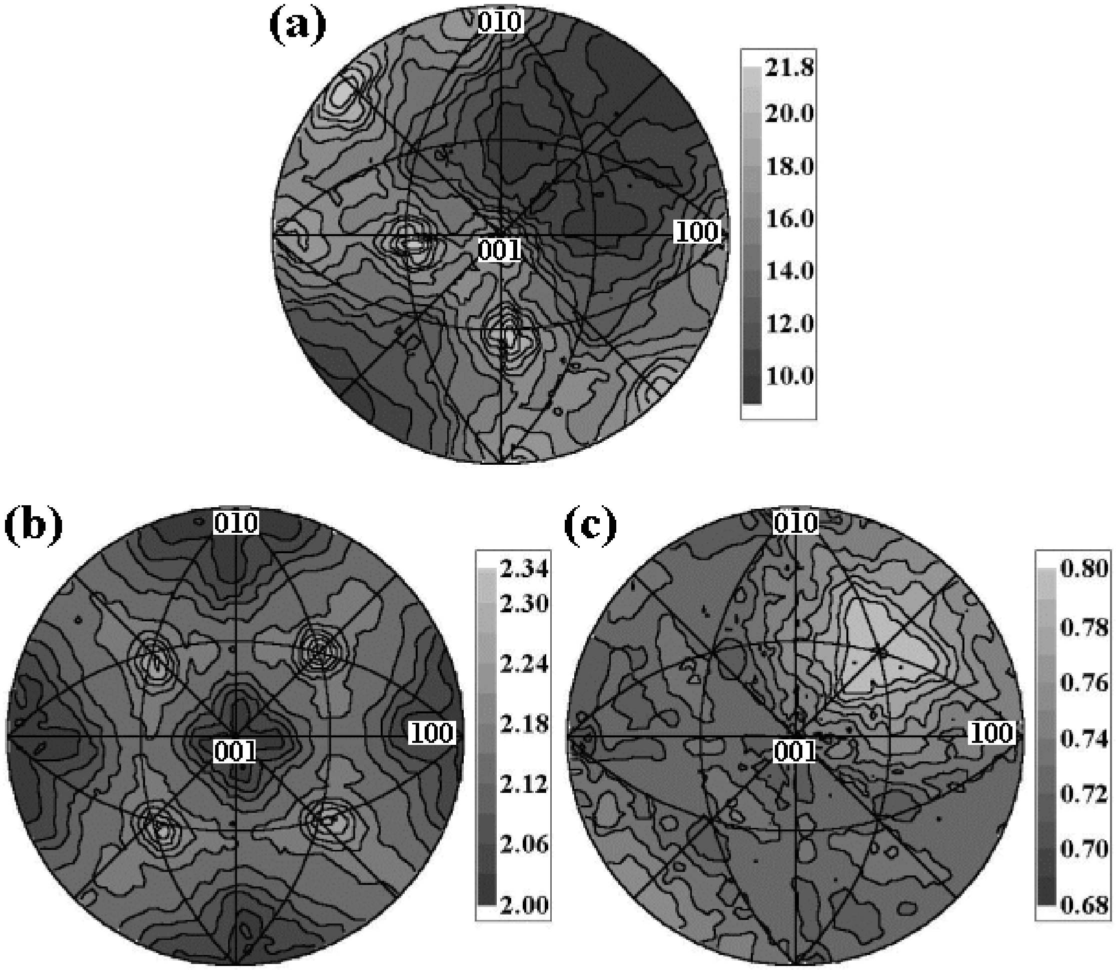

Figure C.23: Grain boundary character and energy distributions for the misorientation corresponding to a 10° rotation about $[111]$. The character distribution is shown in (a), while (b) and (c) show the boundary energy estimated from the surface energies and reconstructed from the triple junction measurements, respectively.

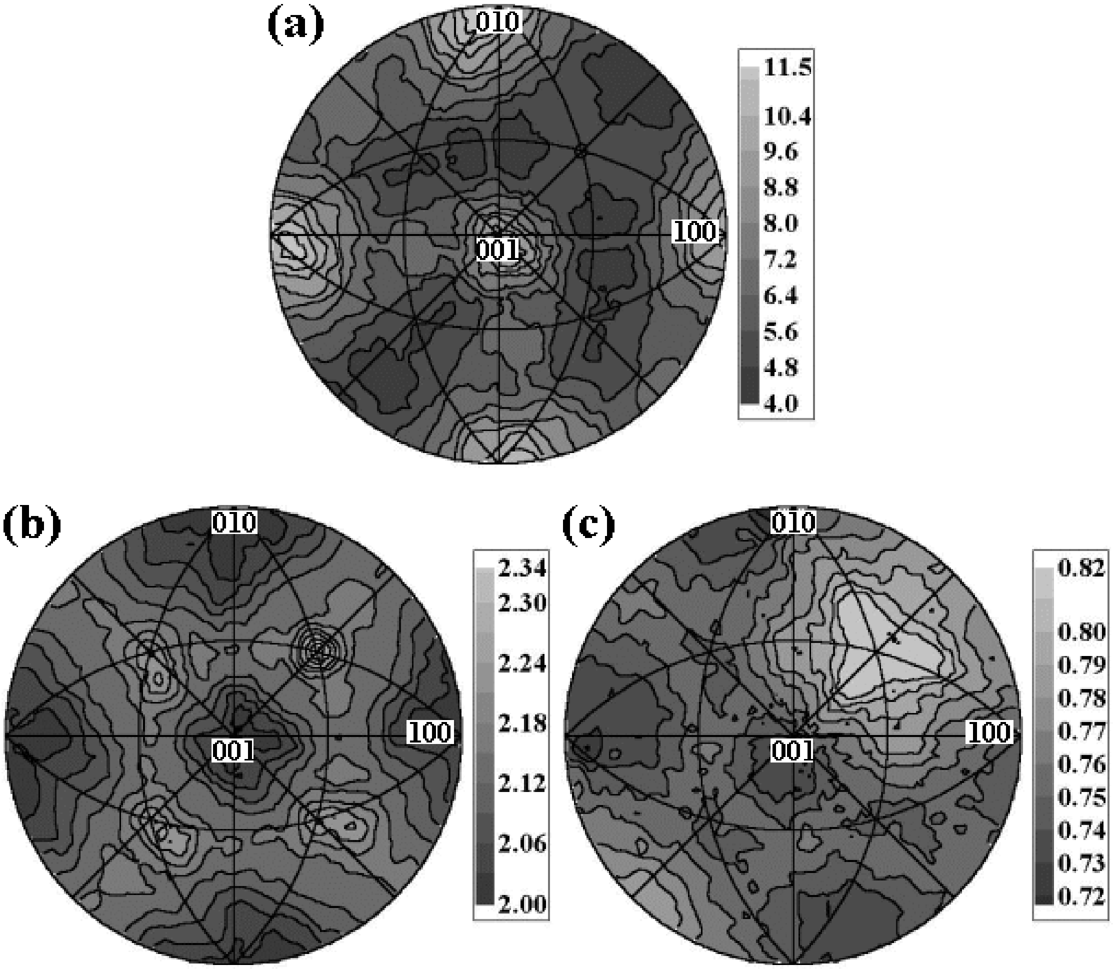

Figure C.24: Grain boundary character and energy distributions for the misorientation corresponding to a $15°$ rotation about $[111]$. The character distribution is shown in (a), while (b) and (c) show the boundary energy estimated from the surface energies and reconstructed from the triple junction measurements, respectively.

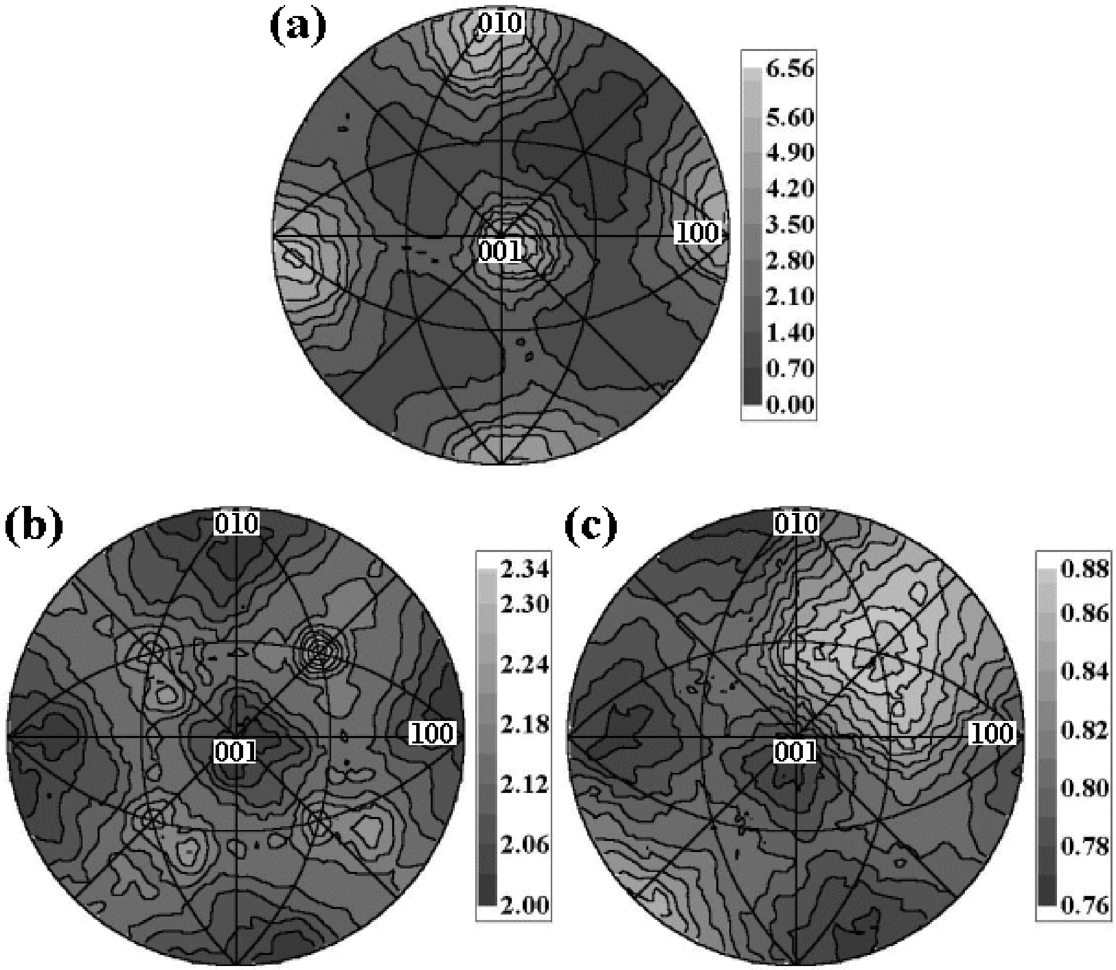

Figure C.25: Grain boundary character and energy distributions for the misorientation corresponding to a 20° rotation about $[111]$. The character distribution is shown in (a), while (b) and (c) show the boundary energy estimated from the surface energies and reconstructed from the triple junction measurements, respectively.

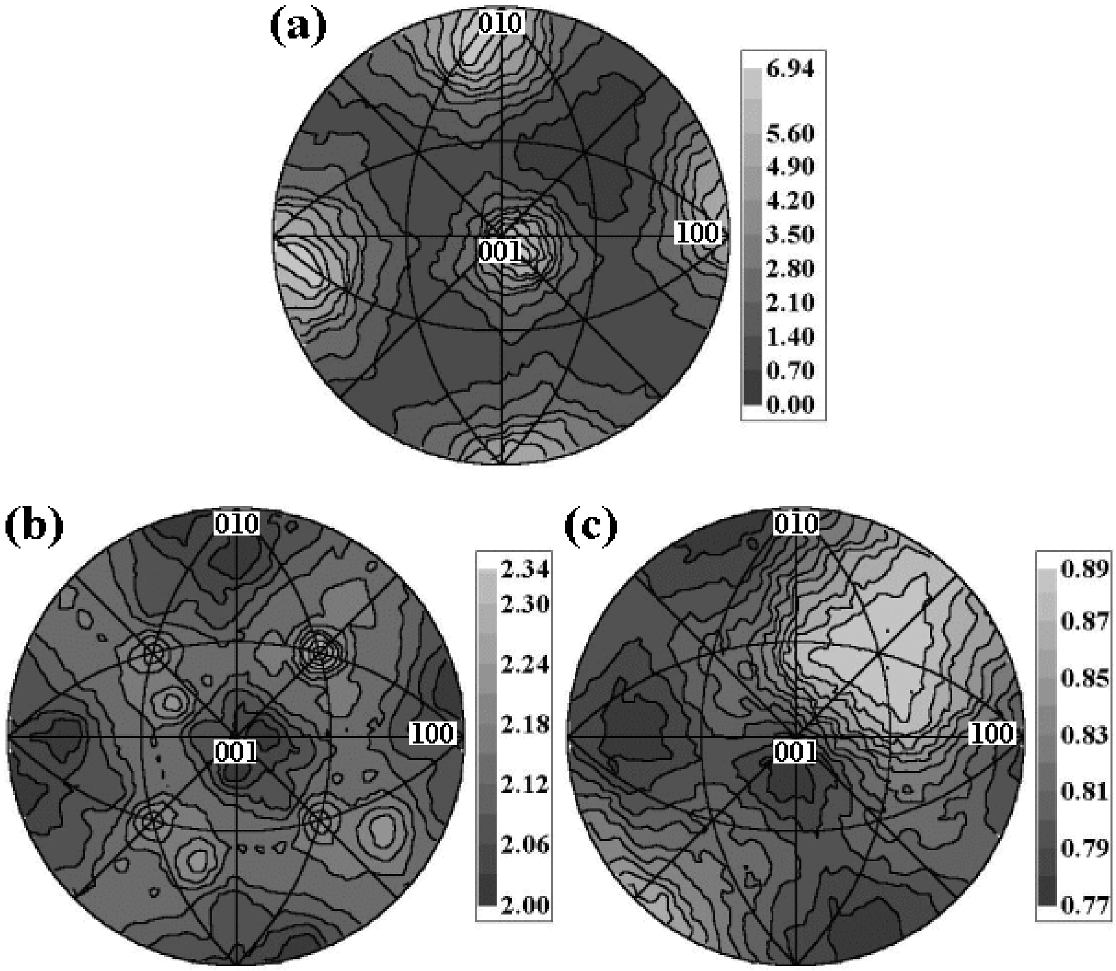

Figure C.26: Grain boundary character and energy distributions for the misorientation corresponding to a 25° rotation about $[111]$. The character distribution is shown in (a), while (b) and (c) show the boundary energy estimated from the surface energies and reconstructed from the triple junction measurements, respectively.

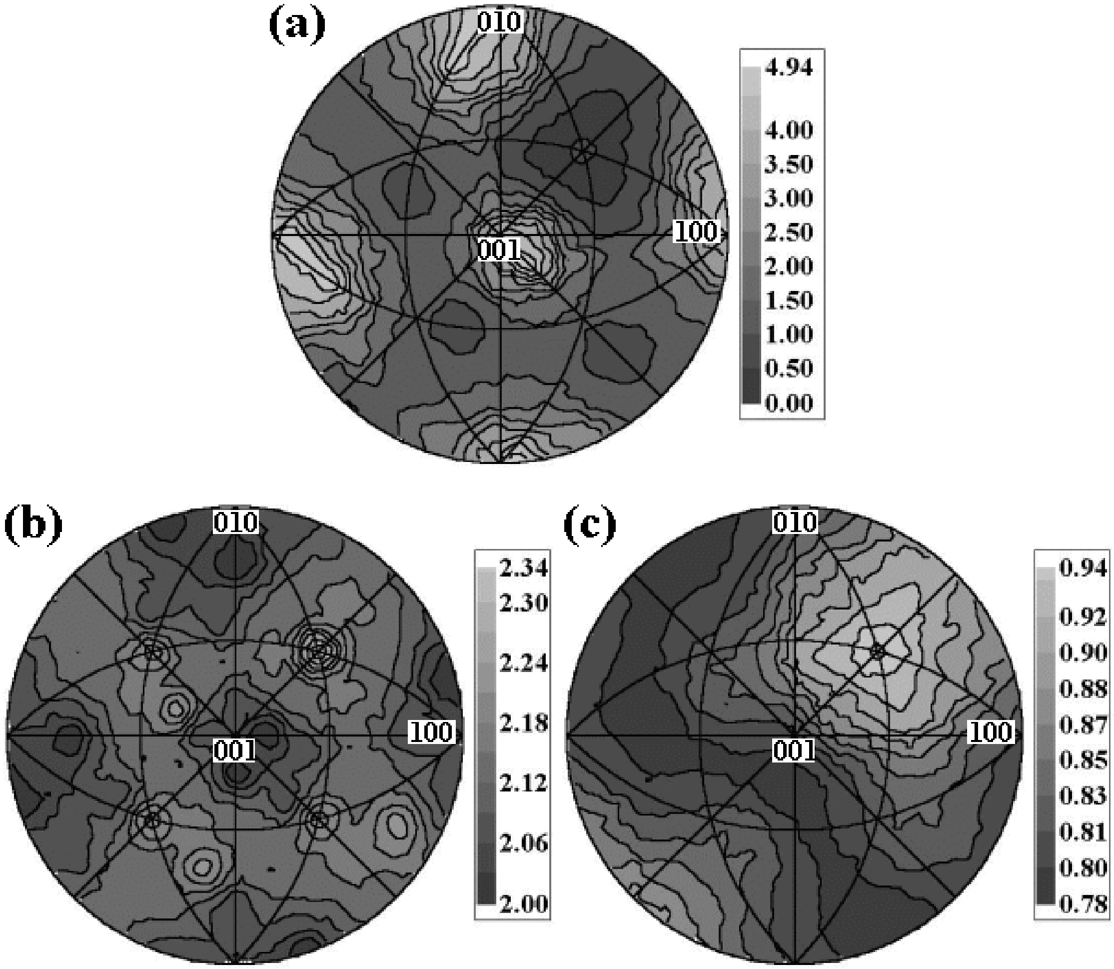

Figure C.27: Grain boundary character and energy distributions for the misorientation corresponding to a 30° rotation about $[111]$. The character distribution is shown in (a), while (b) and (c) show the boundary energy estimated from the surface energies and reconstructed from the triple junction measurements, respectively.

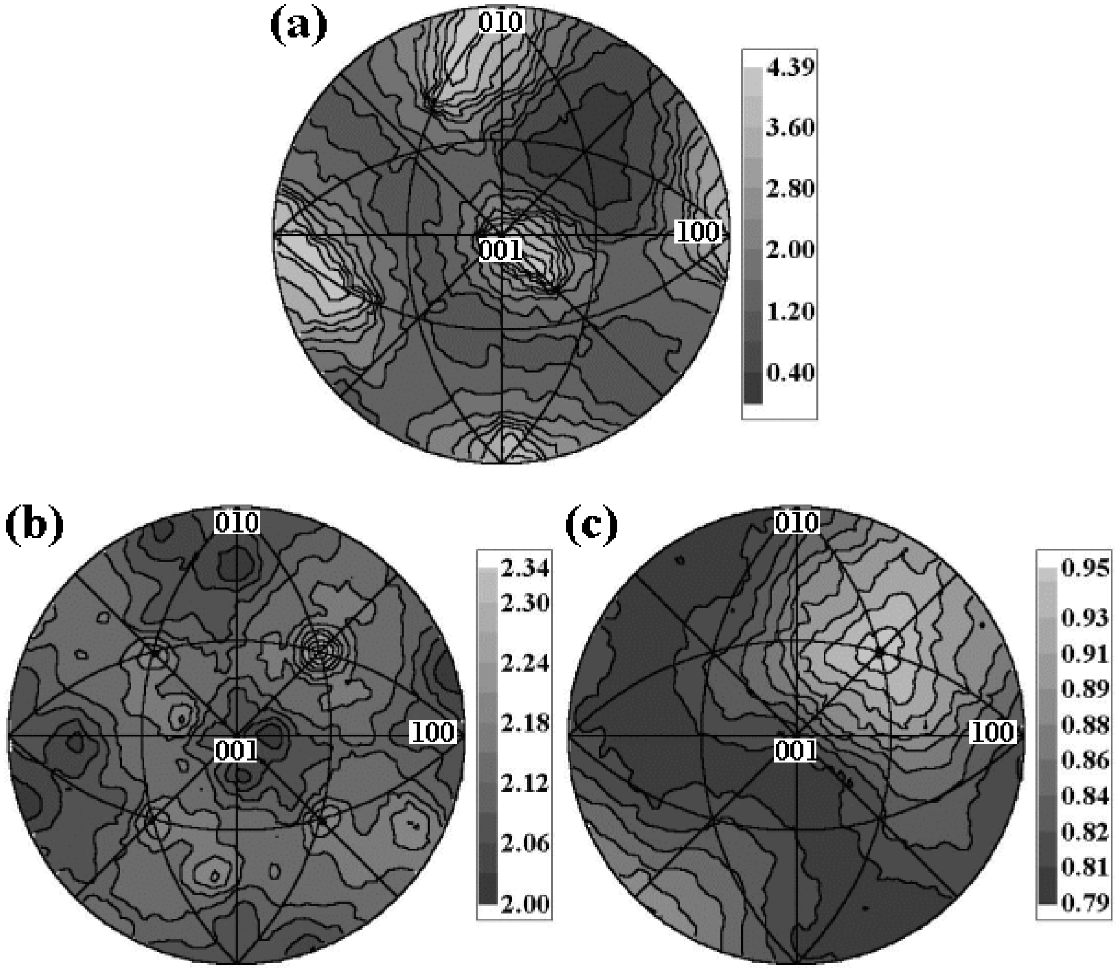

Figure C.28: Grain boundary character and energy distributions for the misorientation corresponding to a 35° rotation about $[111]$. The character distribution is shown in (a), while (b) and (c) show the boundary energy estimated from the surface energies and reconstructed from the triple junction measurements, respectively.

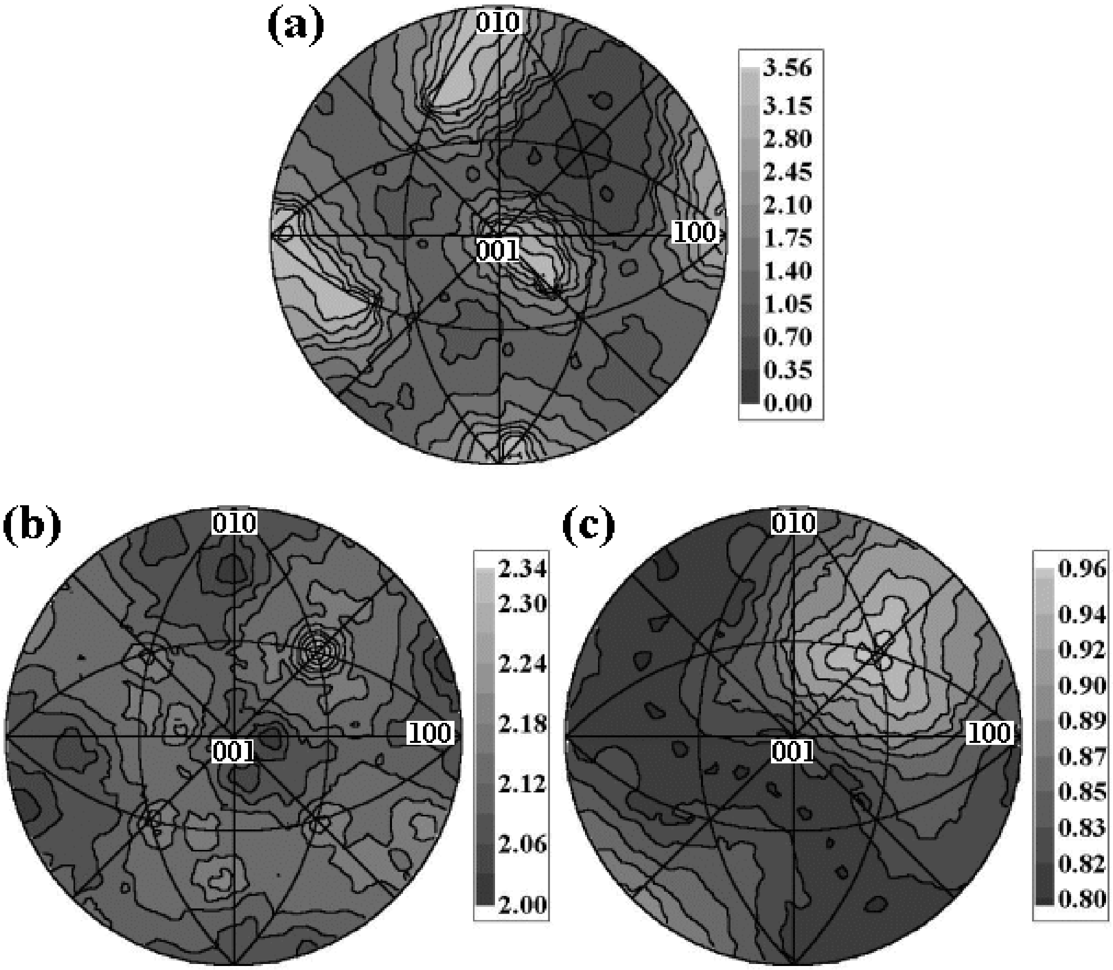

Figure C.29: Grain boundary character and energy distributions for the misorientation corresponding to a 40° rotation about $[111]$. The character distribution is shown in (a), while (b) and (c) show the boundary energy estimated from the surface energies and reconstructed from the triple junction measurements, respectively.

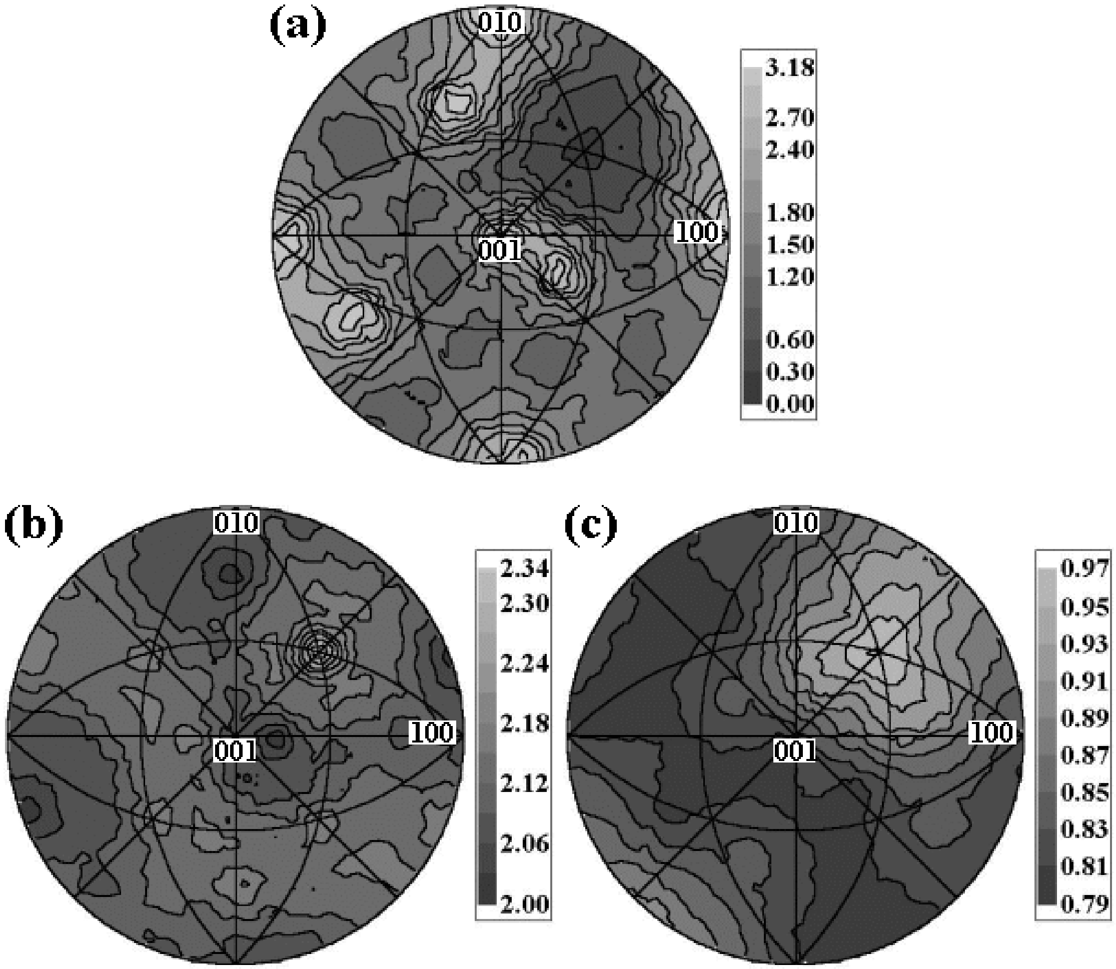

Figure C.30: Grain boundary character and energy distributions for the misorientation corresponding to a 45° rotation about $[111]$. The character distribution is shown in (a), while (b) and (c) show the boundary energy estimated from the surface energies and reconstructed from the triple junction measurements, respectively.

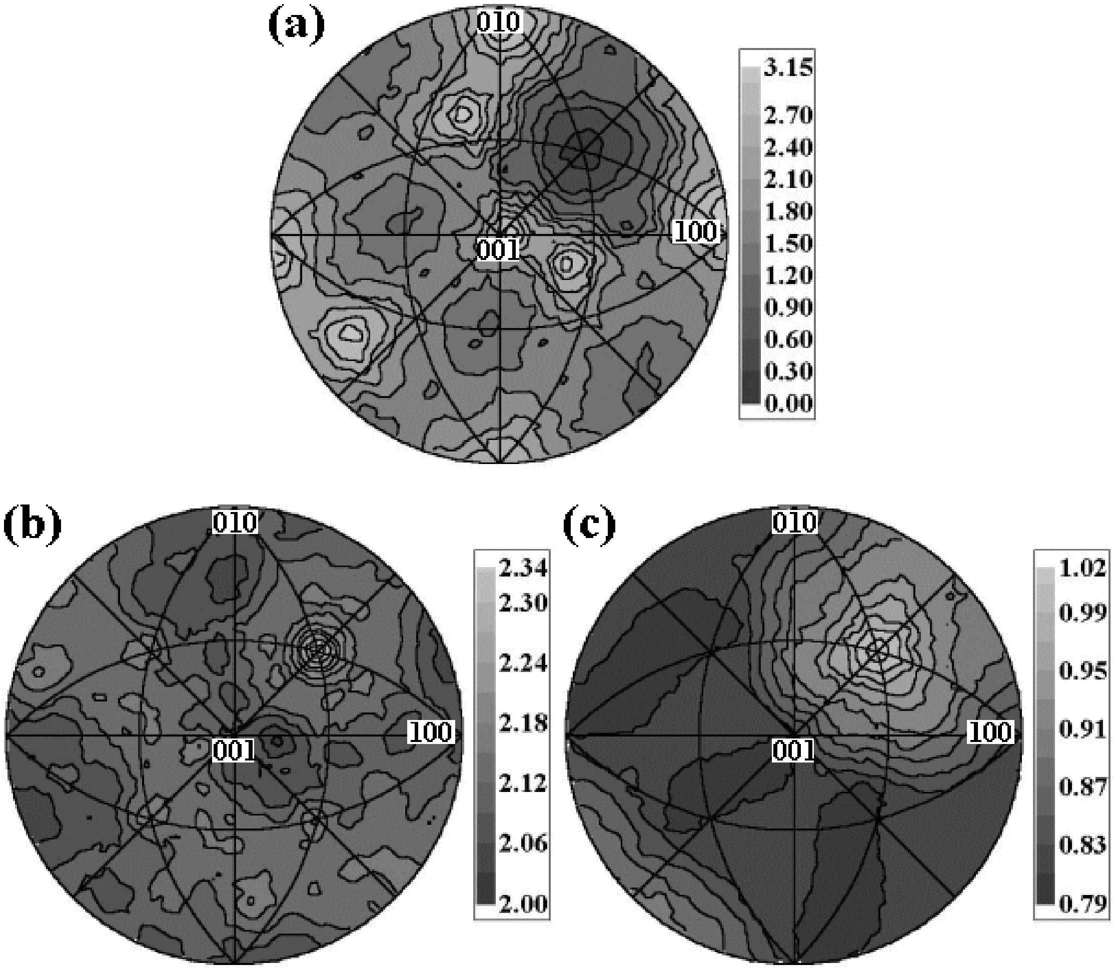

Figure C.31: Grain boundary character and energy distributions for the misorientation corresponding to a 50° rotation about $[111]$. The character distribution is shown in (a), while (b) and (c) show the boundary energy estimated from the surface energies and reconstructed from the triple junction measurements, respectively.

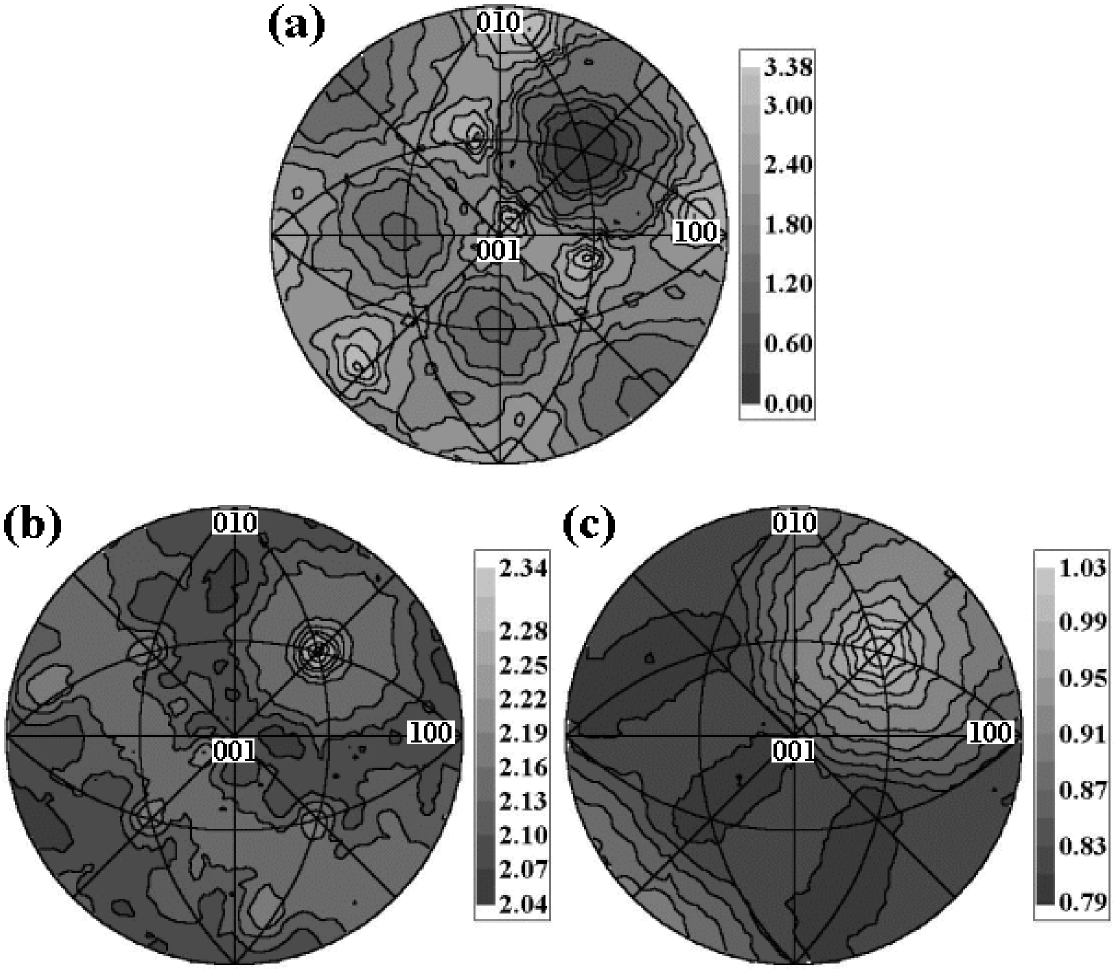

Figure C.32: Grain boundary character and energy distributions for the misorientation corresponding to a $55°$ rotation about $[111]$. The character distribution is shown in (a), while (b) and (c) show the boundary energy estimated from the surface energies and reconstructed from the triple junction measurements, respectively.

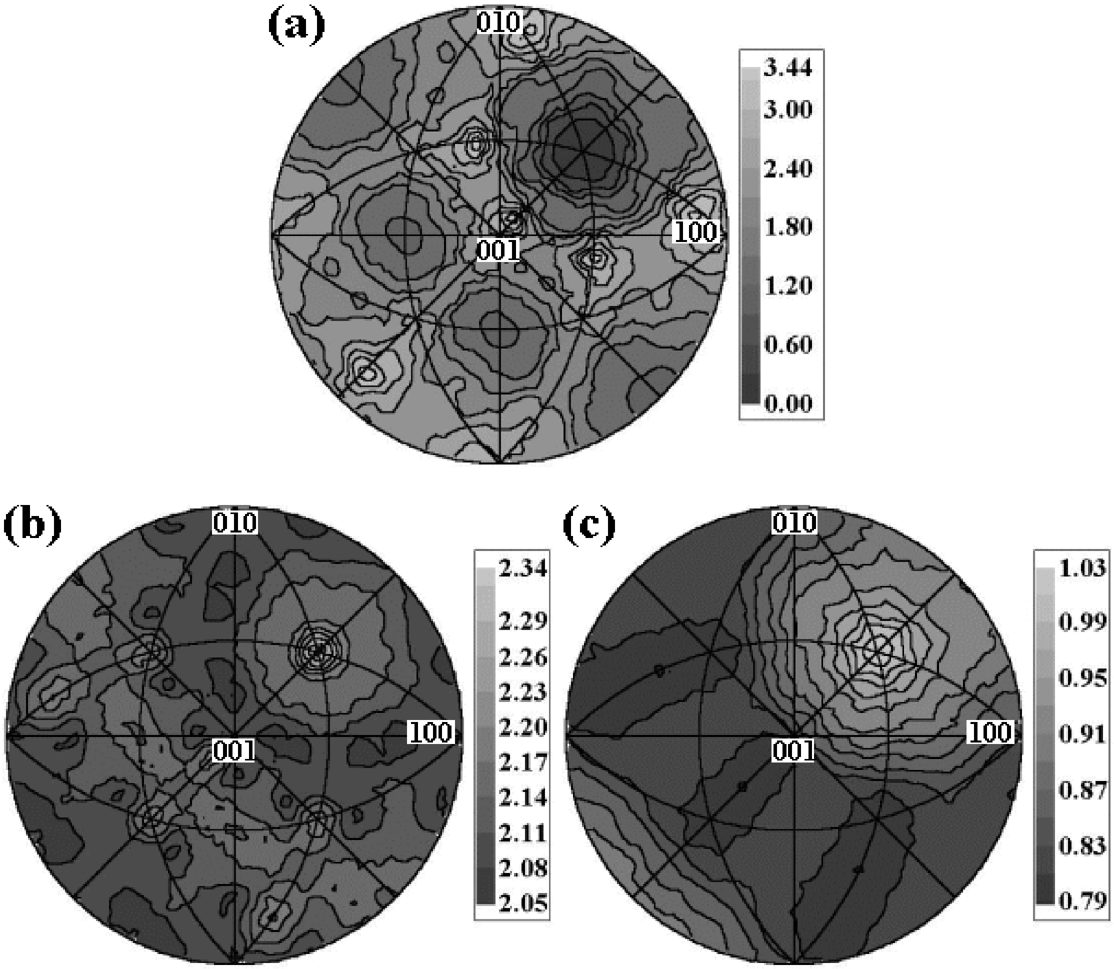

Figure C.33: Grain boundary character and energy distributions for the misorientation corresponding to a 60° rotation about $[111]$. The character distribution is shown in (a), while (b) and (c) show the boundary energy estimated from the surface energies and reconstructed from the triple junction measurements, respectively.

C.4 $[952]$ misorientations

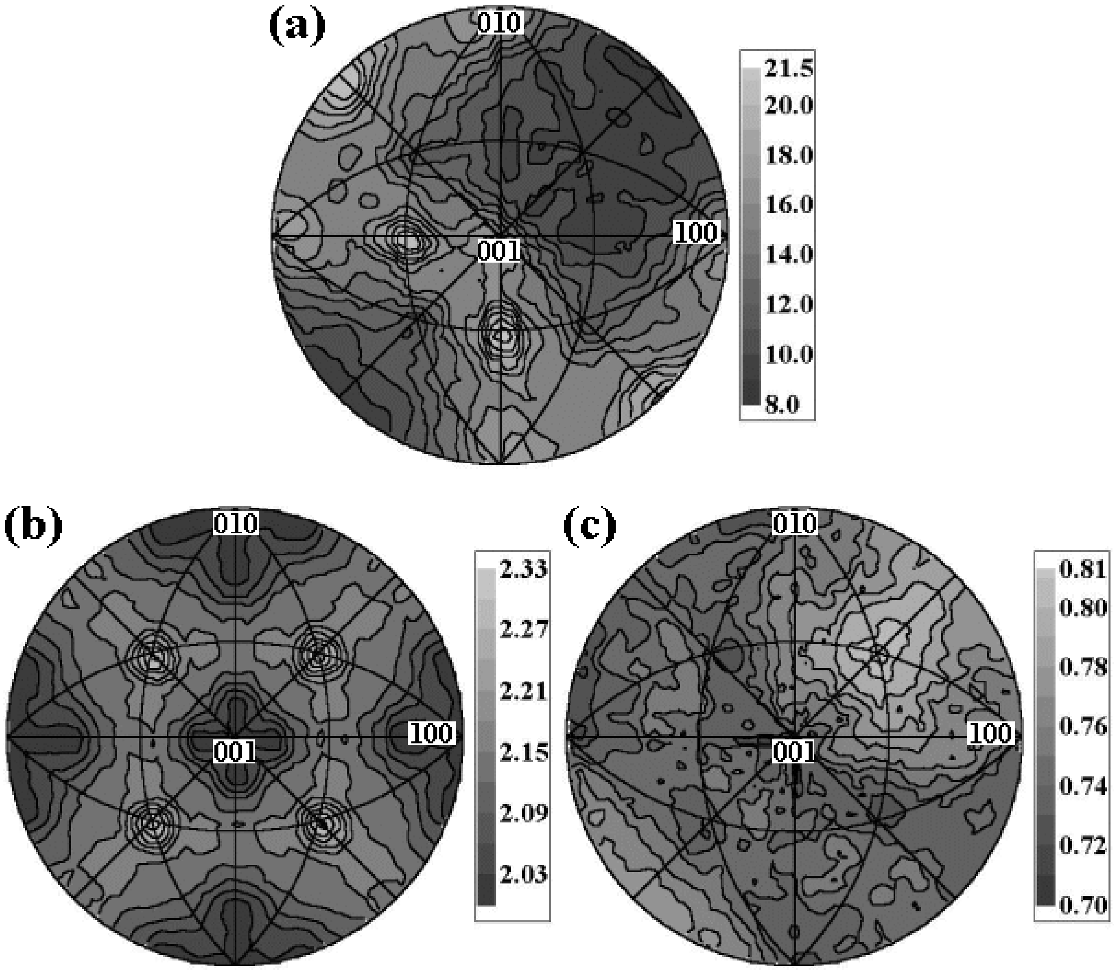

Figure C.34: Grain boundary character and energy distributions for the misorientation corresponding to a $5°$ rotation about $[952]$. The character distribution is shown in (a), while (b) and (c) show the boundary energy estimated from the surface energies and reconstructed from the triple junction measurements, respectively.

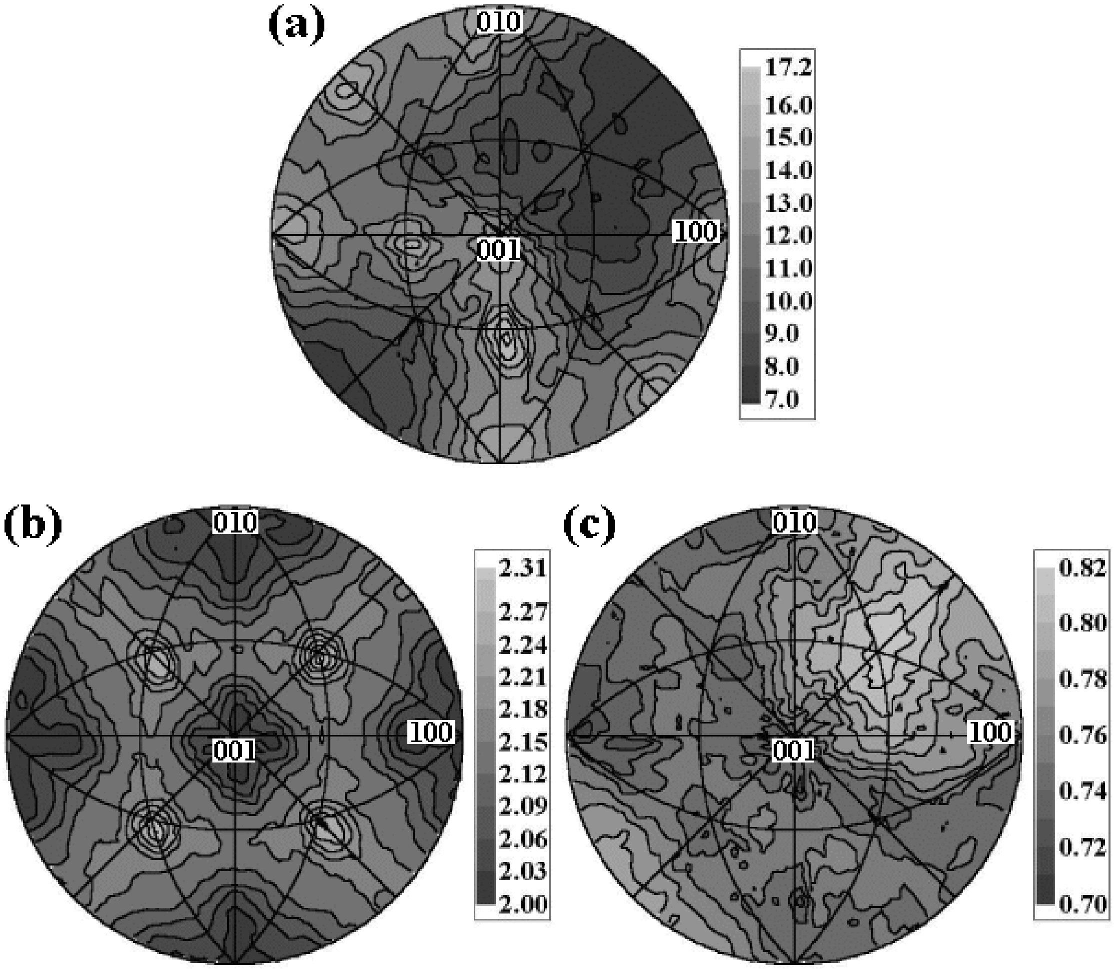

Figure C.35: Grain boundary character and energy distributions for the misorientation corresponding to a $10°$ rotation about $[952]$. The character distribution is shown in (a), while (b) and (c) show the boundary energy estimated from the surface energies and reconstructed from the triple junction measurements, respectively.

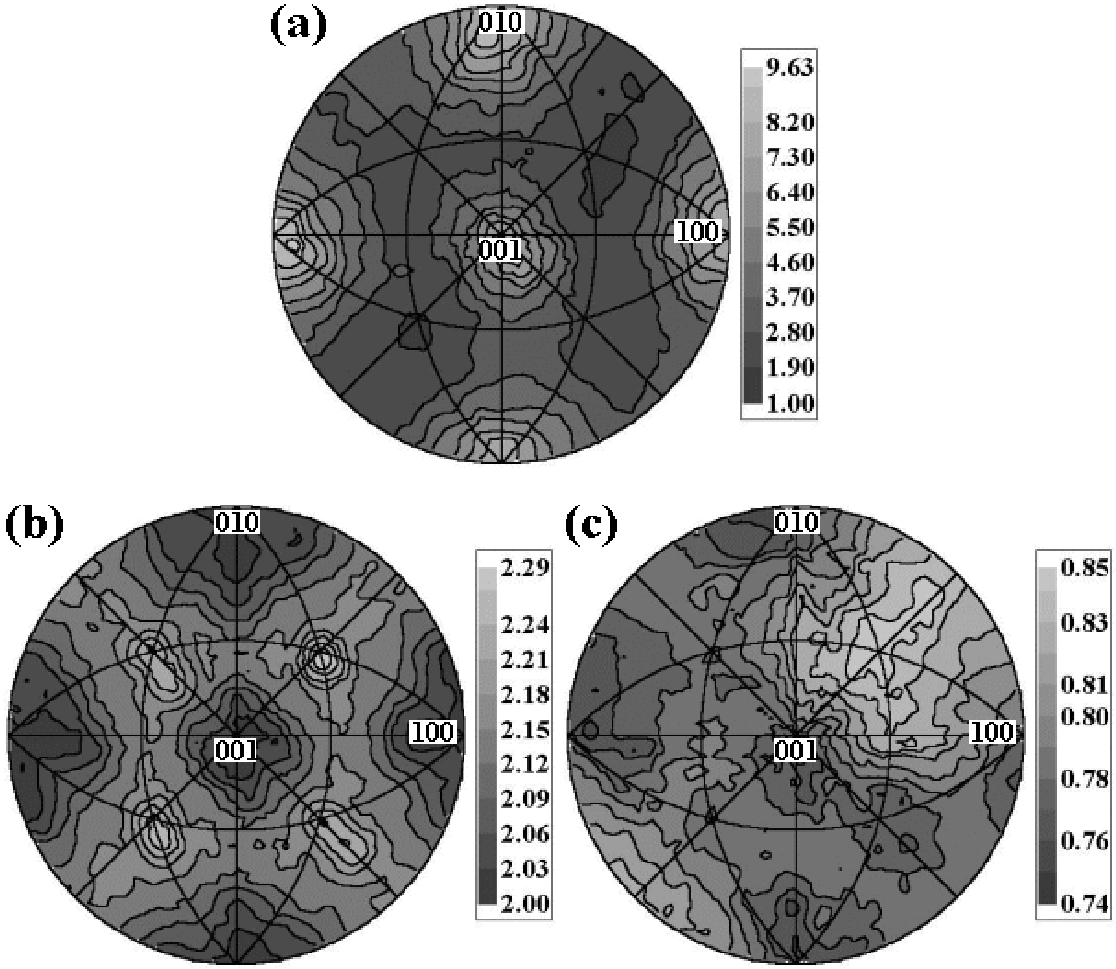

Figure C.36: Grain boundary character and energy distributions for the misorientation corresponding to a 15° rotation about $[952]$. The character distribution is shown in (a), while (b) and (c) show the boundary energy estimated from the surface energies and reconstructed from the triple junction measurements, respectively.

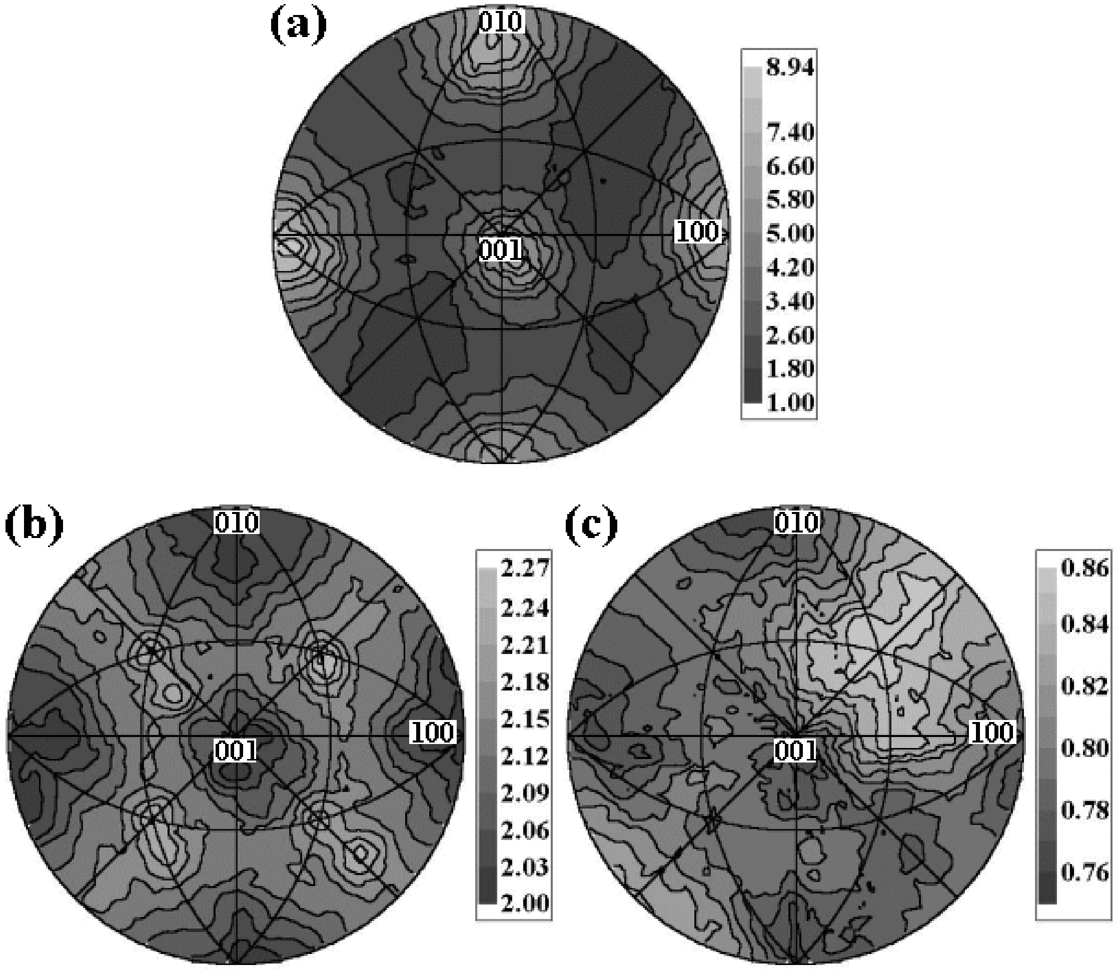

Figure C.37: Grain boundary character and energy distributions for the misorientation corresponding to a 20° rotation about $[952]$. The character distribution is shown in (a), while (b) and (c) show the boundary energy estimated from the surface energies and reconstructed from the triple junction measurements, respectively.

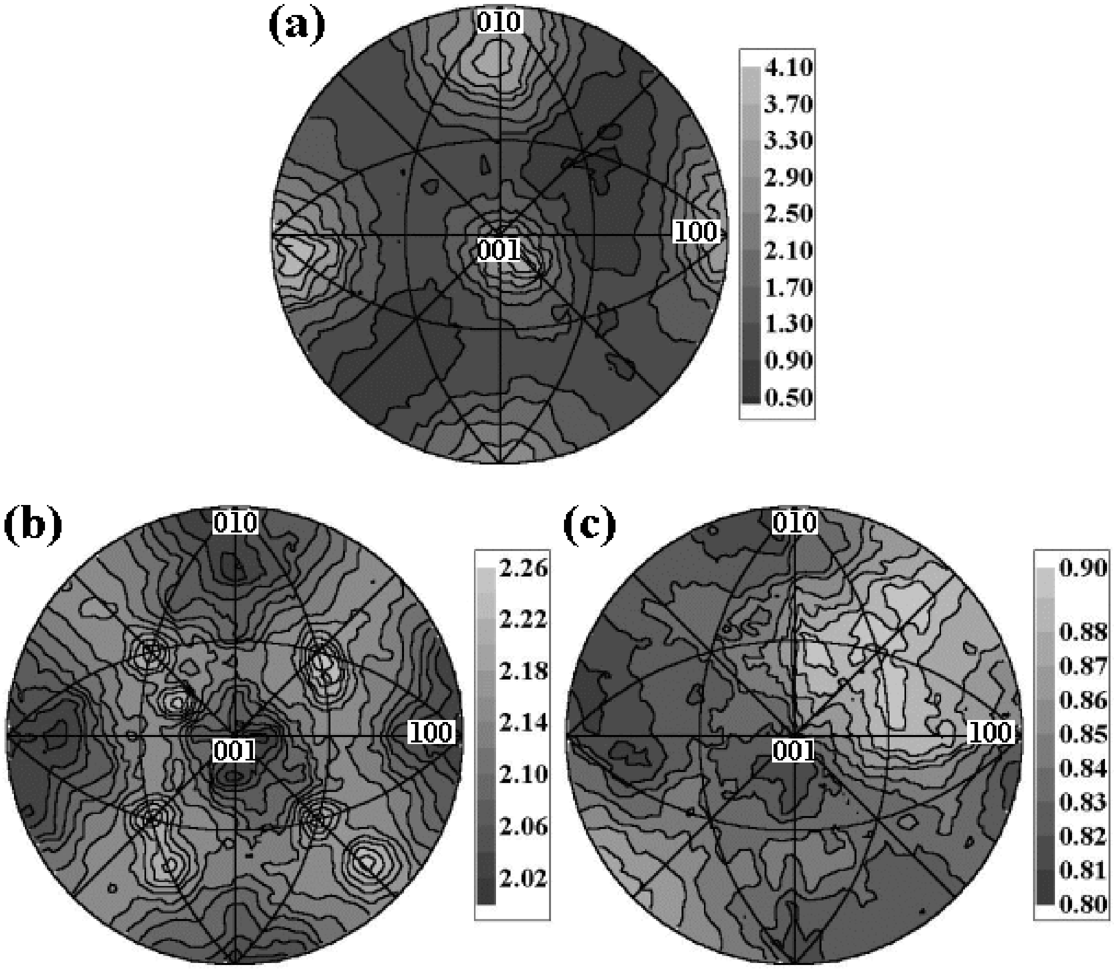

Figure C.38: Grain boundary character and energy distributions for the misorientation corresponding to a $25°$ rotation about $[952]$. The character distribution is shown in (a), while (b) and (c) show the boundary energy estimated from the surface energies and reconstructed from the triple junction measurements, respectively.

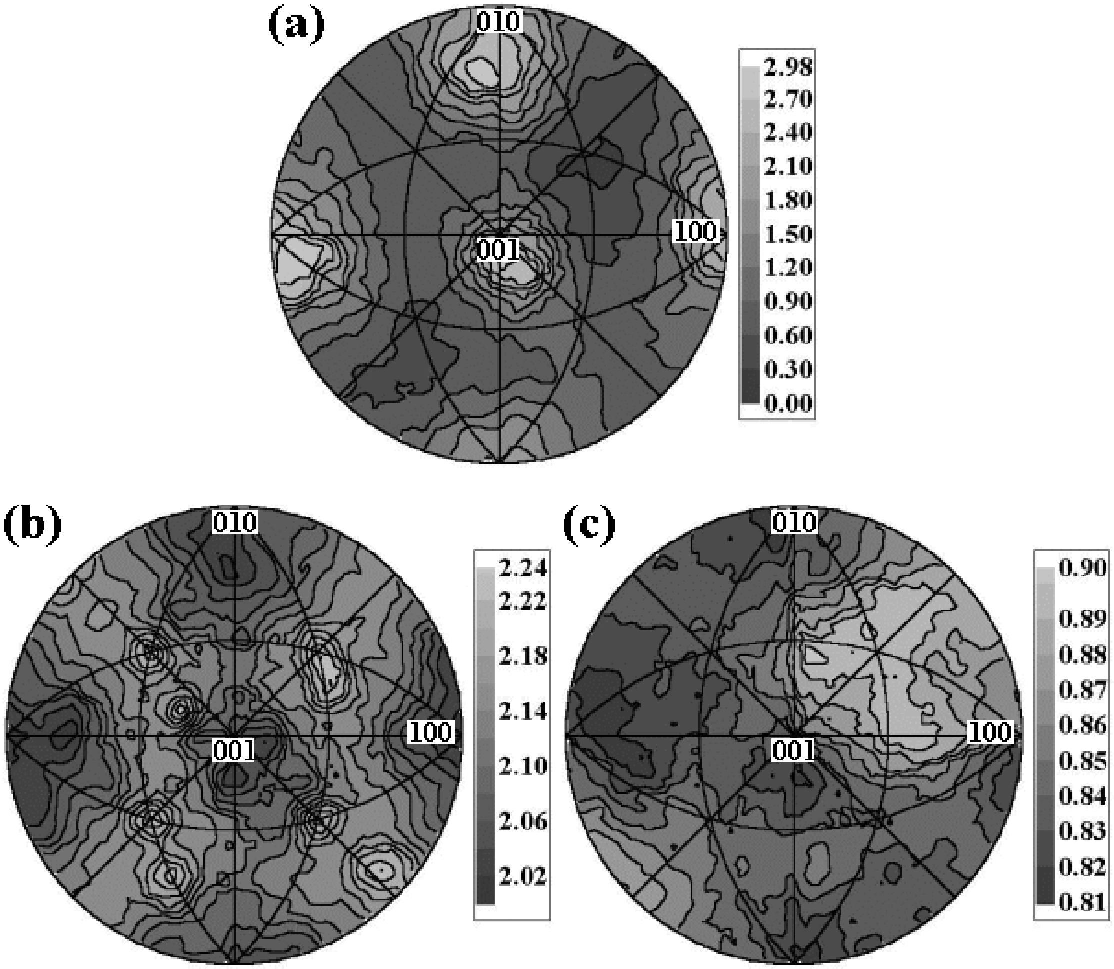

Figure C.39: Grain boundary character and energy distributions for the misorientation corresponding to a 30° rotation about $[952]$. The character distribution is shown in (a), while (b) and (c) show the boundary energy estimated from the surface energies and reconstructed from the triple junction measurements, respectively.

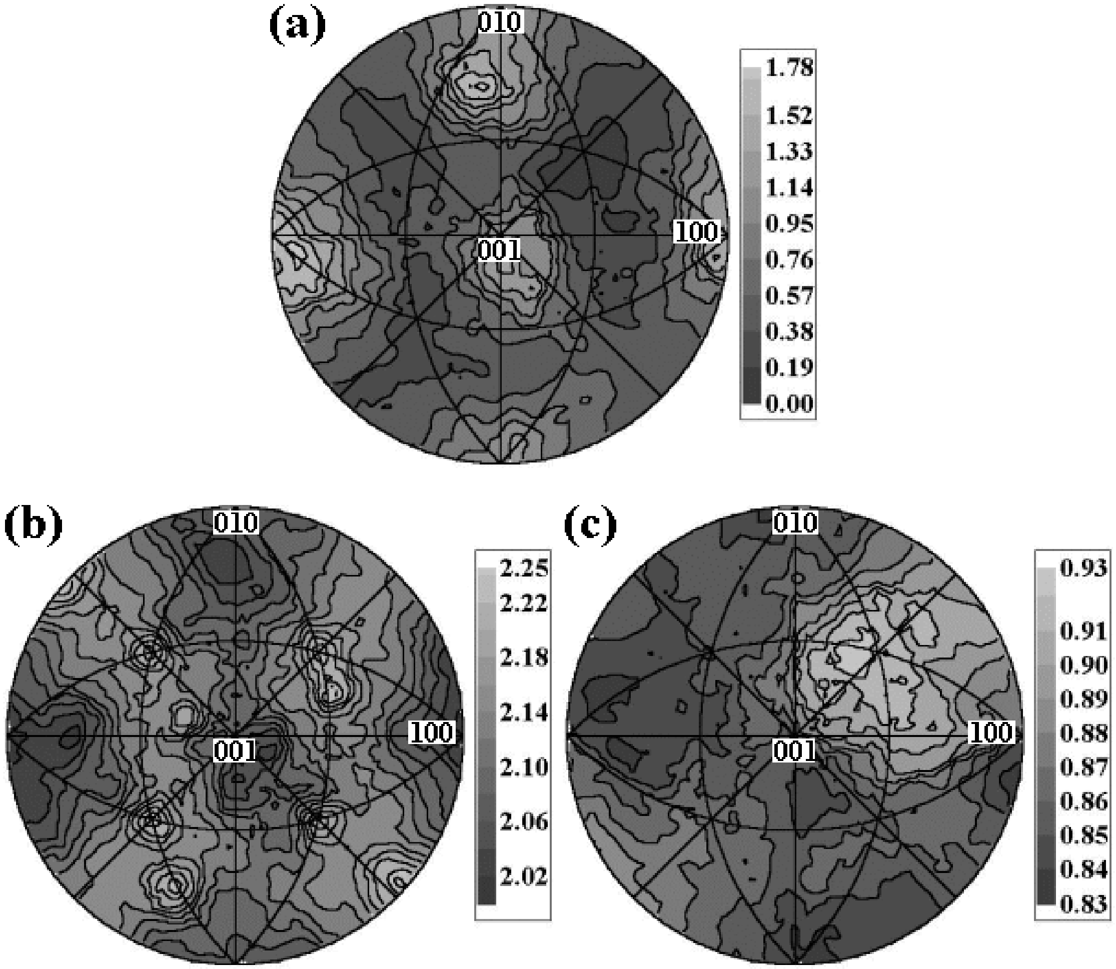

Figure C.40: Grain boundary character and energy distributions for the misorientation corresponding to a 35° rotation about $[952]$. The character distribution is shown in (a), while (b) and (c) show the boundary energy estimated from the surface energies and reconstructed from the triple junction measurements, respectively.

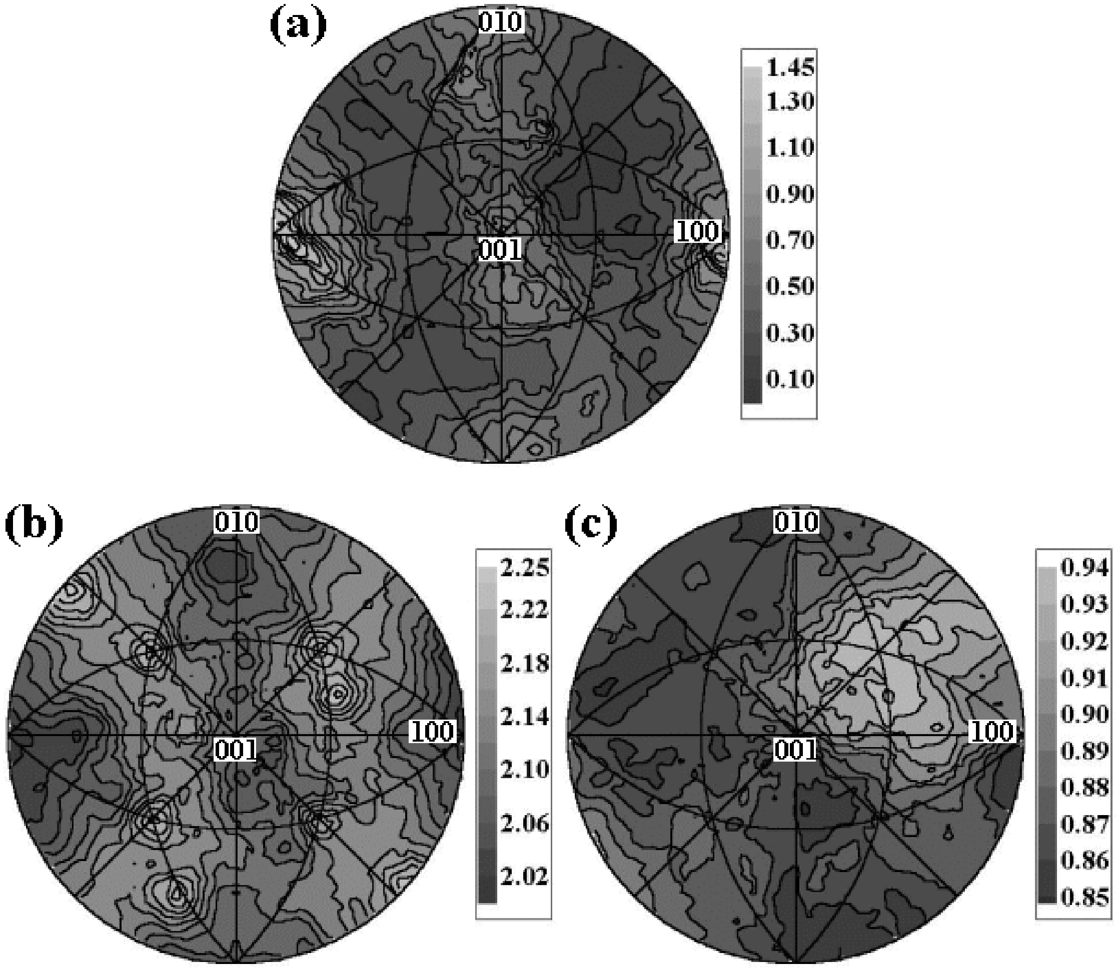

Figure C.41: Grain boundary character and energy distributions for the misorientation corresponding to a $40°$ rotation about $[952]$. The character distribution is shown in (a), while (b) and (c) show the boundary energy estimated from the surface energies and reconstructed from the triple junction measurements, respectively.

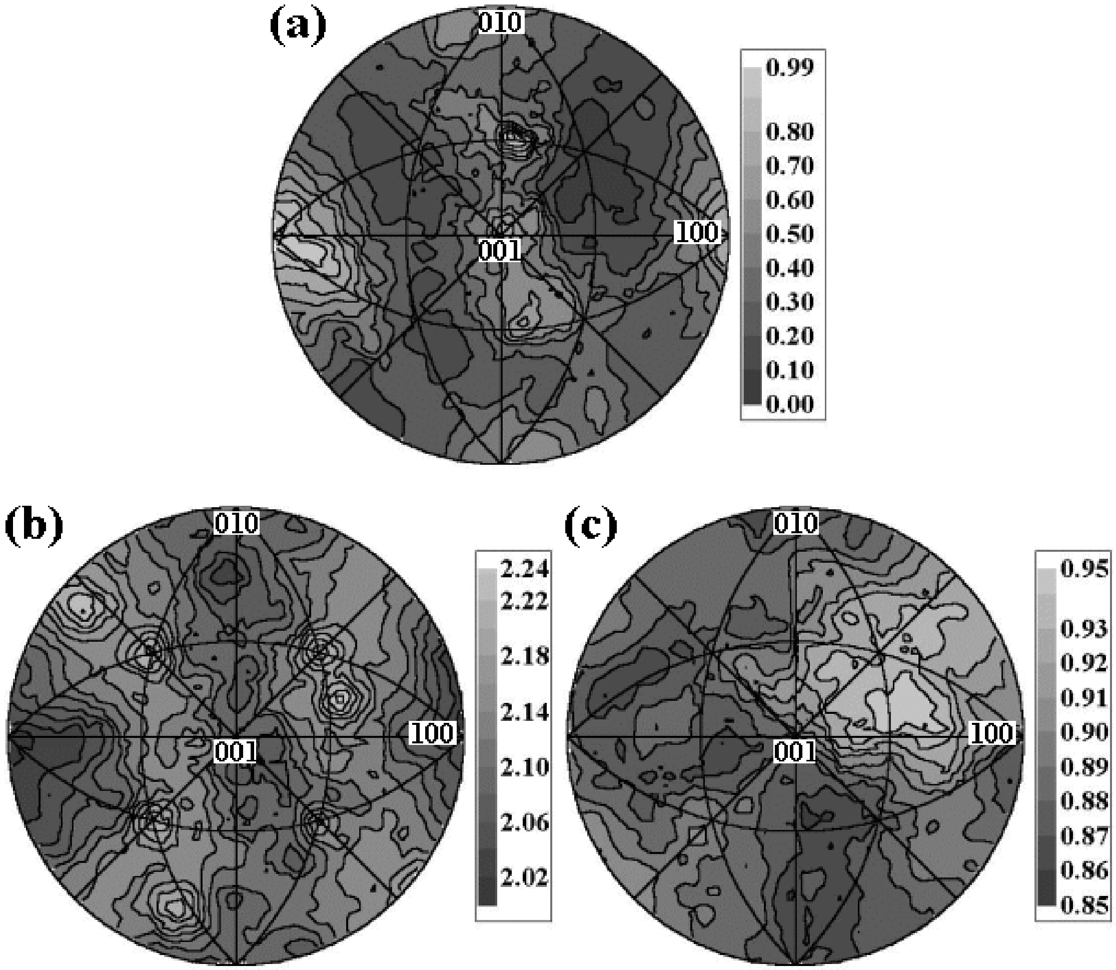

Figure C.42: Grain boundary character and energy distributions for the misorientation corresponding to a 45° rotation about $[952]$. The character distribution is shown in (a), while (b) and (c) show the boundary energy estimated from the surface energies and reconstructed from the triple junction measurements, respectively.

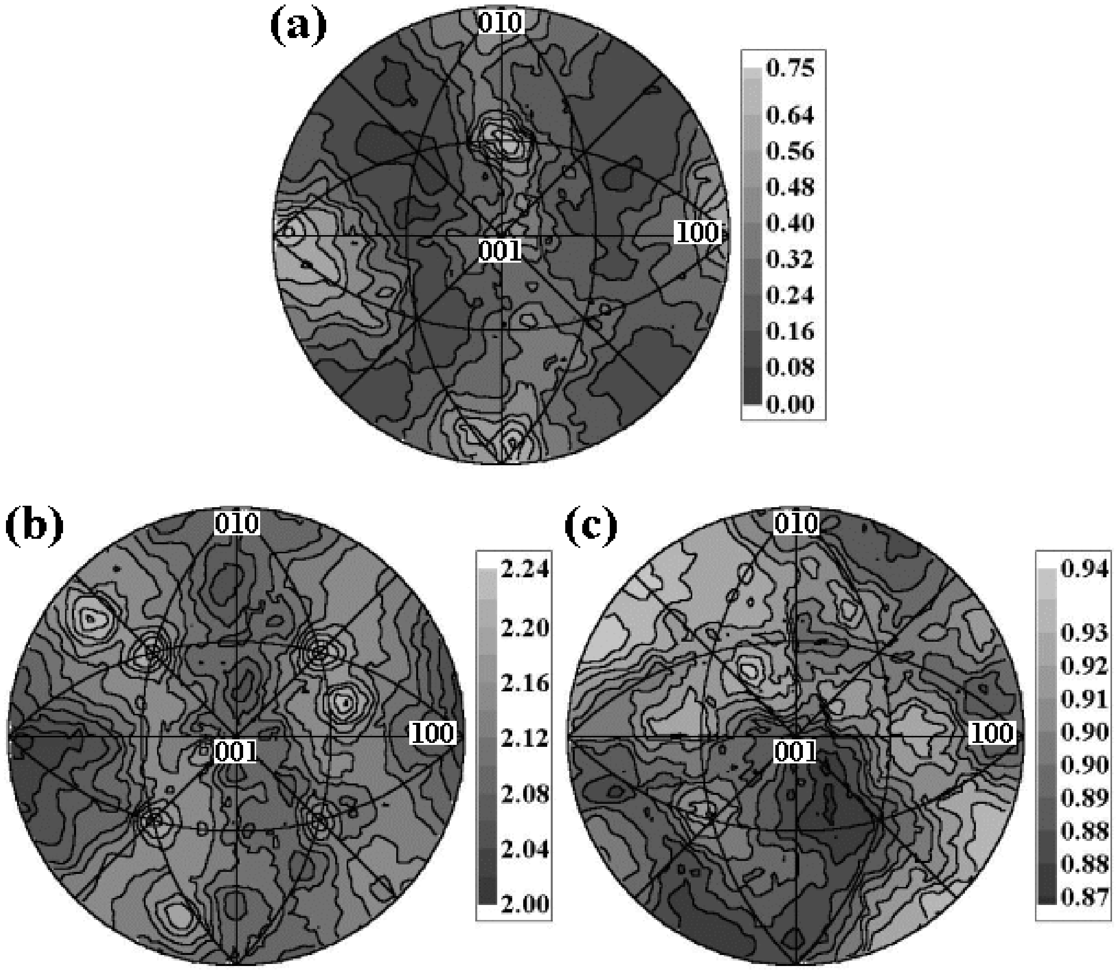

Figure C.43: Grain boundary character and energy distributions for the misorientation corresponding to a 50° rotation about $[952]$. The character distribution is shown in (a), while (b) and (c) show the boundary energy estimated from the surface energies and reconstructed from the triple junction measurements, respectively.

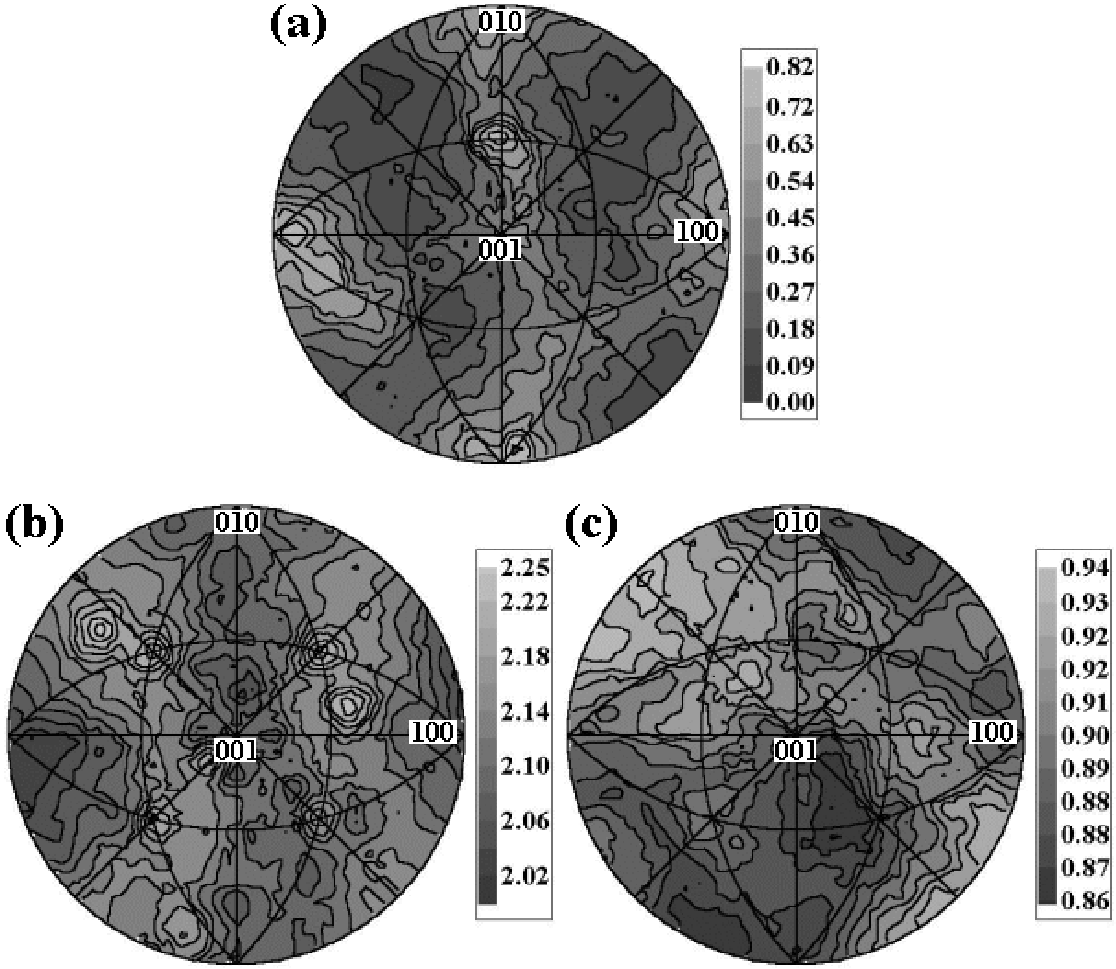

Figure C.44: Grain boundary character and energy distributions for the misorientation corresponding to a 55° rotation about $[952]$. The character distribution is shown in (a), while (b) and (c) show the boundary energy estimated from the surface energies and reconstructed from the triple junction measurements, respectively.

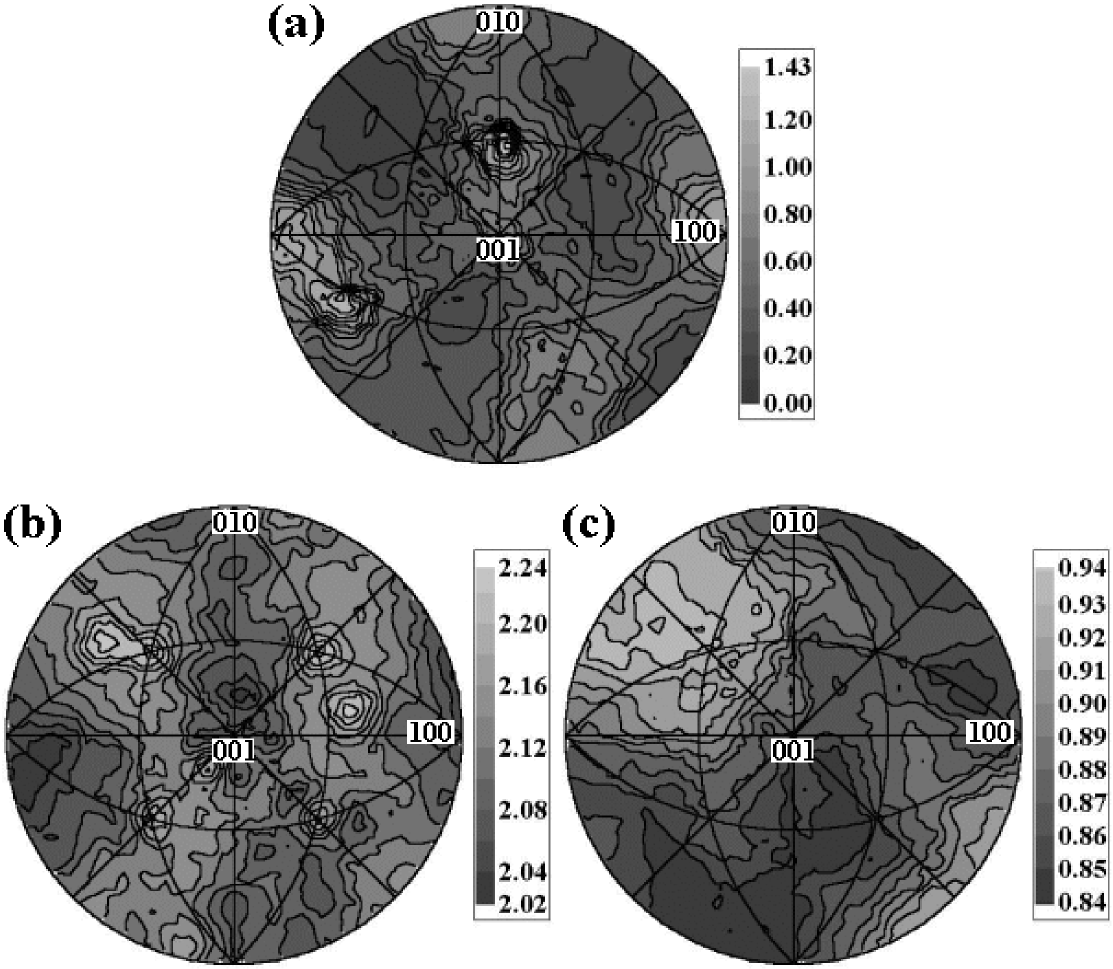

Figure C.45: Grain boundary character and energy distributions for the misorientation corresponding to a 60° rotation about $[952]$. The character distribution is shown in (a), while (b) and (c) show the boundary energy estimated from the surface energies and reconstructed from the triple junction measurements, respectively.